Multiple-Wake Vortex Lattice Method for Membrane-Wing Kites

Master of Science Thesis

Presented for the degree of
Master of Science in Aerospace Engineering

Rachel Leuthold
15 December, 2015

Faculty of Aerospace Engineering · Delft University of Technology

"[T]he two sisters... had in time come to share many enthusiasms, most especially a fondness for aeolian machines. Margaret and Isobel had fashioned their own pinwheels, weather vanes, and toy sailboats. They'd constructed soaring paper birds and fluttering parchment butterflies. They'd stretched red silk handkerchiefs on birch-wood frames, launching each kite to such an altitude that it became an ominous crimson comet hanging in the Mistley sky...

"Isobel... was a small woman, compact as a stone, intense as an owl. ***'[We] took our pastimes seriously, child. We ne'er confused fun with frivolity.'"***

JAMES MORROW, *The Last Witchfinder*
Harper Collins, New York, NY, USA, 2006.

TU Delft

Delft University of Technology
Faculty of Aerospace Engineering
Department of Aerodynamics, Wind Energy, Flight Performance and Propulsion
Wind Energy Chair

The undersigned hereby certify that they have read and recommend to the Faculty of Aerospace Engineering for acceptance a thesis entitled **Multiple-Wake Vortex Lattice Method for Membrane-Wing Kites**, by **R. C. Leuthold**, in partial fulfillment of the requirements for the degree of **Master of Science**.

15 December, 2015

Supervisor:	Dr.-Ing. Roland Schmehl
Potential Flow Methods:	Dr.Ir. Carlos Simao Ferreira
Aeroelasticity:	Dr.Ir. Alexander van Zuijlen

Abstract

The leading edge inflated (LEI) surf-kite is a suitable wing design for pumping kite power generation because the bridling and leading edge design allow the wing to be de-powered while retaining good steer-ability.

Current LEI kite design is typically empirical. Fluid-Structure Interaction (FSI) modelling is necessary to decrease design time [183] and gain insight into the physical processes driving kite performance.

Unfortunately, the current kite aerodynamic models do not meet the requirements for LEI-kite FSI modelling: they are either fast but insufficiently accurate, or accurate but computationally expensive. In particular, the current fast aerodynamic models are not able to represent the effects of the multiple flow separation regions - such as behind the LEI tube and above the canopy's trailing edge - inherent to a LEI kite flying at a large range of angles of attack.

It is well established that 2D multiple wake vortex models can model multiple separation regions over membranes (de Matteis & de Socio [47]; Wilkinson [196]; Cyr & Newman [43]; Bailey et al [21]; Shukla & Eldredge [160]). Consequently, it is probable that a multiple-wake vortex lattice method (VLM_{MW}) could model the multiple separation regions expected on a 3D membrane-wing surf-kite. To the author's present knowledge, no such VLM_{MW} aerodynamic model has yet been constructed for 3D membrane-flow problems.

This master's thesis is intended to evaluate the hypothesis that a quasi-steady multiple-wake vortex lattice method can quickly and accurately model surf-kite aerodynamics to generate aerodynamic surface load distributions.

This VLM_{MW} models the vorticity generation in the flow with multiple vortex lattices shed from the separation locations, as well as the standard bound vortex lattice. The separation locations are fixed at known locations. The VLM_{MW} uses the Vatistas Core Model to allow for simple comparisons between different vortex models, as used by Sebastian & Lackner [157]. The impermeability boundary conditions allow for membrane deformation such that the model could be used for FSI functions.

The pressure distributions generated by the VLM_{MW} have been compared to experimental measurements from flat plates at high angles of attack. Further, the aerodynamic coefficients have been compared to the 3D Lifting Line model and 3D steady-state Reynolds-Averaged Navier-Stokes (RANS) simulation results of an arc-shaped Clark Y wing, calculated by Leloup [105] and Maneia [120]. Finally, the pressure distribution and aerodynamic coefficients have been compared to the 3D steady-state RANS results of one of the TU Delft Airborne Wind Energy (AWE) group's LEI kites, as determined by Deaves [51].

The VLM_{MW} is strongly limited, in the case of thickness-free surfaces like membrane-wing kites, by an inability to enforce the Kutta condition on a reattachment-line when this reattachment-line crosses a separation-line. Further, the model appears to require - near a reattachment-location - a very high body- and wake-resolution to extend the proper enforcement of the flow-tangency constraint to the space between the collocation points and ensure that geometric surfaces are impermeable to the separation stream-surfaces.

However, it appears that a careful selection of resolution parameters for the LEI-kite geometry can bring double-wake model errors for net lift and drag coefficient predictions with the VLM_{MW} to approximately ten percent of the RANS simulation results. That is, it appears possible for the VLM_{MW} to have the same order of uncertainty with respect to RANS results as is generated by the geometric approximations made in the TU Delft AWE group's RANS studies of 3D LEI kites [51]

The author believes that with further development the LEI-kite aerodynamic modelling method tested in this proof-of-concept thesis could be a useful module within the AWE's FSI-modelling code-base. However, in its current form, good engineering judgement is necessary to restrict the use of the VLM_{MW} to situations where flow-reattachment is either avoided or does not coincide with a separation-location, and where boundary-layer effects are small.

Acknowledgments

There are a number of people without whom this thesis would not have been possible.

First, thank you to Dr.-Ing. Roland Schmehl, who introduced me to the field of kite-power. Since first taking his course, he has truly been a mentor, encouraging both my interest in the complex physical behaviors of LEI-kites and my professional growth. Thank you for lending all of the time, energy, and problem-solving experience without which my work in the kite-power group would certainly have stalled.

Thank you to Dr.Ir. Carlos Simao Ferreira for taking such an interest in this thesis project outside of any obligation. His support and patient problem-solving methodology were critical in the development of this thesis work.

I'd like to express my gratitude to Prof. Dr. Moritz Diehl, for the motivating example of his curiosity and the inspiration given by a fresh viewpoint. I'm also very thankful for the help of Prof. Dr. Gerard van Bussel, who gave me the key to resolving my last sticking point.

I am, further, grateful to two PhD candidates for the advice and planning from which this project was born: Ir. Gaél de Oliveira Andrade and Will Anderson, MSc.

Thank you to all of my lab-mates from the TU Delft Airborne Wind Energy research group and Enevate Kite Power team, who provide such a welcoming and encouraging work-environment. Among these fantastic people, a special thanks to: Julius Berens, my first Dutch friend and a consistent inspiration; Lukas Braun, for a shared appreciation of cuteness and a wicked sense of humor; Andres Moreno, for conversations that are actually about something; Michael Deaves, whose logic and light-heartedness kept me afloat; John van den Heuvel, in agreement that whatever is worth doing is worth trying to do well; Johannes Peschel, Felix Friedl, Moritz Windbiel, Christoph Grete and Pietro Faggiani, for life - and puzzles - outside of work; and Rolf van der Vlugt, for his advice, enthusiasm and the invitation to the flight test that opened my eyes to the beauty of kites.

Thank you, also, to Rotterdam Roller Derby, the Rotterdam Parkour/Freerunning Community, and the Eerste Haagse Rolschaats Club Marathon for developing my creative problem-solving ability and teaching me Dutch. (Het was super leuk; bedankt!) In particular, my personal thanks go to Patrick van der Tas, Will Logan, Rory Ferguson, Fernanda Garcia, Sofie Wentholt, Linda van Meurs, Quentin Brenot, and Vief Cumberbatch for their support, advice and life example.

Mostly, I want to thank my parents for their unwavering faith in me, their help in all manner of things, and for raising me to be the person I am today. If I succeed now, it is your success that's visible.

Thank you.

Rachel Leuthold
Delft, the Netherlands
15 December, 2015

Contents

Nomenclature

Symbols

$\mathbf{A}$	Biot-Savart aerodynamic influence matrix	[1/m]
AR	aspect ratio	[-]
a_V	altitude of an evaluation point from a filament	[m]
B_L	2D empirical linear-lift coefficient	[-]
$B_{m,r}$	rigidity of the membrane	[N]
b	kite wingspan	[m]
$\hat{b}$	span-wise direction unit-vector	[-]
b_{max}	wingspan	[m]
b'	kite-section span length	[m]
C_D	(3D) drag coefficient	[-]
C_L	(3D) lift coefficient	[-]
$C_{L,\alpha}$	(3D) lift coefficient slope wrt. the angle of attack	[1/^{o}] or [1/rad]
C_S	(3D) steering-force coefficient	[-]
C_y	membrane Cauchy number	[-]
C_ν	effective viscous parameter for the Vatistas vortex core model	[-]
c	kite chord	[m]
$\hat{c}$	chord-wise direction unit-vector	[-]
$c_{d,SY}$	(2D) drag coefficient, as calculated with the Squire-Young drag formula	[-]
c_l	(2D) lift coefficient	[-]
c_{MAC}	mean aerodynamic chord	[m]
$\hat{\mathbf{D}}$	the unit vector in the drag direction	[-]
D_{LEI}	diameter of the kite's LEI tube	[m]
$\mathtt{d}$	downwash	[m/s]
E_m	canopy-membrane Young's modulus	[Pa]
f	frequency	[Hz]
f_F	force-response frequency	[Hz]
f_R	reduced aerodynamic frequency	[-]
f_S	separation concentration factor	[-]
f_a^*	characteristic aerodynamic frequency	[Hz]
$f_{centerline}$	function of the idealized kite center-line	[m]
$\mathbf{f}_{centerline}$	a point in body-fixed coordinates that lies on $f_{centerline}$	[m]
f_m	membrane fundamental frequency	[Hz]
H	tension coefficient	[-]
H_{TE}	boundary layer shape function at the trailing edge	[-]
h	canopy thickness	[m]
h_K	kite arc-height	[m]
j_b	span-wise collocation point index, from 1 to $N_B - 1$	[-]
j_c	chord-wise collocation point index, from 1 to $N_C - 1$	[-]
K_m	membrane curvature	[1/m]
k_m	canopy-membrane stiffness	[N/m]

k_{re}	surface roughness length	[m]
k_∞	ratio of the fixed-wake to free-wake radius	[-]
$\hat{\mathbf{L}}$	the unit vector in the lift direction	[-]
L'	Lift per unit span	[N/m]
L/D	lift-to-drag ratio	[-]
L_{VR}	length of a vortex ring	[m]
l	chordwise canopy fabric length	[m]
l_0	initial chordwise canopy fabric length	[m]
M	Mach number	[-]
$\mathcal{M}$	mass ratio	[-]
$\mathbf{M}_R$	Rotation matrix from cross-sectional coordinates to body-fixed coordinates	[-]
m_m	kite-section membrane mass	[kg]
N_B	the number of span-wise nodes of the vortex lattice	[-]
N_C	the number of chord-wise nodes of the bound vortex lattice	[-]
N_I	the number of wake-convection to circulation-solution iterations	[-]
N_J	the number of collocation points, generally $(N_B-1)(N_C-1)$	[-]
N_L	the number of chord-wise collocation points used to discretize the canopy	[-]
N_P	the number of chord-wise nodes or collocation points used to discretize the LEI tube	[-]
N_W	the number of downstream (chord-wise) nodes of the trailing vortex lattice discretizing the free-wake region	[-]
N_Γ	the number of unknown vortex ring circulation-strength, generally $(N_B-1)(N_C-1)$	[-]
$\hat{\mathbf{n}}$	membrane-surface normal unit vector	[-]
n_b	span-wise vortex lattice node index, from 1 to N_B	[-]
n_c	chord-wise bound vortex lattice node index, from 1 to N_C	[-]
n_j	column index of a collocation point, from 1 to $N_J=(N_B-1)(N_C-1)$	[-]
n_k	dimension index, where 1 refers to $\hat{x}$, 2 to $\hat{y}$ and 3 to $\hat{z}$	[-]
n_{VCM}	vortex selection parameter for the Vatistas vortex core model	[-]
n_w	downstream (chord-wise) trailing vortex lattice node index, from 1 to N_W+1	[-]
n_γ	column index of an unknown vortex ring circulation-strength, from 1 to $N_\Gamma=(N_B-1)(N_C-1)$	[-]
$\mathbf{O}$	the origin point of the (2D) cross-sectional reference frame	[-]
Δp	pressure difference between suction- and pressure-sides of the membrane	[Pa]
p_v	influence parameter of the induced velocity on the apparent velocity	[-]
q	dynamic pressure	[Pa]
R_e	Reynolds number, wrt. the kite chord	[-]
$R_{e,k}$	Reynolds number, wrt. the canopy surface roughness	[-]
$R_{e,LEI}$	Reynolds number, wrt. the LEI tube diameter	[-]
r_{Canopy}	the LEI-kite airfoil profile description, radius of the canopy normalized by the chord	[-]
r_c	vortex core radius	[m]
$r_{eff,c}$	effective vortex core radius after vortex ring stretching	[m]
r_{LEI}	the LEI-kite airfoil profile description, radius of the LEI tube normalized by the chord	[-]
r_w	the radius of the free-wake region, as measured from the trailing edge	[m]
$\hat{\mathbf{S}}$	the unit vector in the steering-force direction	[-]
$\mathbf{S}$	location of the attachment point between the LEI tube and the canopy in the cross-sectional reference frame, normalized by c; related to x_{attach}	[-]
S	projected area onto $\hat{x},\hat{y}$ plane	[m^2]
S_t	Strouhal number	[-]
$S_{t,Lock}$	Strouhal number at which the vorticity shedding frequency locks onto the structure vibration frequency	[-]

s_1	distance from LE to pressure-side leading-edge separation bubble reattachment point	[m]
s_2	distance from TE to suction-side trailing-edge separation location	[m]
s_3	distance from LE to suction-side leading-edge separation bubble reattachment point	[m]
T	canopy tension	[Pa m]
t_F^*	characteristic force-response time-scale	[s]
t_a^*	characteristic aerodynamic time-scale	[s]
U_A	kite apparent velocity magnitude	[m/s]
$\mathbf{U}_A$	kite apparent velocity vector	[m/s]
U_i or U_{ind}	induced velocity	[m/s]
$U_{ind,surf}$	induced velocity by bound vortices on the kite surface	[m/s]
$U_{ind,wake}$	induced velocity by trailing vortices in the wake	[m/s]
$U_{i,w}$	induced velocity as experienced within the wake at the vortex lattice nodes	[m/s]
$U_{membrane}$	local membrane velocity	[m/s]
U_∞	free-stream velocity	[m/s]
U^*	characteristic boundary layer velocity	[m/s]
$\mathbf{x}$	position of the kite-surface (collocation points) or the vortex lattice, can be normalized by chord-length	[m] or [-]
x_{attach}	chordwise location of the attachment point between the LEI tube and the canopy, can be normalized by chord-length	[m] or [-]
α	kite angle of attack	[^{o}] or [rad]
α_{L0}	zero-lift angle of attack	[^{o}] or [rad]
α_s	angle of attack shift for VACM	[rad]
β	kite side-slip angle	[^{o}] or [rad]
β_Z	membrane fundamental frequency proportionality constant	[-]
δ	boundary layer displacement thickness	[m]
ϵ	membrane strain	[-]
ϵ_L	sail excess length	[-] or [%]
ϵ_{OT}	divide-by-zero prevention ϵ used in the Vatistas Core Model	[m] or [m^2]
ϵ_{VR}	change in length of a vortex ring	[-]
Γ	circulation, vortex strength	[m^2/s]
Γ_F	net circulation at front of vortex ring	[m^2/s]
Γ_d	local dihedral angle	[rad]
γ_s	sweep angle	[rad]
Λ_{LEI}	LEI tube diameter to chord ratio	[-]
λ	inverse of the tension coefficient	[-]
ν_{air}	air kinematic viscosity	[m^2/s]
ν_m	canopy Poisson ratio	[-]
ϕ_{Roj}	Rojratsirikul linear-elastic membrane natural frequency correction factor	[-]
Π	membrane aeroelastic number	[-]
Π_E	membrane aeroelastic number, when tension is dominated by elastic strain	[-]
Π_{cc}	critical concavity membrane aeroelastic number, for fully-attached flow	[-]
Π_σ	membrane aeroelastic number, when tension is dominated by pre-tension	[-]
Ψ	coordinate transformed membrane slope, for the Thwaites Sail Equation	[-]
ψ	membrane slope for the Thwaites Sail Equation	[-]
ψ_R	roll angle for the cross-sectional coordinate transformation	[rad]
ρ_{air}	air density	[kg/m^3]
ρ_m	canopy areal mass density	[kg/m^2]
$\rho_{m,V}$	canopy volumetric mass density	[kg/m^3]
σ_m	canopy porosity	[-]
σ_0	canopy pre-stress	[Pa]
τ_w	pseudo-timestep in wake vortex lattice node convection	[s]
$\tau_{w,\infty}$	convection pseudo-timestep for a purely fixed-wake model	[s]
θ	boundary layer momentum thickness	[m]

θ_P	the angle between the vortex lattice nodes of the LEI tube, in cross-sectional representation	[rad]
θ_0	the angle between the $\hat{x}'$ axis and the first LEI tube vortex lattice node ($n_c = 1$), in cross-sectional representation	[rad]
θ_R	pitch angle for the cross-sectional coordinate transformation	[rad]

Abbreviations

AWE	Airborne Wind Energy
BALM	Breukels Aerodynamic Load Model
BBM	Black Box Model
BEM	Boundary Element Method
CFD	Computational Fluid Dynamics
CP	Collocation Point
DLM	Doublet Lattice Method
DM	Deformation Mode
DNS	Direct Numerical Simulation
FEM	Finite Element Method
FMM	Fast Multipole Method
FP2D	Flat-Plate 2D geometry
FP3D	Flat-Plate 3D geometry
FSI	Fluid-Structure Interaction
KFM	Kernel-Function Method
LBM	Lattice Boltzmann Method
LE	Leading Edge
LEI	Leading-Edge Inflated
LES	Large Eddy Simulation
LLKG	Lifting-Line Kite Geometry
LLT	Lifting-Line Theory
MAV	Micro Air Vehicle
MFP	Method of Fixed Positions of nascent vortices
MVP	Method of Variable Positions of nascent vortices
MVS	Method of Velocity Singularities
MWVM	Multiple-Wake Vortex Method
NE	y-Negative Edge of the kite, vortex ring, or geometry element
PE	y-Positive Edge of the kite, vortex ring, or geometry element
PSS	Pressure-Surface Separation
PVM	Point Vortex Method
RANS	Reynolds-Averaged Navier Stokes
SFVR	Single Flat Vortex Ring
SSS	Suction-Surface Separation
TAT	Thin Airfoil Theory
TE	Trailing Edge
TU Delft	Technical University of Delft
UAV	Unmanned Aerial Vehicle
UVLM	Unsteady Vortex Lattice Method
VACM	Viscous Angle of attack Correction Method
VCM	Vatistas Core Model
VIC	Visual Image Correlation
VLM	Vortex Lattice Method
VLM_{MW}	Multiple-Wake Vortex Lattice Method
$\text{VLM}_{\text{N-VK}}$	Nonlinear Vortex Lattice Method as implemented by Van Kappel
VPM	Vortex Particle Method
VVPM	Viscous Vortex Particle Method

WInDS	Wake Induced Dynamics Simulator
W12F	Warren 12 planform with Flat-plate profile geometry

Sub- and Super-Scripts

$\square_{AM}$	corrected for added-mass
$\square_{air}$	related to the air
$\square_{BE}$	related to the bunny-ear flapping deformation mode
$\square_{b}$	in the span-wise direction, or related to the span-wise vortex lattice node index
$\square_{CB}$	related to the canopy billowing deformation mode
$\square_{Collapse}$	related to the collapse deformation mode
$\square_{c}$	in the chord-wise direction, or related to the chord-wise vortex lattice node index
$\square_{calc}$	calculated
$\square_{cntl}$	describing the LEI centerline of a modelled kite
$\square_{depower}$	during the depower phase of the pumping cycle
$\square_{FD}$	related to the flight dynamic period
$\square_{fill}$	in the woven canopy fill direction
$\square_{g}$	evaluated at the geometric meshpoints
$\square_{IDM}$	related to the leading edge indentation deformation mode
$\square_{i}$	related to a vortex filament i
$\square_{ind}$	induced
$\square_{JF}$	related to the jellyfishing deformation mode
$\square_{j}$	related to collocation point at $j_b,\ j_c$; for j_b between n_b and (n_b+1) and j_c between n_c and (n_c+1)
$\square_{KJ}$	referencing the Kutta-Joukowski equation for force per unit span
$\square_{k}$	related to the direction index
$\square_{LE}$	on or related-to the leading edge
$\square_{M}$	midpoint, when determining the vortex lattice node locations during grid generation
$\square_{MD}$	coordinates in Deaves' cross-sectional reference frame
$\square_{m}$	related to the canopy membrane
$\square_{max}$	maximum expected value
$\square_{min}$	minimum expected value
$\square_{PS}$ or $\square_{PSS}$	related to the pressure-surface separation surface
$\square_{power}$	during the power phase of the pumping cycle
$\square_{R}$	at the flow reattachment point
$\square_{S}$	at the flow separation point
$\square_{Sep.}$	related to a general separation surface
$\square_{SS}$ or $\square_{SSS}$	related to the suction-surface separation surface
$\square_{SR}$	related to the seam-rippling deformation mode
$\square_{surf}$	describes the influence of the bound vortices
$\square_{TE}$	on or related-to the trailing edge
$\square_{TEF}$	related to the trailing edge flutter deformation mode
$\square_{w}$	in the wake-downstream direction, or related to the wake-downstream direction vortex lattice node index
$\square_{wake}$	describes the influence of the wake vortices
$\square_{warp}$	in the woven canopy warp direction
$\square_{\mu}$	at the force-evaluation points
$\square_{\theta}$	in the tangential direction
$\square_{1/4}$	evaluated at the quarter-chord location

$\square_{3/4}$	evaluated at the three-quarter-chord location
$\square_8$	related to the flight manoeuvre period
$\square_\infty$	evaluated - or approximated as - "infinitely-far" downstream
$\underline{\square}$	indication that a typically scalar value is multiplied with vortex filament direction
$\square^{2D}$	two-dimensional
$\square^{3D}$	three-dimensional
$\overline{\square}$	average expected value
$\tilde{\square}$	a column-rearrangement of a geometrically-indexed matrix
$\square^*$	characteristic value
$\square'$	in the cross-sectional reference frame coordinates, or defined per-unit-span

Chapter 1

Introduction

1.1 Motivation

Kites provide the ability to generate renewable electricity from the high energy-availability and -constancy of the wind at altitude. Archer & Caldeira [16], notably, measured mean energy densities of 10kW/m^2 at 1km altitude in parts of eastern China and north-eastern Africa.

The kite used by the TU Delft's Airborne Wind Energy (AWE) group is a leading edge inflated (LEI) surf-kite: a span-wise arc-shaped compliant [175] structure, with a frame composed of a cylindrical inflated-tube at the leading edge and thinner inflated-tube struts, over which a pre-tensioned membrane wing is stretched as the primary aerodynamic structure. The membrane is a flexible material with a very small thickness in comparison to its span-wise length and chord-wise length, and can carry tension but not compression [22].

The behavior of an LEI kite in a flow is a complex physical phenomenon, due to the strong aeroelastic coupling between the membrane wing's deformation and the flow pattern. That is, the membrane wing deforms, causing the flow about the wing to change; this new flow pattern produces a different pressure distribuition on the kite, again deforming the kite geometry. This fluid-structure interaction (FSI) is especially important considering the high flexibility of the membrane wing and the high variability of the inflow conditions on the kite during its periodic figure-eight-shaped flight path. Consequently, the behavior of a given power-kite in a flow cannot be modelled with any certainty without considering the FSI effects.

Experimental studies show that membrane wings, such as the LEI-kite, have the potential for higher lift-to-drag ratios, higher maximum lift coefficients, and delayed stall in comparison[1] with rigid wings. These facts suggest the application of FSI-modelling to system design for AWE systems with LEI-kites could improve the system efficiency and total power production. Further, a system-design and -optimization procedure based on FSI-modelling has been estimated to be signiciantly less expensive - Breukels [29] suggests a time-savings of 75 percent - than the current empirical design procedure which requires the construction and flight-testing of many preliminary designs.

Such a FSI-modelling based iterative design procedure requires not just a large number of simulations within some Design of Experiments, but also an iteration of alternating aerodynamic- and structural-model solutions for each design simulation. Analysis of a large number of these FSI solver steps, for each of a large number of simulations, is only feasible if the runtime-cost of the individual aerodynamic model steps is small. That is, for FSI-modelling to be possible, the aerodynamic module of the FSI-solver must be both fast and accurate.

However, the current kite aerodynamic models do not meet the requirements for LEI-kite FSI modelling: they are either fast but insufficiently accurate, or accurate but computationally expensive.

[1] See Section 2.3 for a description of membrane wing behavior, including the relevant citations.

The Breukels aerodynamic load model (BALM), correlated from airfoil CFD data along a 2D strip-theory approach, is fast; but the accuracy is questionable and the weight function requires empirical "tuning" such that it cannot be used for design work prior to flight testing [183]. Bosch produced a working FSI model built with the Breukels model; it is supposed that if there were a "replacement" for the Breukels method within this program, Bosch's program could be used for iterative design [28].

Computational fluid dynamics (CFD) models set the standard for LEI-kite flow modelling accuracy, but are not viable for iterative design work due to their high computational cost. The recent 3D Reynolds-Averaged Navier-Stokes (RANS) model of Deaves [51] required a computational time on the order of 30 hours for one steady-flow simulation.

Van Kappel's implementation of a nonlinear vortex lattice method ($\text{VLM}_{\text{N-VK}}$) gives accurate results, but its real time factor of 1100x is too slow for iterative design [183]. The accuracy of this method suggests that it is possible to quickly and accurately model kite aerodynamics with an adapted vortex lattice method (VLM).

Due to the ability of existing 2D multiple wake vortex models to model membrane-flows with multiple separation regions, it is probable that a multiple-wake vortex lattice method (VLM_{MW}) could model the multiple separation regions expected on a 3D membrane-wing surf-kite. To the author's present knowledge, no such VLM_{MW} aerodynamic model has yet been constructed for 3D membrane-flow problems.

If such a VLM_{MW} is well suited to modelling the pressure distribution on an LEI-kite, its inclusion as the aerodynamics module of a FSI solver could be expected to decrease the development cost of airborne wind energy systems, and further allow the development of renewable electricity generation from the wind.

The information in this report is divided into chapter, following the sequence described below:

- *Chapter 2*: a description of the LEI-kite and its flight environment during normal operation, as it can be used - in combination with the experimentally-determined trends in membrane-wing behaviors - to determine the assumptions of an aerodynamic model;
- *Chapter 3*: a history of aeodynamic simulation methods as applicable to membrane wing problems, with the aim of selecting a method to apply to the LEI-kite problem;
- *Chapter 4*: a detailed description of the information a user needs to run the resulting aerodynamic code, the VLM_{MW};
- *Chapter 5*: a description of the physical theory used by the VLM_{MW} to predict the pressure distrbution over a body in a flow, including the relationship between the various portions of the theory and the predictions of the method for well-known geometries;
- *Chapter 6*: the application of the VLM_{MW} to a sample LEI kite, and a comparison of the found results to the predictions for the same kite by a Reynolds-Averaged Navier-Stokes (RANS) solver, as determined by a previous AWE group-member;
- *Chapter 7*: a conclusion considering the usefulness of the VLM_{MW} as a portion of the AWE's modelling code-base, and suggestions for future development; and
- *Appendices*: the detailed geometric methods for creating input files for the VLM_{MW}, as used in testing.

1.2 Hypothesis

This thesis is intended to evaluate the hypothesis that:

A quasi-steady multiple-wake vortex lattice method can quickly and accurately model surf-kite aerodynamics to generate aerodynamic surface load distributions.

1.3 Objective

The objective of this work is to produce a proof-of-concept aerodynamic model that could be a useful module within the AWE's FSI-modelling code-base. Consequently, the goal of this thesis is to produce a method that is:

- able to find aerodynamic force distributions for a power-generation LEI kite, with the particular requirements of strong flow-three-dimensionality and significant flow separation,
- without relying on empiricism and previous results [2],
- with inputs and outputs that are consistent with, or easily converted to-and-from, the other codes in the AWE's FSI-modelling code-base,
- producing pressure-distribution predictions that qualitatively resemble those produced by RANS solutions, with some small degree of error,
- where that error can be justified by a significant run-time savings, in comparison to the RANS solution.

Each of these objectives appears to be reasonable within the frame-work of a VLM_{MW}.

1.4 Success Criterion

Success is defined as the ability to evaluate and make a feasibiliy statement relative to the computational speed and model accuracy - in comparison to either windtunnel measurements or CFD results - for well-known comparison geometries, including an LEI kite used by the TU Delft AWE group.

[2] Though the development of the VLM_{MW} within the scope of this thesis is limited to using assumed or previously-known separation locations, the VLM_{MW} is constructed such that future development would be able to remove this restriction.

Chapter 2

Problem Definition

We can consider the normal operating conditions of an LEI-kite in a power-generating pumping-cycle, and the known trends in membrane-flow problems, to determine what assumptions are reasonable when modelling.

2.1 Power-Generation with Leading-Edge Inflatable Kites

2.1.1 Airborne Wind Energy Concept

The TU Delft airborne wind energy system - otherwise referred to as a kite-power system - is a ground-based power generation system. The tether of a kite is wound around the drum of a generator, such that extension of the kite tether generates electricity and allows the kite to gain altitude. As the kite rises, it flies cross-wind in figure-eights, which increases the apparent wind velocity by about a factor of five [28] with respect to the atmospheric wind velocity. Once the kite has reached its maximum altitude, it pitches down to decrease its angle of attack with respect to the free-stream - and consequently the lift force on the kite - and is pulled back towards the ground by running the generator as a motor. One full extension of the tether, or reel-out, and the following full retraction of the tether, or reel-in, make up a pumping cycle.

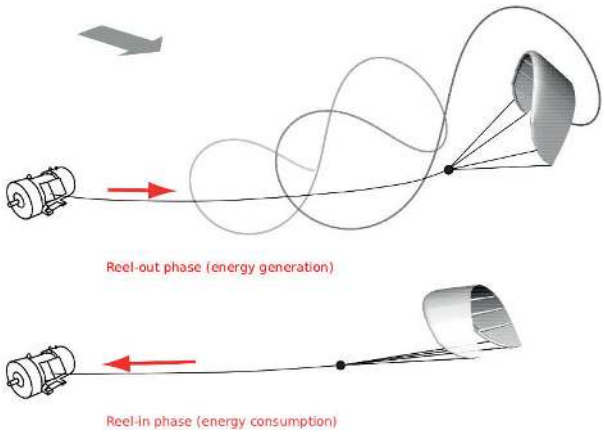

Figure 2.1: A concept sketch of the TU Delft airborne wind energy system, as reproduced from Ruppert. [153]

For a more thorough explanation of airborne wind energy systems, the reader is referred to the Airborne Wind Energy text edited by Ahrens, Diehl and Schmehl. [7]

2.1.2 Leading-Edge Inflatable (LEI) Kite

The TU Delft Airborne Wind Energy system currently uses the 25 square meter TUD-25mV3 kite design.

The kite under consideration is a leading edge inflated (LEI) surf-kite: a span-wise arc-shaped compliant [175] structure, with a flexible membrane wing as the primary aerodynamic structure, pre-tensioned to stretch over a cylindrical inflated-tube at the leading edge, and thin cylindrical inflated-tube struts extending from the leading edge inflated-tube to the trailing edge. The form of an LEI kite is shown in Figure 2.2.

There is a thin wire running along the trailing edge of the canopy to prevent the trailing edge from being completely free. The kite is divided spanwise into nine canopy sections by the eight inflated-tube struts. The membrane which makes up each canopy section is a tensile structure with a very small thickness in comparison to its spanwise length and chordwise length. The membrane can carry tension but not compression. [22] It further has a very small bending stiffness and a low porosity.

Figure 2.2: One of the LEI kites designed and used by the TU Delft AWE group for power-generation

Typical Kite Dimensions

The kite wingspan $b = 11.18$m, with an at-rest projected span of 8.313m and an at-rest projected arc-heigh of 2.825m. Dividing the wingspan evenly between the 9 canopy sections, gives an average section span $\bar{b}' = 1.24$m [72].

The diameter of the kite's LEI tube is $D_{LEI} = 0.20$m. [72]

The canopy is assumed to be attached at the exact top-and-center of the LEI tube. Following the example of Den Boer [53], it is assumed that the chordwise slopes of the LEI tube and the canopy are continuous at the attachment point:

$$\left(\frac{dy}{dx}\right)_{LEI}(x_{attach}) = \left(\frac{dy}{dx}\right)_{canopy}(x_{attach})$$

At the kite root, the chord $c = 2.63$m; at the tips, the leading edge and trailing edge join smoothly, such that the chord at the tips is 0m.

2.1.3 Flight Path

The TU Delft kite power system currently operates under a ceiling of 700m altitude, though discussion exists about flying at 1km altitude to increase the available wind power.

During typical pumping cycles, the apparent velocity U_A ranges between 20m/s and 40m/s, with an average apparent velocity on the order of 30m/s. The global apparent velocity maxima are at 0m/s and 45m/s. The altitudes and velocties during a typical flight can be seen in Figure 2.5.

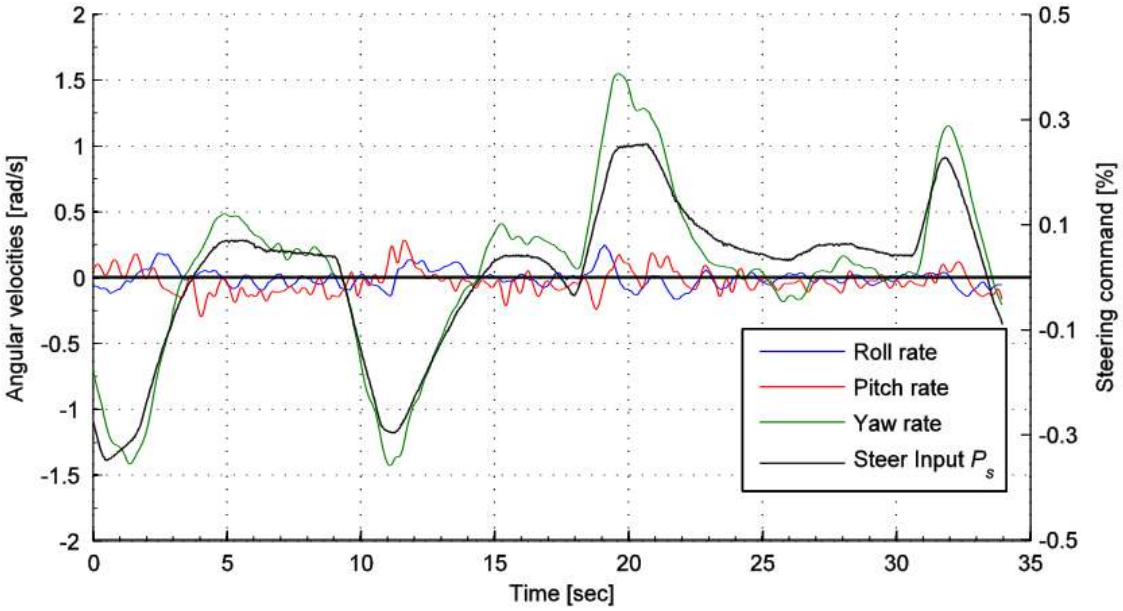

Figure 2.3: A typical steering response during power-generating operation, as reproduced from Ruppert. [153]

According to Ruppert [153], the TU Delft kite power system experiences angular velocities between -15rad/s and $+15$rad/s, centered around a rotation rate of 0rad/s. (See Figure 2.3)

Ruppert [153] also measures (see Figure 2.4) that the kite angle of attack α varies by about 50^o during normal operation; the kite side slip angle β has been measured to vary between -35^o and $+35^o$.

Angle-of-attack measurements on the LEI-kites are well known within the AWE group to have significant uncertainty. The sensor from whose data the angle of attack is determined - the X-Sens sensor is fixed to one of the inflated beams of the LEI kite. These beams bend under loading, such that the zeroing angle of the X-Sense, even without the influence of gusts, is variable.

It is therefore conservative to consider that the possible range of angles of attack during normal operating conditions to be wider than that measured during live testing.

However, we know that a kite in full stall exhibits a distinctive "tripping back" movement, which is not seen in normal operating conditions. Consequently, while significant separation is expected during flight, the LEI kite does not experience full stall in normal operation.

2.1.4 Atmospheric Properties

The atmospheric properties of the kite flow problem are approximated with the international standard atmosphere, though this representation assumes that the influence of humidity and local weather phenomena are negligible. [3]

Between the extreme altitudes of 0m and 1km, the international standard atmosphere's density varies, respectively, between $\rho_{air,max} = 1.225\text{kg/m}^3$ and $\rho_{air,min} = 1.112\text{kg/m}^3$. At an average altitude of 500m, the air density is expected to be $\bar{\rho}_{air} = 1.167\text{kg/m}^3$. [3]

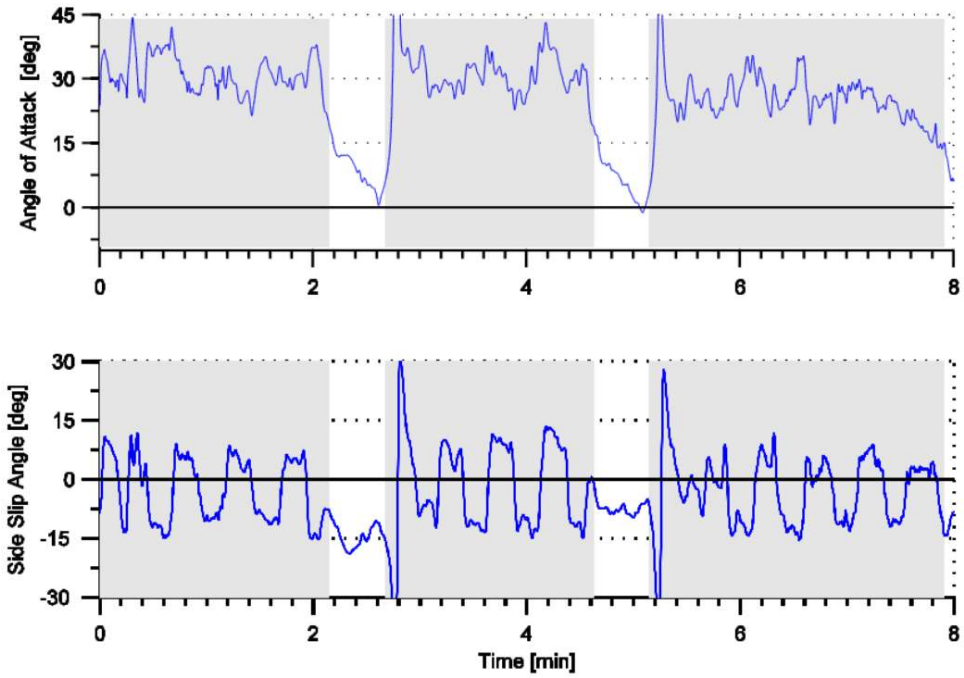

Figure 2.4: Typical angles of attack and side-slip angles in normal power-generating operation. [153]

Between altitudes of 0m and 1km, the international standard atmosphere's kinematic viscosity varies, respectively, between $\nu_{air,min} = 1.461 \cdot 10^{-5}\text{m}^2/\text{s}$ and $\nu_{air,max} = 1.581 \cdot 10^{-5}\text{m}^2/\text{s}$. At an average altitude of 500m, the air kinematic viscosity is expected to be $\bar{\nu}_{air} = 1.520 \cdot 10^{-5}\text{m}^2/\text{s}$. [3]

The freestream turbulence intensity is likely to be very low, as flight tends to be above open fields - such as the current TU Delft test location at Vliegkamp Valkenburg, the Netherlands.

Combining the average operating air density with the average apparent velocity, the minimum operating air density with the minimum typical operational apparent velocity, and the maximum operating air density with the global maximum apparent velocity, give an average dynamic pressure $\bar{q} = \frac{1}{2}\rho_{air}U_A^2$ of 525Pa, with a conservative operational range of $222\text{Pa} \leq q \leq 1240\text{Pa}$.

2.1.5 Typical Reynolds Numbers and Aerodynamic Coefficients

Using the chord as the characteristic length, the expected Reynolds number $R_e = \frac{U_A c}{\nu_{air}}$ ranges conservatively between a minimum of $3.33 \cdot 10^6$ - for the combination of 1000m altitude atmosphere and 20m/s apparent velocity - and a maximum of $8.10 \cdot 10^6$ - for the combination of sea-level altitude and 45m/s apparent velocity.

Ruppert [153] measures the lift coefficient to range between $0 \leq C_L \leq 0.7$; the drag coefficient to range between $0.05 \leq C_D \leq 0.3$. Ruppert [153] further measured lift-to-drag values for the TU Delft's kite during multiple pumping-cycle test-flights to have an average value of $\overline{L/D}_{power} = 5.9$ during the power phase of the pumping-cycle, and the fairly constant average value of $\overline{L/D}_{depower} = 1.8$ during the depower phase of the pumping cycle. These aerodynamic coefficient measurements are shown in Figure 2.6.

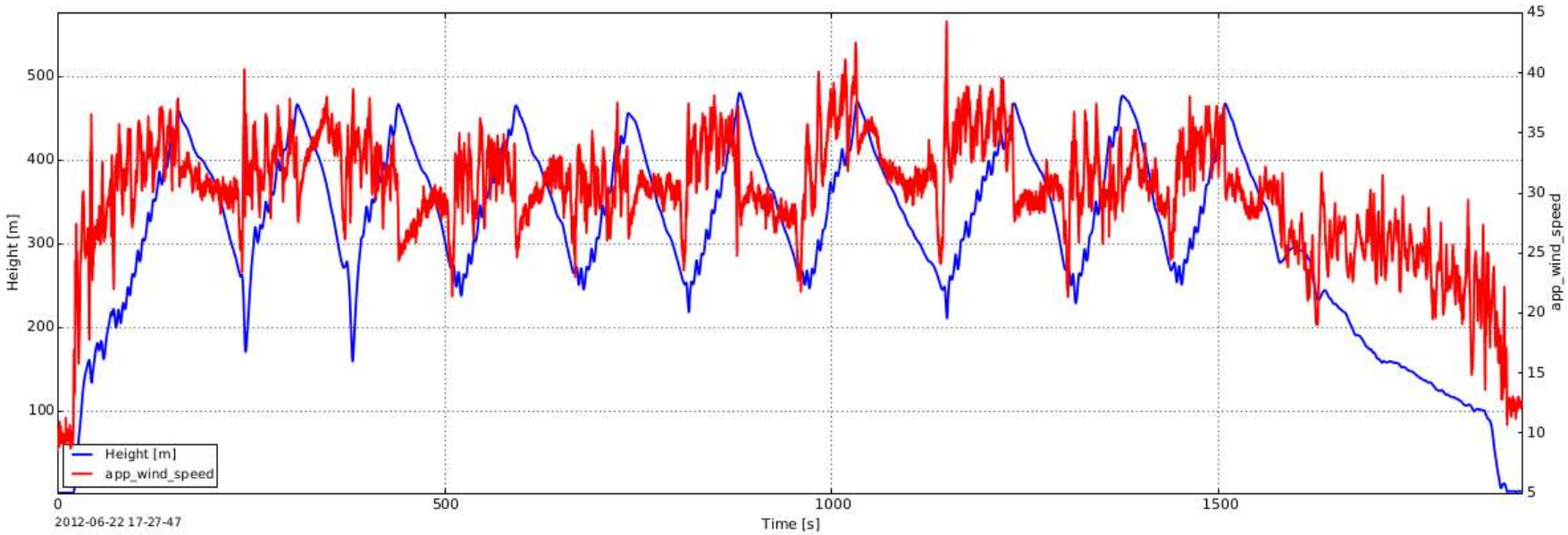

Figure 2.5: Typical altitudes and apparent velocities during normal power-generating operation. [73]

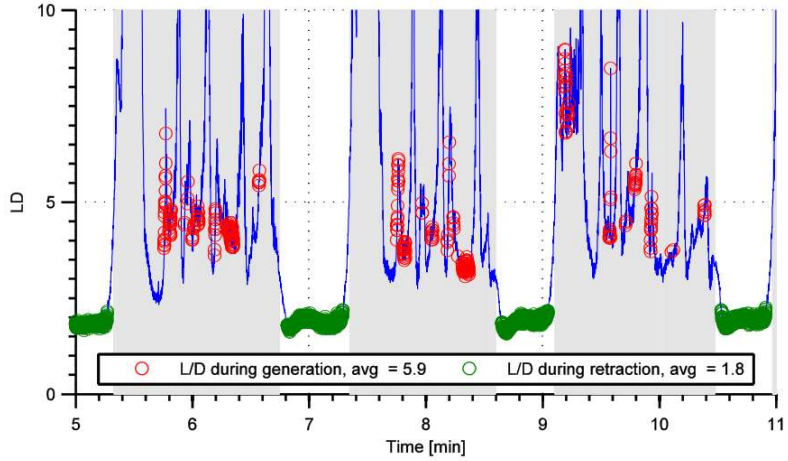

(a) Lift-to-drag ratio according to pumping cycle phase

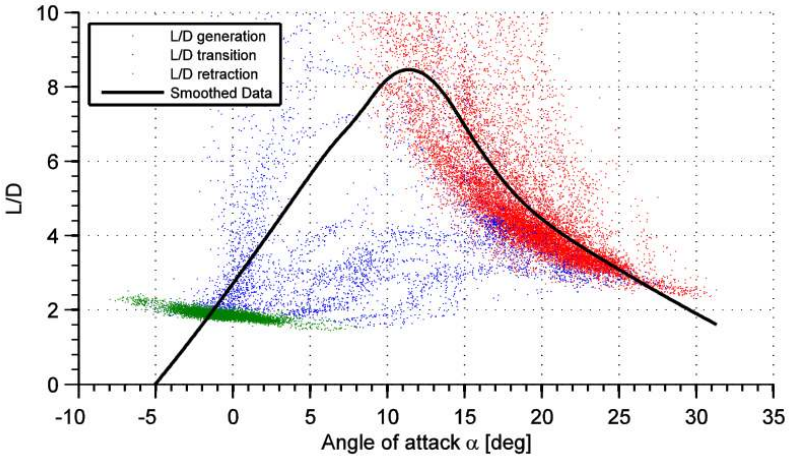

(b) Compilation of lift-to-drag ratio measurements

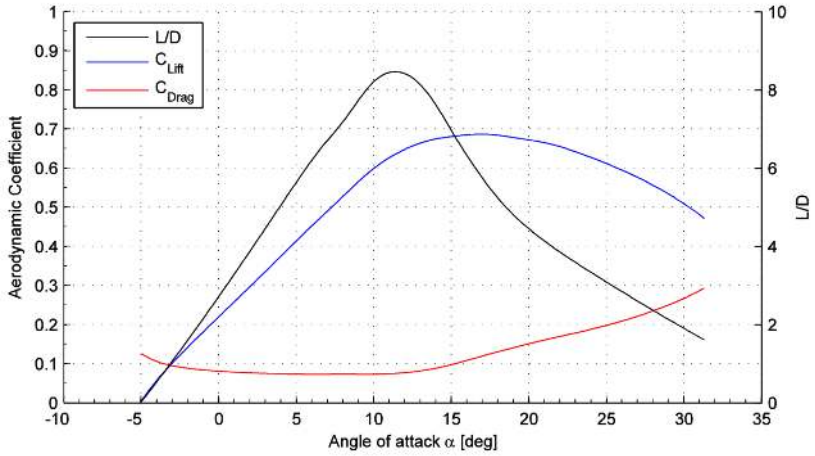

(c) Smoothed aerodynamic coefficient polars

Figure 2.6: Aerodynamic coefficients measured during normal pumping-cycle operation of an LEI kite, all reproduced from [153].

2.2 Experimental Studies of Membrane Flows

The difficulty in making accurate measurements for angle-of-attack during the flight-testing of an LEI kite has already been mentioned. Lacking confidence in our angle-of-attack measurements, we cannot well use our flight-testing experience to design future kite geometries, flight paths, or other system aspects.

But, we might still wonder why it is not sufficient to use other available sources of shape, flow, and pressure relationship information - such as from wind tunnel testing of either the LEI kite or other similar membrane wings - to design future LEI kite and kite-power systems. After all, there exist many natural analogies[1] to the LEI-kite shape: such as in pterosaur wings [144] [195], bat wings [169] [191], and veined leaves [45]. Other examples of membrane structures with similar geometries can be seen in yacht sails [66], paragliders [148] [130], sail-bladed wind turbines [125] [65], micro UAVs [109] [171] [79] [152], canvas structures such as tents [48] and convertible roofs [101], and newspaper printing webs [193].

However, the behavior of a membrane in a flow is so heavily dependent on the particular details of the membrane in question, that it is very difficult to make specific predictions based on the total sum of experimental membrane data. That is, the behavior of a membrane wing cannot be extrapolated from the known behavior of a membrane wing which is not fundamentally similar in all of the material qualities[2] which determine its aeroelastic response to a flow. To demonstrate the non-transferability of membrane flow-behavior specifics, some experimentally-measured values for the relevant angles-of-attack of a membrane-wing FSI problem - zero-lift, luffing-onset, separation-onset, and complete-stall - are assembled in Table 2.1.

If we could match all of the relevant qualities to the problem, then windtunnel testing might give us useful results. However, given that LEI kites are typically woven, it is difficult to correctly scale-down all aspects of the LEI-kite flight environment. While Reynolds number matching may be possible, it is not inherently obvious how a model should reproduce the inhomongenous stiffness caused by the ripstop weaving and sewing of the kite fabric, as well as the stiffness of the inflated beams.

One possibility would be to use a full-scale kite in wind-tunnel testing. The associated cost, both in the materials, labor and time needed to construct the kite as well as the cost of the reserving a suitably large wind-tunnel to minimize wall effects for flow around such a large object, make full-scale wind-tunnel testing ill suited to design work.

It has been suggested[3] that an alternative to the wind-tunnel testing of the dynamic aeroelasticity of the kite, would be to run wind-tunnel tests of scaled, rigid LEI deformation states. The results might not be obviously useful for the future design of kites that take advantage of their aeroelastic behavior, but it may serve as a validation testing for the AWE's aerodynamic code-base, all of whose current predictive aerodynamic codes assume quasi-steady flow. The author is not aware of the existance of such a study at this point in time, but would heavily recommend that some future student consider undertaking such testing.

If we have determined that the results of live testing are not - at present - useful decision-making tools during kite design, there remains the possibility that the numerical modelling could provide the necessary information to make design-decisions.

Increasing computational power allows for shorter turn around times for flow simulation. The accuracy of the results however depends on choosing the right input assumptions. If we want to avoid "garbage-in garbage-out" scenarios we need to asses the kite's flow situation with an eye on possible modelling assumptions.

[1] There are also many studies of membrane wings without prominent leading-edge cylinders, but we known that the inclusion of a leading-edge cylinder has a large influence on the pressures experienced by a rigid, flat wing [130]. We must therefore be extra cautious when we extrapolate behaviors of membrane wings with significant leading edge supports - such as the LEI kite - from the studied behavior of membrane wings without such supports.

[2] It is these material properties that are used, in addition to the standard flow descriptions, to determine the dimensionless aeroelastic numbers that are discussed further on in Section 2.2.1.

[3] during lunch-hour discussions among the AWE group members

Table 2.1: Some experimentally-measured relevant α values in membrane flow problems

Study	2D/3D	α Measured Range [deg]	R_e [-]	Rigid/ Flexible Mmbn.	Single/ Double Mmbn.	Planform Shape	Planar/ Arc Shape	LEI Tube Shape	α_{L0} [deg]	α Luffing Onset [deg]	α Separation Onset [deg]	α Complete Stall [deg]
Bruining, 1979 [31]	2D	$[-10,\ 90]$	$6 \cdot 10^4$, $1 \cdot 10^5$	Rigid	Single	Straight	Planar	Round	3	NR	6	$[15,\ 16]$
den Boer, 1980 [52]	2D	$[3,\ 10]$	$1.95 \cdot 10^5$, $5 \cdot 10^5$	Flexible	Single	Straight	Planar	None	NR	NR	$[7.5,\ > 10]$	$[9,\ > 10]$
den Boer, 1982 [53]	2D	$[2.4,\ 10]$	$2 \cdot 10^5$, $5 \cdot 10^5$	Flexible	Double	Straight	Planar	None	NR	NR	10	NR
Greenhalgh et al, 1983 [82]	2D	$[5,\ 20]$	$1.3 \cdot 10^6$	Flexible	Single	Swept	Conical Sections	None	NR	$[-1.7,\ -3.3]$	NR	NR
Newman & Low, 1984 [139]	2D	$[-2.5,\ 27.5]$	$1.2 \cdot 10^5$, $7 \cdot 10^3$	Flexible	Single	Straight	Planar	Round	NR	$[-2.5,\ -1]$	$[5,\ 20]$	$[12,\ 40]$
van den Borne, 1984 [180]	2D	$[-8,\ 24]$	$9 \cdot 10^5$	Flexible	Double	NR	NR	None	$[-4,\ -6]$	NR	8	12
Newman & Païdoussis, 1991 [140]	2D	NR	$1 \cdot 10^5$	Flexible	Single	Straight	Planar	None	NR	$[-1.5,\ -2.5]$	NR	NR
Hubner & Hicks, 2011 [91]	2D	$[0,\ 20]$	$4.6 \cdot 10^4$	Rigid, Flexible	Single	Straight, Scalloped TE, Swept	Planar	None	NR	NR	$[8,\ 12]$	$[12,\ > 16]$
Fink, 1967 [67]	3D	$[-8,\ 20]$	$9.2 \cdot 10^5$	Flexible	Double	Straight	Planar	None	-6	NR	NR	15
Mendenhall et al, 1968 [130]	3D	$[-20,\ 70]$	$1 \cdot 10^4$, $6 \cdot 10^5$	Rigid	Single	Swept	Planar, Conical Sections	None, Round	$[-20,\ 0]$	NR	$[-8,\ 8]$	$[10,\ 20]$
Fink, 1969 [68]	3D	$[-6.7,\ 19.3]$	NR	Flexible	Double	Straight	Planar	Round	-5	NR	NR	17
Maughmer, 1976 [125]	3D	$[-12,\ 24]$	$2.5 \cdot 10^5$	Flexible	Single, Splitter-Plate, Semi-Sailvane	Straight	Planar	Airfoil, Reversed-Airfoil, Round	$[-3,\ 1]$	NR	$[3,\ 11]$	$[11,\ 22]$
Kroo, 1981 [102]	3D	$[-30,\ 45]$	$1.35 \cdot 10^6$, $2.7 \cdot 10^6$	Flexible	Single	Swept, Trapezoidal	Planar	None	$[-8,\ 15]$	0	$[18,\ 28]$	$[23,\ 40]$
Greenhalgh, 1983 [81]	3D	$[5,\ 20]$	$6 \cdot 10^5$	Flexible	Single	Swept	Conical Sections	Airfoil	NR	$[5,\ NR]$	$[11,\ 16]$	$[16,\ 20]$
Tamai et al, 2008 [174]	3D	$[-6,\ 20]$	$7 \cdot 10^4$	Ribbed	Single	Straight, Scalloped TE, Swept	Planar	None	$[-2,\ 0]$	NR	$[6,\ 12]$	$[12,\ 20]$
Rojratsirikul et al, 2009 [151]	3D	$[3,\ 30]$	$1.06 \cdot 10^5$, $5.31 \cdot 10^4$	Flexible	Single	Straight	Planar	Airfoil	NR	2	8	NR
Hu et al, 2010 [90]	3D	$[-10,\ 25]$	$2 \cdot 10^4$, $8 \cdot 10^4$	Rigid, Flexible	Single	Irregular Elliptical Polygon	Planar	None	0	NR	$[8,\ 25]$	$[20,\ > 25]$
Rojratsirikul et al, 2010 [152]	3D	$[0,\ 30]$	$5.31 \cdot 10^4$, $7.94 \cdot 10^4$, $1.06 \cdot 10^5$	Flexible	Single	Straight	Planar	Airfoil	NR	$[2,\ 4]$	NR	NR
Rojratsirikul et al, 2011 [150]	3D	$[0,\ 30]$	$2.43 \cdot 10^4$, $3.65 \cdot 10^4$, $4.87 \cdot 10^4$	Flexible	Single	Straight	Planar	Airfoil	< 0	NR	$[15,\ 18]$	$[16,\ 20]$
Béguin et al, 2012 [24]	3D	$[-20,\ 40]$	$2.3 \cdot 10^5$, $4.6 \cdot 10^5$	Flexible	Double	Straight, Swept	Planar	None	NR	NR	$[5,\ 10]$	NR
Waldman & Breuer, 2013 [190]	3D	$[0,\ 25]$	$8 \cdot 10^4$	Flexible	Single	Straight	Planar	None	NR	NR	11	$[12,\ > 20]$

2.2.1 The Dimensionless Aeroelastic Parameter for Membrane Flow Problems

Based on the work by de Matteis & de Socio [47] and Sneyd [167], and following the derivation by Smith [166], the aeroelastic behavior in membrane flow problems can be characterised according to two parameters which split the tension of the membrane into the elastic-strain tension and the membrane pre-tension.

For a linearly elastic membrane, the tension T can be written as:

$$T = (E_m \epsilon + \sigma_0)h$$

with E_m the elastic modulus of the membrane material, ϵ the membrane strain ($\epsilon = \frac{l-l_0}{l_0}$), σ_0 the pre-stress, and h the membrane thickness. For most membrane applications, the tension caused by the membrane's own weight is negligible in comparison to - qualitatively, less than 0.1 percent of - the tension caused by the pre-tension and aerodynamic tensions [202].

For a membrane in equilibrium, the membrane curvature K_m is determined by the balance between the pressure difference across the membrane Δp and membrane tension T:

$$K_m = \frac{d^2y}{dx_i^2}\left(1 + \frac{dy}{dx_i}^2\right)^{-3/2} = -\left(\frac{\Delta p}{T}\right)$$

where y is the membrane deflection distance perpendicular to the span and chord, and x_i is conceptual two-dimensionalized membrane distance.

If x_i is normalized by c, and Δp by the dynamic pressure $\frac{1}{2}\rho U_A^2$, the membrane equilibrium equation becomes:

$$K_m = -\frac{1}{\Pi}\left(\frac{\hat{\Delta p}}{\hat{T}}\right)$$

where the aeroelastic number Π relates the dominant tension to the dynamic pressure and chord. That is, for a membrane[4] whose tension is dominated by elastic strain:

$$\Pi = \Pi_E = \frac{E_m h}{\frac{1}{2}\rho_{air} U_A^2 c}$$

For a membrane whose tension is dominated by pre-tension, as the case for a close-to-inextensible membrane:

$$\Pi = \Pi_\sigma = \frac{\sigma_0 h}{\frac{1}{2}\rho_{air} U_A^2 c}$$

The aeroelastic number Π compares the canopy stiffness to the flow dynamic pressure [69] and provides a measure of how much a membrane will resist deformation for a given aerodynamic line load. The smaller the aeroelastic number, the more compliant - the more deformable - the membrane is. Membranes with small aeroelastic numbers will self-camber more than membranes with high aeroelastic numbers, and consequently produce higher lift coefficients under attached flow conditions [190].

Increasing the (3D) canopy pretension [171] is expected to decrease drag [75], decrease the time-averaged lift, decrease $C_{L,\alpha}$ [142], preserve flow-attachment to linearize lift behavior [164], increase α_{L0} [136], cause a more abrupt stall [75], decrease the membrane oscillation mode [79], and decrease the vortex shedding Strouhal number [79].

For fully-attached [140], inviscid flow, the aeroelastic parameter can be used to predict whether the canopy remains "wholly concave," when the $0 \leq \frac{1}{\Pi} \leq \frac{1}{\Pi_{cc}}$, where the value for $1/\Pi_{cc}$ was found by Thwaites [176] to be 2.316, by Voelz [189] to be 2.299, by Dugan [58] to be 2.310, by Nielsen [141] to be 2.3155, Irvine [93] to be 2.547 [117]. For further information concerning the effect of the nondimensional membrane aeroelastic number on classical yacht-sail behavior, the, the reader is referred to Newman & Low [139], Greenhalgh at al [82], Jackson & Fiddes [95], and Sneyd [167].

[4] As a note, there exists an alternate version of the dimensionless aeroelastic number for elastic membranes - typically found in the research done by the University of Florida, Gainesville [163] and the University of Alabama, Tuscaloosa [203] groups - where $\Pi_1 = (\Pi_E)^{1/3}$ based on Seide's finding that elastic membrane deformation [158] is proportional to $(\Pi_E)^{-1/3}$.

Unfortnately, there is - as of the author's current knowledge - no consistent measurement method to determine a single dimensionless membrane aeroelastic parameter for a given LEI-kite, for whom the degree of pre-tension on a canopy section varies significantly by measurement location and measurement direction. That is, for an LEI kite, the pre-tension near the LEI tube is fairly large, while the tension near the trailing edge is small but non-zero due to the wire along the trailing edge. We also expect that the tension is likely to be significantly higher in the canopy fabric warp- and weft- directions than skew to these directions. Further, the tension in the canopy can be expected to increase when the kite experiences high loading.

It becomes especially difficult to make predictions based on other experimental studies within the membrane-flow field when there are neither values for the relevant dimensionless numbers, nor standard conventions for the calculation of these dimensionless numbers.

2.3 Typical Membrane-Flow Behavior

It is important that the general behavior of membrane-flows be considered when assembling the model assumptions. These behaviors can be considered in generalities, even if the specific flow behaviors cannot be transfered.

As for rigid wings, the behavior of the flow changes dramatically between the attached-flow and separated-flow regimes. The behavior in these two regimes is discussed in the following sections.

2.3.1 Attached Flow Trends

We know that as the angle of attack of a membrane wing increases, the aerodynamic loading increases. This increased loading deforms the trailing edge of the membrane upwards. This causes the wing to experience an effective reduction in angle of attack - as the chord-line is tilted tail-up and effectively nose-down. This "adaptive washout" decreases the rate at which the angle of attack grows even as the incoming freestream direction shifts [5]. The decrease in effective angle of attack due to membrane wing deformation has been confirmed by Lian et al [109] and Lian & Shyy [108] This decrease in effective angle of attack has the general effect of delaying separation, and then stall past the angles of attack where these flow-behaviors might occur in rigid wings [149]. This ability of a membrane wing's flexibility to delay stall is shown in Figure 2.7.

Further, as the wing deforms under increasing angle of attack, the canopy billows. This "adaptive camber" or "self-camber" of the wing increases the wing's lift and lift slope [171] with respect to angle of attack. Two examples of the many visual image correlation (VIC) studies of membrane wings can be found from Albertani et al [12] for elliptical micro air vehicle (MAV) membrane wings, and from Breukels [30] for the mostly-planar LEI-framed kiteplane membrane wing used by the TU Delft's Airborne Wind Energy group prior to the use of surf-kites. Because the deformation increases as the aerodynamic loads on the wing increase, the lift and drag will both increase as Reynolds number increases [149].

The flexibility of a membrane delays separation and stall, increases the maximum lift coefficient, and causes stall to occur much more suddenly for a given membrane wing in comparison to an equivalent rigid wing [192]. Further the delayed separation due to the effective washout of a membrane wing can increase the lift-to-drag ratio of a 3D membrane wing compared to an equivalent rigid wing [46].

Depending on the shape of a 3D membrane wing's frame, the lift-slope can be higher than the theoretical thin-airfoil lift slope $C_{L,\alpha}$ [125]. A membrane-wing frame with a fixed trailing edge will generate adaptive camber but no adaptive washout, resulting in the significantly higher lift slope than a membrane-wing with a free trailing edge [12]. The TU Delft LEI surf-kite has a wire running through the trailing edge to provide tension, in part to minimize the experienced adaptive washout.

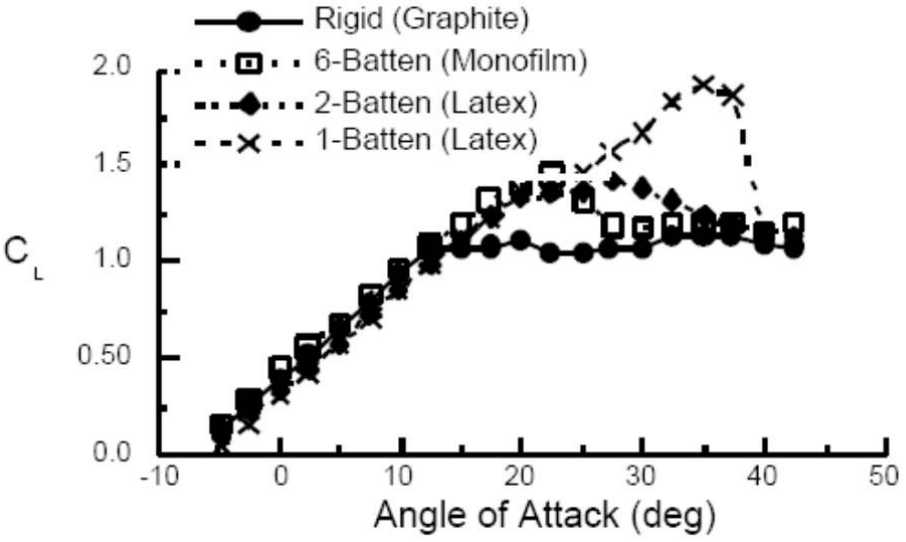

Figure 2.7: The influence of wing membrane flexibility on lift coefficient over a 3D membrane wing, where a greater number of spars ("battens") and/or a stiffer material decreases flexibility [192].

The incidence range of linear, fully-attached flow is quite small; for descriptive purposes, this validity range has been found to lie between 5^o and 8^o angle of attack for a 2D mylar membrane airfoil [82]. Nielsen [141] suggests that separation occurs, and the flow leaves the attached, linear lift-alpha relation, regime when a membrane reaches an adaptive camber above 15 percent. It should be noted that Mendenhall et al [130] found that the inclusion of a prominent leading-edge cylinder to a flexible membrane delays leading-edge separation to higher angles-of-attack, although the delay is more noticeable for supercritical Reynolds numbers than subcritical Reynolds numbers.

For fully attached flow on an inextensible, purely-concave sail[5] - without a LEI tube - Voelz [189], Thwaites [176], Nielsen [141] and Greenhalgh at al [82] find independently the empirical approximation for the 2D lift coefficient:

$$c_l \approx 2\pi\alpha + B_L\sqrt{\epsilon_L}$$

Where Thwaites finds $B_L = 0.636$, Nielsen $B_L = 0.72784$, and Greenhalgh et al $B_L = 0.70$, and ϵ_L is the sail excess length $\epsilon_L = (l - l_0)/c$. [117].

2.3.2 Nonlinear Flow Trends

There are two main nonlinear flow regimes relevant to membrane wings. The first of these hysteresis regimes occurs when the lift force is low, near $C_L \approx 0$. The other is a strong fluid-structure interaction as a result of vortex shedding after flow separation.

Low-Lift Hysteresis

When the lift on a membrane wing is low, small variations in aerodynamic lift due to small inflow variations can change the direction in which the wing billows. This hysteresis becomes more extreme when the membrane pretension is low and the flow velocity is high, and is not a flow-separation phenomenon [24].

[5]As a note, the sail literature frequently makes a reference to a "design" or "optimum" incidence. This "design" or "optimum" incidence is the angle of attack, which in combination with a given tension coefficient ($H = \frac{T}{qc}$), allows the Kutta condition to be satisfied at both the leading and trailing edges [140] [176]. In the remainder of this work, any further usage of the word "optimum" or its derivatives - such as "optimize" refers to its standard definition as a value which maximizes some desired quality or minimizes some undesired quality.

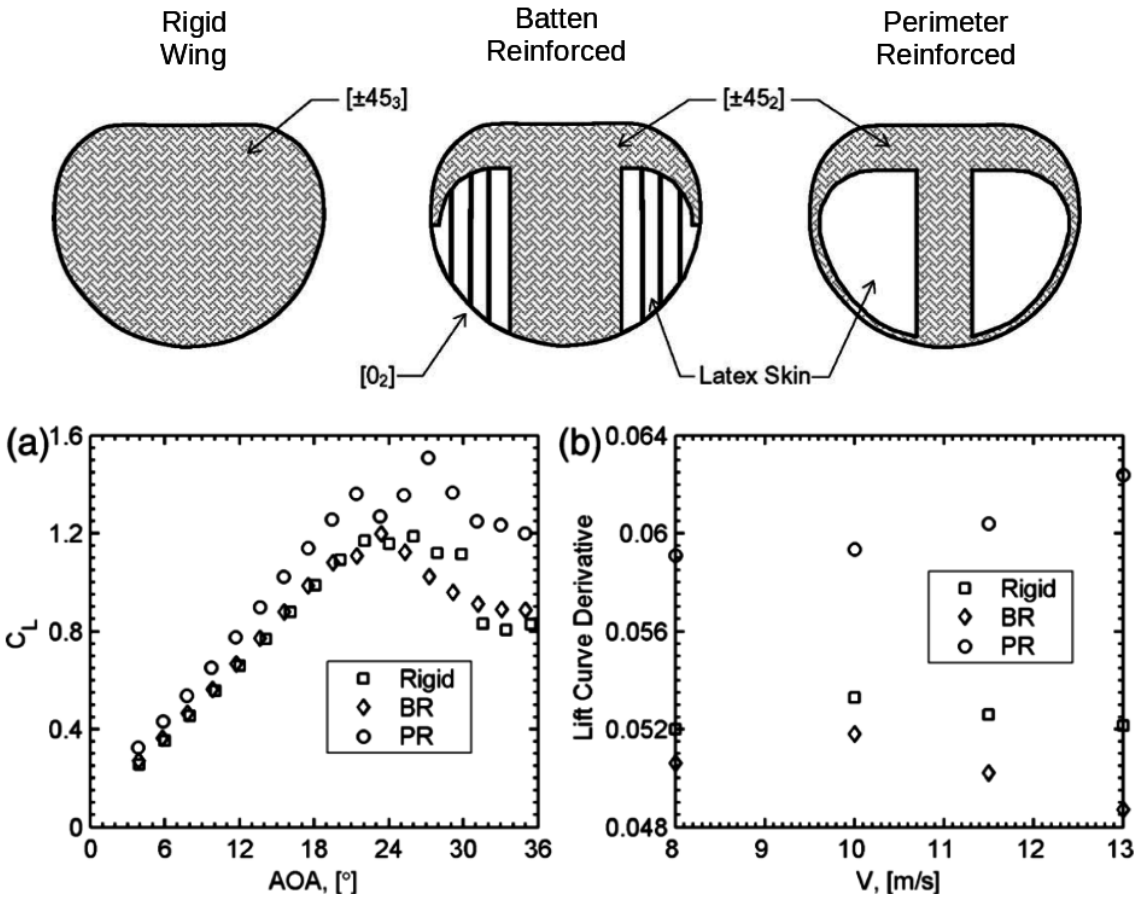

Figure 2.8: The effects of adaptive washout, as demonstrated by a batten-reinforced wing, and adaptive camber as demonstrated by a perimeter-reinforced wing. Reproduced from Albertani et al [12].

From sailing, this low-lift, bistable-instability [151] is called 'luffing.' For analytical solutions of the critical membrane-tension below which luffing may occur in yacht-sails, the reader is referred to Nielsen [141], Newman & Low [139], and Newman [138].

As a note, there is debate whether prominent, very-thick (in comparison to membrane thickness) leading edges on 3D membrane wings can prevent the membrane wing from experiencing luffing at angles of attack near the zero-lift angle of attack α_{L0}, as suggested by the sailwing windmill research group of Princeton University [125], but refuted by Waldman & Breuer [190]. Analysis of crashes during AWE test flights suggests that Waldman & Breuer have the correct impression.

In practical kite flight, this low-lift oscillation can cause an unrecoverable one-way deformation: near α_{L0} a shift in inflow direction causes the canopy billow to reverse directions, and the lift vector to invert. When the wind is strong, the inverted lift can be enough to overcome the tension in the kite and buckle the LEI tube, leading to the destruction of the kite's steering ability, and an almost-certain crash. That is, when the low-lift oscillation is large enough in magnitude, it can lead to kite collapse. Consequently, the low angles of attack associated with the low-lift hysteresis regime are strongly avoided during kite operation.

Given that this motion pattern is not within the normal-operating conditions of the kite-power system, it is assumed that the ability to model luffing is not of primary importance in the selection of modelling method.

Flow Separation

The primary source of discrepancies between experimental and modelled flow over membrane wings is separation [139] [166], and as an LEI kite flies to high angles of attack during power-production operation and has a large wind-shadow region behind the LEI tube, it certainly experiences separation.

Conceptually speaking, there are three possible separated-flow recirculation regions that may come into play on an LEI kite. Following the abbreviations (shown in Figure 2.9) used by Newman & Low [139] who performed a study on the separation - and reattachment - of flow on 2D, impermeable and slack sails being held by various supports, we can use a set of abbreviations to describe certain recirculation regions:

1. a *pressure-side leading-edge separation* bubble, analogous to the wind-shadow region behind the LEI tube;
2. a *suction-side trailing-edge separation* region, as seen on any airfoil at high incidence; and
3. a *suction-side leading-edge separation*, as seen on sharp leading-edged surfaces like flat-plates.

The specific findings of Newman & Low are reproduced in Figure 2.10. If we generalize the specific trends[6] that they found, we see that:

- As the angle of attack increases, the wind-shadow region of a kite shrinks, corresponding to the shrinking of the separation bubble (1).
- As the angle of attack increases, the trailing edge separation location (2) moves forward.
- The suction-side leading-edge separation bubble (3) primarily occurs at moderate angles of attack, before which there is no leading-edge separtion, and after which the bubble has popped to join (2).

That is, we can expect that the canopy separation and reattachment behavior follows the same general trends as we would expect on a thin airfoil, with the addition of the separation bubble after the LEI tube.

Deaves [51], who performed a steady RANS analysis of a rigid LEI kite with smoothed profiles, finds that suction-surface separation begins at the tips at around 16 degrees angle-of-attack; then appears on a strip on the quarter- and three-quarter span locations of the kite; moves to the root; and returns again to the quarter- and three-quarter span locations. There does not appear to be a consistent way to predict the separated locations on the kite suction-surface, and the separation line is discontinuous.

Deaves also presents some results for separation on the pressure-surface. Unsurprisingly, at the angles of attack within normal operating conditions, there is always pressure-surface separation. Unfortunately for the development of this thesis-work's method, the location of the separation line is difficult to determine from his reported values and appears to lay on the portion of the kite where his study's profile smoothing is in effect.

[6] as the wire at the trailing edge of the kite is intended to decrease the canopy slackness, and two-dimensionality does not represent the LEI kite's low aspect ratio and highly non-planar nature particularly well.

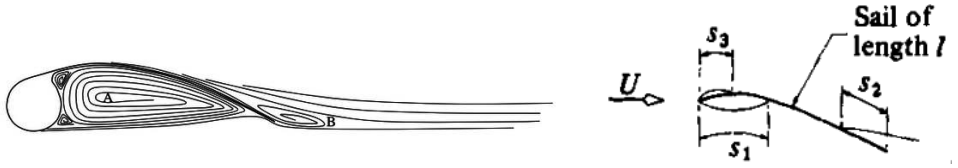

(a) A schematic of flow separation regions over an LEI kite - from Anderson et al [14], with region A comparable to the Newman & Low [139] region S_1, and region B comparable to the Newman & Low region S_2.

(b) The defining dimensions of the three types of separation, as reproduced from Newman & Low [139].

Figure 2.9: Separation sketches over LEI membrane-wing kites and 2D sails.

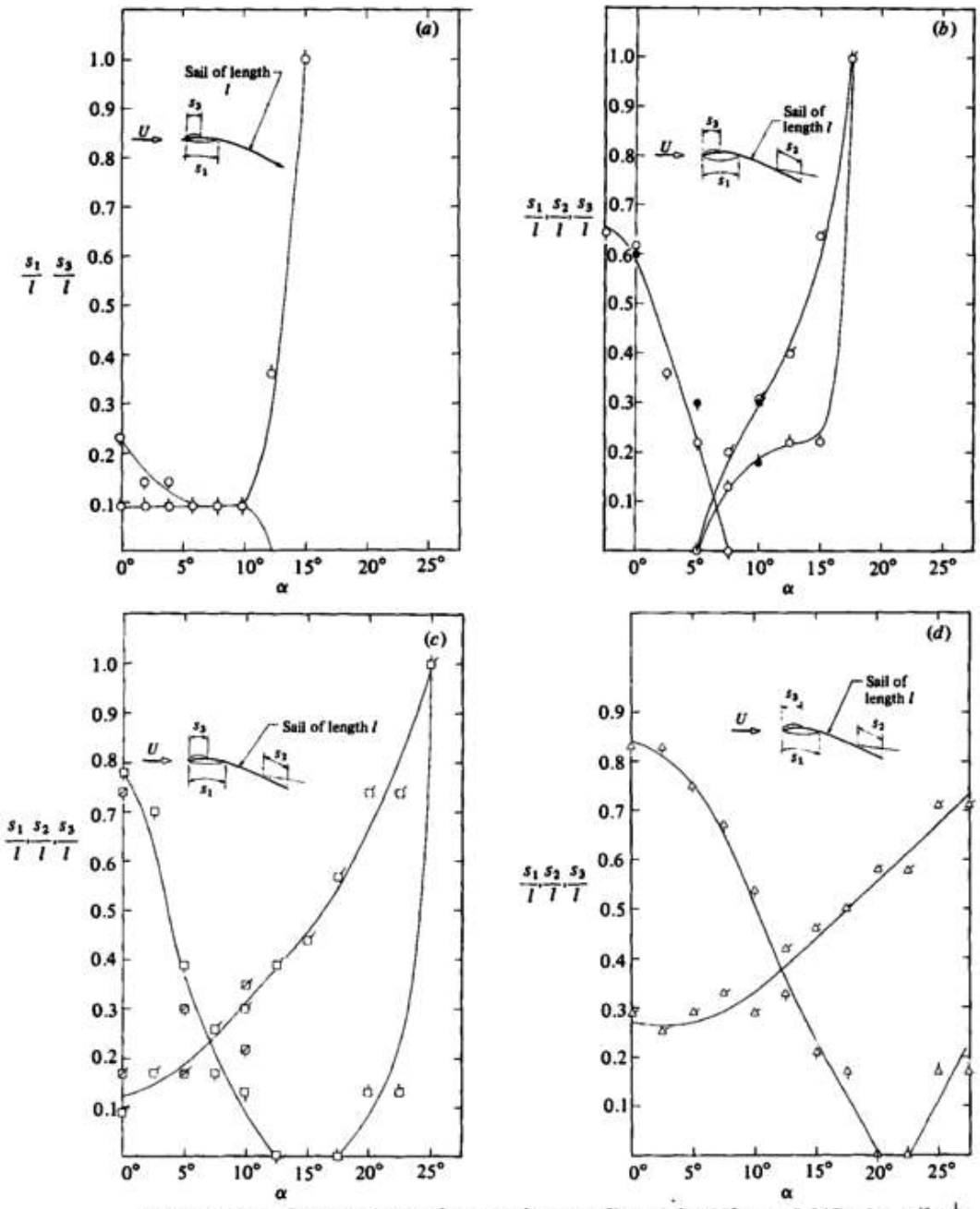

(a) Positions of separation and reattachment; $Re = 1.2 \times 10^5$, $\epsilon = 0.017$: ○, s_1/l; ○, s_3/l; wedge supports. (b) $\epsilon = 0.03$: ○, s_1/l; ○, s_2/l; ○, s_3/l; open symbols: thin supports; solid symbols: thick supports. (c) $\epsilon = 0.05$: □, s_1/l; □, s_2/l; □, s_3/l; open symbols: $Re = 1.2 \times 10^5$; diagonal line through symbols: $Re = 0.7 \times 10^5$. (d) $\epsilon = 0.10$: △, s_1/l; △, s_2/l; △, s_3/l.

Figure 2.10: Positions of separation and reattachment for a 2D membrane wing - where the value $\frac{s_1}{l}$ is indicated with a flap pointing down, the value $\frac{s_2}{l}$ is indicated with a flap pointing diagonally upwards, the value $\frac{s_3}{l}$ is indicated with a flap pointing up. ϵ indicates the degree of slack on the wing, and the four graphs represent different support shapes. (a) with wedge shaped supports, for $R_e = 1.2 \cdot 10^5$ and $\epsilon = 0.017$; (b) with thin (open symbols) vs. thick supports (solid symbols), for $R_e = 1.2 \cdot 10^5$ and $\epsilon = 0.03$; (c) with $R_e = 1.2 \cdot 10^5$(uncrossed symbols) vs. $R_e = 7 \cdot 10^4$(crossed symbols), for $\epsilon = 0.05$; and (d) $\epsilon = 0.10$, as found by Newman & Low [139].

The separation lines found by Deaves for various angles of attack on the suction- and pressure-surfaces can be found in Figure 2.11.

Consequently, whatever model is developed must be applicable under separated flow conditions.

Vortex Shedding Hysteresis

Flow separation results in oscillatory vortex shedding. When the membrane's natural frequency and the vortex shedding frequency are close, the pressure jump on the membrane surface caused by the nascent vortex forces the deformation of the membrane [168] [132]. Oscillatory vortex shedding produces an oscillatory aerodynamic force, which causes an oscillatory adaptive camber. Consequently, the character of membrane-wing oscillations depends primarily on the vortex shedding off the membrane - which is determined by the location and size of the flow separation region [149].

It is generally found that a flow-excited membrane will vibrate as a sum of standing wave modes [168] [79] [151] [15] [177], though there is a disagreement over the point where the standing wave frequencies shift from periodic harmonic frequencies to a chaotic spectrum of frequencies. Gordnier [79] computes that 2D membrane oscillation in laminar flow will become more chaotic as flow Reynolds number increases; Alben & Shelley [10] model the oscillation frequencies will become more chaotic as $B_{m,r}/(\rho_{air}U_A^2c^3)$ increases, where $B_{m,r}$ is the rigidity of the membrane. Analysis of flight videos suggests that the oscillation of the LEI-kite's trailing edge flutter deformation is periodic - or sufficiently periodic that the chaotic behavior cannot be seen visually.

Where the deformation is periodic, the dominant mode is expected to provide approximately 90 percent (See Figure 2.12) of the canopy deformation [190]. The remaining canopy deformation is caused by the higher harmonic standing wave modes; Rojratsirikul et al [152] suggest that the effect of the first six - for small membrane wings - overlapping harmonics is sufficiently great that any further harmonics do not have any practical effect.

That is, we predict the higher deformation mode harmonics - which would be expected to be the high frequency deformations - have both a small amplitude and are present only in the small region of the canopy near the trailing edge. We might, therefore, assume that the influence of the high frequency deformations would be fairly small on the pressures experienced by the kite.

As a result, we assume that we can neglect the influence of these higher mode deformations. That is, we assume that the errors introduced by neglecting the higher harmonics of a dominant deformation mode are on the same order or smaller than the errors introduced by the other sources of modelling error, particularly for a fast aerodynamic modelling method.

The next question, concerning the requirements of the aerodynamic model, is what sort of dominant deformation mode are we expecting the LEI kite to experience?

It has been suggested [81] that the only factors which the dominant periodic deformation frequency and amplitude of a membrane wing are the free-stream dynamic pressure, the angle of attack, the tension in the membrane, and - to a much smaller extent - the membrane twist.

We know that this dominant perdiodic deformation mode increases with flow Reynolds number. This increase is not a smooth increase, but discontinuous: the dominant membrane oscillation mode is expected to jump mode harmonics in a discrete stepping process. This is represented in Figure 2.13. Song et al [168] propose that this frequency jumping occurs because the vortex shedding frequency increases - possibly as vortex shedding Strouhal number increases with Reynolds number due to varying separation locations, asymptotically approaching the structure-specific constant value at high Reynolds number [49] - triggering resonance with the closest harmonic of the membrane natural frequency. The amplitude of the deformation does not tend to depend on the flow velocity [151].

Further, Rojratsirikul et al [152] suggest that a pre-tensioned membrane deformation will deform at lower mode numbers than a slack membrane.

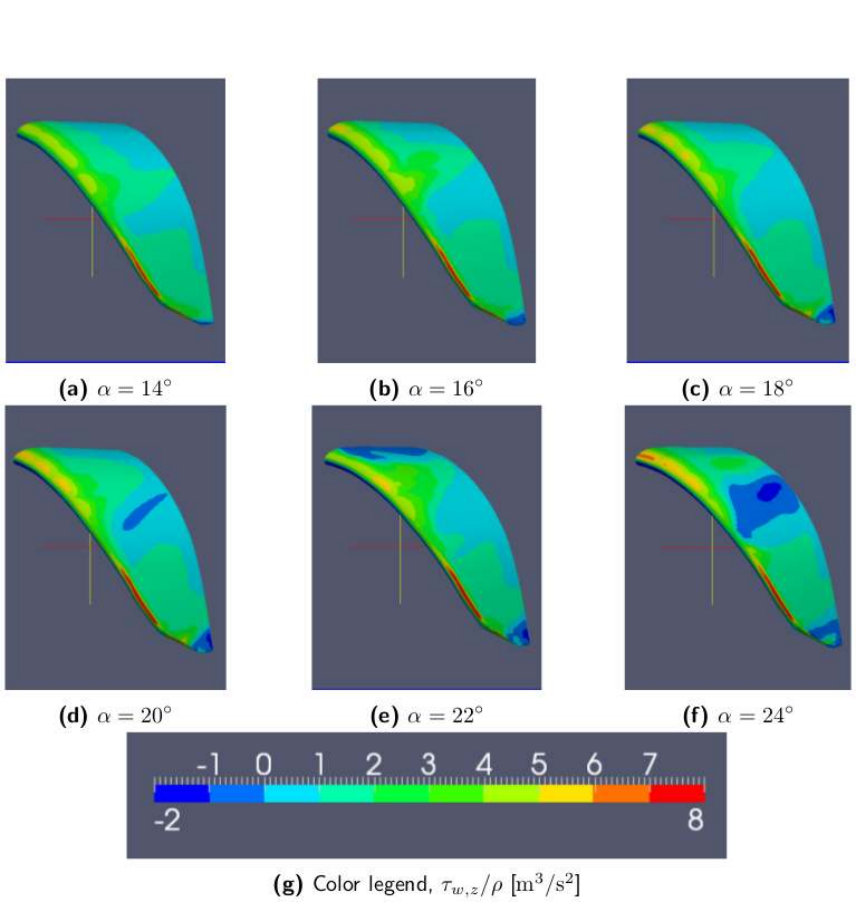

(a) suction-surface

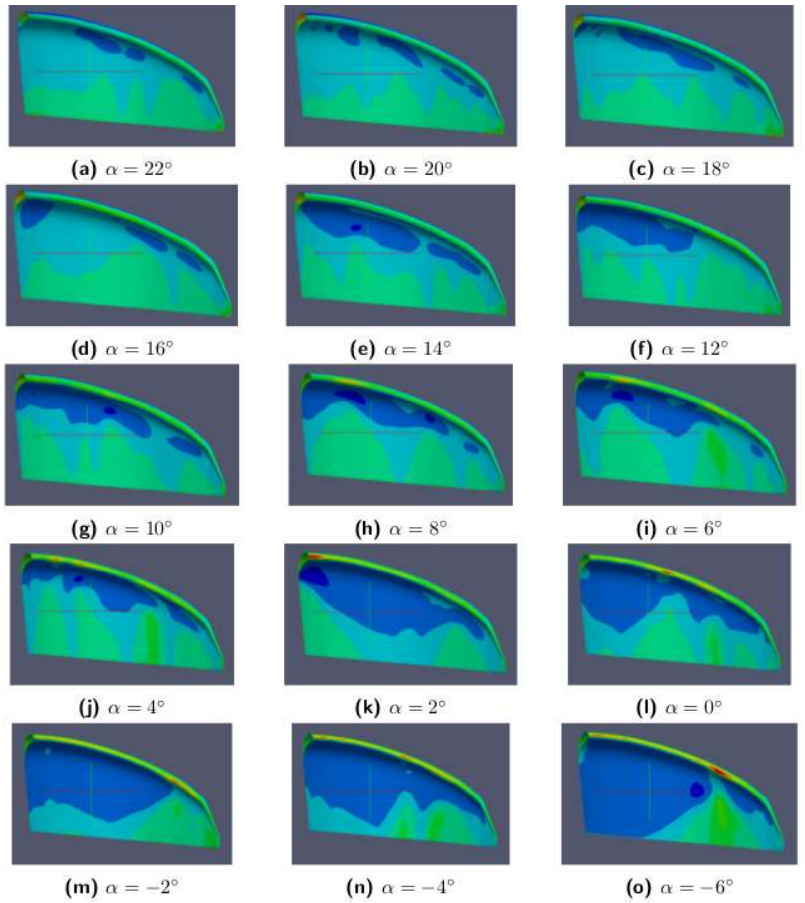

(b) pressure-surface, same legend as (left)

Figure 2.11: Negative shear stress results indicate the positions of flow separation, for steady-flow at various angles-of-attack on a rigid LEI kite wing, as found by Deaves [51]. (Presumed to be at Reynolds number $3 \cdot 10^6$.)

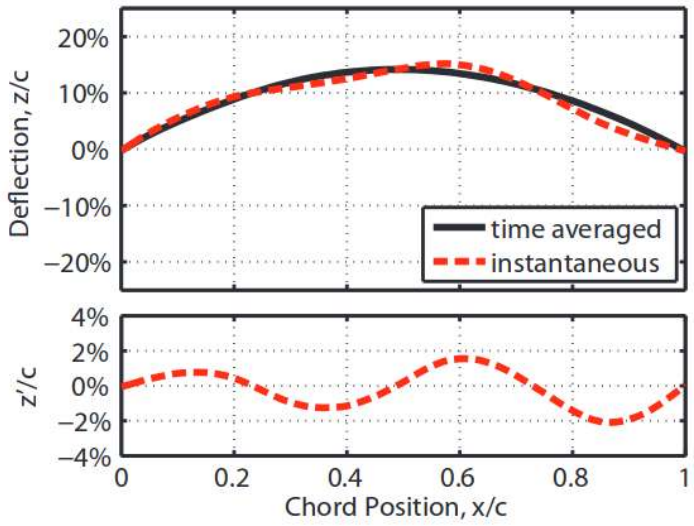

Figure 2.12: Time-averaged and instantaneous membrane deformation at mid-half-span for $\alpha = 10$deg and $U_\infty = 10m/s$, dominated by the primary standing wave mode [190].

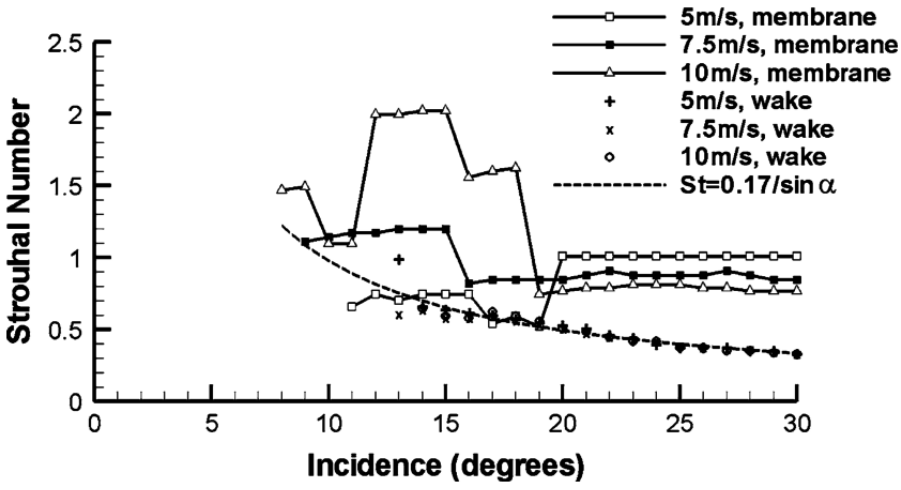

Figure 2.13: Membrane oscillation mode jumping to harmonics of the membrane natural frequency, as measured by Rojratsirikul et al [151] for low Reynolds number membrane wing flow ($5.31 \cdot 10^4 \leq R_e \leq 1.06 \cdot 10^5$).

Increasing the angle of attack is expected to decrease the dominant deformation mode number, as well as increase the amplitude of the deformation oscillations. [151] This can be seen from one of the Rojratsirikul et al deformation studies, as reproduced in Figure 2.14.

Given that the LEI kite membrane sections are tensioned by the LEI-tube, the inflated struts, and - to a lesser extent - the wire at the trailing edge, we can expect that the canopy sections that are not near the trailing edge will deform with a low mode number.

This dominant mode number may not be one due to the moderate Reynolds numbers over the large range of angles of attack, but we would still expect the dominant mode number to be on the order of one. The parabolic or catenary deformation assumptions - where the dominant membrane deformation mode is the second mode - are particularly well represented in the membrane-flow aeroelasticity research [190] [202] [190] [168].

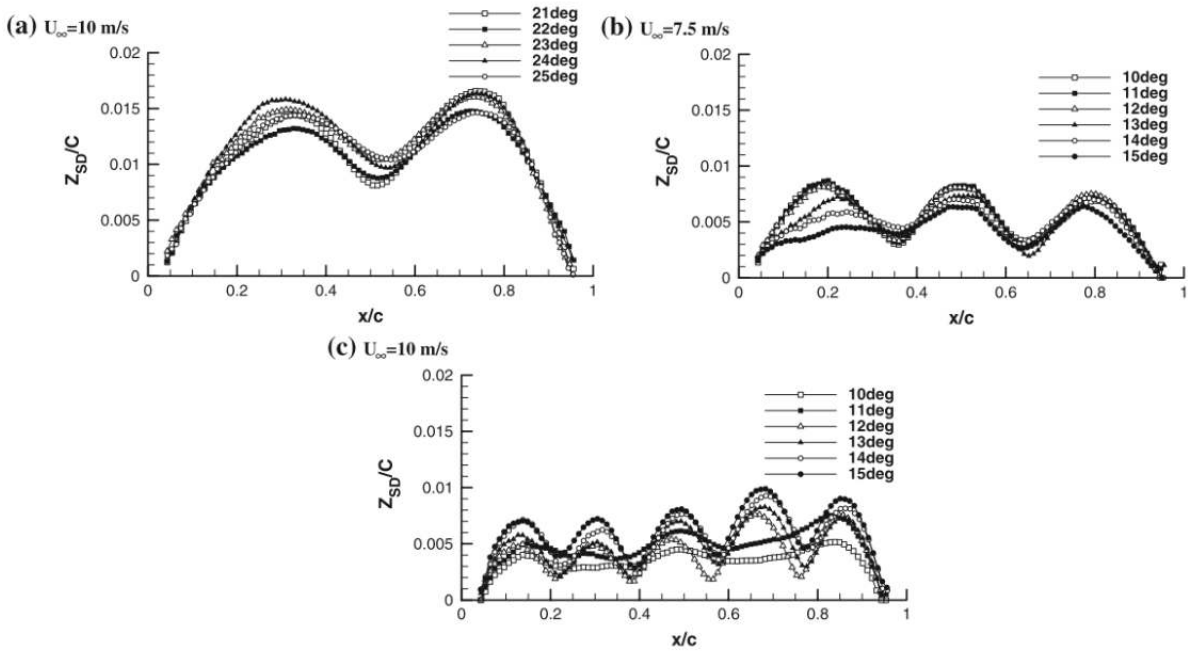

Figure 2.14: Influence of angle of attack and free-stream velocity on membrane deformation mode shape [151].

In model construction, the method will have much more flexibility if it is not assumed that the deformation follows a specific deformation mode number, other than to resign high-frequency harmonics to the unresolved sub-scale.

2.4 Quasi-Steady Flow Assumption

2.4.1 Flow Steadiness Analysis with Reduced Frequency

The reduced aerodynamic frequency f_R is a measure of whether a problem should be described as quasi-steady or unsteady.

If a fluid element crosses the wing faster than the kite can react to the force-change the element brings, then that fluid element will effectively see a steady kite.

This situation can be represented as a short time required for the flow to travel over the chord t_a^* in comparison to the time required for the kite to react to a force t_F^*. That is, a quasi-steady situation is described by: $t_a^* \ll t_F^*$.

In comparison, if the kite reacts at the same speed or faster than the fluid element travels, then the kite will be deforming as the fluid element passes over it. This situation - $t_a^* \not\ll t_F^*$ - must be modelled as unsteady.

Because the flight path and many of the deformations are approximately periodic, it is easier to express the reduced frequency of the kite FSI problem in the frequency domain than in the time domain. Then, the reduced frequency depends on the characteristic aerodynamics frequency $f_a^* = 1/t_a^*$, and the frequency with which the kite reacts to force f_F. Here, the frequency with which the kite reacts to force contains the frequency with which the position, angle of attack, camber, and global kite geometry change. Consequently, f_F must consider the flight path frequencies as well as the large-scale deformation mode frequencies.

Then, the problem can be considered quasi-steady if: $f_F^* \ll f_a^*$; and the problem must be considered unsteady if: $f_F^* \not\ll f_a^*$. Defining the reduced frequency as $f_R = \frac{f_F}{f_a^*} = \frac{t_a^*}{t_F^*}$, this can be summarized:

$$f_R \begin{cases} \ll 1 & : \text{Quasi-Steady} \\ \not\ll 1 & : \text{Unsteady} \end{cases}$$

2.4.2 Characteristic Aerodynamic Frequency

A characteristic fluid element, travelling with a representative velocity will take some characteristic amount of time to pass over the surface of the kite. Because flow effects are convected in a Lagrangian fashion, the characteristic amount of time it will take for flow conditions to vary over the kite travelling at subsonic speeds must be the same as the the characteristic time for the fluid element to travel the characteristic length of the kite [156] [69]. Consequently,

$$t_a^* = c/U_A$$

Considering the average apparent velocity, the minimum typical operational apparent velocity, and the global maximum apparent velocity, the relevant range of characteristic aerodynamic time for a fluid particle to travel over the chord range is between 0.06s and 0.13s, with an average value of 0.09s.

Following Flay & Jackson [69], the characteristic aerodynamic time is inverted to find a characteristic aerodynamic frequency:

$$f_a^* = 1/t_a^* = U_A/c$$

For this problem, this frequency is between 7.6Hz and 17.1Hz, with an average value of 11.4Hz.

2.4.3 Flight Path Frequencies

Characteristic Manoeuvre Frequency

During the course of the power (or reel-out) phase of the power-generation pumping-cycle, the kite flies "figure-eight" shaped manoeuvres.

Because the shapes of these figure-eights are similar with respect to a fairly-uniform wind field at altitude, the inflow conditions at equivalent points along the figure-eight path are close to periodic. That suggests that there is a characteristic period for one "figure-eight" manoeuvre, corresponding to a characteristic manoeuvre frequency.

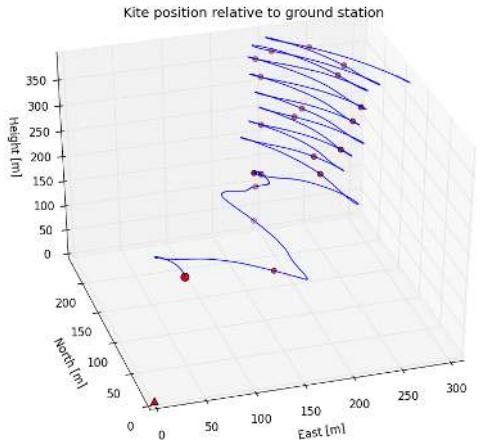

(a) A typical power-phase of the power-generation pumping cycle, demonstrating "figure-eight" manoeuvres. The pink circles correspond to ten second marks [73].

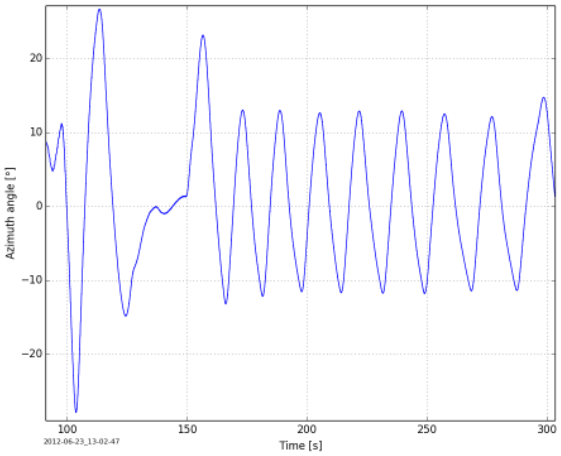

(b) A typical progression of azimuthal angle over time during the power-phase of the power-generation pumping cycle, where one wavelength corresponds to a manoeuvre period [73].

The characteristic manoeuvre period tends to be between 25 and 15 seconds, with a mean value of 20 seconds. These values correspond respectively to a characteristic manoeuvre frequency f_8 between

$$0.04Hz \leq f_8^* \leq 0.067Hz$$

with a representative value of $0.05Hz$.

Flight Dynamic Frequency

The figure-eight flight manoeuvre is composed of four consecutive periods of constant steering input. This suggests that there is a second characteristic period - and frequency - associated with the kite flight path, that is approximately four times the characteristic manoeuvre frequency:

$$0.16Hz \leq f_{FD}^* \leq 0.27Hz$$

with a representative value of $0.20Hz$.

2.4.4 Kite Deformation Modes

In typical operation, an LEI kite experiences multiple typical deformation modes. In order from generally fastest deformations to generally slowest deformations, these are: trailing edge flutter, seam-rippling, canopy billowing, jellyfishing, bunny-ear flapping, and leading edge indentation which can lead to kite collapse.

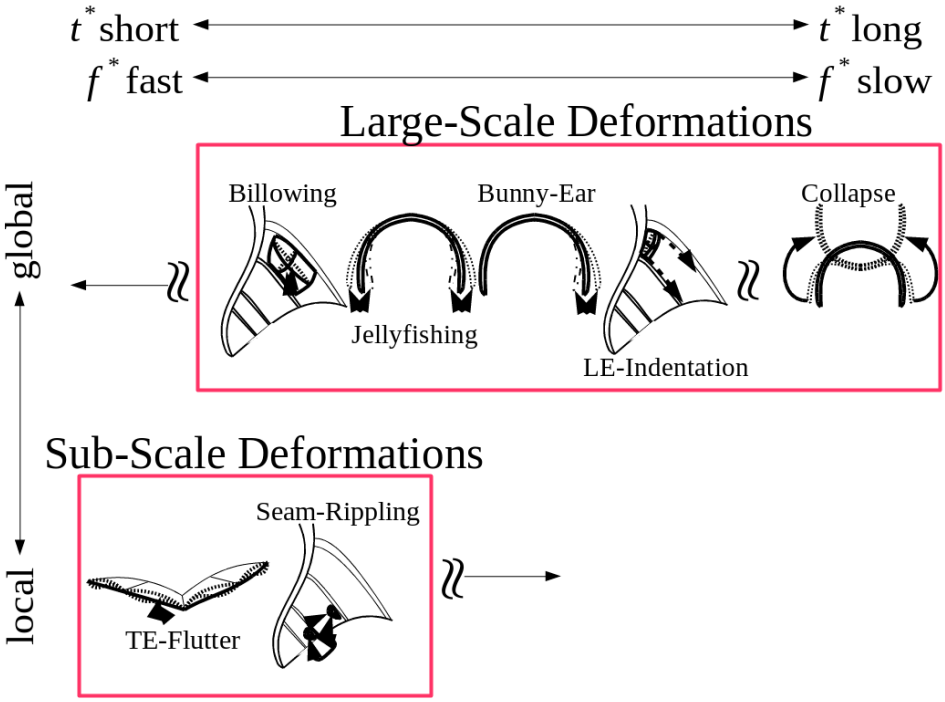

Figure 2.16: The typical deformation modes seen in normal pumping-cycle kite operation.

Trailing Edge Flutter Deformation Mode

Trailing edge flutter is the deformation of the canopy's free trailing edge as a result of the periodic aerodynamic force oscillation caused by vortex shedding.

Because the trailing edge flutter produces an audible buzz, and the audible frequency range for humans is generally accepted to be between 20Hz and 20kHz [85], it is expected that the characteristic trailing edge flutter frequency $f^*_{TEF} > 20$Hz.

This audio-bound is supported by video analysis. For an LEI kite in normal power-production operation, the trailing edge flutter is faster than video analysis can confidently capture at 30 frames per second. The Nyquist Shannon sampling theorem says a behavior of a given frequency can only be observed if the sampling frequency is twice the behavior frequency. This would suggest that the characteristic trailing edge flutter frequency $f^*_{TEF} > 15$Hz.

This deformation is relatively local, as it is confined to the small band of the canopy along the trailing edge. It consequently has a small effect on the aerodynamic force distribution over the total body of the kite, and can be resigned to the sub-scale. Resolution of the trailing edge flutter deformation mode is outside of the scope of this thesis.

For completeness's sake, an order-of-magnitude upper limit on the trailing edge flutter frequency can be estimated.

One estimation method follows the the correction method of Rojratsirijul et al [151] to the membrane flutter frequency estimation method developed by Zhang et al [202], and used by Song et al [168] and Waldman & Breuer [190]. The basis of this first-order estimation method is the work of Rojratsirikul et al [150], and Michelin & Smith [131] showing that the trailing edge flutter frequency for membrane wings - stretched over aerodynamicially negligible frames - tends to the harmonics of the membrane natural frequency.

A second estimation method follows the work of Strouhal-locking of membrane splitter plate oscillation behind non-negligible circular cylinders by Allen et al [13] and Shukla et al [161].

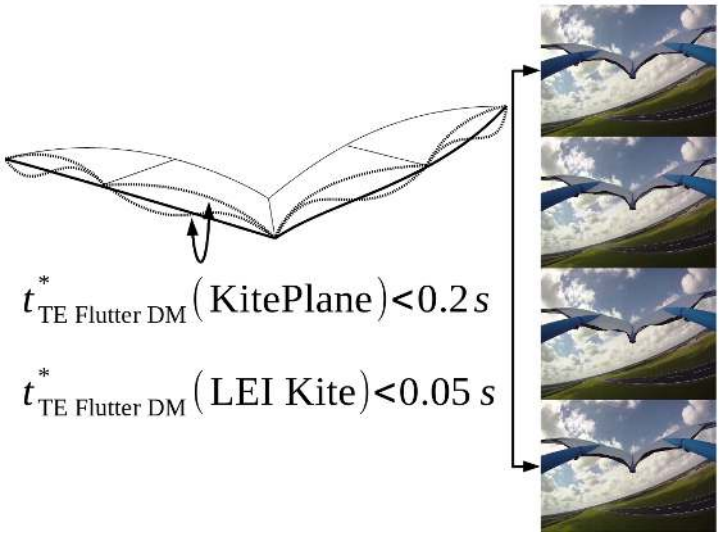

Figure 2.17: A concept sketch and video frame-extraction from flutter-experiment flight demonstrate the trailing edge flutter deformation mode on the TU Delft KitePlane. Trailing edge flutter is difficult to see on an LEI kite in power-production operation due it's high frequency, but produces an audible hum.

Rojratsirikul Correction to the Zhang Approximation Method for Membrane Flutter Frequency The membrane natural frequency can be estimated very roughly from the membrane tension using linear elastic theory. The membrane tension can be estimated from an estimated membrane deformation, which is itself derived from known material properties and an estimate of forces. Rojratsirikul et al [151] found that approximating the membrane flutter frequency with this first-order method predicts frequencies that are about half of what can be measured experimentally, for membrane wings without an LEI tube.

According to the Zhang approximation method, a membrane wing or canopy-section that is attached at the leading-edge, and two side edges, with a free trailing edge, will vibrate analogously with a 2D membrane that is tensioned in the span-wise direction. The fundamental frequency for this vibration can be found with:

$$f_{m,calc} = \beta_Z \sqrt{\frac{T}{m_m b'}}$$

where β_Z is a proportionality constant, which is expected to be greater for a pre-tensioned canopy than the value $\beta_Z = 1/2$ of a tensioned string; m_m is the membrane mass $m = \rho_m(b'c)$; and b' is the canopy-section span.

Because the trailing edge is free, the tension in the span-wise direction should be much greater than the tension in the chord-wise direction [202]. Consequently, for the process of roughly estimating the expected membrane natural frequency, the effect chord-wise tension is neglected. This is a reasonable approximation towards the trailing edge of the canopy, but not necessarily near the connection point with the LEI tube.

$$T = |T_b\hat{b} + T_c\hat{c}| \approx T_b$$

Zhang et al [202] measure β_Z to fit to the relationship:

$$\beta_Z = \frac{0.83}{H^{0.337}}$$

from tests with a membrane $E = 450$kPa, $h = 0.32$mm, and $q = 15, 60, 135$Pa; $E = 500$kPa, $h = 0.62$mm (note that there is an inconsistency within this paper, that the experimental-description reads $h = 0.52$mm, and the graph-legend reads $h = 0.62mm$), and $q = 60$Pa; $E = 1900$kPa, $h = 0.08$mm, and

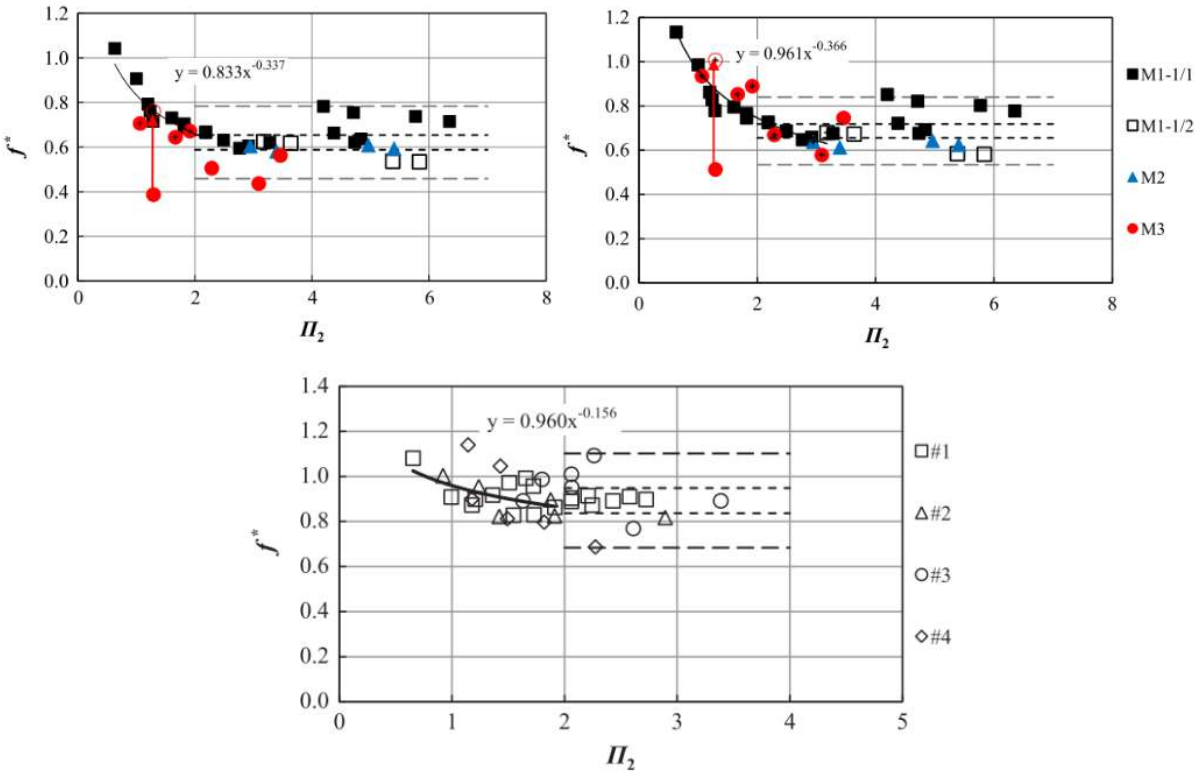

Figure 2.18: The relationship between membrane fundamental frequency scaling constant β_Z and the membrane pre-tension parameter (top left) as measured by Zhang et al, (top right) as corrected for added mass due to membrane oscillation, and (bottom) as reported in previous literature. The legends apply: (M1-1/1, black-square) $E = 450$kPa, $h = 0.32$mm, $q = 15, 60, 135$Pa, and $AR = 1$; (M1-1/2, white-square) $E = 450$kPa, $h = 0.32$mm, $q = 60$Pa, and $AR = 0.5$; (M2, blue-triangle) $E = 500$kPa, $h = 0.62$mm, $q = 60$Pa, and $AR = 1$; (M3, red-square) $E = 1900$kPa, $h = 0.08$mm, $q = 60, 135$Pa, and $AR = 1$, [202]; (#1, square) Timpe et al [177]; (#2, triangle) Zhang et al [203], (#3, circle) Hubner & Hicks [91], and (#4, diamond) Scott et al [202]

$q = 60, 135$Pa, and correct this measured β_Z value for the expected added mass caused by the membrane oscillation to

$$\beta_{Z,AM} = \frac{0.961}{H^{0.366}}$$

From their results, when $H > 1$, $\beta_{Z,AM}$ remains well between

$$0.5 \leq \beta_{Z,AM} \leq 0.9$$

Applying the first order estimate that:

$$0.5 = \beta_{Z,AM,min} \leq \beta_{Z,AM} \leq \beta_{Z,AM,max} = 0.9$$

and the estimation that the canopy-section tension in the span-wise direction $T_{b'}$ is likely on the order of

$$16.1\text{N} = T_{b',depower} \leq T_{b'} \leq T_{b',power} = 104\text{N}$$

with an upper bound at 1900N, predicts that the canopy natural frequency will likely be on the order of

$$4.45\text{Hz} = f_{m,calc,min}(T_{b',depower}, \beta_{Z,AM,min}) \leq f_{m,calc} \leq f_{m,calc,max}(T_{b',power}, \beta_{Z,AM,max}) = 20.4\text{Hz}$$

with an upper bound at $f_{m,calc,maxBound}(T_{b',power,maxBound}, \beta_{Z,AM,max}) = 87.1$Hz.

The canopy trailing edge flutter frequency can be found by multiplying the calculated linear-elastic membrane natural frequency by the factor $\phi_{Roj} = 2$ found empirically by Rojratsirikul et al [151]:

$$f_{TEF} = \phi_{Roj} f_{m,calc}$$

That is, the Rojratsirkiul Correction to the Zhang Method suggests that the maximum trailing edge flutter frequency will be somewhere between 40.7Hz and 174Hz.

Strouhal-Locking Flutter Frequency Estimation Method The TUD-25mV3 surf kite has a characteristic LEI tube diameter to chord ratio $\Lambda_{LEI} = \frac{c}{D_{LEI}} = 13.15$.

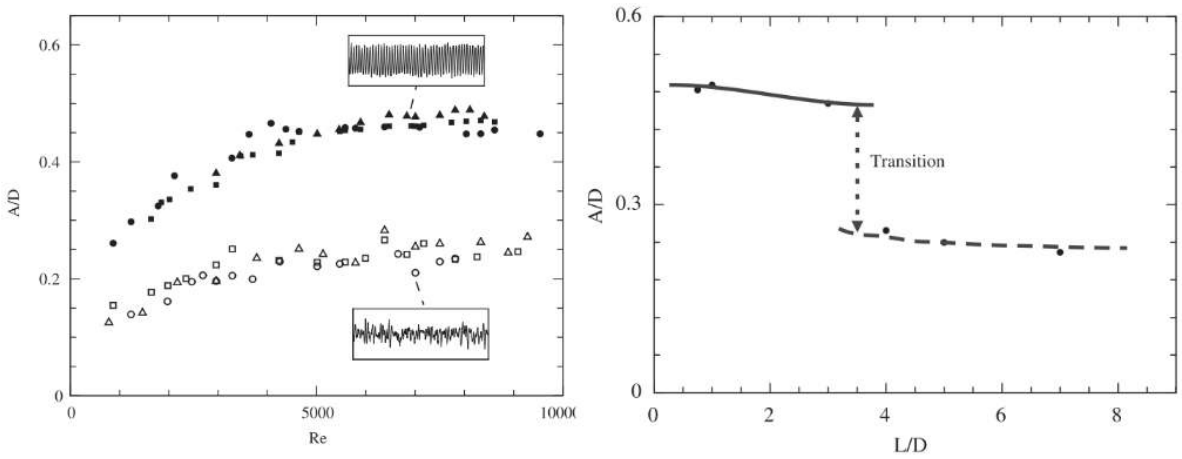

Figure 2.19: The shift between small Λ_{LEI} and large Λ_{LEI} behavior, as found by Shukla et al [161] for a hinged splitter plate behind a cylindrical cylinder, where Λ_{LEI} is written as "L/D", the splitter plate oscillation amplitude is A and the cylinder diameter is D

Shukla et al [161] found that there is a marked difference in membrane flutter behavior at a threshold value $3 \leq \Lambda_{LEI} \leq 4$. Consequently, the LEI Λ_{LEI} values can be considered large. When Λ_{LEI} is large - the oscillation frequency of a membrane streamer ("eel") behind a bluff body no longer depends on the length of the membrane, but is highly dependent on the ability of the membrane to damp out oscillations [13].

When Λ_{LEI} is large and the Reynolds number is small, ie. ($\mathcal{O}(10^3)$), membrane oscillations for an "eel" behind a bluff body will be infrequent, with small amplitudes [13].

For an intermediate-low Reynolds number and large Λ_{LEI}, such as the values given by Allen et al [13] ($\mathcal{O}(10^4) \leq R_{e,LEI} \leq \mathcal{O}(4{\cdot}10^4)$), any given Reynolds number is expected to correspond to a fairly constant periodic membrane-oscillation Strouhal number. The Strouhal number increases with the Reynolds number until it reaches a threshold value; for Allen et al's particular experiment, this threshold value is at approximately 0.16. At these intermediate-low Reynolds numbers, the membrane-oscillation is not yet fully coupled to the flow, such that the membrane-tension damps the oscillations.

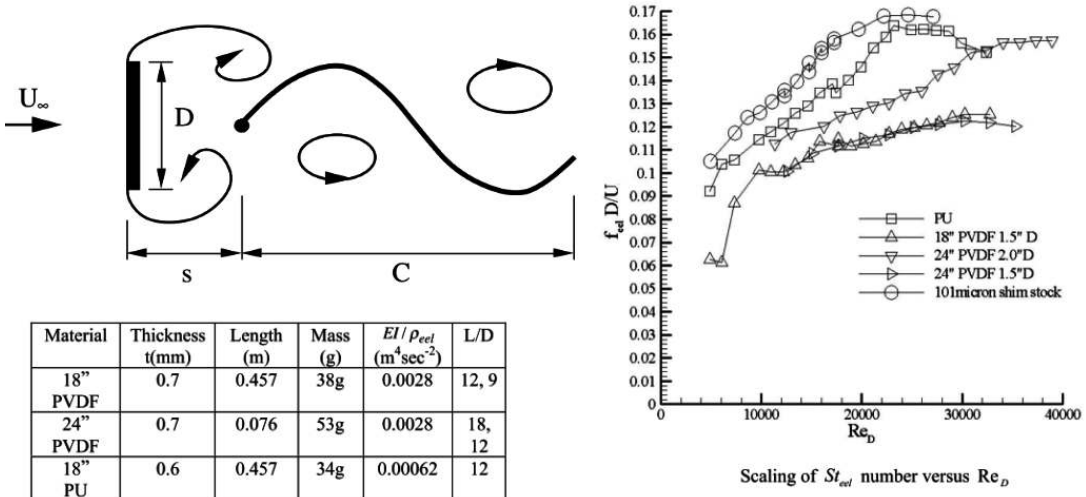

Material	Thickness t(mm)	Length (m)	Mass (g)	EI/ρ_{eel} (m^4sec^{-2})	L/D
18" PVDF	0.7	0.457	38g	0.0028	12, 9
24" PVDF	0.7	0.076	53g	0.0028	18, 12
18" PU	0.6	0.457	34g	0.00062	12
18" Shim	0.1	0.457	7g	0.0021	12

Figure 2.20: Trends in the relationship between vortex shedding Strouhal number, the flow Reynolds number based on bluff body width, and membrane-geometry, including the ratio between the bluff body width and membrane "eel" length, as measured by Allen et al [13].

When Λ_{LEI} is large and the Reynolds number increases past the point where the Strouhal number reaches the threshold value, the membrane oscillation frequency approaches the bluff-body vortex shedding frequency with decreasing membrane stiffness - and consequently, for a membrane whose stiffness is primarily determined by the membrane tension, rather than material stiffness - decreasing membrane tension. The wavelength of membrane-oscillation is expected to trend to the van Karman street wavelength behind the bluff-body alone; the membrane oscillation amplitude to tend to the wake width of the van Karman street behind the bluff-body alone. In this region, the membrane oscillation amplitude is constant as Reynolds number increases, and the membrane oscillation Strouhal number increases linearly with the Reynolds number until it levels out at a maximum Strouhal number. This maximum Strouhal number is a function of the bluff-body shape and the flow speed. [13]

The assumption that the kite canopy membrane oscillation frequency will approach (or "lock" on to) the vortex shedding frequency behind the LEI tube is restricted by the fact that the LEI tube diameter-based Reynolds number range ($2.53 \cdot 10^5 \leq R_{e,LEI} \leq 6.16 \cdot 10^5$) is within the region described by Lienhard [110] where there is no one specific vortex-shedding frequency, but rather a spectrum of vortex shedding frequencies. Lienhard gives an approximate range of relevant Strouhal numbers as $0.17 \leq S_{t,Lock} \leq 0.4$. As these values correspond to apparent velocities between 20m/s and 45m/s, the estimated locking-on membrane flutter frequencies $f_{TEF,Lock} = \frac{S_{t,Lock} U_A}{D_{LEI}}$ are between:

$$17\text{Hz} \leq f_{TEF,Lock} \leq 90\text{Hz}$$

It should be noted, with respect to this Stouhal-locking estimation method, that Rojratsirikul et al [151] suggest that the locking-on Strouhal number of membrane wings at the high incidences near- and post-stall decreases proportionally (refer back to Figure 2.13) to the inverse of the sine of the the angle of attack:

$$S_t \propto \frac{1}{\sin \alpha}$$

If it is assumed that flow separation begins around 15^o angle of attack for an LEI kite - which is an intermediate value between the values reported in the literature - and the reported relationship extends outside of the low Reynolds number flow regime of the Rojratsirikul test, the relationship would suggest that the membrane flutter frequency range at high angle of attack may shift down by up to a factor of

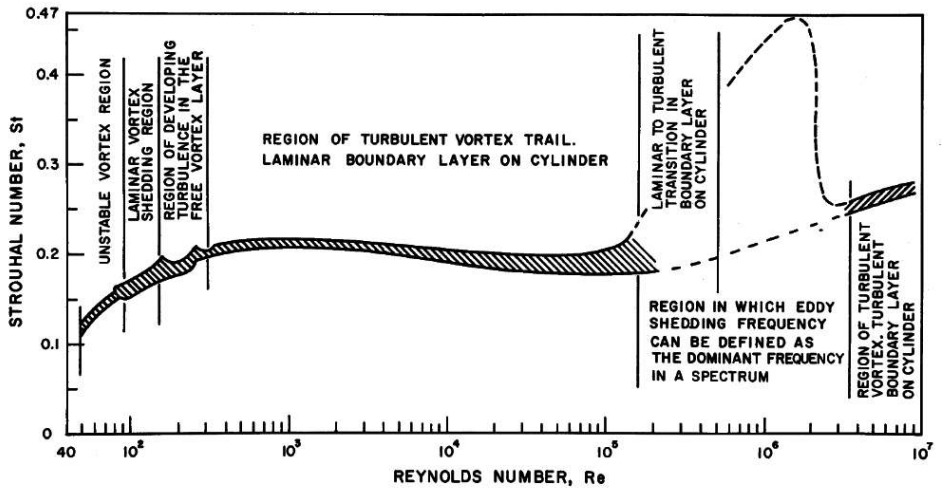

Figure 2.21: Strouhal Number vs. Reynolds Number for the Vortex Shedding van Karman streets behind a rigid circular cylinder, as reproduced from Lienhard [110].

$\left(\frac{\sin(15^o)}{\sin(50^o)} = 0.34\right)$. This would shift the maximum trailing edge flutter frequency, at high angles of attack, down to

$$f_{TEF,Lock,High\ \alpha} \leq 30.4\text{Hz}$$

which would still be within the audible spectrum.

Seam-Rippling Deformation Mode

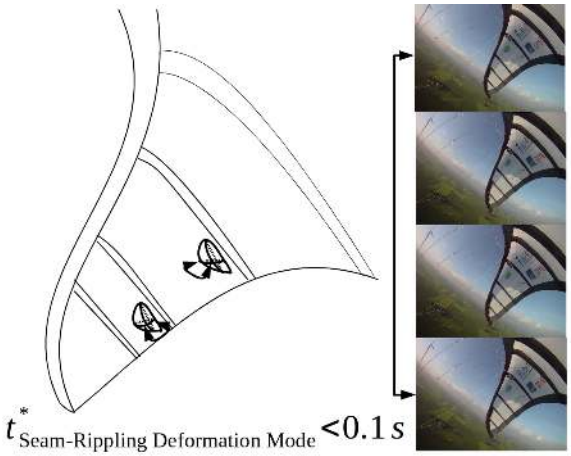

Figure 2.22: A concept sketch and video frame-extraction from power-production operation demonstrate the seam-rippling deformation mode on an LEI kite.

Seam-rippling (see Figure 2.22) is the small-scale travelling wave that occurs near the struts close to the trailing edge, where the tension in the span-wise direction is much greater than the tension in the chord-wise direction.

This deformation is extremely local in nature, and occurs faster than video analysis can confidently capture at 30 frames per second. Confidence can only be given that a full seam-rippling wave period must be less than 3 frames, so the characteristic time of this deformation mode must be less than $t^*_{SR} < 0.1$s. This corresponds to a confidence-limit of the characteristic deformation frequency at $f^*_{SR} > 10$Hz.

Because of the local nature of the deformation mode, and its small influence on the aerodynamic force distribution over the whole kite, seam-rippling is a sub-scale behavior. Resolution of the seam-rippling deformation mode is outside of the scope of this thesis.

Canopy Billowing Deformation Mode

Canopy billowing (see Figure 2.23) is the "adaptive camber" of the LEI kite under strong aerodynamic forces. This is a global deformation mode, and relevant to the power-production kite FSI problem. Video analysis of typical kite power-production operation shows that this global deformation mode has a characteristic time on the order of 0.6s. This corresponds to a characteristic deformation frequency on the order of $f^*_{CB} \approx 1.7$Hz.

Jellyfishing Deformation Mode

Jellyfishing (shown in Figure 2.24) is the oscillatory behavior where the canopy arc flattens and tightens repeatedly as the kite corners. This is a global deformation mode, and relevant to the power-production kite FSI problem. Video analysis of typical kite power-production operation shows that this global deformation mode has a characteristic time on the order of 0.7s. This corresponds to a characteristic deformation frequency on the order of $f^*_{JF} \approx 1.4$Hz.

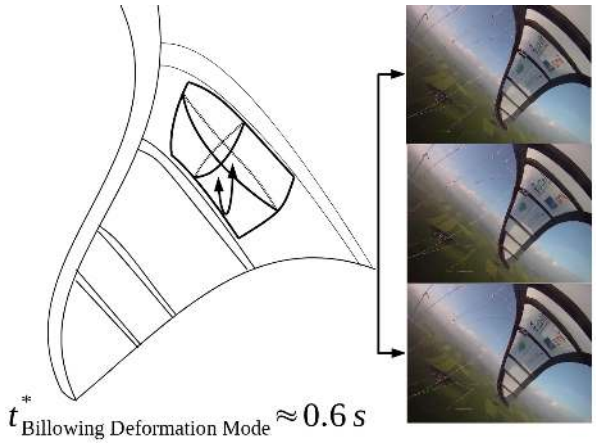

Figure 2.23: A concept sketch and video frame-extraction from power-production operation demonstrate the canopy billowing deformation mode on an LEI kite.

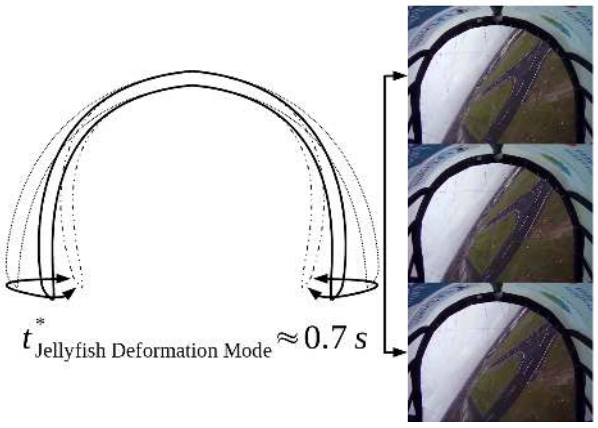

Figure 2.24: A concept sketch and video frame-extraction from power-production operation demonstrate the jellyfishing deformation mode on an LEI kite.

Bunny-Ear Flapping Deformation Mode

Bunny-ear flapping (see Figure 2.25) is the oscillatory behavior where only one tip of the kite flaps in and out repeatedly, as the kite corners. This deformation mode is distinct from the jellyfishing deformation mode, as the jellyfishing mode flaps both tips of the kite synchronously. Bunny-ear flapping is associated with the deformation that enables kite steering. Bunny-ear flapping is a global deformation mode, and relevant to the power-production kite FSI problem. Video analysis of typical kite power-production operation shows that this global deformation mode has a characteristic time on the order of 0.8s. This corresponds to a characteristic deformation frequency on the order of $f^*_{BE} \approx 1.3$Hz.

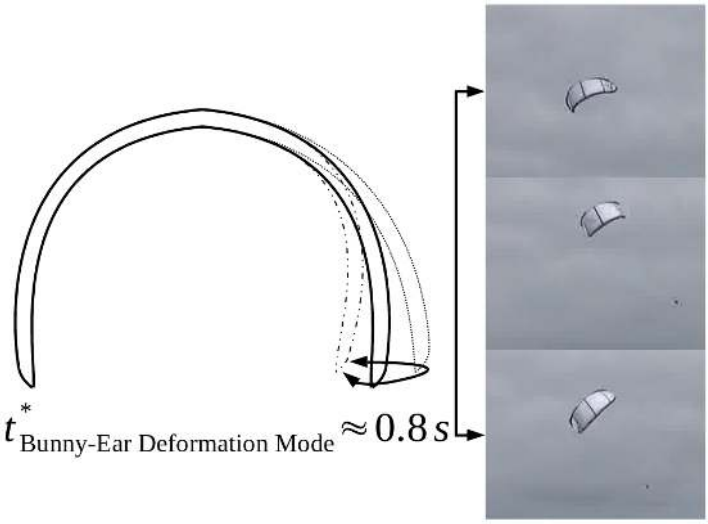

Figure 2.25: A concept sketch and video frame-extraction from power-production operation demonstrate the bunny-ear flapping deformation mode on an LEI kite.

Leading Edge Indentation Deformation Mode

Leading edge indentation (see Figure 2.26) is the behavior where the canopy attached to the LEI tube is indented inwards at low angles of attack. This deformation is the initial phase of kite collapse, where the deformation has not yet caused an irrecoverable aerodynamic-force direction change. Considering LEI kite flight video for the cases where the leading edge indentation recovers, without leading to kite collapse and crash, the deformation occurs over a characteristic time on the order of $t^*_{IDM} \approx 0.9$s, which corresponds to a characteristic frequency on the order of $f^*_{IDM} \approx 1.2$Hz.

Leading edge indentation is a global phenomenon, and has a large effect on the aerodynamic force distribution over the whole kite.

Collapse Deformation Mode

The collapse (shown in Figure 2.27) of an LEI kite is half of the low-lift bistable luffing instability typical in membrane flow problems. In this case, the angle of attack decreases sufficiently for the the leading edge indentation to push to the trailing edge. The kite inverts, such that the adaptive camber faces ground-wards rather than upwards. Because the kite no longer responds predictably to the steering commands, kite collapse nearly always crashes the kite.

In that collapse is a cause of mission-failure for power-production kites, it is important that the aerodynamic model be able to predict this phenomenon.

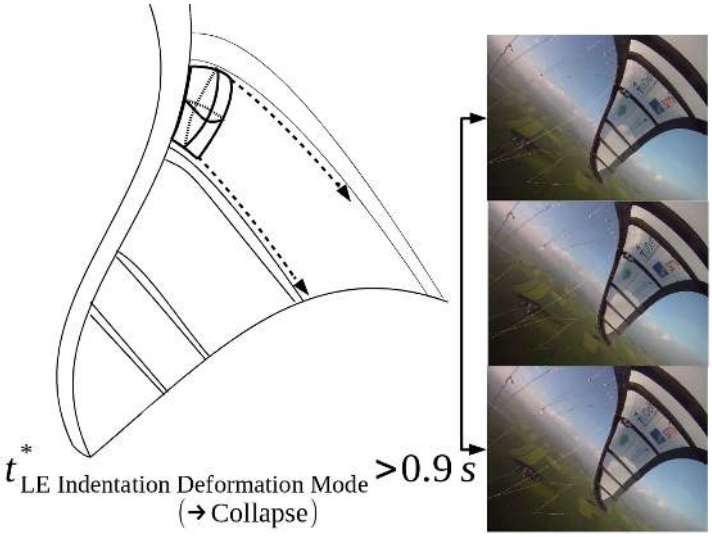

Figure 2.26: A concept sketch and video frame-extraction from power-production operation demonstrate the leading edge indentation deformation mode on an LEI kite.

Video analysis of typical kite power-production operation shows that this global deformation mode occurs over a characteristic time on the order of $t^*_{Collapse} \approx 3$s. Though the behavior is not even close to periodic, an artificial characteristic frequency can be found $1/t^*_{Collapse} = f^*_{Collapse} \approx 0.3$Hz.

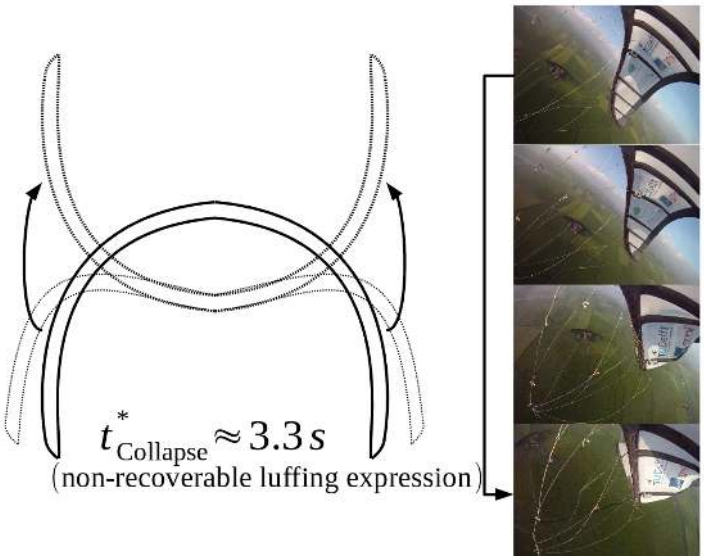

Figure 2.27: A concept sketch and video frame-extraction from power-production operation demonstrate the collapse of an LEI kite.

2.4.5 Justification of the Quasi-Steady Flow Assumption

The flight path and global deformation mode frequencies can be compared with the characteristic aerodynamic frequency of the kite in normal operating conditions.

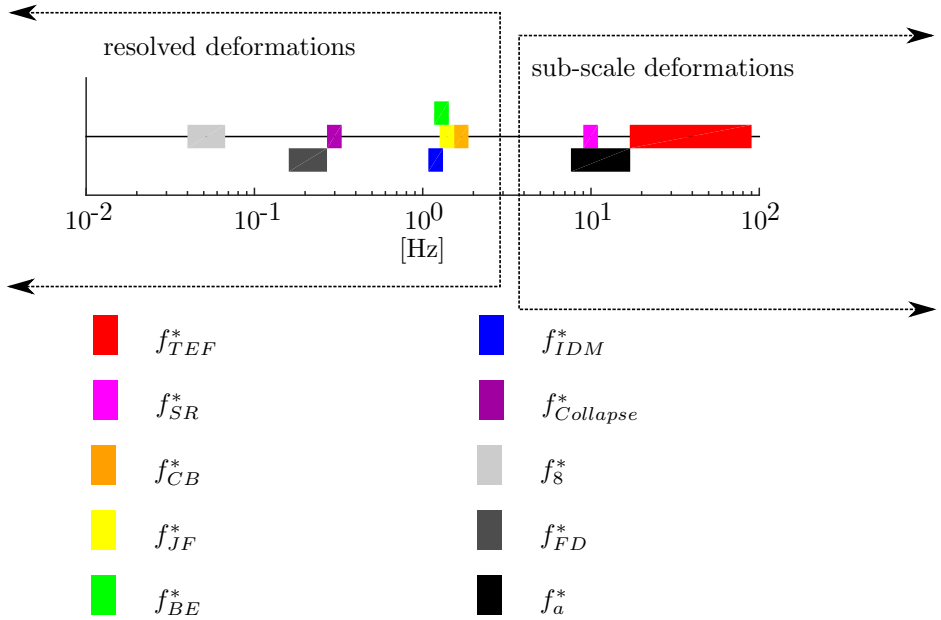

Figure 2.28: Summary of relevant frequencies to the kite FSI problem, from the kite flight path in standard operation and the observed kite deformation modes. Note that rainbow-colors correspond to deformation mode frequencies and grey-tones correspond to flight-path frequencies. When deformation mode characteristic frequencies are estimated with the singular average values found from video analysis, the effect of this frequency is conservatively expected to be "smeared" by ten percent in either direction.

With the frequencies relevant to the kite FSI problem ranging between 0.04Hz for the slowest expected manoeuvre frequency f_8 and approximately 1.7Hz for the canopy-billowing frequency f_{CB}, and a typical characteristic aerodynamic frequency of $f_a = 11.4$Hz, the range of reduced frequencies relevant to the kite FSI problem are:

$$0.0035 \leq f_R \leq 0.15$$

This reduced frequency range should allow the kite FSI problem to be modelled under the assumption of quasi-steady flow, when neglecting the sub-scale deformations.

The validity of the quasi-steady flow assumption for LEI kites under power-production conditions might be criticized with the analogy that the quasi-steady assumption has been shown to be invalid [20] [70] for yacht-sail FSI problems. However, Augier et al and Fossati & Muggiasca give values for the maximum typical reduced frequency relevant to the yacht-sail FSI problem of 0.47 [20], 0.43 [70] and 0.33 [71], which are rather higher than the maximum typical reduced frequency in the LEI kite FSI problem. Intuitively, it would appear that because yacht-sails are constrained in the span-wise direction, the primary deformations of a yacht sail must include the trailing edge flutter, a high frequency behavior that is overshadowed by the other global deformation modes in the case of an LEI kite.

Ultimately, the fact that previous quasi-steady aerodynamic flow-models of LEI kites - such as Van Kappel's nonlinear extensions to a quasi-steady vortex lattice method [183] - have been successfully validated against real performance data suggests that the quasi-steady assumption is acceptable.

2.5 Further Modelling Assumptions

2.5.1 Material Assumptions

The canopy of the TUD-25mV3 kite is constructed from $h = 0.08$mm-thick Ripstop Nylon (Spinnaker), whose material properties were tested by Dr. Cédric Galliot of the EMPA Center for Synergetic Structures [74].

The canopy areal mass density is $\rho_m = 50\text{g/m}^2$ [74]. A thickness $h = 0.08 \cdot 10^{-3}$m, gives a volumetric canopy density of $\rho_{m,V} = 625\text{kg/m}^3$.

The canopy membrane has a stiffness in the warp direction $k_{m,warp} = 111.8$kN/m, and a stiffness in the fill direction $k_{m,fill} = 72.3$kN/m [74]. In keeping with Bosch [28], the assumption will be made that we can use an **assumption for average canopy stiffness** of $k_m = 100$kN/m.

The elasticity of a membrane is dependent on strain, such that it follows a j-shape stress-strain curve [15]. However, due to the inavailability of the original data and the fact that the measurement of the membrane elasticity is outside of the scope of this thesis, the linearized value found by EMPA, and reported by Bosch [28] will be used. Consequently, the Young's modulus E_m is assumed to be 1250MPa. A **linear Young's modulus assumption** is known to be reasonable for membrane wings when the canopy strain is less than 10 percent [170] [202].

Despite the fact that membrane wing shape, and consequently the pressure distribution over the wing, is very sensitive to the membrane length [53], the extension of the membrane as a result of aerodynamic force is expected to be sufficiently small that the membrane can be assumed inextensible.

With a Young's modulus $E_m = 1250$MPa, expected apparent velocities U_A between 20m/s and 45m/s, and air densities ρ_{air} between 1.225kg/m^3 and 1.112kg/m^3, the membrane Cauchy number ($C_y = \frac{\rho_{air} U_\infty^2}{E_m}$) can be conservatively expected to range between $3.55 \cdot 10^{-7}$ and $1.98 \cdot 10^{-6}$. As the membrane Cauchy number described the extent of membrane deformation under the flow effects, the small membrane Cauchy numbers supports the **inextensible membrane assumption**.

The canopy Poisson ratio, as measured by Galliot [74], is $\nu_m = 0.35$.

Canopy porosity decreases the pressure difference between the suction and pressure surfaces, and consequently decreases the lift on the canopy [138]. The porosity σ_m of the TUD-25mV3 canopy material has not been measured. Such porosity tests, and the influence of porosity on the force distribution over the canopy, fall outside of the scope of this thesis. For the purposes of this thesis, it is assumed that the LEI-kite has a non-porous canopy ($\sigma_m \approx 0$), despite the lack of material testing data for the exact TUD-25mV3 Nylon Ripstop. This assumption follows the general suggestion by the published specification sheet of Bainbridge [1], manufacturer of general kite-canopy fabrics. With respect to numerical simulation validity, Newman [138] suggests that practical values of yacht-sail porosity - typically around $\sigma_m \approx 0.03$ - are small enough that the **impermeable membrane assumption** is generally valid, producing only small errors.

For information about the kite inflated-beam frame, the reader is directed to the PhD theses of Breukels [30] and Veldman [185].

2.5.2 The Smooth Surface Assumption

As long as the surface roughness elements are smaller than the viscous sublayer, the roughness may be neglected. The viscous sublayer will become thinner as the Reynolds number increases, consequently, the "smooth surface" approximation becomes progressively less likely for a given surface as the Reynolds number increases [32].

The critical Reynolds number $R_{e,k,crit}$ at which surface roughness becomes relevant is based on the

average roughness-element size k_{re} [32]:

$$R_{e,k,crit} = 100 = \frac{k_{re,crit} U_A}{\nu_{air}}$$

For the conservative estimate of maximum operational apparent velocity $U_{A,max} = 40\text{m/s}$ and minimum operational atmospheric kinematic viscosity $\nu_{air,min} = 1.461 \cdot 10^{-5}\text{m}^2/\text{s}$, this suggests that for the smooth surface assumption to be valid in the case of the kite, the surface roughness length must be less than:

$$k_{re} < k_{re,crit} = 3.6525 \cdot 10^{-5}\text{m}$$

As reported by Kawabata & Niwa [99] the geometrical roughness of a plane-woven material tends to be between 1/40 and 1/100 of its fabric thickness.

Given that the canopy material has a thickness of $h = 8 \cdot 10^{-5}\text{m}$, the **smooth surface assumption** appears reasonable, despite utilizing a Ripstop- rather than plane-weave.

2.5.3 Flow Envelope Assumptions

As the Reynolds number with respect to chord is significantly greater than one, we can say that that intertial forces on the flow outside the boundary layer significantly outweigh the viscous forces on the external flow. This is consistent with an **inviscid external flow assumption**.

As the turbulence intensity is expected to be low for the freestream flow, and the wind velocity is high enough that the kite does not encounter its own wake, or other sources of externally-generated vorticity, the flow outside the boundary layer can be assumed to fit a **irrotational external flow assumption**.

Given that the flow mach number ($M \approx \frac{U_A}{330\text{m/s}} \leq 0.14$) is low, we can reasonably make an **incompressible flow assumption**.

Flow - external to the boundary layer - which can be described as inviscid, irrotational and incompressble, meets the requirements for the **external potential flow assumption**.

As found by Mendenhall et al [130] - who had access to unpublished Langley Research Center data for 2D parawings with cylindrical leading edge booms, onto which a flat plate is connected tangent to the top of the leading edge cylinder - the critical Reynolds number for such a combined parawing is equivalent to the critical Reynolds number for the leading edge cylinder alone. The Reynolds number based on the LEI tube diameter is expected to range between $2.53 \cdot 10^5 \leq R_{e,LEI} \leq 6.16 \cdot 10^5$. This would suggest that Reynolds regime would be expected to include the transition between laminar- and turbulent- flow regimes, as compared to critical cylinder Reynolds numbers on the order of $4 \cdot 10^5$ reported by Mendenhall et al [130].

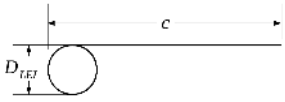

Figure 2.29: Schematic of Mendenhall et al [130] parawing cross-section, adapted to current nomenclature.

However, 2D EllipSys2D CFD studies of LEI kite profiles at the Danish Technical University [146] found that there is litte to no difference - for moderate angles of attack between $-10^o \leq \alpha \leq 15^o$ - in pressure distribution and aerodynamic force generation when the model is forced to be fully turbulent or allowed to transition at will (See Figure 2.30b). As these CFD studies were run at a Reynolds number of $0.195 \cdot 10^6$, this result suggests that the transition critical Reynolds number must be below this test Reynolds number. That is, $R_{e,crit} < 1.95 \cdot 10^5$, such that the kite will always experience turbulent flow.

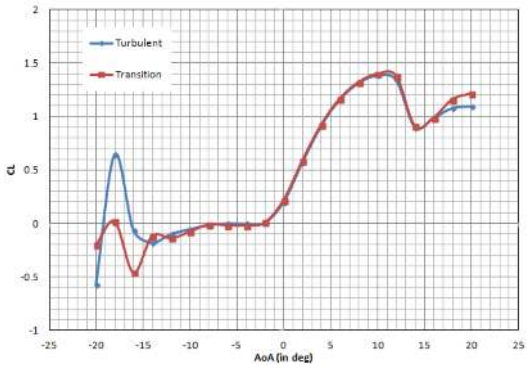

(a) Difference between the 2D Lift Coefficient for a Fully Turbulent vs. Transitioning Flow for an LEI Profile, reproduced from Raj [146].

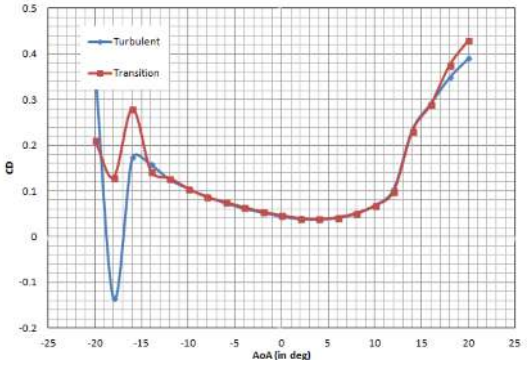

(b) Difference between the 2D Drag Coefficient for a Fully Turbulent vs. Transitioning Flow for an LEI Profile, reproduced from Raj [146].

The large difference between the Mendenhall et al [130] and DTU [146] results may be due to the influence of the wind tunnel testing method on which Mendenhall et al did not comment, the DTU group's transition-prediction or SST $k-\omega$ turbulence modelling. This difference is unlikely to be the effect of aeroelastic deformation or flow unsteadiness, as both models apply a rigid profile and a steady inflow. To limit the scope of this thesis work, we will make a **fully-turbulent boundary-layer assumption**, however this assumption introduces a great deal of uncertainty and would be worth assessing in a further work.

Due to the low aspect ratio [152] and high anhedral [200] of the kite wing, we can expect that a **highly-three dimensional flow assumption** would be reasonable (See Figure 2.31). Further, the separation bubble expected in the wind-shadow region behind the kite canopy, and the separation region above the canopy tail at high angles of attack, are associated with secondary flow vortices [179].

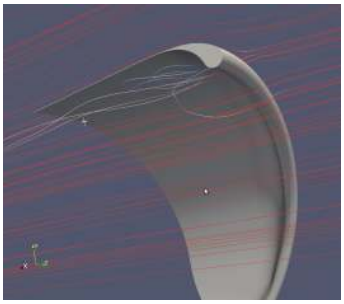

Figure 2.31: RANS-solution streamlines around a half kite showing recirculation and secondary-flow under an LEI-kite, colored by velocity, as produced by May [126].

The analytical prediction of turbulent boundary layer separation locations [35] lies outside of the scope of this work. Instead, we will make the **assumption of a known steady-flow separation-line location**. Then, we can model the flow on the kite using pre-determined separation locations drawn either from the existing literature - such as Deaves' [51] RANS results, given previously - or a geometric argument.

The dimensionless mass ratio $\mathcal{M} = \frac{\rho_{m_i} V}{\rho_{air}}$ relevant to this thesis varies between $510 \leq \mathcal{M} \leq 562$, depending on the flight altitude. The mass ratio describes the relative importance of added mass caused by the canopy motion on the system inertia. For these large values of $\mathcal{M}$, it is fair to **assume a negligible inertial effect of added-mass** [45].

Chapter 3

Comparison of Aerodynamic Models Applied to Membrane-Flow Problems

There are many possible aerodynamic modelling methods. To select a method for the LEI-kite problem, we should consider those models that have been previously used for membrane-flow problems, in terms of their ability to satisfy both the practical requirements generated by the model's intended use in iterative-design and fluid-structure interaction modelling, as well as their suitability for the problem assumptions described in the last chapter.

3.1 Fluid-Structure Interaction (FSI): A Concept Summary

In fluid-structure interaction (FSI) problems, the aerodynamic forces and structural deformations are strongly coupled. That is, a given aerodynamic force will deform the body sufficiently to alter the aerodynamic force, and so on. In the words of Waldman & Breuer [190]: "[T]he wing loading depends on the camber, which in turn depends on the wing loading."

Because of its extreme flexibility, the in-flight behavior of an LEI surf-kite is an FSI problem.

3.1.1 Monolithic and Partitioned FSI Solvers

FSI solvers can be broadly divided into two groups: monolithic and partitioned FSI solvers [61].

In a monolithic FSI solver, the entire aeroelastic behavior of the system is modelled within one set of equations, including both the structural deformations driven by and driving the aerodynamic forces. Banerjee & Patil [22], Peskin [145], as well as Argentina & Mahadevan [17] are examples of monolithic FSI solvers for membrane flows.

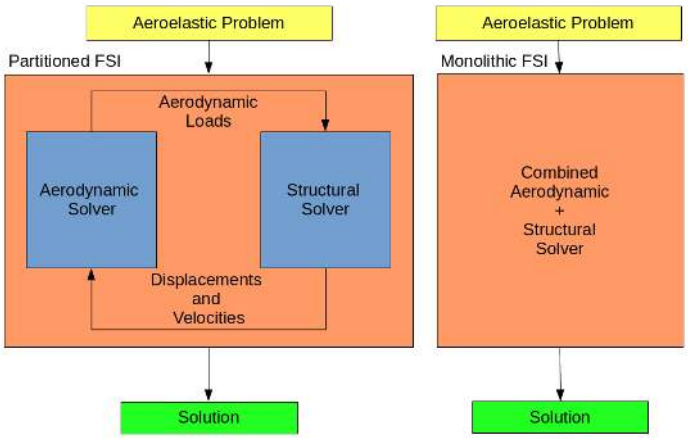

Figure 3.1: Conceptual difference between a partitioned and monolithic FSI solver.

In a partitioned FSI solver, the aeroelastic model is divided into two separate models - for the fluid and structural behaviors respectively - who exchange end information, but whose mechanics do not interfere. Once the boundary conditions are determined appropriately, the aerodynamic model can calculate the pressure distribution for a given body shape, and the structural model can calculate a deformation for a given aerodynamic loading. It is assumed that while the aerodynamic forces are resolved, the deformation is unchanged; and while the deformation is resolved, the flow is unchanged. A partitioned FSI solver requires a coupling mechanism between the fluid solver and the structural solver, to ensure that the boundary conditions are consistently applied. Without such consistency, it is unlikely for the complete solver to be accurate and stable. The FSI code currently in use by the TU Delft airborne wind energy group is a partitioned FSI solver, consisting of an FEM structural solver [28] and a 2D finite-strip aerodynamic load model [30].

Monolithic solvers have the advantage that they can be customized to a particular problem, and are certain to model all interface effects. However, it is logically more difficult to apply any given monolithic solver to an arbitrary physical problem, and it is more difficult to update the FSI solver to reflect field-specific advances.

The advantage of a partitioned FSI solver is the modularity of the fluid and structural solvers. That is, as long as the requirements of the structural solver are met, a developer is able to vary the fluid solver at will, in order to improve accuracy or efficiency, or simply to test new concepts. Particularly during the development of a fairly young concept, such as industrial kites for electricity generation, there exist multiple directions which a solver can take. With the modularity of the partitioned FSI solver, it is possible to determine the tradeoffs between model-accuracy and -speed under a range of conditions, thus directing future development more than would be possible with a monolithic FSI solver.

This thesis will focus on an aerodynamic model for a kite-design-purposed partitioned FSI solver.

3.2 Kite FSI Structural Models

There are many classes of kite structural models, ranging in model complexity and calculation speed. [28]

These aerodynamic models are briefly described in Figure 3.4. For a more detailed description of the assumptions behind various kite structural models, see Ruppert [153] and Bosch [28].

Kite FSI modelling requires the ability to simulate the deformation of the kite in both the chordwise and spanwise directions. Consequently, kite structural models for FSI problems are typically restricted to multibody or finite element models (FEM).

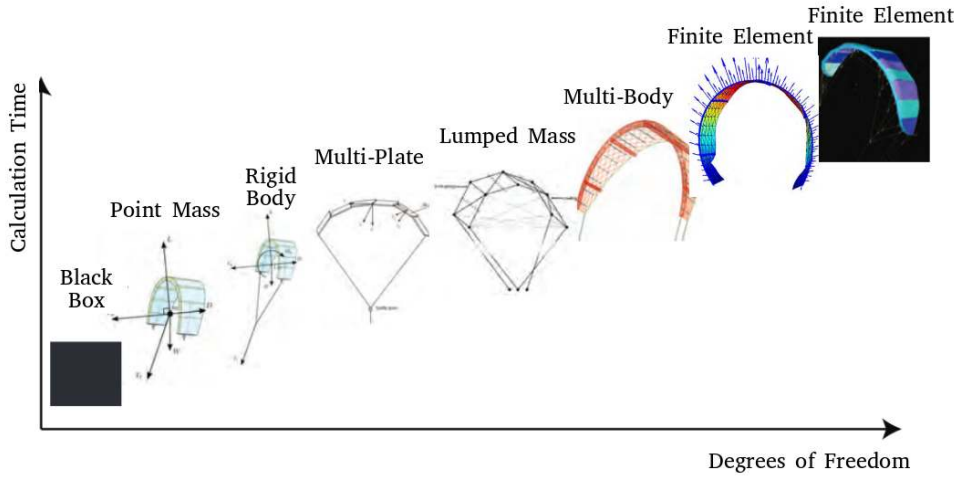

Figure 3.2: Kite structural models by calculation speed and degrees of freedom, as adapted from Bosch [28].

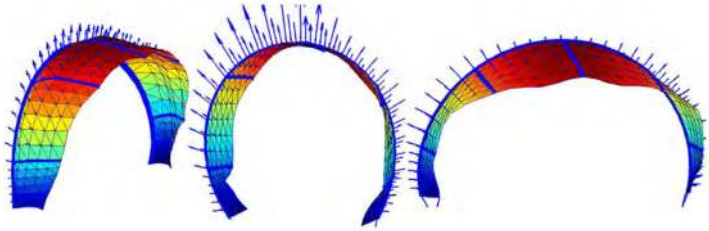

Figure 3.3: The Bosch FEM model depicting kite deformation behaviors [28].

Currently, the full-kite structural model intended for FSI consideration is the Bosch FEM built from triangular elements in the spanwise direction, and five sections in the chordwise direction. The kite tip mesh is built with a finer resolution than the canopy center, to model the large deformations during steering and buckling. The ultimate model contains 107 beam elements, 360 shell elements, 222 nodes, and 1332 degrees of freedom. [28]

A FEM detailed kite canopy-section is currently under construction by Berens, in order to study the aerodynamic damping caused by kite deformation during flight, an effect neglected in the Bosch full-kite FEM. The Berens canopy-section is modelled as a cantilevered flexible plate for quasi-steady, variable flow. [25]

Because the Bosch FEM full-kite and the Berens FEM test-canopy are built to use the Breukels aerodynamic load model (BALM), a discussion of which follows, they require aerodynamic forces distributed across n=6 chordwise nodes as functions of kite surface node displacement and velocity. The force vectors must be defined per node [28].

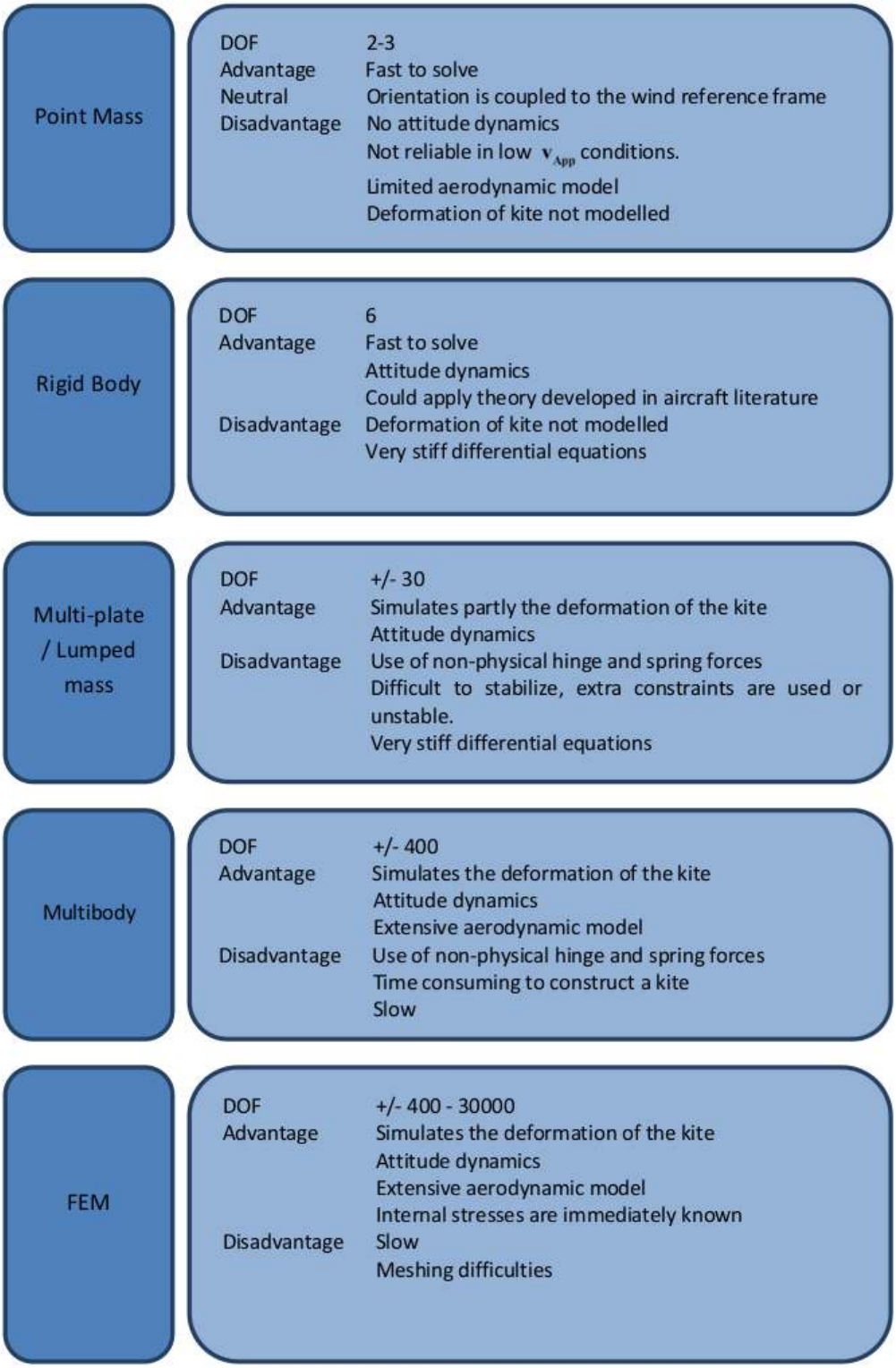

Figure 3.4: A summary of kite structural models, as reproduced from Ruppert [153].

3.3 Kite FSI Aerodynamics Models

An overview of aerodynamic models as applicable to kite FSI problems is given below. For further information about the potential flow methods, please see - in order of increasing mathematical thoroughness - the discussions in Katz & Plotkin [98], Cottet & Koumoutsakos [42], and Wu et al [199].

3.3.1 Black Box Model

Black box models (BBM) use lookup tables that connect or interpolate the state of the system from aerodynamic force coefficients that have been experimentally determined. Though fast and accurate when used with the kite for which they have been designed, it is not possible to use such BBMs for design work, which must necessarily take place before wind tunnel or flight testing.

Fechner et al [64] uses a BBM to determine the lift and drag coefficients on a point-mass kite to predict kite flight paths, however this model is not useful for design-purpose kite FSI modelling [183].

3.3.2 2D Finite-Strip Approximation

In 2D finite-strip approximation, a wing is assumed to be a spanwise assembly of 2D airfoil sections. The flow around each of the 2D sections can be found with different - but typically inviscid - methods, see particularly the sections on thin-airfoil theory and CFD. Because the entire wing is assembled from sections of infinite-wings, 2D strip-theory does not include any finite-wing or 3D flow phenomena like wing-tip effects or the interaction between wakes and lifting surfaces [137].

Two-dimensional strip-theory is most applicable where flow has a "characteristic dominant direction" [137]. Due to the low Aspect Ratio of the kite and the high angles of attack that occur in normal flight, there is enough spanwise secondary-flow that the kite-flow does not have this "characteristic dominant direction" [109]. Further, because membrane wings deform under varying-flow conditions, it is not possible to separate 3D drag effects from 2D profile drag [125]. Mendenhall et al [130] [129], who preformed a strip-theory analysis of two-lobed para-wings with high slack, high aspect ratio and prominent leading edge booms, found it difficult to model flow separation at high angles of attack with 2D strip-theory. It follows that the use of a 2D finite-strip method to model 3D kite aerodynamics will leave "a lot to be desired quantitatively" [125].

Smith [166] discusses the concatenation of inviscid 2D membrane theory by a finite-strip method, as used by Nielsen [141], Sneyd [167], and Ormiston [142].

Because the strip-theory method is very simple and there exist correction methods for some 3D, viscous, and unsteady [137] phenomena, corrected finite-strip approximations have been used to model kite-aerodynamics where load-calculation speed is more important than accuracy.

Breukels Aerodynamic Load Model

The aerodynamic model currently used by the TU Delft Airborne Wind Energy group for kites is the Breukels aerodynamic load model (BALM). The BALM is the only fast kite aerodynamic model that also allows for section deformation. The BALM creates polynomials to approximate the aerodynamic loads on a kite airfoil section along a number of discrete nodes (typically n = 6, after the sufficiency analysis by Mendenhall et al [130]) in the chord-wise direction. The polynomials, and consequently the BALM force distribution are a function of camber, angle of attack, and thickness. The spatial discretization distributes forces - found from 2D CFD analysis for angles of attack between $-20^o < \alpha < 20^o$, smoothed into Spierenburgs flat plate empirical formulas outside of this range - according to weight factors such that the discretized moment profile creates the same moment as the CFD analysis. This CFD analysis used a RANS solver in Fluent for combinations of the independent variables used in the polynomial load approximations: 15%, 20% and 25% thickness, 0%-12% camber, and $0^o - 25^o$ angle of attack [30].

Unfortunately the BALM is set up such that the weight factors are the solutions of an underdetermined problem - with n unknowns and only 1 known relationship from the moment constraint - and are consequently considered somewhat arbitrary [27]. Further, it is unclear exactly what moment coefficient polynomial the BALM uses as this constraint. The BALM suggests a distribution of weighting functions that approximately recreates the force distribution on a generic kite, where the total force was validated against line forces measured on two looping kites: the North Rhino 16m^2, and the Naish Aero 6 [30]. However, the adaptation of the generic kite weight functions to specific kite use - particularly for initial design work - has a great deal of confusion, as judged by the three distinct values of weighting factors mentioned between the Breukels thesis, the Breukels code, and the Bosch adaptation of the BALM [27].

There are a number of functional criticisms of the BALM:

- The lift coefficient is high in comparison with that of rigid aircraft wings [28]. The fact that membrane wings are typically found to be able to attain higher $(L/D)_{max}$ than rigid wings [52], suggests that this criticism of BALM may not be valid.
- Increasing camber does not always increase the drag force [28].
- The moment coefficient curve is modelled as linear, where the Breukels CFD results suggest it behaves nonlinearly [28].
- The influence of the span-wise velocity component is ignored, because the apparent velocity is projected onto the airfoil section [28]. For a highly three-dimensional flow such as is expected over a low aspect ratio kite, this is a significant concern.
- When the magnitude of the weighting function parameter a is very large, the lift forces point in opposite directions, resulting in completely unrealistic force distributions [28].
- When the angle of attack is either very large in the positive or negative directions or very close to zero, the pressure distributions are unrealistic [28].
- When local node deformation velocities are included in the apparent velocity calculation in order to generate aerodynamic damping, the model becomes unstable [28].
- While RANS steady-state analysis is typically used for turbulent flows, it is not well-suited for modelling flow conditions that are at-, near-, or post-stall [118]. Consequently, Breukel's steady-state RANS analysis of kite sections at high angles of attack - such as 20 degrees - cannot be expected to provide accurate results.
- For LEI kites, the leading edge inflated tube diameter determines both the airfoil thickness and camber, such that they are intrinsically linked [14]. The BALM force-approximation polynomial treats thickness and chord as independent variables and may therefore be over-emphasizing the effects of certain variable interactions.

Breukels mentions a 3D correction method for the BALM that relies on the assumptions that the lift curve slope is linear, and that the relation between the lift curve slope and anhedral angle is independent of airfoil shape [30]. These two assumptions are difficult to justify for kite flight, respectively, given the near-stall flight regime and the large kite deformations. Further, this 3D correction method is based on a Tornado vortex lattice method (VLM) analysis of a particular kite, and is not validated for other kite shapes [183]. Bosch states that "Discussions with [Breukels] led to the conclusion that the uncertainty of the three dimensional correction is so significant that it is not clear whether this correction actually improves the model or not" [28].

The BALM is certainly a valid kite aerodynamic model for applications where the requirement for computational speed outweighs that for accuracy. However, it is less-than-ideal for design-purpose kite FSI modelling.

3.3.3 Method of Aerodynamic (Stability) Derivatives

The method of aerodynamic derivatives linearizes the nonlinear functions which determine forces and moments from the equilibrium conditions and perturbations from equilibrium. Due to their speed, aerodynamic derivatives are generally used in the analysis of aircraft dynamics [88]. De Groot uses the method of aerodynamic derivatives according to the parameter identification technique to model the dynamics of a rigid body kite [44].

Because the aerodynamic derivatives calculate global forces and moments - rather than local forces and moments - they are not applicable to the study of highly-flexible kite FSI models. It should be mentioned, however, that stability derivatives may be an analysis end-product - rather than analysis method - as in Müller's [134] ram-air parachute FSI study.

3.3.4 Potential Flow Methods

Potential flow methods reduce 3D flow to a surface problem, assuming the flow is irrotational, and frequently also incompressible [172] or inviscid [97]. Physically, potential flow methods represent thin shear layers in flows where the Reynolds number approaches infinity [8].

The basic principle is the superposition of source-sink doublets - each solutions to the linear Laplace equation for the velocity potential - to create lift by circulating the flow. These source-sink doublets are called "vortex particles" or "point-vortices" individually, "vortices" when placed continuously along closed loops, and "vortex sheets" for continuous surfaces. At every point, the vortex induces velocity according to the Biot-Savart law: proportional to the vortex strength, and inversely proportional to the distance between the vortex and the point. Further, the lift generated by a vortex is proportional to that vortex's strength, as found with the Kutta-Joukowski equation.

The boundary conditions for the resulting underconstrained Laplace equation typically include: the assumption that surfaces are impermeable such that surface flow is purely tangential such that the surface-velocity from the global kite motion and the local membrane velocity must equal the surface-normal velocity induced by the bound vortices on the surface and shed vortices in the wake

$$(\mathbf{U}_A + \mathbf{U}_{membrane}) \cdot \hat{n} = (\mathbf{U}_{ind,surf} + \mathbf{U}_{ind,wake}) \cdot \hat{n};$$

that the flow at the trailing edge must leave smoothly as per the Kutta condition; and that disturbances vanish in the far-field [22].

In order to conserve circulation and enforce the Kutta condition, vorticity is shed from some given location in the domain - typically the leading and trailing edges where flow separation is anticipated, or purely the trailing edge when the flow is expected to remain attached. The vorticity can be shed discretely or continuously. If the vorticity is shed discretely, it is represented as point-vortices separated by some finite distance; if the vorticity is shed continuously, it is represented as vortices in the 2D case or as a vortex-surfaces in the 3D case [131].

Physically speaking: as the shed vorticity is convected downstream, it experiences a Kelvin-Helmholtz instability, which causes the vorticity to roll up in large spirals. The rate at which the instability grows is high for sharply increasing velocities, which is necessarily the case for the velocity-jump over a potential-singularity [8].

There exist a number of different wake-behavior models. The free-wake model is the most complex wake model, as it convects the trailing wake vorticity according to the sum of the freestream velocity and the velocities induced by all of the other vortices, in order to best represent the physical behavior of the wake. In a free-wake model, there are multiple options for describing the wake-vortex velocity: the Birkhoff-Rott equation [8], a smoothed version of the Birkhoff-Rott equation [9], the point-vortex equation, the Brown-Michael equation, or the point-singularity equation [116]. These convected wake vortices are usually tracked for distances up until eight or ten chord-lengths, after which it is assumed that they can no longer influence the velocity-field over the model [22]. The prescribed wake shape assumption forces the wake vortices to hold to either an empirically-found path, or just to convect with the freestream velocity. Third, the flat-wake assumption assumes that the wake is a rigid plane regardless of the shape of the flow obstacle [137]. Naturally, in the quasi-steady potential flow models, the wake is fixed in time, though the vortices may be distributed as though they had been convected along free-wake, prescribed-wake or flat-wake paths. Banerjee & Patil suggest that the wake-behavior of potential flow problems involving large deformations are best modelled with free-wake models [22].

Potential flow models have the well-analyzed problem that the induced velocities near vortex locations can be unrealistically high - causing artificially high circulations - particularly when two vortices become close (as in the wake) or the wake runs into a lifting surface [137]. There exist techniques to avoid these errors, by appropriately recursive sub-panelling or splitting a problematic vortex loop into multiple smaller loops, or by merging (or pseudo-merging [154]) neighboring vortices [66]

Further, most potential flow computations are open to parallelization, as the calculations of the individual induced velocities are independent operations [137].

The general consensus is that pure potential flow methods cannot solve membrane airfoil aerodynamics for large angles of attack, because of their inability to model viscous effects and flow separation [30] [151]. However, it is suggested that when viscous and separation corrections are added to potential flow methods, it is possible to model membrane airfoil aerodynamics [15]. Van Kappel [183] successfully found accurate results for kite aerodynamics with such a corrected potential flow method.

Vortex Particle Methods

In vortex particle methods, the vortex particles are placed in space, so as to represent the direction of the flow. As the vortex particles represent, in an intuitive manner, the air particles, they are subject themselves to the boundary conditions on the flow [197].

Thin-Airfoil Theory Thin-airfoil theory (TAT) models a 2D airfoil by placing vortex particles along the camber-line of the airfoil. TAT makes the assumptions that the flow streamlines include the camber-line; that the maximum camber and thickness are small (less than 30 percent [137]); and that the angle of attack is small (α less than one degree) [55]. TAT is a purely 2D theory, and must be combined with some method of three-dimensionalization - such as the 2D finite-strip theory - in order to represent a finite wing.

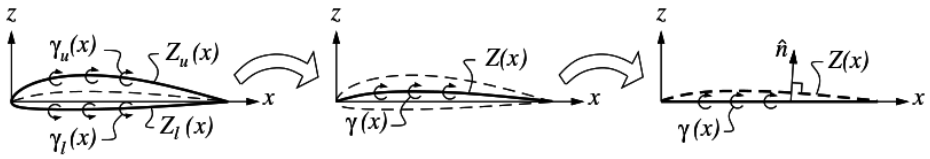

Figure 3.5: Reduction of a thin airfoil to vortex particles along the camber-line, as reproduced from Drela [55].

The classic integro-differential Thwaites [176] Sail Equation for the shape of a 2D inextensible, impervious membrane is based on a linearized TAT model, assuming negligible viscous shearing force and a constant membrane tension:

$$1 - \frac{H}{2} \int_0^1 \frac{d^2(y/\alpha)/d\zeta^2}{2\pi(\zeta - x)} d\zeta = \frac{d(y/\alpha)}{dx}$$

Thwaites [176] also gives an expression of the Thwaites Sail Equation in terms of the sail geometry:

$$\Psi(\theta) + \lambda \left(-\frac{1}{2\pi} \int_0^\theta \sin^2\theta \int_0^\pi \frac{\Psi(\phi) d\phi}{\cos\theta - \cos\phi} d\theta + \frac{1}{4\pi} \int_0^\pi \sin\theta \int_0^\theta \sin^2\theta \int_0^\pi \frac{\Psi(\phi) d\phi}{\cos\theta - \cos\phi} d\theta d\phi \right)$$

$$+\lambda \left(\frac{3}{8}\pi - \frac{1}{2}\theta - \frac{1}{2}\sin\theta \right) \left(\frac{1}{\pi} \int_0^\pi \Psi(\theta) d\theta \right) = \lambda \left(\frac{3}{8}\pi - \frac{1}{2}\theta - \frac{1}{2}\sin\theta \right)$$

where θ and ϕ are transformed versions of chord-wise x and camber-wise ζ distances

$$x = \frac{1}{2} c (1 - \cos\theta)$$

$$\zeta = \frac{1}{2} c (1 - \cos\phi)$$

and Ψ is a transformed version of the membrane slope ($\psi = d\zeta/dx$)

$$\psi(x) = \alpha \Psi(x)$$

and λ is the inverse of the normalized tension coefficient

$$2\frac{\rho_{air} U_\infty^2 c}{T} = \lambda = \frac{1}{H}$$

Chambers [36] reformulated the Thwaites Sail Equation, such that the Kutta condition can be applied to the leading-edge as well as the trailing-edge of the membrane. Nielsen [141] and Jackson [94] derived similar results from the application of TAT to, respectively, a 2D Fourier-Series-shaped membrane, and a 2D cubic-shaped elastic membrane. Further, Gerhardt et al [77] have used unsteady TAT to model the flow interaction between two rigid, high aspect ratio sails

Argentina & Mahadevan [17] present a small-deflection, small-incidence, quasi-steady variation on the classic TAT for the purpose of modelling flag flutter, which equates the frequency of oscillation of a freely-hinged rigid plate that is approximately parallel to the freestream with the frequency of the lowest-mode of free-bending vibrations of a flexible plate to find the critical velocity at which a flag will begin to flutter. From the flapping instability frequency, they determine the strength of a quasi-steady vortex whose bound filament is located at some unknown location along the chord, and whose shed filament is at some unknown location in the wake on the axis of the LE.

Greenhalgh et al [82] found from experiments on a mylar membrane that Thwaites Sail Equation, the Chambers reformulation, and the Nielsen and Jackson methods are, logically, only valid (see Figure 3.6) where the flow is fully attached and outside of the low-lift hysteresis region. That is, these results are only valid when, approximately, $5^o \leq \alpha \leq 8^o$.

Because of this inability to model separated flow, TAT is not particularly useful for 3D kite aerodynamic modelling.

Point Vortex Method The point vortex method (PVM) is the conceptually-simplest, typically unsteady, 3D vortex particle method - to the extent that it is alternately called the vortex particle method(VPM). The point vortices are placed wherever the model wishes to describe vorticity, with whatever level of uniformity is required to resolve the flow sufficiently. Frequently, these "point vortices" are modelled as bodies with some finite volume - called "vortex blobs" - which contain some amount of fluid [23]. The flexibility of this method means that it is well suited for the modelling of problems with "unsteady flow around morphing bodies."

Naturally, due to the independence of the individual point vortices, the system of equations required to solve for the flow is very large. Even when the system has been reduced, possibly with the precorrected-FFT algorithm (p-FFT) or the Fast Multipole Method (FMM), the solution requires $\mathcal{O}(N \log(N))$ operations [197].

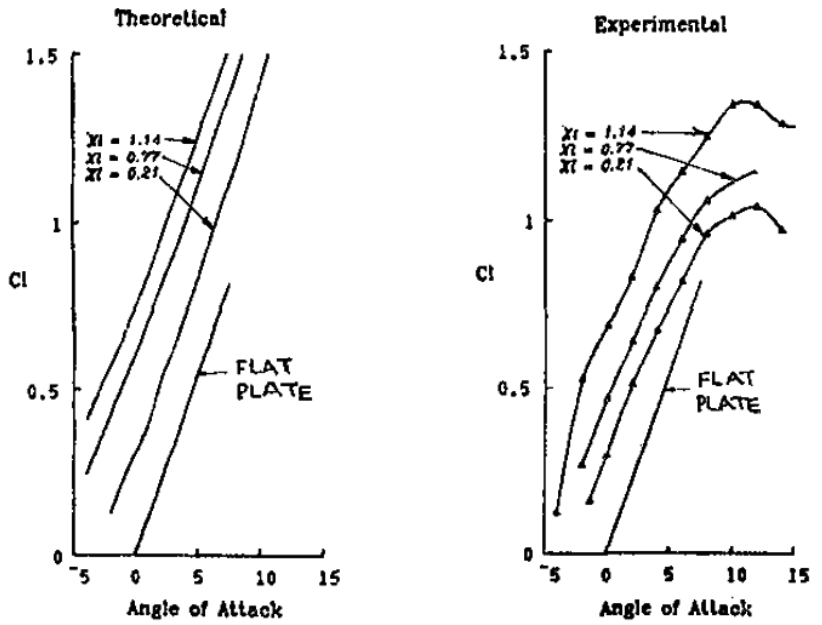

Figure 3.6: Differences between TAT and wind-tunnel results for a 2D membrane wing with varying excess lengths: $\epsilon = XL = 1.14\%,\ 0.77\%,\ 0.21\%$, and 0 (flat plate), as found by Greenhalgh et al [82].

Michelin & Llewellyn Smith [132] used a point vortex method to study the effect of flexibility on 2D membrane wing-sections in an insect-flight-inspired heaving motion. Michelin et al [133] use a 2D point vortex method to model the flutter of a flag at small angles of attack. Further, Charvet et al [37] modelled the flow over a racing-yacht sail, including its interactions with other sails, yachts, and the sea-surface, with a point vortex model.

Due to the fact that Van Kappel [183] showed that computationally-simpler methods are able to capture the aerodynamics of the kite FSI problem, the computational cost of PVM is not considered necessary for the kite FSI model.

Viscous Vortex Particle Method Part of the attraction of particle-type vortex methods are the many method extensions to model viscosity. For details into the mechanics of these methods, the reader is referred to Barba et al [23].

A viscous extension of the PVM - a viscous vortex particle method (VVPM) - was developed by Eldredge [60] and demonstrated on the oscillation of a 2D fish tail. Eldredge's particular VVPM variation uses blobs of vorticity that are periodically remeshed in order to exchange particle strength.

As VVPM is more accurate than the inviscid PVM, but still computationally slower. It is not a good choice for iterative-design kite-flow FSI problems.

Vortex Filament Methods

In vortex filament methods, vortex particles are arranged into a long string-like construct, called a vortex. The vortices used in potential flow models must follow rules determined by Helmholtz and Kelvin. [98]

- Helmholtz's First Theorem: circulation is constant along a given vortex.
- Helmholtz's Second Theorem: a vortex must form a closed loop, end at a solid boundary or continue on infinitely; it cannot end in a fluid.

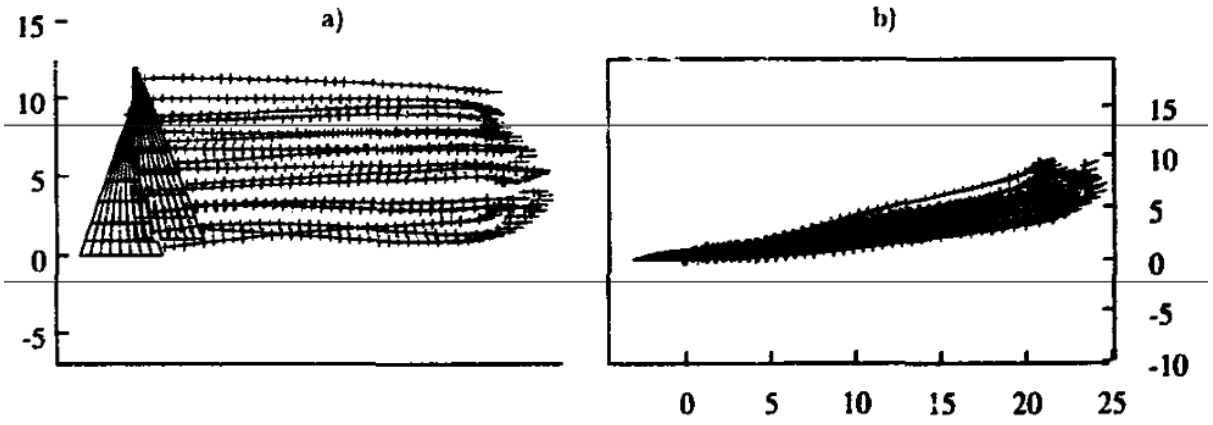

Figure 3.7: Vortex particles distributed through the wake of sails, as seen from the side and top, as modeled by Charvet et al [37].

- Helmholtz's Third Theorem: vortex strength is conserved in inviscid flow, such that an irrotational fluid cannot become rotational without rotational forces.
- Kelvin's Circulation Theorem: the circulation is constant over a closed curve containing an inviscid, incompressible flow, acted upon by conservative forces.

Lifting-Line Theory The simplest of the 3D potential flow models, Prandtl's classic lifting-line theory (LLT) assumes that a wing in quasi-steady flow can be modelled with closed vortex loops, each with a bound segment running spanwise through the wings quarter-chord line and trailing segments convecting parallel to the freestream flow - called collectively horseshoe lattices - connected where the loop closes (for quasi-steady flows, infinitely-far) downstream [56].

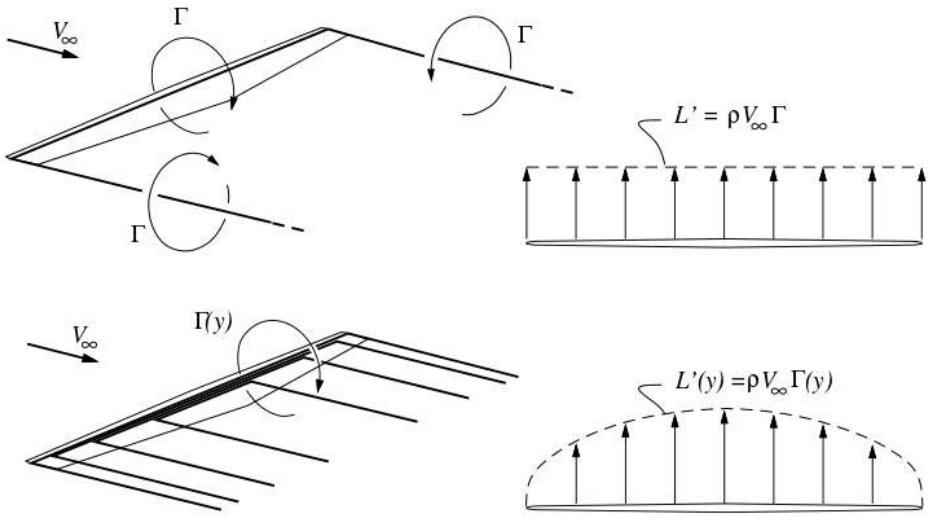

Figure 3.8: Vortex Arrangement for the Prandtl Lifting-Line Theory, reproduced from Drela [56].

Sugimoto [173] uses a combined LLT with thin-airfoil theory (TAT) sectional-flow to describe the flow over inextensible, flexible and slack high-aspect ratio sails, with fully-attached flows and small angles-of-attack and deformations.

There also exist unsteady versions of LLT, such as that described by Ahmadi and Widnall [6] for low-frequency vertical oscillations of spanwise-flexible wings.

Leloup [105] distributed the span-wise section loads calculated for an LEI kite using LLT, chord-wise according to the 2D XFOIL section pressure-distribution. While this 3D LLT is fast, and has been validated against the Navier-Stokes solutions of Maneia [120] for curved paraglider wings for fully-attached flow - in the linear c_l-α region - the Leloup 3D LLT is less able to reproduce flow with separation. Also, because the pressure distribution is determined according to 2D XFOIL analysis, it is not certain that the influence of secondary-flow is well represented. Judging from the comparison between 3D LLT calculated- and validation- lift coefficients, the 3D LLT method is restricted in validity to angles of attack between -10^o and $+10^o$.

Modified LLT provides a promising method for fast aerodynamic modelling, however, the difficulty of including separation effects in LLT prevent its general use in power-production kite FSI problems.

Vortex Panel Methods: Thickness-Free Panel Methods

Vortex panel methods tesselate a surface with closed vortex rings, to either model a thickness-free surface, or wrap the entire contour of a body with this tesselate surface to account for thickness and camber.

Vortex Lattice Model The vortex lattice model (VLM) constructs lattice surfaces from - typically quadrilateral - vortex ring[1] elements, which have collocation points at their centers. The wake is typically also represented by vortex rings. All of the vortices induce velocity on the collocation points, and the collocation point velocities, in turn, determine with what apparent velocity the vortex rings will create lift. It is at the collocation points that the impermeable-surface boundary condition is enforced. The vortex lattice method is suitable for flows that only contain vorticity in the boundary layer and wake [20].

The system of equations for VLM typically take the form:

$$\mathbf{A\Gamma} = \mathbf{U}_{membrane}$$

where Γ_i is the strength of the vortex i, $U_{membrane,j}$ is the surface velocity at collocation point j and $\mathbf{A}$ determines the influence of each vortex on the collocation points by the Biot-Savart law [22].

The VLM cannot itself model thickness, and is best suited to thin bodies with small angles-of-attack and sideslip [54], however there exist methods of joining vortex lattices in order to model finite body thickness.

Smith [166] compares a VLM of flow over a 3D membrane wing with a CFD model in order to study the effect of viscosity on membrane wing models at $10^3 < R_e < 10^4$ with fully attached flow. His vortex lattice is sketched in Figure 3.9.

There exist versions and corrections of the standard quasi-steady, linear VLM that are corrected for unsteady, nonlinear high incidence conditions. Van Kappel [183], in particular, demonstrated that kite-deformation aerodynamics can be accurately modelled with Gaunaa et al's [76] viscous angle of attack correction method to a quasi-steady VLM. Further, de Matteis & de Socio [47] were able to model laminar flow separation as well as the effect of elasticity and porosity of a 2D sail for angles of attack up to 18 degrees with a 2D-Double Wake VLM concept.

Due to its relative simplicity, a quasi-steady VLM with appropriate viscous corrections could make for a good model for kite FSI aerodynamics.

Viscous Angle-of-Attack Correction Method to the Vortex Lattice Method Van Kappel [183] built a nonlinear viscous VLM ($\text{VLM}_{\text{N-VK}}$) for kite analysis using a viscous angle-of-attack correction method (VACM) with a standard XFLR5 VLM. The VACM, an iterative angle-of-attack correction procedure, corrects for viscosity and thickness in the VLM.

[1] also called "closed vortex frames" by Ginevsky & Zhelannikov [78] "closed [vortex] loops" by Wu et al [199].

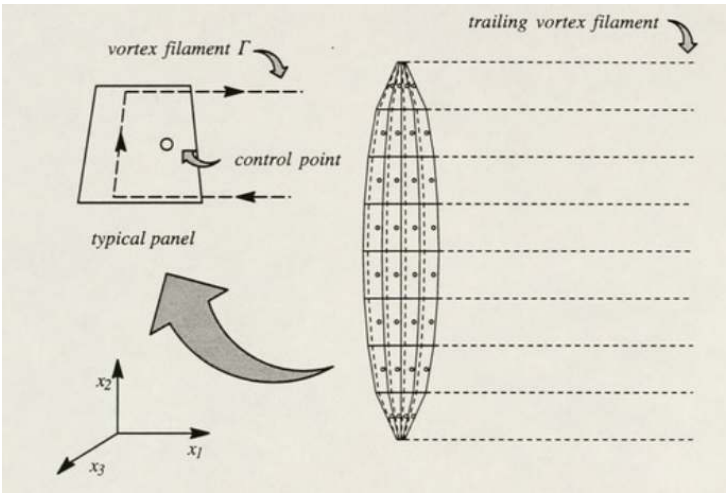

Figure 3.9: Vortex Arrangement, as used by Smith [166] for a thin, elliptical wing with a fixed-wake VLM.

For a profile, with known inviscid and viscous lift-vs-alpha curves, a given angle of attack corresponds to different inviscid and viscous lift coefficents. Consequently, an inviscid lift coefficient can be adjusted to the corresponding viscous lift coefficient for a given angle of attack. However, if the lift - and circulation - changes, then the downwash experienced by the profile, and consequently the angle of attack of the profile will change. That is, the change in angle of attack induced by the change in circulation strength compensates partially for the change in lift resulting from the shift between the inviscid and viscous solutions. The angle of attack can be iteratively found, stepping between the inviscid-viscous correction and the induction-change correction, until the required angle-of-attack changes become small and the solution converges. This method - VACM - is further described by its initial developers Horsten & Veldhuis [87], and section 2.3 of Carqueija [34].

The VACM approach is based on the assumption that the behavior of a 3D-finite membrane airfoil is similar to that of its infinite, rigid representation with an effective angle of attack correction. According to Van Kappel [183]: There is no real background, neither theoretical nor experimental, to support this approach. However, the results of Horsten (initial proposer of this method) and Gaunaa show significant improvement on the results when compared to experimental and CFD data.

The VACM iteration used by Van Kappel follows the adaptation by Gaunaa et al [76] of Horsten & Veldhuis's method:

1. Perform an inviscid VLM calculation to find the $C_{l,ori}$ for each spanwise section i.
2. Initialize the alpha correction $\Delta\alpha_i$ for each spanwise section.
3. Find the new effective angle of attack for each spanwise section: $\alpha_{eff,i} = C_{l,ori}/C_{l,\alpha} + \alpha_0 - \Delta\alpha_i$.
4. Find $C_{l,\alpha}$ and $C_l(\alpha)$ from XFOIL for given profile shape, and the local Reynolds number $Re_{local} = \frac{V_\infty c_{local}}{\nu}$.
5. Calculate the angle shift $\alpha_s = \frac{\Delta C_l}{C_{l,\alpha,inv}}$
6. Update the flow-tangency condition velocity of the VLM for the new angle of attack α_s, $\mathbf{A\Gamma} = \mathbf{U}_{membrane} = \mathbf{U} \cdot \hat{n}(\alpha)$.
7. Perform a new inviscid VLM calculation, to find a new $C_{l,new}$ for each section.
8. Calculate for each spanwise section the new alpha correction: $\Delta\alpha_i = \frac{1}{C_{l,\alpha}}(C_{l,ori} - C_{l,new}) - \alpha_s$
9. Rerun steps 3-7 until convergence or the iteration limit is achieved
10. Use the found α_{eff} to calculate the profile drag from an XFOIL viscous $C_d(\alpha)$ curve.

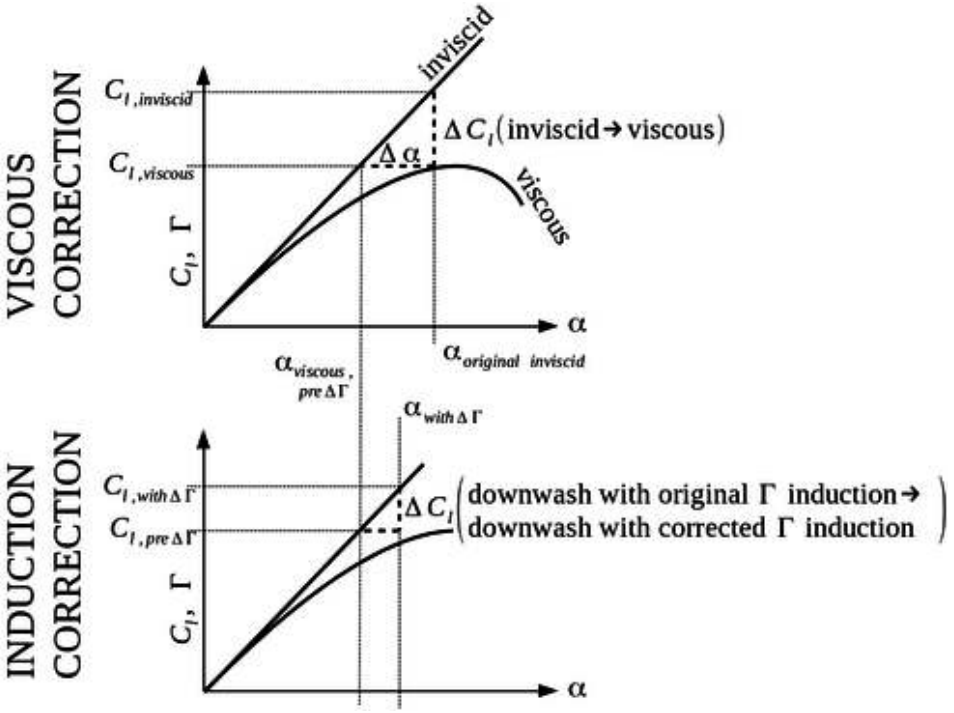

Figure 3.10: The two-step viscous α correction method, applied iteratively until convergence.

Further the influence of kite dihedral is represented in $\text{VLM}_{\text{N-VK}}$ [183] by using the above-iterated angle shift α_s and section dihedral angle Γ_d to adjust the apparent velocity at the spanwise sections.

$$\begin{aligned} u_x &= \cos(\alpha_s \sin(\Gamma_d)) \cos(\alpha + \alpha_s \cos(\Gamma_d)) \\ u_y &= \cos(\alpha + \alpha_s \cos(\Gamma_d)) \sin(\alpha_s \sin(\Gamma_d)) \\ u_z &= \cos(\alpha_s \sin(\Gamma_d)) \sin(\alpha + \alpha_s \cos(\Gamma_d)) \end{aligned}$$

Van Kappel's nonlinear VLM specifies the following XFLR5 program settings: Dirichlet boundary conditions such that the total potential inside the body is equal to the freestream velocity potential, and a free-wake Tilted Geometry to avoid the small angle of attack assumption made by a fixed-wake.

One criticism of $\text{VLM}_{\text{N-VK}}$ is a possible flaw in the calculation of the induced angle of attack. The induced angles are, rather arbitrarily, divided by 2 in order to fix a discrepancy between the values found with $\text{VLM}_{\text{N-VK}}$ and the values expected from 3D panel method and LLT. Though the $\text{VLM}_{\text{N-VK}}$ code gives accurate end-results, in comparison to Gaunaas validation arc-kite CFD data, this arbitrary factor of suggests that there may be a process-flaw in the calculation of the induced angle of attack.

A further criticism of $\text{VLM}_{\text{N-VK}}$ is the use of a rigid-profile polar, such that $C_{l,\alpha}$ is constant - for example $C_{l,\alpha} = 2\pi/\text{rad}$, while it has been known since Maughmer's sailwing wind-turbine studies [125] that flexible membrane wings have nonlinear, non-constant $C_{l,\alpha}(\alpha)$. That is, a flexible membrane wing will have large $C_{l,\alpha}$ for small angles of attack, and small $C_{l,\alpha}$ when less deformation is possible at large angles of attack. However, the inaccuracy caused by this rigidity assumption appear to be small - in relation to wind tunnel validation data - when the angle of attack is relatively small, such that the predictions of the $\text{VLM}_{\text{N-VK}}$ are still very accurate. The author has not seen validation data comparisons for conditions near the maximum angle of attack seen in normal operating conditions.

Graf et al [80] compared the aerodynamic force coefficient polars found in a windtunnel for rigid sails, a 3D RANS simulation, and a LLT model with a VACM and found that that the LLT-with-VACM model was able to predict the loads about as well as the 3D RANS solver.

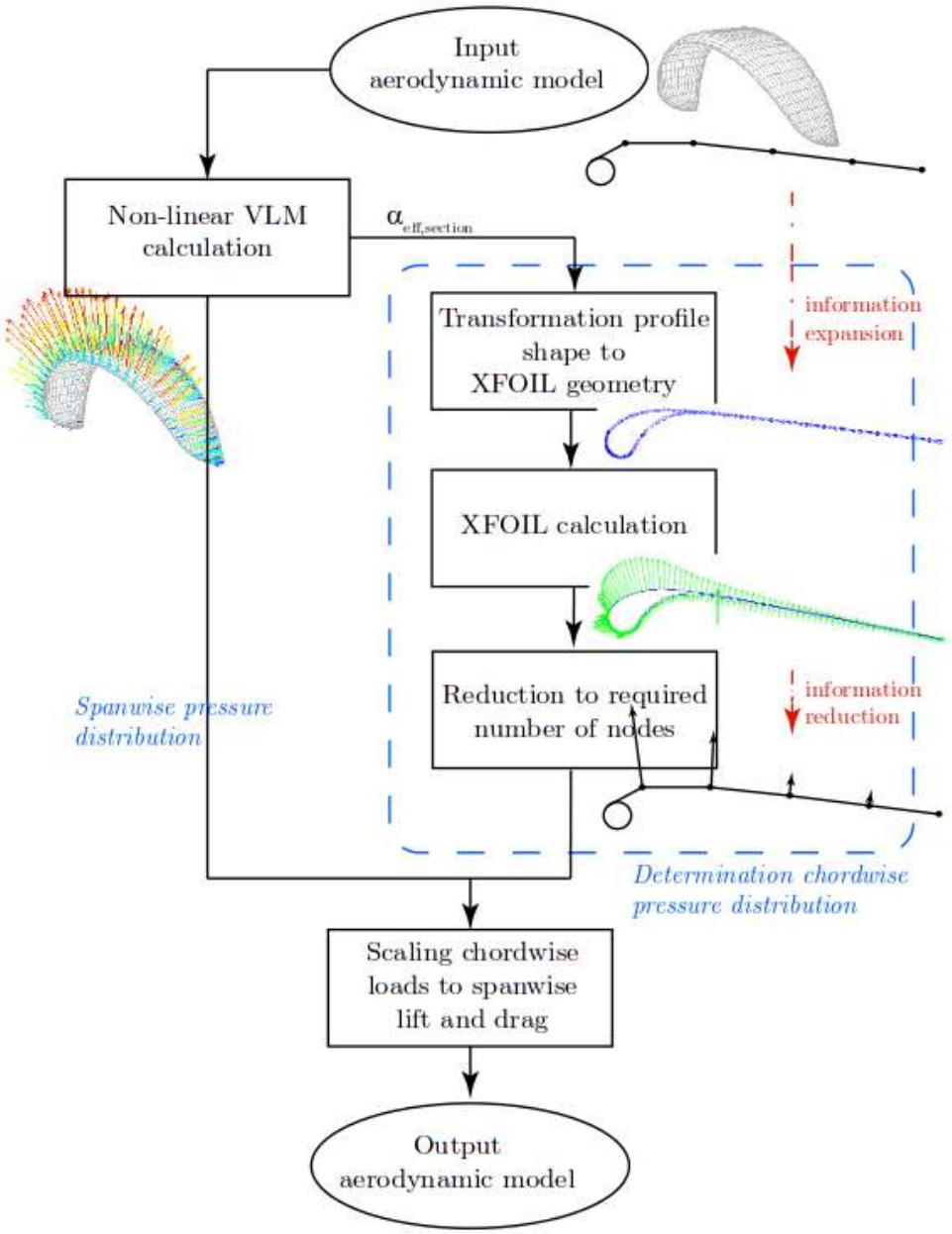

Figure 3.11: A diagram of the VACM procedure implemented in the $\text{VLM}_{\text{N-VK}}$, reproduced from [183]

Overall, van Kappel's implementation of the VACM was able to capture well the relationship between total lift, drag, and angle of attack of an arc-shaped kite, as validated with Gaunaa's CFD measurents - though the CFD model assumes that the Reynolds number is constant over the span, and consequently has higher local Reynolds numbers than the $VLM_{N\text{-}VK}$.

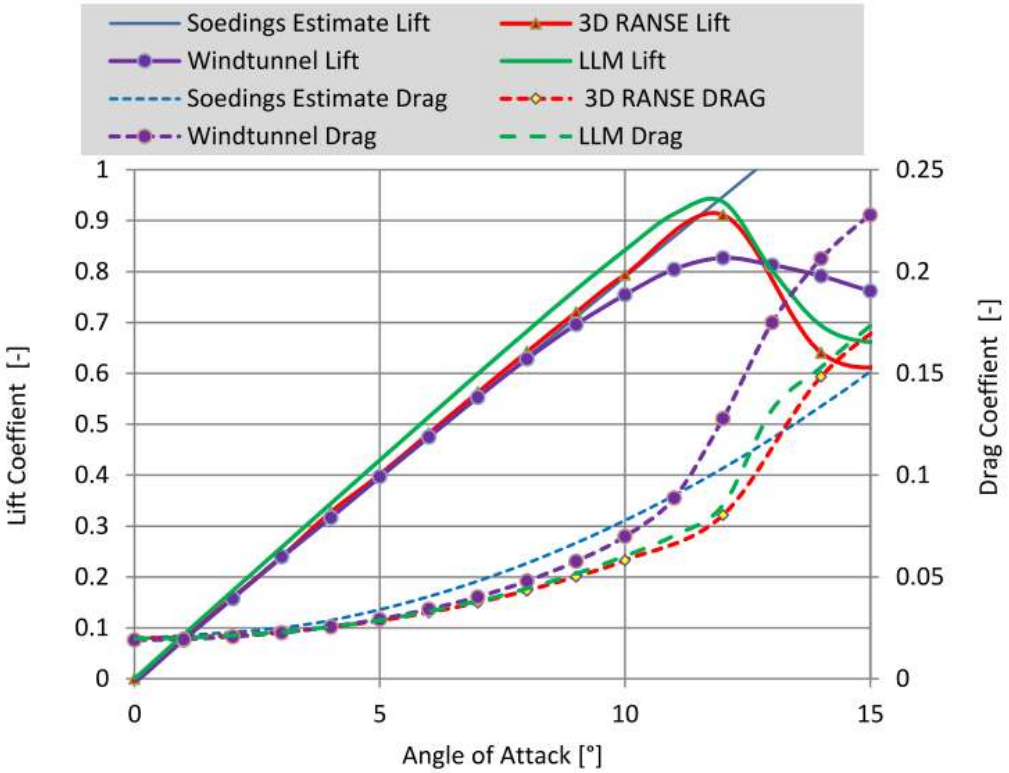

Figure 3.12: General accuracy of a VACM on a rigid sail of Aspect Ratio 4.5, as compared to a Soedings Estimate, a 3D RANS solution, and a wind tunnel measurement, as reproduced from Graf et al [80].

Within the overall accuracy of the $VLM_{N\text{-}VK}$, the model over-predicts the lift and under-predicts the drag at high angles of attack - e.g. by about 25% for $\alpha = 16^o$. Van Kappel [183] suggests that this discrepancy is caused by the tendency for XFOIL to delay stall. Further, the $VLM_{N\text{-}VK}$ tends to overemphasize tip losses, which results in a redistribution of lift from the tips to the span-wise center of the arc shaped kite.

The main criticism of the $VLM_{N\text{-}VK}$ is its slow speed. As described, when the $VLM_{N\text{-}VK}$ is used as the aerodynamic model in Bosch's FSI solver, it has a real-time factor of 1100x, which results in a cost of 18.9 hours for 60 seconds of simulation time. This is too slow to be useful for iterative design work, where an engineer may want to test the effects of potential design changes. In comparison, when the BALM is used in the same FSI solver, it has a real time factor of 25x, and consequently a cost of 24 minutes for 60 seconds of simulation time.

Van Kappel calculates that approximately 96% of the computation time required by the $VLM_{N\text{-}VK}$ is used to repeatedly determine the inviscid and viscous lift vs. alpha curves within XFOIL, often at high angles of attack. Without this viscous correction method, Van Kappel gives a real-time factor - within the Bosch FSI simulation - of 65x or 1.1 hours for 60 seconds simulation time. Unfortunately, he does not give the expected loss in accuracy by neglecting this "On-The-Fly XFOIL" method.

Van Kappel suggests some further possible methods to decrease computation time:

- As XFOIL polars are found, save them to a database, to avoid running the simulation for the same inflow and deformed profiles multiple times. Van Kappel suggests that the $\text{VLM}_{\text{N-VK}}$ computation time (for a model with 640 panels and 32 spanwise sections) would asymptotically approach 200 ms, from the baseline 5000 ms.
- Assume a-priori a given pressure distribution, such as that used by the BALM. Van Kappel gives no estimate for the approximate decrease in accuracy with this simplification.
- Improve the given $\text{VLM}_{\text{N-VK}}$ algorithm efficiency, though Van Kappel gives no estimates for the potential resulting increase in computation speed.
- Only apply XFOIL where the section inflow and profiles vary significantly along the span, and interpolate the 2D polars for intermediate sections. No estimates for increased speed and decreased accuracy are given.
- Replace the viscous airfoil analysis program with a program faster than XFOIL. Again, no estimates for increased speed and change in accuracy are given.

Schmehl [155] adds a possible method to decrease the computation time. Because it relies on open-source programs, the $\text{VLM}_{\text{N-VK}}$ includes the XFLR5 gui functionality instead of purely the VLM core-solver functionality, Schmehl suggests that an in-house purpose-built-for-FSI-iteration $\text{VLM}_{\text{N-VK}}$ solver without XFLR5's gui functionality and multi-purposing may increase the computation speed.

Ranneberg [147] incorporated a similar induction-correction for a kite VLM directly within the formulation of the Kutta-Jouwkowski lift-circulation association:

$$\begin{aligned} \mathtt{d}_{3/4}^{2D} &= \frac{1}{2\pi \cos \gamma_s}\Gamma \\ c_l^{2D}\left(\alpha - \arctan\left(\mathtt{d}_{3/4}^{3D}\Gamma + \mathtt{d}_{3/4}^{2D}\Gamma\right)\right) &= U_A \times \Gamma \end{aligned}$$

where $\mathtt{d}_{3/4}^{3D}$ is the 3D downwash experienced at the quarter-chord location, $\mathtt{d}_{3/4}^{2D}$ is the 2D downwash experienced at the quarter-chord location, and γ_s is the wing sweep angle. The use of the arctangent adds the nonlinearity caused by the difference between the apparent velocity and induced velocity when downwash is large in comparison with the free-stream velocity. Ranneberg's method also relies on applying 2D airfoil calculations to 3D kite wings, and therefore has some of the same uncertainties for the self-cambering over membrane wing kites.

Unsteady Vortex Lattice Method Unsteady vortex lattice method (UVLM) is an unsteady expansion to the classic VLM, where the wake vortex rings travel in both space and time. UVLM can model both 3D effects and wake interference. Unless a correction method is used, UVLM is not appropriate for modelling stall, viscous drag, or - less relevant to the kite aerodynamics - low Reynolds numbers or the rarefied gases [137] present at altitudes above 80km [135]. UVLM is typically a good choice for problems where the wake wavelength is on the order of the chord [137].

Shukla & Eldredge [160] extended Jones' UVLM model [96] to a deformable 2D membrane section. Though Jones' method is described as a 2D vortex-sheet method [9] where the vorticity is distributed continuosly over a panel rather than concentrated at the rim of the panel, the continuous distribution in Jones' two dimensional cross-section appears to have been replaced with discrete closed rings in the Shukla & Eldredge extension.

A UVLM with viscous-corrections could accurately model kite aerodynamics. However, given that model speed is a design driver and that the flow is quasi-steady, the choice must be to prefer VLM over UVLM.

Doublet Lattice Method The doublet lattice method (DLM) is an analogue to UVLM, in that it models the distribution of a solution to a Laplace equation along a thickness-free surface. However, the singularity in the DLM is not a potential singularity, as is generated by the typical potential-flow vortex particles, but a pressure singularity. Because the relationship between acceleration and a pressure singularity is the same as the relationship between velocity and a velocity-potential singularity, also known as a vortex particle, DLM is sometimes designated an "acceleration potential" method [38]. That is, there is a pressure - and consequently acceleration - jump across the pressure singularity, which ultimately corresponds to the velocity jump across a vortex particle [26].

The DLM system of equations typically takes the form:

$$\mathbf{Dp} = \mathbf{x}'_{membrane}$$

where $\mathbf{D}$ is an aerodynamic influence coefficient matrix, $\mathbf{p}$ contains the pressures, and $\mathbf{x}'_{membrane}$ contains the surface slope at the control points [86].

Holla et al [86] use DLM to model the fully-attached flow over a rectangular membrane wing with uniform biaxial tension, whose frame is small such that its influence on the flow can be neglected, at angles of attack less than 10 degrees.

DLM is not well suited to problems with large deformations. First, the shape of the wake is prescribed, which is not typically appropriate for complex or large deformations. Similarly, the DLM boundary conditions are linearized, and difficult to enforce on deformed geometry [137]. Consequently, DLM is not an appropriate tool to model kite FSI.

Vortex Panel Methods: Finite-Thickness Panel Methods

2D Panel Method On a 2D airfoil, the countour is wrapped in finite-length vortex filaments between a given number of nodes. The standard airfoil analysis code XFOIL, which contains a viscous-correction option, is a 2D panel model [54].

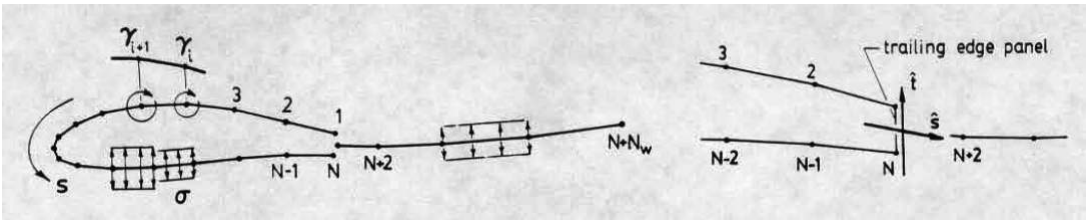

Figure 3.13: An example of panels wrapped around a 2D airfoil, as reproduced from Drela [54].

Waldman et al [191] model the inviscid flow at $R_e < 10^5$ about a bat membrane-wing, which bears a remarkable resemblance to an LEI kite membrane-wing, using XFOIL 2D section aerodynamics and an unspecified 3D composition method.

3D Panel Method On a 3D wing, the 3D Panel Method means that the upper, lower and edge surfaces are modelled. The space interior to the vortex surface has one potential function, and the exterior another, where the influence of the interior potential on the exterior domain must be zero. One difficulty of the standard panel method formulation is that an accurate solution requires the panel size to be comparable to the body thickness; for a very thin membrane, this makes the model very computationally heavy [197]. Viscous corrections for the 3D panel method are still limited. There exists a potential correction method using inviscid-viscous interaction which extend boundary layer methods, but this method has only yet been fully explored for two-dimensional problems [41].

For three-dimensional flow, the 3D panel method is limited to small regions of separation [59] With large regions of separation, as occur behind the leading-edge tube and canopy of the kite at high angles of attack, 3D panel method algorithms become numerically unstable. Van Kappel [183] verified that this instability occurs when kite aerodynamics were modeled with 3D panel method.

In comparison, Den Boer [53] successfully modelled 2D double-membrane wings, which have neither a large separation region behind the LEI tube nor a very thin body limitting the resolution required for convergece.

The 3D panel method is not an applicable method to model the aerodynamics of kites.

Boundary Element Method Boundary element method (BEM) is a method of extending the surface mesh into the surrounding space. The internal and external boundaries are discretized, and used as boundary conditions to assumed fundamental solutions to the differential equation. Because BEM only requires surface discretization, rather than volume discretization, it can be significantly less computationally expensive than other volume methods. Particularly, re-meshing during deformation is much faster [186].

However, because of the requirement for a fundamental solution, BEM generally cannot solve nonlinear problems [186]. Given the kite's near-stall flight regime, BEM is not a safe choice of aerodynamic model.

Multiple-Wake Panel Methods

In a single-wake vortex method, vorticity is shed exclusively from the trailing edge. With a multiple-wake vortex method (MWVM), vorticity is shed both from the trailing edge, and from the locations of flow separation. The typical construction of an MWVM is a double-wake vortex method, with flow separating from one separation-line on a single surface of the airfoil. It appears conceptually possible to shed vorticity from one separation-line along the suction surface and one separation-line along the pressure surface - representing an LEI airfoil at high incidence with additional separation behind the LEI tube - though the author has not at present seen such an example in the literature.

It is uncertain that fully stalled flow can be modelled with multiple-wake vortex models [128], however partially separated flow - even over flexible membranes at extreme angles of attack [133] - is generally accepted to be well represented with multiple-wake vortex models. This restriction is not particularly limiting even though separation is absolutely relevant to the kite FSI-problem, because full stall is not expected to occur during normal power-kite operating conditions.

There are a number of 2D multiple-wake vortex methods modelling separated flow, particularly over membranes.

- De Matteis & de Socio [47] were able to model laminar flow separation, from experimentally determined separation locations, as well as the effect of elasticity and porosity of a 2D sail for angles of attack up to 18 degrees with a 2D-Double Wake VLM concept.
- Wilkinson [196] uses a 2D triple-wake doublet-panel-method to model leading-edge flow separation bubbles on the suction- and pressure- surfaces, as well as the trailing edge suction-surface of a mast-and-sail combination, where separation is assumed to occur where the free-stream is tangent to the mast, and the pressure within the separation bubbles is constant. Wilkinson enforced bubble reattachment locations from experimentally-found values, as he found that assuming a constant pressure within the separation bubble did not allow the flow to reattach on its own. This difficulty in modelling reattaching flow is of some concern, as the separated flow behind the kite's LEI tube does typically reattach itself to the pressure surface of the canopy. See Figure 3.14a for the separation regions in Wilkinson's 2D mast-and-sail model.
- Cyr & Newman [43] use a double-wake model with a single vortex loop, with an unknown strength and chordwise location, to reverse the flow and model trailing edge separation on a 2D slack membrane wing. Notably, Cyr & Newman use a "modified pressure" correction in the "dead-water" separated-flow region, based on the pressure at the separation point of the surface where the flow is still attached. This "modified pressure" introduction is shown in Figure 3.14b.

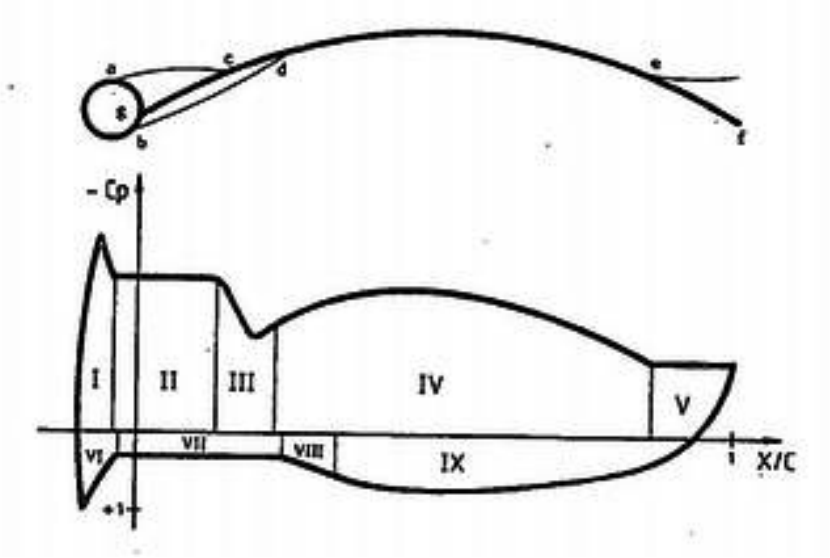

(a) Separation regions and pressure distribution, as used by Wilkinson [196].

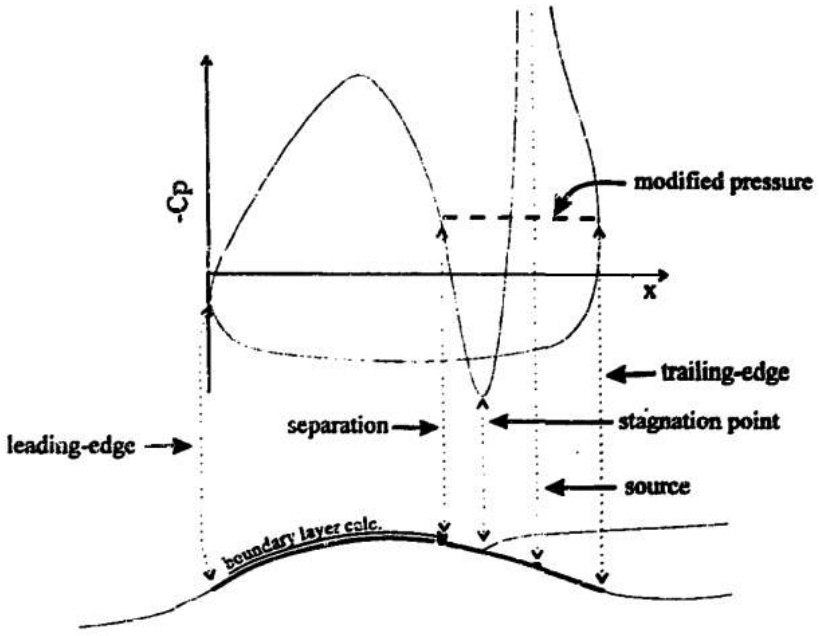

(b) Cyr & Newman [43] pressure distribution and trailing edge separation vortex location.

Figure 3.14: Schematics of the Wilksinson [196] and Cyr & Newman [43] MWVM.

- Bailey et al [21] model the separation bubbles next to a 2D mast-and-sail joint at small incidence with two cubic arcs of point-vortices joined to a thin-airfoil-theory representation of the sail between the reattachment points and the trailing edge; the cubic arcs stretch between the geometric center of the leading-edge of the mast and given reattachment points on the upper and lower sail surface calculated empirically from backward-facing step data.
- Shukla & Eldredge [160] extended Jones' 2D double-wake model [96] to a deformable 2D membrane section, producing results that are comparable with the results obtained by Heathcote et al [84] for water-tank tests of a 2D oscillating membrane.

The primary concerns for a multiple wake vortex method are the determination of separation-location [47] and rate of vorticity release [96], and wake smoothing [154].

When the numerical determination of separation-location - via a method of variable positions of nascent vortices (MVP) - is outside of the scope of a project, a method of fixed positions of nascent vortices (MFP) is applied for known separation locations [100]. These known separation locations can be imported from a previously found separation locations as done by de Matteis & de Socio [47], or by fixing the minimum pressure location of the single-wake solution, as suggested by Clements & Maull [39].

The rate of vorticity shedding is determined to satisfy Helmholtz's third theorem which conserve the total amount of vorticity in an inviscid fluid [112]. The addition of circulation into the boundary layer

$$\frac{d\Gamma}{dt} = \frac{1}{2}U^{*2}$$

depends on a boundary layer characteristic velocity U^* to use. This characteristic boundary layer velocity can be determined from the velocity at the separation point outside of the boundary layer [39], the velocity difference about the edge of the shear layer at the separation point [100], a combination of the shear-layer velocities over multiple - such as, four - vortices near the separation point [100], or the fore-aft surface velocity difference at the separation point [106]. A measure of how well the two wakes approximate streamlines can be found by determining the change in mass-flow rate between the two wakes at different locations downstream.

Wake smoothing may be required when the shedding-rate of the nascent vortices is sufficiently high that the velocity singularity at a particular vortex begins to influence that vortex's neighbors [154], causing nonphysical, very-large velocities on the order of $100U_\infty$ [39]. With respect to a multiple wake vortex method representation of the flow in the shadow of a sharp obstruction, such as a back-wards facing step or the LEI tube, shed vortices within some given distance - suggested as 0.005-0.05 obstruction heights - of the shadowed surface can be removed unilaterally [39].

The fact that potential flow methods are - generally speaking - inviscid, it is standard practice to add a simple profile-drag estimate to the calculated pressure distribution for membrane-flow vortex-method models [19]. Fiddes & Gaydon [66] were able to successfully model flow over yacht sails by introducing profile-drag calculated strip-wise with the Squire-Young drag formula. The Squire-Young drag formula approximates the 2D drag coefficient based on the momentum thickness infinitely-far downstream as a function of the boundary layer momentum thickness at the trailing edge, and is particularly accurate for flows that include a transition region:

$$c_{d,SY} = 2\left(\frac{\theta_{TE}}{c}\right)\left(\frac{U_{TE}}{U_\infty}\right)^{\frac{5+H_{TE}}{2}}$$

where θ_{TE} is the boundary layer momentum thickness at the trailing edge, and H_{TE} is the boundary layer shape function at the trailing edge, defined as $H_{TE} = \delta_{TE}/\theta_{TE}$ giving the ratio of the trailing edge displacement thickness to momentum thickness [40].

It appears conceptually possible to use a 3D triple-wake vortex method to model leading-edge flow separation bubbles on the suction- and pressure- surfaces, as well as the trailing edge suction-surface of an LEI kite - though the author has not at present seen such an example in the literature.

3.3.5 Transformation Methods

There are a number of not-necessarily related methods that rely on the use of transforming coordinates to solve the potential flow problem.

Method of Conformal Tranformations

Conformal transformation maps a complex function in terms of a secondary complex variable - whose definitions are required to be differentiable over the whole functional domain - such that angles remain constant during transformation. Two dimensional flows that are incompressible and irrotational are necessarily holomorphic - that is, valid as conformal mapping functions. Further, potential flow solutions are harmonic, and harmonic functions remain harmonic over conformal transformations. Consequently, potential flow solutions for arbitrary, 2D, simply-connected airfoils can be easily found by conformally mapping the given airfoil to a circle, whose potential flow solution is known [83]. The typical form of this 2D cusped-trailing-edge airfoil-to-circle conformal transformation is the Joukowski transformation, using the relationship

$$w = w(z) = \frac{1}{2}\left(z + \frac{1}{z}\right)$$

where $z = x + iy$ is the complex representation of dimensions in the 2D physical plane [119]. Conformal mapping techniques are normally used for steady flow problems [122].

It is possibly to apply hyperdimensional (logically, with a particular focus on $n = 3$ dimensions) conformal mapping techniques for certain [113] [114] [178] transformation types - homothetic transformations comprising translations and homogeneous scalings, isometries comprising rotations and reflections, and inversions - which limits the practical application of 3D conformal mapping to bodies of revolution.

Cyr & Newman [43] used Joukowski transformations to predict the potential flow around arbitrary 2D membranes and Lorillu et al [117] use conformal mapping to solve for 2D flow about a sail with a non-negligible mast, but 3D kite flow modelling is not possible with conformal mapping.

Hodograph Method

The hodograph method - as developed by Levi-Civita [107], and adapted by Dugan [58] for the analysis of 2D sails with small deflections, and applied by Alben et al [11] to study the curl-up of a "1D leaf in a 2D wind" - determines what sail-shape and surface velocity correspond to any given angle of attack and tension, using a series of sequential conformal transformations. These conformal transformations occur between a complex W plane that represents the potential- and stream-functions ($W_{plane} = 1/(U_\infty c)(\phi + i\psi)$), an 'auxiliary' t plane, and a complex ζ plane that represents the 2D velocities ($\zeta_{plane} = 1/(U_\infty)(u - iv)$). Dugan describes the advantages of the hodograph method, as compared to the vortex filament methods: the influence of the wake is already included in the description of the flow and does not need to be 'tracked'; the model is not limited to small angles of attack; and the model does not inherently suggest that pressure drag is zero, as in d'Alembert's paradox.

The hodograph method is an inverse method, meaning that the method solves for the shape around which a given velocity-field exists [111]. Consequently, it is not particularly useful for kite FSI modelling, where - by virtue of the partitioned FSI structure - the flow must be found for a given structural deformation.

Method of Velocity Singularities

As developed by Mateescu [122] the method of velocity singularities (MVS) solves potential flow around arbitrary 2D or 3D airfoils, by defining the velocity as the sum of complex symmetrical and anti-symmetrical terms, whose real and imaginary components describe different directions. The flow is determined by the influence on the Trefftz plane of velocity singularity points, such as at the leading edge of the airfoil and at any geometrical discontinuities, such as flaps, ridges, camber, or - presumably the LEI tube-canopy interface. It is assumed that the flow is quasi-steady and fully attached, such that the impermeable boundary condition can be enforced for the airfoil's given chordwise distribution of camber and thickness. The MVS then applies a turbulent flat plate boundary layer correction.

The MVS appears to have been well validated for viscous - fully attached - effects, membrane wings [123] and finite-span wings [124].

Given that the primary source of discrepancies between experimental and modelled flow over membrane wings is separation, and that a LEI kite in power-kite operation certainly experiences separation, the MVS does not appear to be a viable method of modelling LEI kite FSI aerodynamics.

3.3.6 Kernel-Function Method

The kernel-function method (KFM) is a 3D approximation method within the potential flow domain, that approximates the lift distribution as a weighted sum of presupposed general lift modes that represent the general character of expected chord-wise and span-wise lift distributions, with the weights as unknowns. To solve for the surface pressure distribution, the downwash distribution is expressed as the correspondingly-weighted sum of definite integrals of the lift distributions [194].

There exist KFM extensions, such as the Vivian-Andrews [188] extension for non-planar wings with blunt- and thick-leading edges, that might be applicable for kite-shaped wings. However, because KFM is configuration dependent [137] by virtue of its dependence on prior knowledge of the lift modes, it is not practical for design-purpose FSI modelling.

3.3.7 Computational Fluid Dynamics

Computational Fluid Dynamics (CFD) encompases the models that analyze flow not just over a surface, but in the entire flow region. Though there are many possible CFD variations, each representing the complete Navier-Stokes equations with different approximations, the most broad CFD model hierarchy includes the Euler, Reynolds-Averaged Navier Stokes, and Full Navier-Stokes models, in increasing complexity [63].

These solutions tend to be quite accurate but very computationally expensive, particularly because they require small spatial meshes near boundary layers. The mesh must be re-created every time the structure deforms, which is particularly expensive for large deformations [137].

Particularly because it has been shown by Van Kappel that sufficient modelling accuracy can be achieved without the flow solution in the full volume, the additional time required for CFD modelling cannot be justified. CFD models are consequently not suitable for FSI problems concerning highly-flexible kites.

Euler Model The Euler model is the full Navier-Stokes model under the assumptions that the flow is inviscid, and adiabatic [63].

Lattice Boltzmann Method The Lattice Boltzmann method (LBM) is a first-order simplificiation of the Navier-Stokes equations, over a non-adaptive grid that does not require re-meshing, where the fluid is considered as a collection of colliding fluid elements. In comparison to the Navier-Stokes, the LBM is viscous, but does not include a nonlinear convective term - convection arises from the advection of the fluid elements - or solve the Poisson equation for pressure. LBM is well suited to parallization, and can be used to solve problems involving multiple phases, complex geometries or material interfaces [103].

Lee & Lee used the LBM to solve the flow over a flexible, thickness-free, 2D plate at low Reynolds numbers [103].

Reynolds-Averaged Navier Stokes Model The Reynolds-Averaged Navier Stokes (RANS) model uses the full Navier-Stokes equation, under the assumption that the flow can be decomposed into a time-averaged flow and a fluctuation flow.

Examples of RANS modelling of flow over membranes can be found for 2D stiffness-free convertible-car roofs in Knight et al [101], and for inextensible, flexible 2D sails with varying excess lengths and Reynolds number $R_e = 1.3 \cdot 10^6$ in Bunge et al [33]. Smith and Smith & Shyy et al used a pressure-based RANS model with a $k - \omega$ turbulence model to study steady laminar [163], unsteady laminar [163], and turbulent [165] flow on 2D and 3D [166] membrane wings.

Specifically in relation to kite-flow problems, Gaunaa et al [76] and Deaves [51] used incompressible RANS solvers to consider the static flow over rigid arc-shaped kites, respectively with a standard airfoil profile, and with an LEI-shaped profile, for various Reynolds numbers, angles of attack, and side-slip angles. Maneia [120] also modelled steady flow over a Clark Y paraglider in the commercial RANS STAR-CCM+ solver.

Large Eddy Simulation Large eddy simulations (LES) solve for large-scale turbulent phenomena, but neglect small flow eddies to reduce computational cost.

De Nayer & Breuer [49] [48] model the aerodynamics of a cylinder trailing a flexible rubber splitter FSI problem at $R_e = 30,407$ with LES.

Direct Numerical Simulation Assuming a perfect fluid that is a continuum and not moving at relativistic speeds, the full Navier-Stokes (NS) relation contains one continuity equation, three momentum equations, and an energy equation [63]. When the full NS relations are solved, without introducing an explicit turbulence approximation, this is called direct numerical simulation (DNS).

Gordnier [79] and Visbal & Gordnier [187] use a sixth-order implicit Navier-Stokes solver to model a 2D membrane wing, and transition in the boundary layer along a 2D flexible panel, respectively, at low Reynolds numbers between $2.5 \cdot 10^3 \leq R_e \leq 10^4$.

3.4 Aerodynamic Model Selection

An aerodynamic model intended as the aerodynamic solver of a partitioned FSI solver must meet three requirements: computational speed, physical accuracy in highly 3D flow with significant separation, and the ability to non-empirically generate both span-wise and chord-wise pressure distributions.

The fast aerodynamic models suffer from one - or more - serious flaws with respect to the kite FSI problem: an inability to model viscous effects such as separation; are by definition unable to describe three dimensionality, whether due to limitations of geometry - as for transformation methods or the resolution requirement for 3D panel method convergence - or due to an inability to describe cross-flow; or are unable to generate chord-wise pressure distributions without resorting to empiricism. The high-accuracy methods model flow very well, but are too slow to use iteratively. The suitability of the various aerodynamic models previously used for membrane-flow problems for steady LEI-kite FSI-analysis and iterative-design is summarized in Figure 3.15.

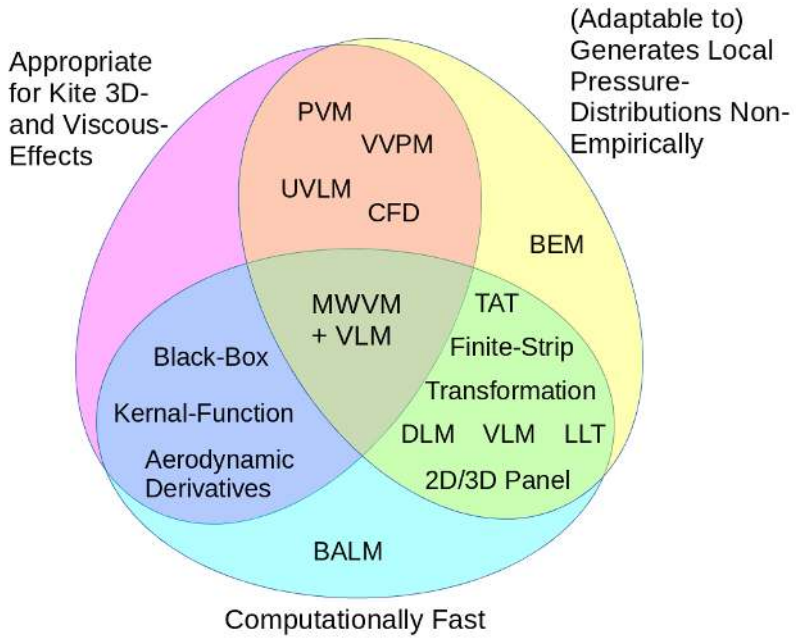

Figure 3.15: A summary of the aerodynamic models suggested by a literature survey in terms of their suitability to a kite FSI problem.

Separation on 2D membranes - notably without the kite's leading-edge inflated tube, which adds a region of semi-permanent separation - has been well modelled with a double-wake VLM. Van Kappel demonstrated that a viscosity-modified VLM is capable of predicting flow over a 3D surf-kite.

The success of the separate 2D multiple-wake VLM membrane models and van Kappel's 3D surf-kite VLM model lead the author to believe that a 3D multiple wake vortex lattice method (VLM_{MW}) can successfully model the 3D, separated flow in the surf-kite FSI problem. It is the success-criterion of this thesis-work (see Chapter 1) to be able to evaluate to what degree that belief is accurate.

Chapter 4

Program Specifics in the Implementation of this Method

The VLM_{MW} code was written to be easy to read and understand. This chapter describes this code for a potential future user:

- the high-level code logic;
- the detailed architecture of the code: the programming language, the data structures, and the required inputs and outputs, especially considering the influence of the LEI-shape and flow separation;
- the direction, sign and normalization conventions that a user needs in order to provide the inputs and interpret the outputs; and
- the geometries-and-flows which are available as test-cases, each having a corresponding comparison (validation) dataset from experimentation or CFD modelling.

4.1 Internal Logic

The internal logic of the VLM_{MW} follows the process conceptualized in Figure 4.1. The details of these process steps are described in the report sections noted next to the step name.

4.2 Architecture

4.2.1 Language Selection

The programming language may have a large influence on the computational speed for any given model resolution, considering the potentially large size of aerodynamic-influence coefficient matrices. The development language of the VLM_{MW} was chosen to be Matlab for a few reasons:

- greater development efficiency due to the author's familiarity with the language;
- increased convenience in future integration of the VLM_{MW} into the pre-existing TU Delft AWE FSI code-base, which is predominantly written in Matlab; and
- greater confidence during development due to the existence of the open-source LLT model Wake Induced Dynamics Simulator (WInDS) [157] - which can be used for method comparison.

To address the concern that Matlab is not known for its speed, we consider that this thesis is a proof-of-concept for the VLM_{MW}, rather than the method's final form. Code-speed up may be a future development step depending on how the VLM_{MW} fits into the code base of the AWE group. In the meantime, computational speed can be increased by compilation of the code into -mex form.

4.2.2 Data Structure

Variables are either used as scalars or arrays of various sizes.

- *Scalar-Constants* for global constants, such as the incompressible air density ρ_{air}.
- *Vector-Constants* for constants that have both magnitude and direction, but do not change over the spacial volume, such as the apparent velocity $\mathbf{U}_A$.
- *Scalar-Variables* for values that do not have an associated direction, but change in space and are defined at particular locations. An example would be the circulation strength of a particular vortex ring, Γ.
- *Vector-Variables* for values that do have an associated direction, and change in space. An example would be the flow velocity at a point, $\mathbf{U}$.

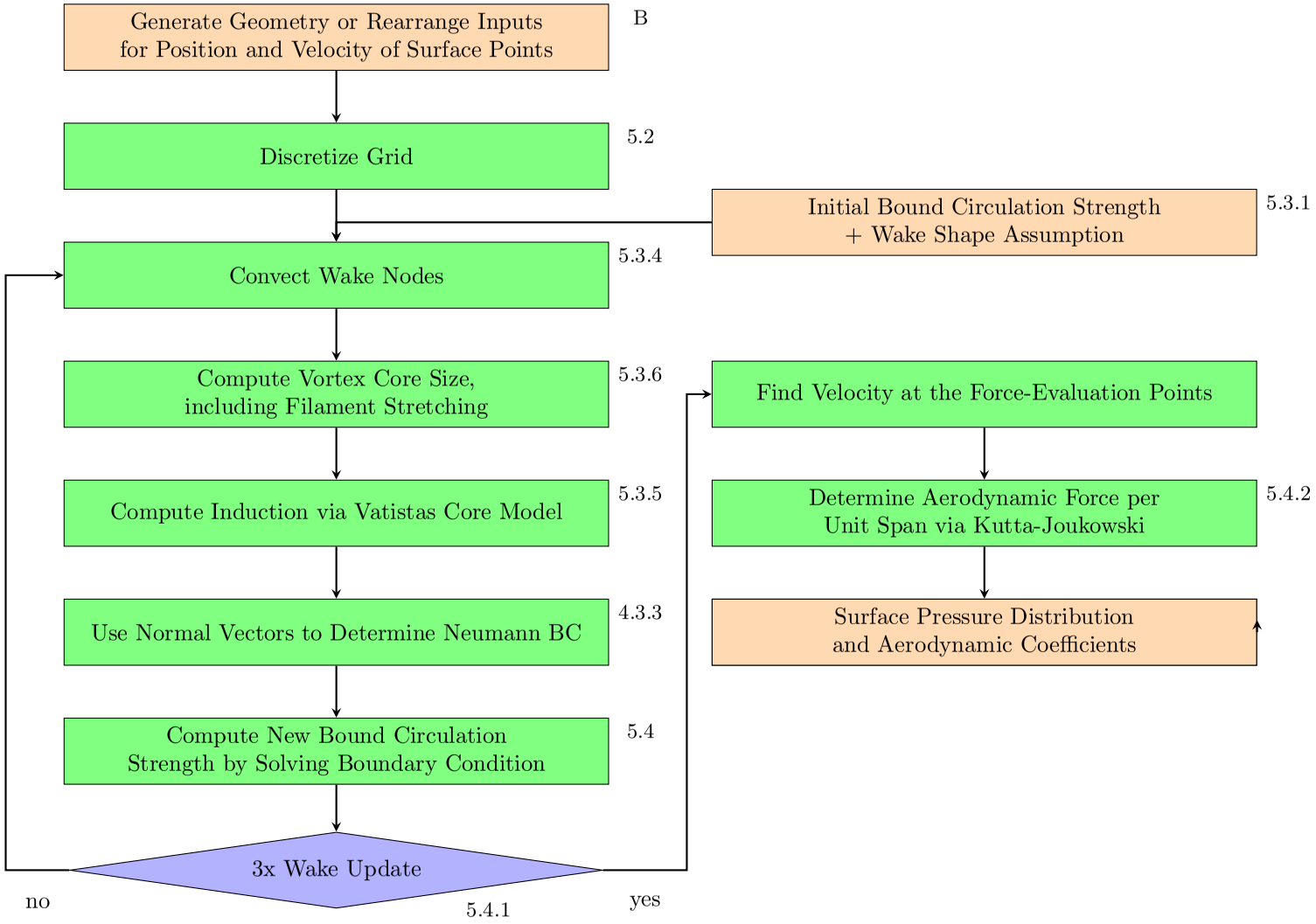

Figure 4.1: Concept of VLM_{MW} Internal Logic

- *Geometric Matrix of Scalar-Variables* stores the Scalar-Variables according to their location within the vortex lattice. The storage indices describe the associate node location with a span-wise index and a chord-wise - or downstream-location[1] - index. Considering a generic variable $\mathbf{v}$:

$$\mathbf{v} = \mathbf{v}\left(\begin{matrix}\overbrace{n_b}^{\text{span-wise node index}} \\ \underbrace{}_{1\to N_B}\end{matrix}, \begin{matrix}\overbrace{n_c}^{\text{chord-wise node index}} \\ \underbrace{}_{1\to N_C}\end{matrix}\right)$$

or

$$\mathbf{v} = \mathbf{v}\left(\begin{matrix}\overbrace{n_b}^{\text{span-wise node index}} \\ \underbrace{}_{1\to N_B}\end{matrix}, \begin{matrix}\overbrace{n_w}^{\text{downstream node index}} \\ \underbrace{}_{1\to N_W+1}\end{matrix}\right)$$

For example, the circulation strength of the vortex-ring around the point (n_b, n_c) would be stored as $\mathbf{\Gamma}(n_b, n_c) = \Gamma_{n_b,n_c}$.

- *Geometric Matrix of Vector-Variables* stores the Vector-Variables according to their location within the vortex lattice and a dimension index describing their $\hat{x}$, $\hat{y}$, $\hat{z}$ components. Considering a generic variable $\mathbf{v}$:

$$\mathbf{v} = \mathbf{v}\left(\begin{matrix}\overbrace{n_b}^{\text{span-wise node index}} \\ \underbrace{}_{1\to N_B}\end{matrix}, \begin{matrix}\overbrace{n_c}^{\text{chord-wise node index}} \\ \underbrace{}_{1\to N_C}\end{matrix}, \begin{matrix}\overbrace{n_k}^{\text{dimension index}} \\ \underbrace{}_{1\to 3}\end{matrix}\right)$$

or

$$\mathbf{v} = \mathbf{v}\left(\begin{matrix}\overbrace{n_b}^{\text{span-wise node index}} \\ \underbrace{}_{1\to N_B}\end{matrix}, \begin{matrix}\overbrace{n_w}^{\text{downstream node index}} \\ \underbrace{}_{1\to N_W+1}\end{matrix}, \begin{matrix}\overbrace{n_k}^{\text{dimension index}} \\ \underbrace{}_{1\to 3}\end{matrix}\right)$$

For example, the y-component of the surface position at the fourth span-wise node and third chord-wise node of the kite, would be stored as $\mathbf{x}(4, 3, 2)$.

- *Column Matrix Rearrangement of Scalar-Variables* is the rearranged form of the Geometric Matrix of Scalar-Variables. It contains the same information, but is reformatted such that the entire body of data is suitable for matrix multiplication. The index of the column matrix counts first along the chord-wise index, then along the span-wise index. Considering a generic variable $\mathbf{v}$:

$$\tilde{\mathbf{v}}\left(\begin{matrix}\overbrace{n_j}^{\text{chord-wise, then span-wise}} \\ \underbrace{}_{1\to N_J=(N_B-1)(N_C-1)}\end{matrix}, 1\right) = \mathbf{v}\left(\text{floor}\left(\frac{(n_j-1)}{(N_C-1)}\right)+1, \text{mod}\left(n_j-1, N_C-1\right)+1\right)$$

The circulation strength and surface-normal velocity are contained in column matrix rearrangements for multiplication processes, then returned back to the geometric form for legibility. This column matrix contains no new information, but is simply a rearrangement of the indexing locations of the existing data; this is a direct data transfer rather than an interpolation or "table-lookup" step.

- *Influence Coefficient Matrix* is the container of the VLM_{MW}'s linear equation. Down the column we see the influence of the vortex rings on a specific point; across the row we see how much influence a specific vortex ring has on the evaluation points. Each of the entries is a scalar.

$$\mathbf{A} = \overbrace{\left.\begin{pmatrix} A_{1,1} & A_{1,2} & \cdots & A_{1,n_\gamma} & \cdots & A_{1,N_\Gamma} \\ A_{2,1} & A_{2,2} & & A_{2,n_\gamma} & & A_{2,N_\Gamma} \\ \vdots & \vdots & \ddots & \vdots & & \vdots \\ A_{n_j,1} & A_{n_j,2} & \cdots & A_{n_j,n_\gamma} & \cdots & A_{n_j,N_\Gamma} \\ \vdots & \vdots & & \vdots & \ddots & \vdots \\ A_{N_J,1} & A_{N_J,2} & \cdots & A_{N_J,n_\gamma} & \cdots & A_{N_J,N_\Gamma} \end{pmatrix}\right\}}^{1\to N_\Gamma=(N_B-1)(N_C-1)} \; {\scriptstyle 1\to N_J=(N_B-1)(N_C-1)}$$

[1] In comparison to the span-wise and chord-wise indices which count respectively from 1 to N_B and from 1 to N_C, the downstream-location index counts from 1 to $N_W + 1$. This is because N_W designates the number of nodes within the free-wake region. The $(N_W + 1)^{\text{th}}$ node sits "infinitely-far" downstream of the N_W^{th} node, and cannot be set by the user.

4.2.3 Program Inputs and Outputs

Due to the intention of ultimately using the VLM_{MW} as a modular aerodynamic model within the Airborne Wind Energy Group's FSI code base, the inputs and outputs of the VLM_{MW} must be as generic as possible and open to easy reorientation.

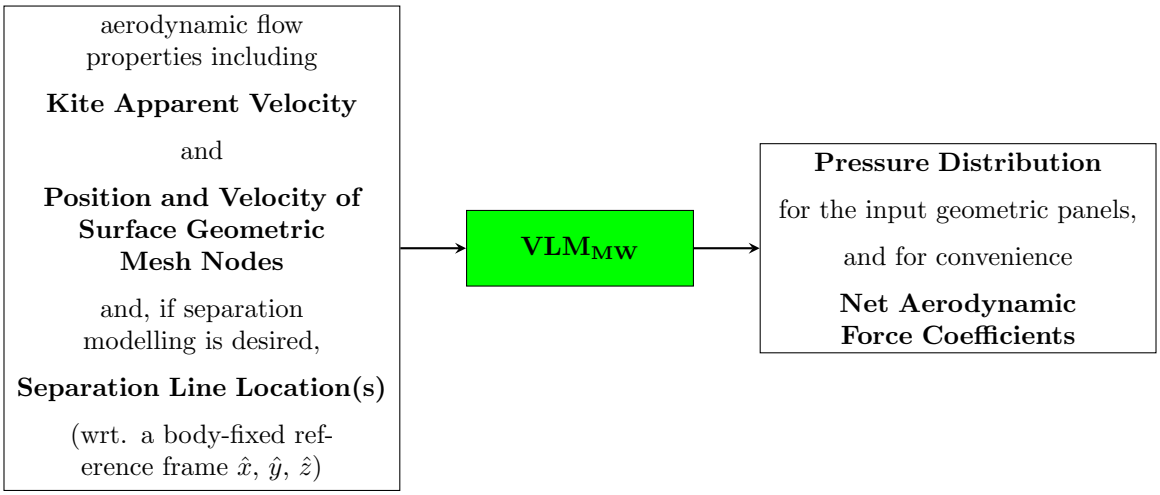

Figure 4.2: Conceptualized inputs and outputs of the VLM_{MW}.

4.2.4 Requirements on the Geometric Mesh

It is fairly logical how to determine or allocate the chord-wise node index to a thickness-free geometry without much wrapping and fully attached flow. However, the introduction of a finite-thickness body and separation modelling require some care when defining points in the chord-wise direction.

Finite-Thickness Indexing

There are several methods that can be used to model thickness with panel methods:

- Crossing two distinct vortex-ring surfaces at the centroid of the thick body and evaluating the boundary conditions at the edges of these surfaces [57]. This model is useful to roughly redirect flow around an obstacle without resolving the flow at the surface. Since we are actively concerned with the effect of the separation on the surface, this is not a good choice.

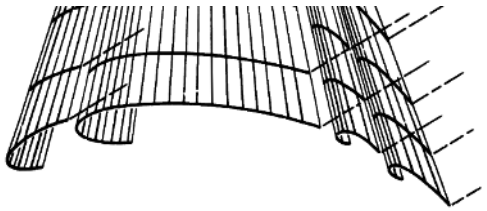

Figure 4.3: Sketch of a "hook" wrapped airfoil with control elements, taken from Smith & Bhateley [162].

- The "hook" wrapping (see Figure 4.3) of the finite-thickness geometry with a thickness-free vortex lattice, such that the suction surface and the portion of pressure surface with strong curvature are covered [162]. This method of modelling thickness is attractive here, because we could easily shed vorticity from the edge past the curved-over LE sheet in a "wind-shadow curtain." However, it is not possible to enforce flow conditions along the back portion of the LEI tube. Further, the risk is that misjudging the separation location may effectively eliminate the separation region all-together.

- The complete wrapping of the finite-thickness geometry with a looped thickness-free vortex lattice that joins the loop's "beginning" and "end" at the intersection location ($n_c = 1$) where the geometry becomes thickness-free. For a thick airfoil, this intersection point is the trailing edge; for an LEI kite the intersection point is at the meeting location of the LEI tube and the canopy. This allows for the placement of vortex rings and control points at every point on the geometry where a velocity shear is materially expected. Consequently, the flow boundary conditions can be enforced over the entire body. This is a necessary ability for a multiple-wake vortex method, to prevent the separated vortex lattices from convecting themselves through the body.

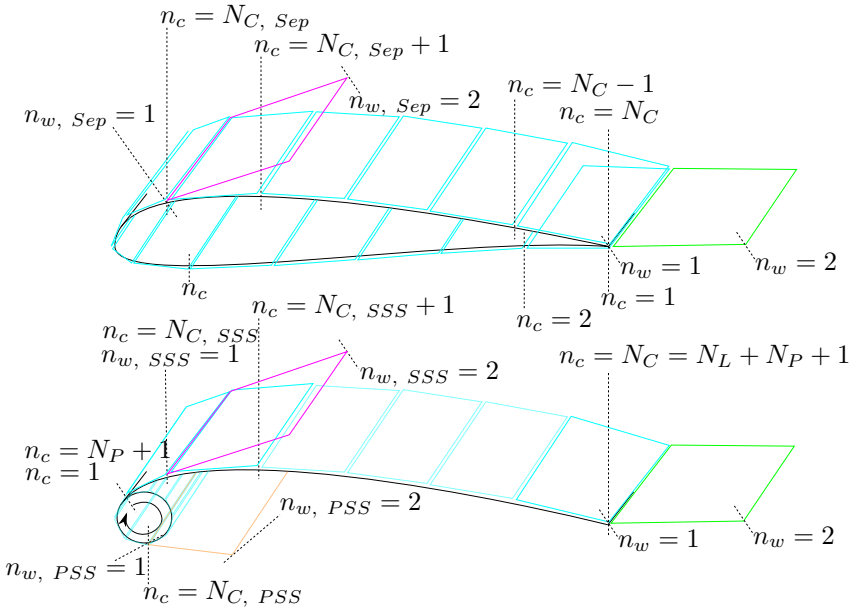

Figure 4.4: Chord-wise indexing in finite-thickness situations

It is reasonable, then, to model finite-thickness regions by wrapping. The chord-wise indexing pattern that corresponds to geometries that contain finite-thickness regions is depicted visually in Figure 4.4.

One critical point, is that care must be taken that the "beginning" and "end" vortex nodes must be placed exactly overlapping at the intersection point. If there is a small offset between these node placements, the induction from each intersection vortex ring may cause unphysical[2] pressure distributions.

Separation Indexing

In order for the flow to leave the surface smoothly at the separation line, we must be able to set the net vortex strength at the separation line to zero. The only way this is possible is if we are able to directly control the discretized vorticity at the separation line. This requires that there always be a vortex filament at the separation line. Consequently, the separation line must be at a constant chord-wise index. That is:

$$N_{C,\ Sep.}(n_b) = N_{C,\ Sep.}$$

This has two follow-up points:

- There may be bunching of vortex rings depending on the chord-wise location of separation. That is, if the suction surface separation line is at twenty percent of the chord ($0.2c$) at root, then the vortex rings at the root will tend to be shorter - in the chord-wise direction - before the separation line than the vortex rings after the separation line.

[2]Sometimes manifesting as negative drag forces, to the delight of those concerned with energy efficiency.

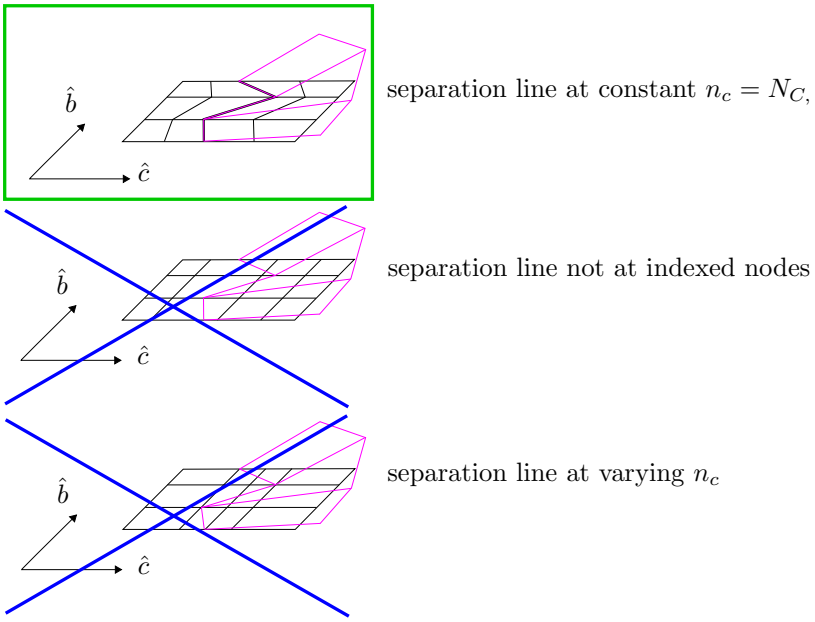

Figure 4.5: Separation line must be at a constant chordwise index

- If the flow separates at any point on one of the two surfaces, the flow must be considered to separate at every span-wise index on that surface. We are unable to model two shed vorticity surfaces from the same location, because this implies two additional unknown shed vortex strengths at the separation location and only one constraint.[3] Consequently, if there is a situation where flow is attached at some span-wise locations and separated at other span-wise locations, the separation location on the attached-flow sections must be assumed to sit some small distance in front of the trailing edge.

The separation mechanism and the enforcement of the smooth-separation assumptions can be found in Chapter 5.

[3]See Section 5.5.1 for more details.

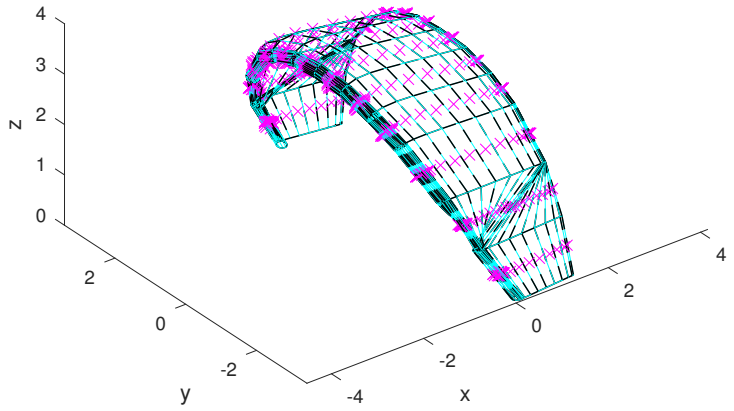

Figure 4.6: A demonstration of the vortex lattice bunching for a possible suction surface separation line.

4.3 Direction, Sign, and Normalization Conventions

4.3.1 Coordinate Systems

The main body of the code uses a standard right-handed body-fixed reference frame, defined with $\hat{x}$ along the root chord line, $\hat{y}$ drawn between the kite tips, and $\hat{z}$ pointing up through the kite. These reference frame axes are shown in Figure 4.7.

As certain geometries are easier to visualize in a 2D format, a cross-sectional right-handed reference frame is also defined, where $\hat{x}'$ is along the section chord, $\hat{y}'$ points through the LEI tube, and $\hat{z}'$ is up through the section. The origin of this cross-sectional reference frame is at the center of the LEI tube.

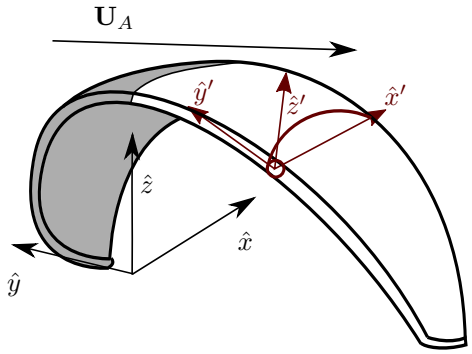

Figure 4.7: Expected Kite Coordinate Systems

The uniform freestream velocity is used as the kite's apparent velocity, oriented according to an angle of attack α and a side-slip angle β, both taken with respect to the body-fixed reference frame.

$$\mathbf{U}_A = U_A \langle \cos(\alpha)\cos(\beta), \ -\sin(\beta), \ \sin(\alpha)\cos(\beta) \rangle$$

4.3.2 Panel Corner Naming Convention

The boundaries of a geometric panel or vortex ring are at corner nodes, which are defined - for convenient correspondence with a clockwise vortex ring direction - starting at the leading-edge and y-negative edge of the panel, travelling clockwise over the y-positive edge to end at the trailing-edge and y-negative edge.

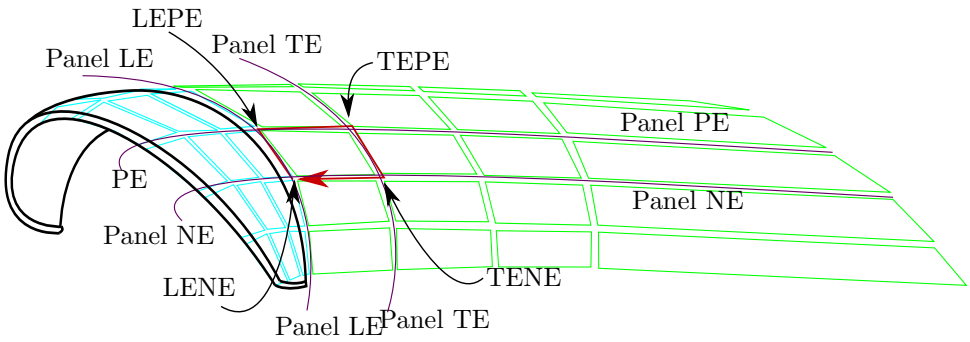

Figure 4.8: Corner Definitions for a Kite Geometric Panel or Vortex Ring

The area of such a quadrilateral, not-necessarily-planar panel can be approximated as the sum of the areas of two diagonal triangles. As the norm of the cross product describes the area in the rectangle between the two multiplied vectors:

$$\begin{aligned} S_j &\approx \frac{1}{2}\left(S_{LEPE,LENE,TENE} + S_{TENE,TEPE,LEPE}\right) \\ &\approx \frac{1}{2}||(\mathbf{x}_{LEPE} - \mathbf{x}_{LENE}) \times (\mathbf{x}_{TENE} - \mathbf{x}_{LENE})|| + \frac{1}{2}||(\mathbf{x}_{TENE} - \mathbf{x}_{TEPE}) \times (\mathbf{x}_{LEPE} - \mathbf{x}_{TEPE})|| \end{aligned}$$

4.3.3 Positive Surface Normal Vector

The surface normal vector is defined as positive such that a flat plate at zero incidence will have a normal vector pointing $\hat{n} = \hat{z}$. Consequently, the normal vector is defined as the cross of the vector from the TENE corner to the LEPE corner with the vector from the TEPE corner to the LENE corner.

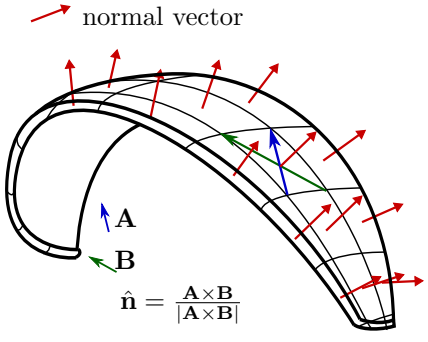

(a) Surface Normal Vectors

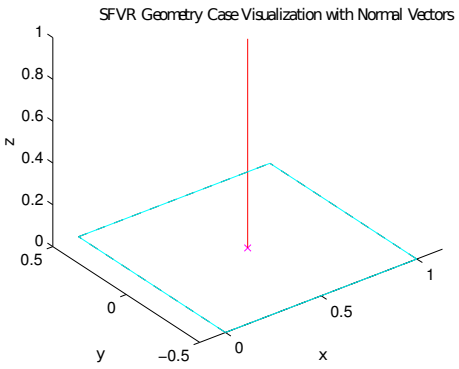

(b) The normal vector of a single flat vortex ring and co-incident geometrical panel

Figure 4.9: Normal vector conventions illustrated

$$
\begin{aligned}
\mathbf{n}(n_b, n_c, :) &= (\mathbf{x}_g(n_b+1, n_c+1, :) - \mathbf{x}_g(n_b, n_c, :)) \times (\mathbf{x}_g(n_b+1, n_c, :) - \mathbf{x}_g(n_b+1, n_c, :)) \\
&= (\mathbf{x}_{TEPE} - \mathbf{x}_{LENE}) \times (\mathbf{x}_{LEPE} - \mathbf{x}_{TENE}) \\
\hat{\mathbf{n}} &= \frac{\mathbf{n}}{|\mathbf{n}|}
\end{aligned}
$$

4.3.4 Positive Vortex Strength

If the strength of the vortex ring is positive, then the front filament will push fluid upwards, and the back filament will push fluid downwards. (See Figure 4.10 for a visualization of the flow behavior around a single flat vortex ring with positive vortex strength.) That is, the front filament of a positive-strength vortex ring causes positive lift and the back filament of the positive-strength vortex ring causes the accompanying downwash. This requires our vortex ring to be defined positive with positive circulation clockwise, when looking down.

The mechanism of the flow redirection - or induction - is described in Chapter 5.

4.3.5 Aerodynamic Coefficient Normalization Conventions

It is standard to normalize the aerodynamic coefficients against the product of a characteristic area and characteristic dynamic pressure.

Here, the characteristic area is chosen to be the projected area of the geometry on the $x-y$ plane. This is due to the design choice that the VLM_{MW} be able to model geometries that are not LEI kites. Projected area can be determined for any collection of $\mathbf{x}_g$ geometric mesh-points with the same simple algorithm regardless of how many folds or finite-thickness regions the geometry contains. That is:

$$
\begin{aligned}
S^* = S &= b_{max} c_{MAC}, \quad \text{where:} \\
b_{max} &= \max_{n_c} \left(\mathbf{x}_g(n_b \text{ with maximum y value}, n_c, 2) + \mathbf{x}_g(n_b \text{ with minimum y value}, n_c, 2) \right) \\
c_{MAC} &= \operatorname*{mean}_{n_b} \left(\mathbf{x}_g(n_b, n_c \text{ with maximum x value}, 1) - \mathbf{x}_g(n_b, n_c \text{ with minimum x value}, 1) \right)
\end{aligned}
$$

The normalization characteristic dynamic pressure term is the dynamic pressure term found within Bernoulli's pressure relation evaluated in the freestream flow:

$$
q^* = q_\infty = \frac{1}{2} \rho_{air} ||\mathbf{U}_A||^2
$$

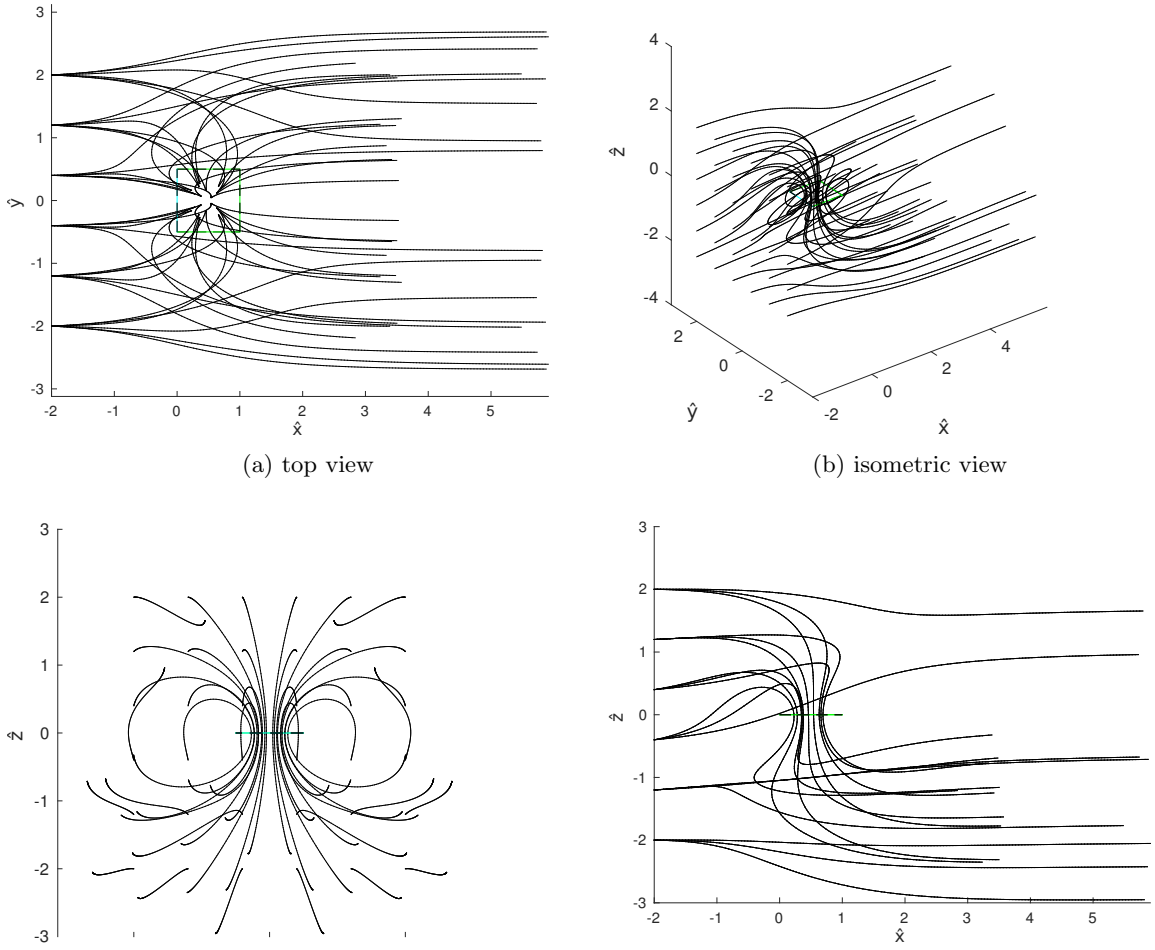

(a) top view

(b) isometric view

(c) front view

(d) side view

Figure 4.10: Visualization of the flow-field for a uniform freestream velocity in the $\hat{x}$ direction and a Single Flat Vortex Ring (SFVR) with positive circulation strength.

4.4 Available Test Cases

The VLM_{MW} will run for a user-input geometric mesh that fits the requirements mentioned previously in this chapter. However it can be handy for a user to have some geometries which have previously been "built" into the code and compared to experimental- or higher-order computational model- results. These available geometry cases, the increase in code functionality demonstrated by each progressive case, and the dataset against which the geometry case results can be compared are described below.

Note that the VLM_{MW} is a vortex method that is not coupled to a boundary-layer-integration method, and predicts results for flow at the Euler limit, where the Reynolds number is infinite.

4.4.1 Two-Dimensional Flat Plate (FP2D)

There is an analytical solution to the circulation distribution on a two-dimensional flat plate with fully attached, potential flow. As a part of this analytical solution, we know the pressure distribution on the 2D plate, as well as the relationship between the lift- and drag- coefficients at small angles of attack.

We can test that the VLM_{MW} produces this analytical solution by considering the behavior at the root of a rectangular flat plate with a large aspect ratio (here $AR = 20$). This test geometry is named the "FP2D" geometry case.

The FP2D case is included in order to ensure that the Biot-Savart and Kutta-Joukowski formulations are working correctly.

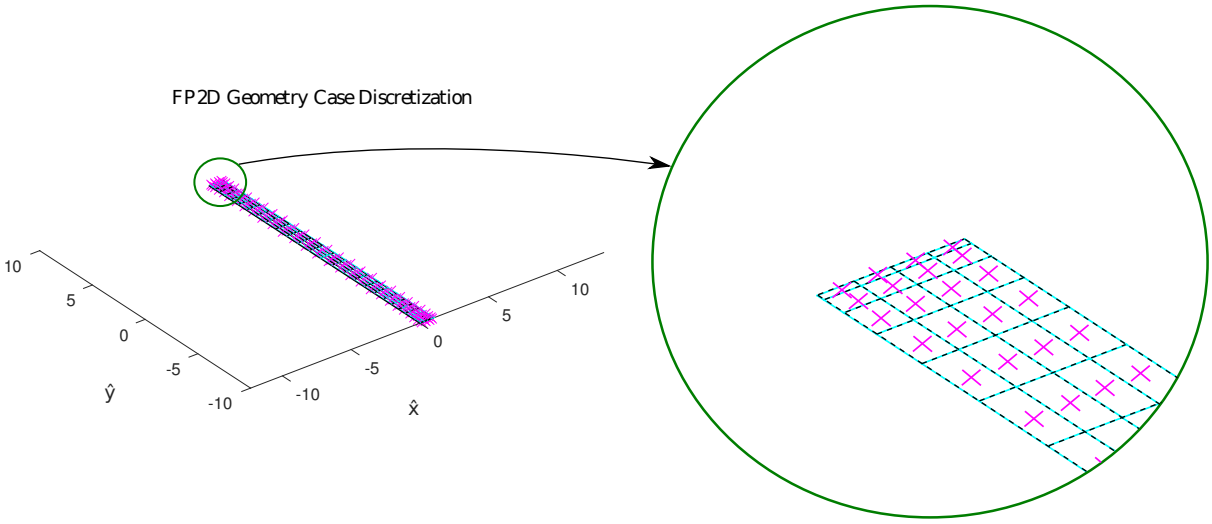

Figure 4.11: Example of an FP2D Geometry Case with Vortex Lattice and Collocation Points

4.4.2 Unity Aspect Ratio Flat Plate (FP3D)

Normal force polars for angles of attack between 0^o and 90^o are given for a rectangular flat-plate of unity aspect ratio (FP3D), as shown in Figure 4.12, by both Winter [198] and, more recently, Ortiz et al [143]. Both polars were determined experimentally, Winter, in a closed wind-tunnel at Reynolds number $1.7 \cdot 10^6$; Ortiz et al, in an open-jet wind-tunnel at Reynolds number $2.1 \cdot 10^5$. Further, Winter gives the pressure distribution for the unity-aspect ratio flat plate at 8^o and 30^o angle of attack.

This test case is included to ensure that the model is able to demonstrate the influence of tip-vortices and correctly predict wake roll-up.

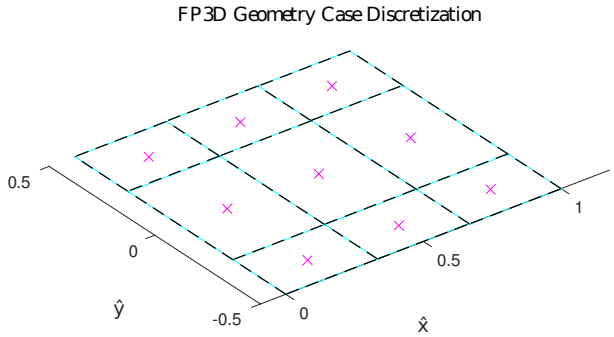

Figure 4.12: Example of an FP3D geometry.

4.4.3 Clark Y Arc-Shaped Wing (CYKG and CYKW)

In order to test the ability of the VLM_{MW} to model the effect of a wing's arc-shape and thickness, the quarter-circle curved extrusion of a Clark Y airfoil was used. There are two available geometry cases built into the VLM_{MW}: the CYKG case, a thickness-free model of the wing where vorticity is discretized purely on the camberline; and the CYKW case, a fully wrapped wing, where vorticity is discretized over the full surface of the Clark Y wing.

Both Leloup [105] and Maneia [120] used this thick-and-arced wing as test geometries for their kite-modelling work. Leloup's results are from a viscous 3D lifting line model: vorticity discretized at the quarter-chord of the wing, and a fixed wake shape. In Leloup's 3D LLT model, pressure distributions are determined by viscous XFOIL boundary-layer coupling, applied in a viscous angle-of-attack correction method. Maneia uses the RANS solver of STAR-CCM+ with a Spalart-Allmaras turbulence model. Leloup and Maneia use a Reynolds number of $3 \cdot 10^6$.

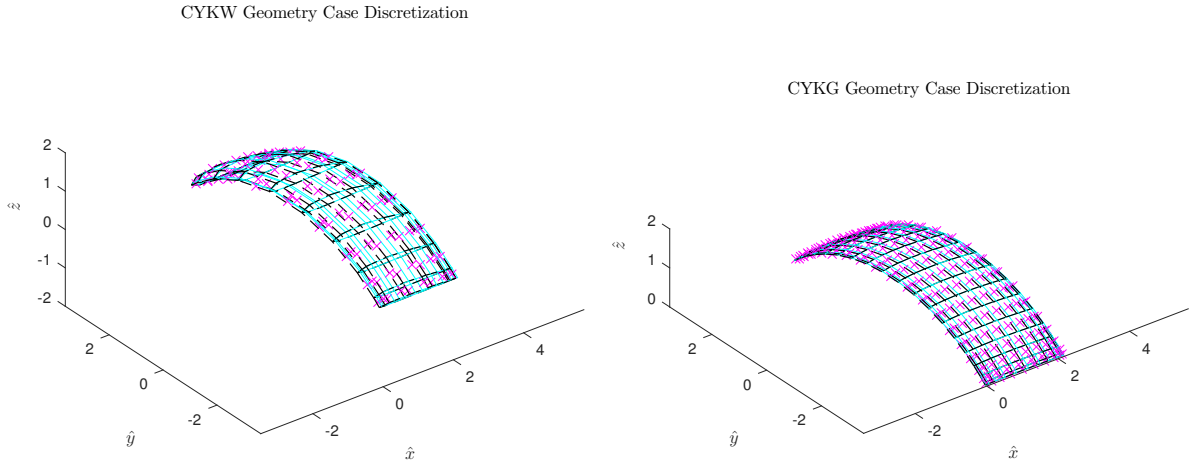

(a) Example of the fully-wrapped finite-thickness CYKW geometry

(b) Example of the camber-line thickness-free CYKG geometry.

Figure 4.13: The arc-shaped Clark Y extruded wing geometries.

It is important to remember when comparing the results of the VLM_{MW} to the Leloup and Maneia data-sets that both are found with computational models rather than live experiments. Consequently, we must consider such a comparison to be less of a "validation" and more of a "analysis to determine whether the general trends are equivalent".

4.4.4 Leading-Edge Inflatable Kite (TUDX)

The included LEI kite geometry is the TUDX[4] geometry case, based on Deaves' [51] representation of the TUD-25mV2 25m^2 kite. Details of how this geometry is "built" can be found in Appendix A.

Due to the difficulty in extracting separation lines from the pressure plots presented by Deaves, due mainly to the graph perspective for the suction-surface, and the fact that the pressure-surface separation point is within the area smoothed in Deaves' profile representation (described below, see Figure 4.15), separation[5] is assumed to occur where the free-stream flow is tangent to the surface. There are three reasons for this assumption, despite it not making full use of Deaves' work:

- First, the collection of flow visualizations presented in van Dyke [181] for flow separation around bluff bodies indicates that increasing Reynolds number drives the separation location to this freestream-surface-tangent point. The LEI tube is such a cylindrical bluff body, and it would appear logical the experimental flow results might be applicable here.
- Second, it is important to the methodology that the initialization of the separation-surface wake nodes place these nodes on the correct side of the geometry, with respect to their separation locations. Since the initial convection of the wake nodes is only due to the free-stream velocity, with the selection of the separation line as the line of freestream-surface-tangent points it becomes much more difficult for the separation-surface initialization method to seriously misplace the wake nodes. The requirements of this initial convection are described in some further detail in Section 5.5.2.
- Third, it would appear to be better - from a physical understanding - to model the separation point too early on the chord than too late. If a line before the true separation-line is chosen, the theoretical fluid element that leaves from the selected line would physically convect itself close to the surface until the true separation-line actually occurs, at which point it would separate from the surface. However, if the selected line is after the true separation-line, then the fluid element which leaves from the selected line would - physically-speaking - already be caught in the recirculation area behind the separation line, and might well never end up convecting along the separation surface. Since the freestream-surface-tangent line is farther towards the leading edge than (by inspection) the separation lines given by Deaves, it appears that the selection of the freesteam-surface-tangent line as a separation line is a conservative option.

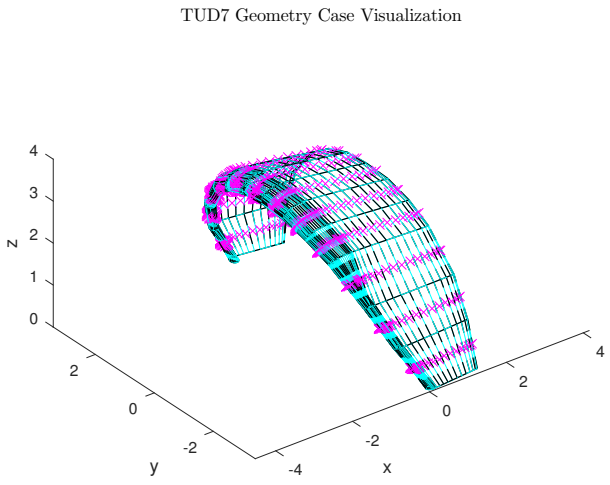

Figure 4.14: Example of a TUDX geometry, with separation lines assumed to be where the freestream flow is tangent to the surface at $\alpha = 0^o$, $N_B = 13$, and $N_P = N_L = 30$.

[4]The TUD7 case is a special sub-geometry of the TUDX case, where no interpolation is needed in the span-wise direction to generate the geometric mesh, because $N_B = 13$ is consistent with the Surfplan datafile generated by Deaves.

[5]unless explicitly mentioned to be otherwise, as in Figure 4.6

Deaves [51] uses a Semi-Implicit Method for Pressure Linked Equations in OpenFOAM to solve the RANS equations for steady-state flow over half of the V2 kite. He uses a Menter SST turbulence model due to its suitability to flow with adverse pressure gradients, and assumes a fully turbulent field. The Reynolds number at which these results are found is not specified for the LEI kite, but is assumed to be $3 \cdot 10^6$ as continued from his validation test-cases. The tested angle-of-attack domain is from -6^o to 24^o.

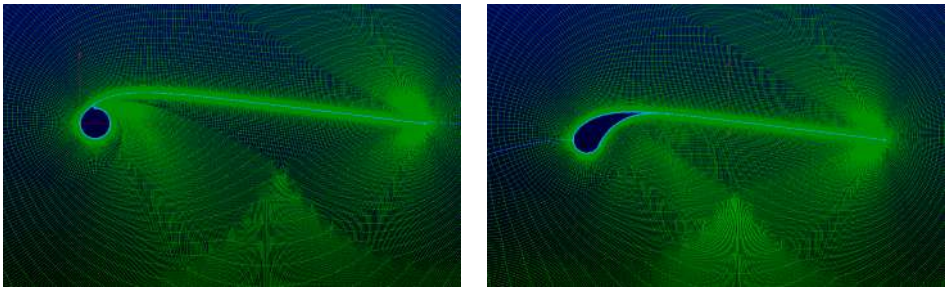

(a) Deaves' "Tight" LEI profile. (b) Deaves' "Filled" profile.

Figure 4.15: "Tight" vs. "Filled" LEI profiles, and their meshes used by Deaves [51].

It should be mentioned that Deaves uses both the physical LEI geometry, as well as a smoothed "filled-in" profile which has no sharp concave corners. The difference between the profiles can be seen in Figure 4.15. Deaves suggests that the net aerodynamic coefficients for both geometries are within ten percent of each other between 0^o and 30^o, but the relationship is irregular and does not lend itself to a great deal of confidence in curve-fitting above 15^o (See Figure 4.16). Consequently, the comparison data-set used further along is that data set which Deaves explicitly gives: that of the "filled" geometry.

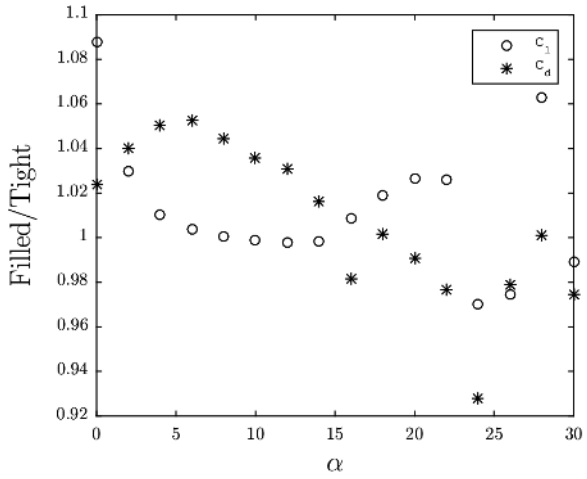

Figure 4.16: Difference-polar between the net aerodynamic coefficients found from a RANS solution for a LEI kite of "tight" and "filled" profiles. [51].

One additional comment with respect to the comparison of steady flow results against Deaves' aerodynamic coefficients: Deaves normalizes his coefficients using the flat area of the kite as the characteristic area. This is a good choice given the deformation of the kite in unsteady situations. As previously mentioned, the VLM_{MW} normalizes the aerodynamic coefficients with the projected area of the kite. The TUD-25mV2 has a flat area of 25m^2 and a projected area of 16.718m^2. Any comparison between Deaves' results and results generated with the VLM_{MW} must correct for this significant normalization difference.

Again, we need to keep in mind that steady-state RANS in a situation with significant separation [92] is already an approximation to the "true" flow solution, such that it would be methodologically inaccurate to speak of "validating" the VLM_{MW} results against RANS results. Instead, we will "compare" the two, with the understanding that steady RANS is - in the case of kite geometries - the closest to a "true" solution we have now and are likely to have in the near future. If, at some point, there becomes available a set of LES results or wind tunnel results where both wall-effects and scaling-difficulties are minimized, they could then be used to properly validate this model for LEI kite-flow.

Chapter 5

Implementation of a Multiple-Wake Vortex Lattice Method

5.1 The Vortex as Discretized Vorticity

Vortex methods arise from discretizing the flow vorticity - the representation of the angular momentum of a fluid element within the flow, and defined mathematically as $\boldsymbol{\omega} := \nabla \times \mathbf{u}$ - into distinct containers called vortices. In a phrasing heavily influenced by Wu et al [199], we define[1] a vortex as *a connected, tube-shaped fluid region with a relatively high concentration of vorticity in comparison to an external flow with a relatively low concentration of vorticity.* Because a vortex is a container for the discretized representation of the flow rotation, the vortex has the property of "inducing" rotation in the flow field, in a vague analogy with the ability of a current-carrying wire to induce a rotational velocity on charged particles within its magnetic field. Stated another way, the vortex induces a tangential velocity jump between the flow to one side of the vortex and the flow on the opposite side of the vortex.

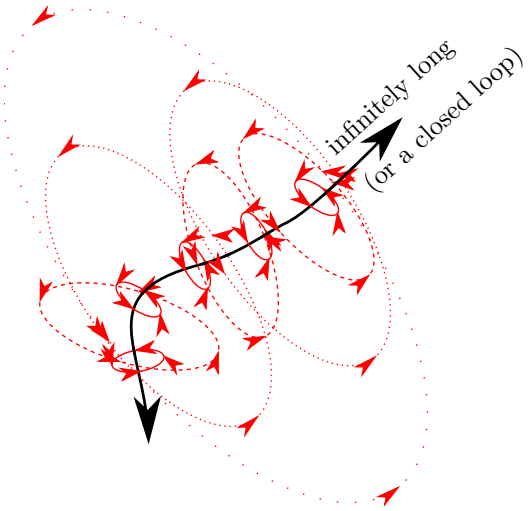

Figure 5.1: The vortex (black) and its induced velocity (red), decreasing in magnitude as the distance from the vortex increases.

[1] For a detailed description of the difficulty in creating a quantitative definition of a vortex, and the criteria for identifying a vortex in "real-life" as opposed to modelled and highly idealized flows, the reader is referred to Section 6.6 of Wu et al [199].

The following derivation for the induced velocity is abbreviated from that suggested by de Oliveira [50], where the process of reaching the Poisson equation for vorticity follows Howe [89], and the Biot-Savart solution follows Katz & Plotkin [98].

Let us decompose a three-dimensional flow-field velocity into a scalar and a vector potential, as must be possible according to Helmholtz's Theorem:

$$\mathbf{u} = -\nabla\varphi + \nabla \times \boldsymbol{\psi}$$

If the flow is incompressible, then continuity holds that $\nabla \cdot \mathbf{u} = 0$. The continuity equation can then be re-written:

$$\nabla \cdot (-\nabla\varphi + \nabla \times \boldsymbol{\psi}) = 0$$

By the distributive property, and the mathematical identity that the divergence of a gradient is zero, this reduces to:

$$\nabla^2\varphi = 0$$

For homogeneous boundary conditions - that is, an inviscid flow without mechanical work being done on or by the flow - the scalar $\nabla\varphi$ is equivalent to the freestream, such that:

$$\mathbf{u} = \mathbf{U}_\infty + \nabla \times \boldsymbol{\psi}$$

As a convenience within this quasi-steady aerodynamic model, the kite apparent velocity can be treated as an effective freestream velocity.

$$\mathbf{u} = \mathbf{U}_A + \nabla \times \boldsymbol{\psi}$$

We can again use Helmholtz decomposition on $\boldsymbol{\psi}$, and the rule that the curl of a gradient is zero:

$$\mathbf{u} = \mathbf{U}_A + \nabla \times \boldsymbol{\psi} = \mathbf{U}_A + \nabla \times (-\nabla\varphi_\psi + \nabla \times \boldsymbol{\psi}_\psi) = \mathbf{U}_A + \nabla \times \nabla \times \boldsymbol{\psi}_\psi$$

Combining the above two statements:

$$\boldsymbol{\psi} = \nabla \times \boldsymbol{\psi}_\psi$$

Because the derivative of a constant is zero, if we take the curl of the velocity:

$$\boldsymbol{\omega} = \nabla \times \nabla \times \boldsymbol{\psi} = \nabla\left(\nabla \cdot \boldsymbol{\psi}\right) - \nabla^2\boldsymbol{\psi}$$

Then, because the divergence of a curl is zero, we end up with a Poisson equation.[2]

$$\boldsymbol{\omega} = \nabla\left(\nabla \cdot \nabla \times \boldsymbol{\psi}_\psi\right) - \nabla^2\boldsymbol{\psi} = -\nabla^2\boldsymbol{\psi}$$

It follows that the vorticity is a Poisson equation, for which three things are known:
1. The solution to a Poisson equation is a Green function.
2. The solution exists.
3. The solution is unique for a particular set of boundary conditions.

The 3D Green function for the Laplacian - a linear differential operator - is:

$$G(\mathbf{x} - \mathbf{x}_0) = \frac{1}{4\pi}\frac{1}{|\mathbf{x} - \mathbf{x}_0|}$$

where $\mathbf{x}_0$ is the infinitesimal point where vorticity is generated. Then, we can integrate over our field V to find the vector field $\boldsymbol{\psi}$:

$$\boldsymbol{\psi} = \int_V G(\mathbf{x} - \mathbf{x}_0)\boldsymbol{\omega} dV$$

We can then retrieve our velocity field from the apparent velocity and the vector potential:

$$\mathbf{u} = \mathbf{U}_A + \int_V \nabla \times G(\mathbf{x} - \mathbf{x}_0)\boldsymbol{\omega} dV$$

[2] As an aside, you could also reach this point by skipping the Helmholtz decomposition step, and directly assuming the existence of a vector potential that satisfies $\mathbf{u} = \nabla \times \boldsymbol{\psi}$. This is the process given in Section 2.11 of Katz & Plotkin. [98]

Let's pause to define a scalar[3] quantity Γ called "circulation" as the flux of vorticity through some area S:

$$\Gamma = \int_S \boldsymbol{\omega} \cdot dS$$

For an infinitesimal volume - determined by the expanding the infinitesimal normal area along the infinitesimally-short vector pointing along the vorticity vector at some point, that is: $dV = dS\ dl$ - we can rewrite the argument of the integral:

$$\nabla \times \frac{1}{4\pi} \frac{\boldsymbol{\omega}}{|\mathbf{x} - \mathbf{x}_0|} dV = \frac{1}{4\pi} \nabla \times \Gamma \frac{\mathbf{dl}}{|\mathbf{x} - \mathbf{x}_0|}$$

If we carry out this vector differentiation with $\mathbf{dl}$, $\mathbf{x}_0$ and - due to Helmholtz's circulation conservation along a given vortex - Γ constant:

$$\frac{1}{4\pi} \nabla \times \Gamma \frac{\mathbf{dl}}{|\mathbf{x} - \mathbf{x}_0|} = \frac{\Gamma}{4\pi} \frac{\mathbf{dl} \times (\mathbf{x} - \mathbf{x}_0)}{|\mathbf{x} - \mathbf{x}_0|^3}$$

Consequently, we find the velocity field:

$$\mathbf{u} = \mathbf{U}_A + \frac{\Gamma}{4\pi} \int \frac{\mathbf{dl} \times (\mathbf{x} - \mathbf{x}_0)}{|\mathbf{x} - \mathbf{x}_0|^3}$$

That is, our solution is the sum of a uniform flow field $\mathbf{U}_A$ and a particular solution dependent on a certain Γ value and a certain vortex location $\mathbf{x}_0$. As already stated, the Poisson equation is linear, so we can assemble any flow field as the superposition of the uniform flow and the sum of particular solutions, by correctly placing vortices corresponding to certain circulation values at certain discrete locations within the field.

The vortex lattice method adheres quadrilateral, straight-edged, not-necessarily-planar, closed (for Helmholtz's Second Theorem) vortex rings, each with constant circulation strength (for Kelvin's Circulation Theorem) to the geometric body in the flow. Vortex rings, with circulation and dimensions consistent with the assumption of steady flow, are modelled as having been convected to locations downstream at times prior to the "time-snapshot" that our steady model represent.

Section 5.2 describes the placement of those vortices found - at the current "snapshot" in time - on the geometric body in the flow. Section 5.3 describes the relationship between the circulation strength of the vortices within the modelled volume and the placement of those vortices who have already been convected away from the body. Section 5.4 then describes the solution method to ensure that the chosen circulation strengths and vortex placements do describe the flow about the geometry in question.

5.2 Geometry Discretization and Grid Generation

If we look microscopically at the surface of a body in a flow, we see that the imperfections in the surface - even down to a molecular scale - impede the motion of the fluid directly next to it. This is the basis for the observation that there is "no-slip" - no tangential velocity - immediately on the surface. That is, the surface of the geometry causes a sharp growth in the tangential velocity of the flow within the boundary layer.

If the boundary layer is thin, we could approximate the situation to say that there is a tangential velocity jump on the surface itself. Being as tangential velocity jumps are the inherent effect of a discrete vortex placement, we could represent the surface in the flow by placing a collection of vortices immediately onto it. If our surface is very thin - practically "thickness-free" - we can ignore the fact that there is a boundary layer on both the suction and pressure surface, and combine both into a single surface onto which vortices are placed.

[3]It can occasionally be handy to speak of a circulation vector $\underline{\boldsymbol{\Gamma}}$, but this is actually the product of the circulation scalar and the unit vector pointing along the vorticity vector $\underline{\boldsymbol{\Gamma}} := \Gamma\ \hat{\boldsymbol{\omega}}$. This combination vector should not be confused with the geometric-matrix and column-matrix-rearrangement of scalars - which we will write as, respectively, $\boldsymbol{\Gamma}$ and $\tilde{\boldsymbol{\Gamma}}$ - that store the scalar circulation strengths according to their geographical location in the programmed "universe".

Because the vortex is a discretization of a quantity that is associated with angular momentum - a conserved quantity in a flow assumed to be inviscid - we know that the vortex must be either infinitely[4] long, or a closed loop. It is conceptually more intuitive[5] to see the relationship between vortex strength and force-distribution on a surface if the surface is covered in small vortex-rings - like quadrilateral doughnuts whose edges have merged while being fried close to one another - than if the surface is covered in large vortex-rings, each one with one edge placed "infinitely-far" downstream. Both methods of describing a vortex lattice are equivalent in terms of the ultimate flow superposition, but it is the former which will here be used.

5.2.1 Determine the Bound Vortex Lattice Nodes

The placement of the vortex in a geometric panel represents the location where the true-solution flow vorticity is integrated and discretized with the Green function integral Dirac delta.

Vortex lattice methods typically lay their bound vortex lattice over the geometric mesh in one of two ways, mostly concerning the location of the first vortex ring leading edge.

Quarter-Chord Overlaying

The quadrilateral bound vortex-ring has each corner at a neighboring vortex lattice node. The vortex filaments in the chord-wise direction lie on the the geometry panel edges. The vortex filaments in the span-wise direction lie one quarter of the way down the panel-edges. The placement of the vortex lattice nodes that define a vortex ring's corners, defined on an arbitrary 3D surface, is graphically explained in Figure 5.2.

This location can be determined intuitively by considering that the vortex is that conceptual structure which causes lift, that aerodynamic forces on a real airfoil are summed at the center of pressure c_p to balance the aerodynamic moment, and that a thin airfoil has its c_p at the quarter-chord location.

For the geometric panel bound by the geometric meshpoints $\mathbf{x}_{LENE}$, $\mathbf{x}_{LEPE}$, $\mathbf{x}_{TEPE}$, and $\mathbf{x}_{TENE}$ as in Figure 5.2, the quarter panel-length position on the y-negative side is at

$$\mathbf{x} = \mathbf{x}_{LENE} + \frac{1}{4}\left(\mathbf{x}_{TENE} - \mathbf{x}_{LENE}\right)$$

and the same pattern is true for the y-positive side.

Then, the chord-wise filaments of the vortex ring will pass between the quarter panel-length position of one panel to the next.

This method is very well suited to thin (or thickness-free) wings, and - for a correct collocation point placement - automatically ensures that the flow leaves the trailing edge smoothly.

Co-incidental Overlaying

In the case of co-incidental overlaying, the bound vortex lattice coincides exactly with the geometric mesh. This can be seen in Figure 5.3.

With co-incidental overlaying, we lose the automatic placement of the leading-edge filament of a single vortex ring placed onto a rectangular, thin, symmetrical wing at the quarter-chord location. However, this method of discretizing the surface vorticity allows us to join the vortex lattice at the trailing edge with a clean connection, without the overhang of the suction-surface trailing edge over the pressure-surface trailing edge. Consequently, co-incidental overlaying is typically more appropriate for wrapped finite-thickness bodies.

[4] Anything which is truly infinite in length is difficult to model numerically, so those vortices which we might like to model as infinitely-long can be considered loops which close so far away from the body that the distance is practically "infinite" in the modelling universe. That is, there is a computational difference between an infinite-length vortex and a vortex ring which closes "infinitely-far" downstream, but the physical difference is very, very small.

[5] in the author's opinion

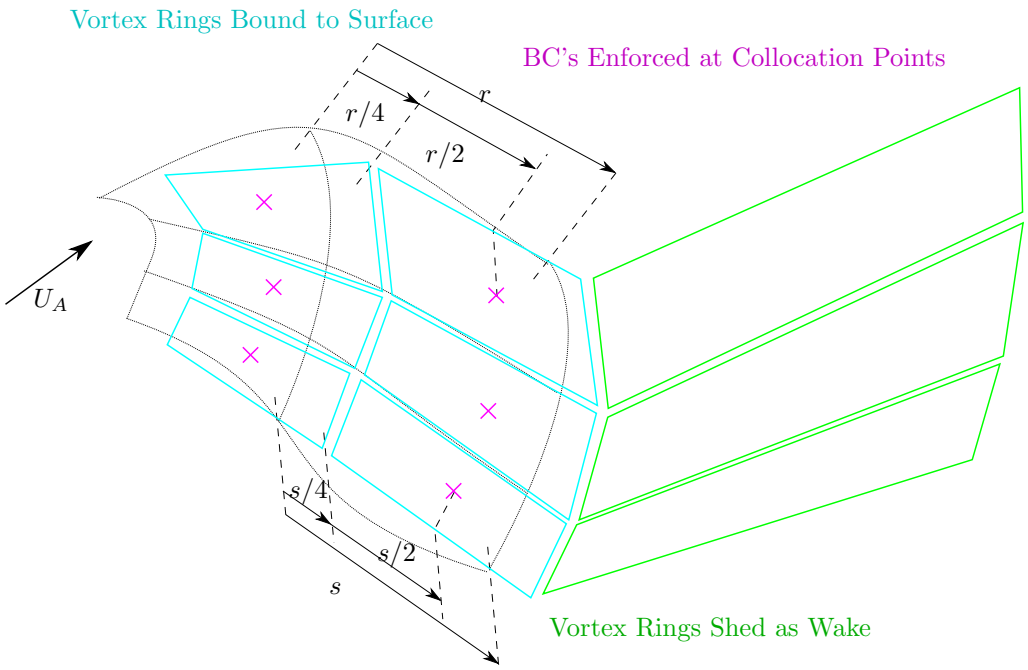

Figure 5.2: A sketch of the Quarter-Chord Overlay of Bound Vortex Node Locations found on an Arbitrary 3D Surface: dotted black is the presumed true surface, cyan is the bound vortex lattice, and magenta are the collocation points.

Because a LEI kite has both finite-thickness and thickness-free sections, it is more appropriate to use co-incidental overlaying than quarter-chord overlaying. Unless otherwise specified, this is the overlaying method used from here on.

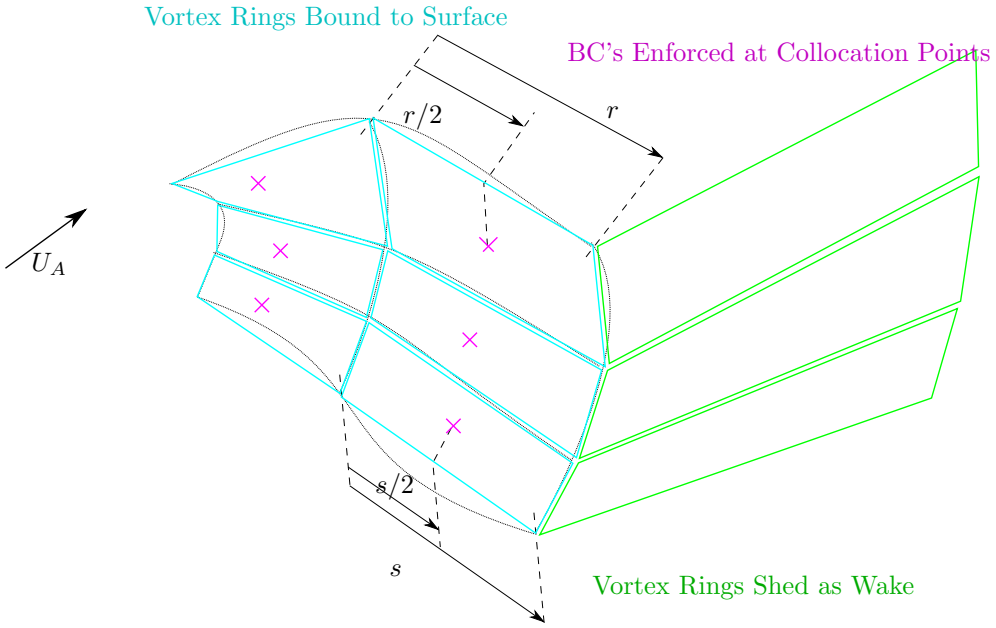

Figure 5.3: A sketch of a Co-incidental Overlay of Bound Vortex Node Locations found on an Arbitrary 3D Surface: dotted black is the presumed true surface, cyan is the bound vortex lattice, and magenta are the collocation points.

5.2.2 Determine the Collocation Points

The collocation point (CP) is the location where the problem boundary conditions are enforced. In the standard case, this is that the body represented is impermeable - that the velocity of the body must be the same as the velocity of the flow, determined as the sum of the free-stream and induced velocities.

Because the enforcement of the boundary conditions - described further along in Section 5.4 - gives us the N_J equations to which there are N_Γ unknowns, each the strength of one bound vortex ring, our ability to find a solution requires that there be as many collocation points as there are bound vortices.

It is standard for panel methods to place the collocation points at the centers of the vortex rings. This is because the enforcement of the Kutta Condition - the boundary condition that the flow along the pressure- and suction-surfaces must be equivalent and purely tangential at the trailing edge - for a 2D flat plate with quarter-chord overlaying of a single vortex ring requires that the collocation point be placed three-quarters-chord down the flat plate.

Again, referring to the sketch in Figure 5.3, the collocation point is placed at the midpoint between two helping edge points:

$$\begin{aligned} \mathbf{x}_j &= \frac{1}{2}\left(\mathbf{x}_{j,NE} + \mathbf{x}_{j,PE}\right) \\ \mathbf{x}_{j,NE} &= \mathbf{x}_{LENE} + \frac{1}{2}\left(\mathbf{x}_{TENE} - \mathbf{x}_{LENE}\right) \\ \mathbf{x}_{j,PE} &= \mathbf{x}_{LEPE} + \frac{1}{2}\left(\mathbf{x}_{TEPE} - \mathbf{x}_{LEPE}\right) \end{aligned}$$

5.2.3 Determine the Surface Velocity at the Collocation Points

The surface velocity at the collocation points is a similar average of the surface velocities defined at the geometric meshpoints.

$$\begin{aligned} \mathbf{U}_{m,j} &= \frac{1}{2}\left(\mathbf{U}_{m,NE} + \mathbf{U}_{m,PE}\right) \\ \mathbf{U}_{m,NE} &= \mathbf{U}_{m,g}(\mathbf{x}_{LENE}) + \frac{1}{2}\left(\mathbf{U}_{m,g}(\mathbf{x}_{TENE}) - \mathbf{U}_{m,g}(\mathbf{x}_{LENE})\right) \\ \mathbf{U}_{m,PE} &= \mathbf{U}_{m,g}(\mathbf{x}_{LEPE}) + \frac{1}{2}\left(\mathbf{U}_{m,g}(\mathbf{x}_{TEPE}) - \mathbf{U}_{m,g}(\mathbf{x}_{LEPE})\right) \end{aligned}$$

5.3 The Dynamics of a Vortex Lattice

It is the circulation strength of a vortex ring which determines the magnitude of the velocity induced by the ring's filaments, just as it is the location of the vortex ring corner-nodes which determine the direction of the induced velocity. With a guessed circulation distribution over the bound vortex lattice, we can then predict the strength and shape of the wake, and the flow field everywhere within the modelled "universe".

5.3.1 Bound Circulation Initialization

The initial circulation is chosen to produce a guessed span-wise-section lift distribution using Kutta-Joukowski:

$$c_l = \frac{2\Gamma_{0,(n_b,\Sigma)}}{U_A c \Delta b}$$

where c_l is the 2D lift coefficient at the spanwise-section, $\Gamma_{0,(n_b,\Sigma)}$ is the initial bound circulation for the row of bound vortex loops within the spanwise-section, and Δb is the width of the spanwise-section.

It is assumed that the initial span-wise-section circulation $\Gamma_{0,(n_b,\Sigma)}$ is then distributed over the chord-wise bound vortex loops according to some simple distribution method to find the initial circulations of all of the bound vortex loops $\Gamma_{0,(n_b,n_c)}$:

$$\sum_{n_c}^{1\rightarrow(N_C-1)} \Gamma_{0,(n_b,n_c)}\Delta c = \Gamma_{0,(n_b,\Sigma)}c$$

where Δc is the chord-wise length of the vortex loop. The simplest method is to assume that the vortex loops within a span-wise-section have an initial circulation distributed according to their chord-wise length, such as:

$$\Gamma_{0,(n_b,n_c)} = \Gamma_{0,(n_b,\Sigma)}\frac{c}{\Delta c}$$

The initial span-wise-section 2D lift coefficient can be taken from any aerodynamic model that generates such c_l values. As a simple - consequently fast - example, the 2D lift coefficient can be generated by assuming a uniform force distribution of the 3D lift coefficient measured by Ruppert [153] for power kite operation to approximate $c_l \approx C_L$.

5.3.2 The Kutta Condition and Wake Circulation Strength

Up until this point, we have mainly discussed the circulation strength Γ as a property of a given vortex ring, rather than the net circulation strength Γ_F at any given location on the geometry.

Due to the property of superposition, we know that the vortex-strengths of co-incidental vortex filaments is summed. This summation is simple, as long as there is no difference in vortex core size between the two filaments[6], as is the case on our bound vortex lattice.

Consequently, when we need to consider the net circulation strength at a given location, we use vector addition of the vectors created by multiplying the filament strength and filament direction.

When a given line-segment in space only ever contains filaments from two vortex rings - as is the case for a thickness-free geometry without separation - we can determine the net circulation by subtracting the strength of that filament which points from the ring positive-edge to the negative-edge, from the strength of that filament which points from the ring negative-edge to the positive-edge. Said another way: to evaluate the net circulation experienced at any vortex lattice node requires the difference between the circulation of the loop for which the node is on the leading edge, and the loop for which the node is on the trailing edge. That is, travelling chord-wise from $n_c = 1$ to $n_c = N_C - 1$:

$$\Gamma_F(n_c) = \begin{cases} \Gamma(n_c) & : n_c = 1 \\ \Gamma(n_c) - \Gamma(n_c - 1) & : 2 \leq n_c \leq N_C - 1 \end{cases}$$

Implicit in this definition is the fact that - because we defined the core-radius-size of the first wake panel to be equivalent to the core-radius-size of the trailing-edge bound panel - the net circulation strength at the trailing edge is also such a summation:

$$\Gamma_F(N_C) = \Gamma_w(1) - \Gamma(N_C - 1)$$

[6] It is unfortunately less simple when the vortex core radius differs between the two vortex filaments, such that we cannot simply cancel out the effects of all of the interior wake vortex filaments, and must still compute their respective Biot-Savart inductions.

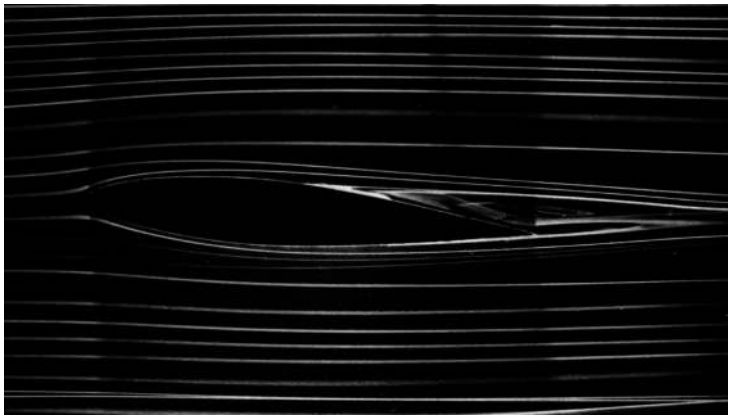

Figure 5.4: Flow at Reynolds number 7000 over a 2D NACA 64A015 airfoil at 5^o angle of attack demonstrates smooth separation in the tangential direction of the flow at the separation point on the suction surface, and at the trailing edge. Reproduced from van Dyke [181].

It is with this trailing-edge circulation that we are able to enforce the Kutta condition at the separation location, which requires that the flow separate "smoothly." What this "smoothness" criteria means, in effect, is that there cannot be a tangential-velocity jump in the flow before and after, or above and below in the case of trailing edge separation, the separation location. That is, the flow at a separation point doesn't rotate around the separation point. We can intuitively-speaking convince ourselves that the Kutta condition has a physical basis[7] by admiring how flow always leaves tangentially to the separation locations in photos[8] of fluid motion. See Figure 5.4 for an example. Since a vortex is by definition an instantaneous tangential velocity-jump, we know that the net circulation strength at the separation location must be zero.

Enforcement of the Kutta condition on a thickness-free geometry then requires that $\Gamma_F(N_C) = 0$. This constraint on our net circulation strength can be re-formulated as a constraint on our wake vortex strength:

$$\Gamma_w(1) = \Gamma(N_C - 1)$$

Of course, since this is a steady, inviscid and incompressible simulation with conservative forces[9], Helmholtz's Third Theorem says that the vortex strength must be equivalent for all of the vortex rings shed from a certain separation location. Consequently, row of trailing vortex loops behind a given separation bound-vortex loop have the same circulation strength:

$$\Gamma_w(n_b, n_w) = \Gamma(n_b, N_C - 1)$$

In the case that we have more than two vortex rings with filaments sharing the same space - as is the case for separation from a thick trailing edge (or from the surface-interior), we need to re-consider the vector-summation method that determines the net circulation strength. This is sketched in Figure 5.6.

Net Circulation at the Intersection of a Finite-Thickness and Thickness-Free Geometry

One further comment concerning the determination of the net circulation strength for an LEI geometry: the intersection point between the LEI-tube and the canopy contains three vortex filaments, two of which are leading-edge filaments. Since it is important that we not double-count the circulation at this intersection point, it would be reasonable to place all of the net circulation on the suction-surface index ($n_c = N_{Intersect}$), and none of the net circulation on the pressure-surface index ($n_c = 1$). This assignment is sketched in Figure 5.7.

[7] In addition to the numerical basis in which the Kutta condition gives one additional boundary condition for the additional unknown of the separated wake circulation strength.

[8] Van Dyke's Album of Fluid Motion [181] is strongly recommended for this purpose.

[9] At least, for the inviscid model to which the flat-plate drag correction has not yet been added, as we as describing now.

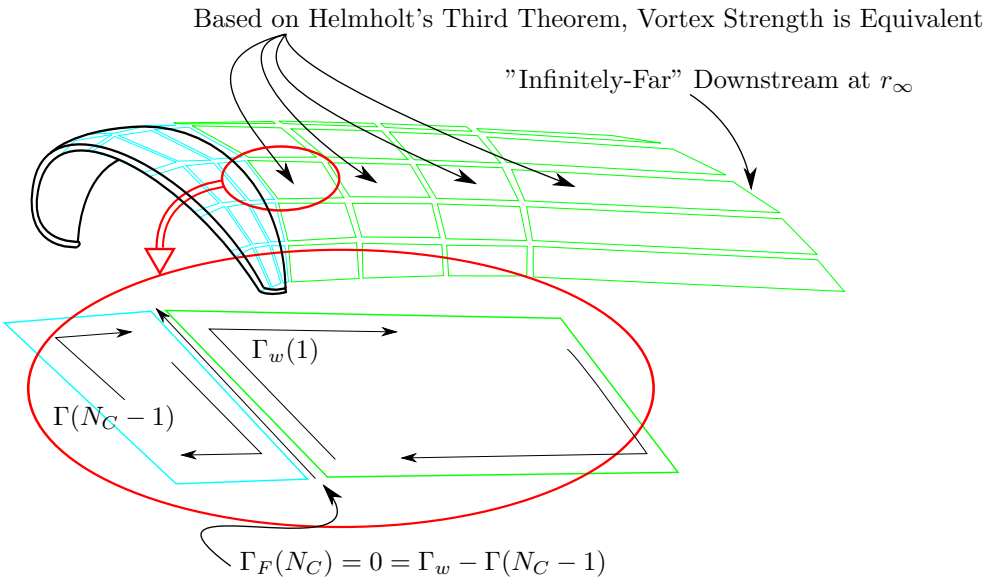

Figure 5.5: A concept sketch demonstrating the Kutta condition at the trailing edge of the thickness-free canopied LEI kite, and the resulting wake circulation strength.

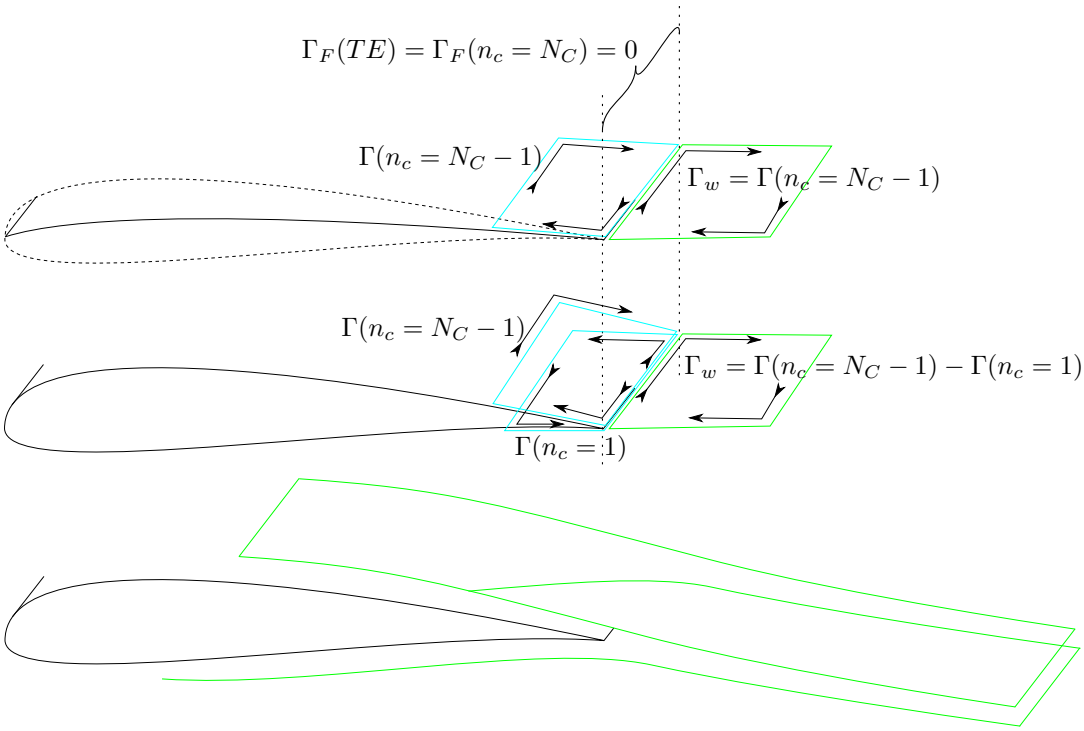

Figure 5.6: The Kutta condition and net circulation summation for smooth separation at the trailing edge.

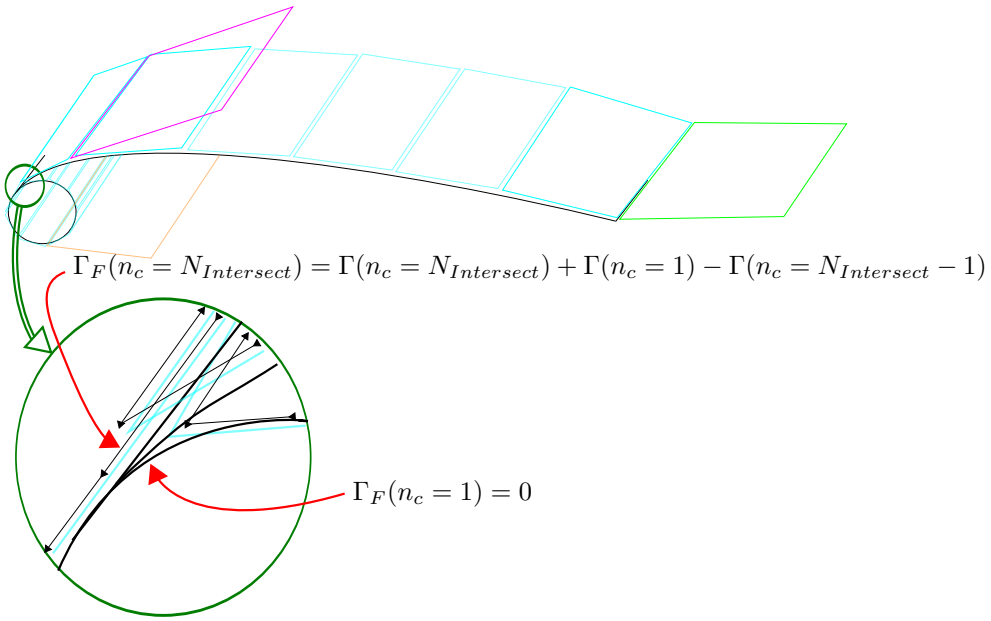

Figure 5.7: Net circulation at the intersection of a finite-thickness and thickness-free geometry.

5.3.3 Wake Relaxation into Free-Wake and Fixed-Wake Regions

To limit the computation required, the wake nodes are freed only up to a certain threshold distance from the trailing edge r_w. Within the free-wake region, the nodes are convected by the total experienced velocity - the sum of velocities induced by the vortex lattice and the the apparent velocity at the node location. Outside of the free-wake region - that is, in the fixed-wake region - the nodes are assumed to convect from their neighboring upstream node according to the kite apparent velocity.

As a first-order estimate, the free-wake in the kite-flow problem could be reasonably fixed at about 5.6 chord lengths - or 15m - downstream from the trailing edge. From Kutta-Joukowski and a 3D lift-coefficient $C_{L,max} = 0.7$:

$$L' = |\rho_{air} U_A \Gamma| \approx \frac{(1/2) C_L \rho_{air} U_A^2 A}{b}$$

This statement can be solved for an estimate of the circulation Γ:

$$\Gamma \approx \frac{C_L U_A c}{2}$$

Applying the 2D Biot-Savart:

$$U_{i,\theta}^{2D} = \frac{\Gamma}{2\pi r_w}$$

When the induced velocity is assumed to be less than $p_v = 0.01 = 1$ percent of the apparent velocity ($U_{i,\theta}^{2D} = p_v U_A$), then the influence range of a vortex - expressed in chord-lengths - is:

$$\frac{r_w}{c} \approx \frac{C_L}{4\pi p_v} \approx 5.57$$

The vortex rings extend to a length "infinitely-far downstream" from the kite. For computational purposes, this "infinite" length must be set as some finite value. Sequeira et al suggest this "infinite" length r_∞ be set to 40 chord lengths [159].

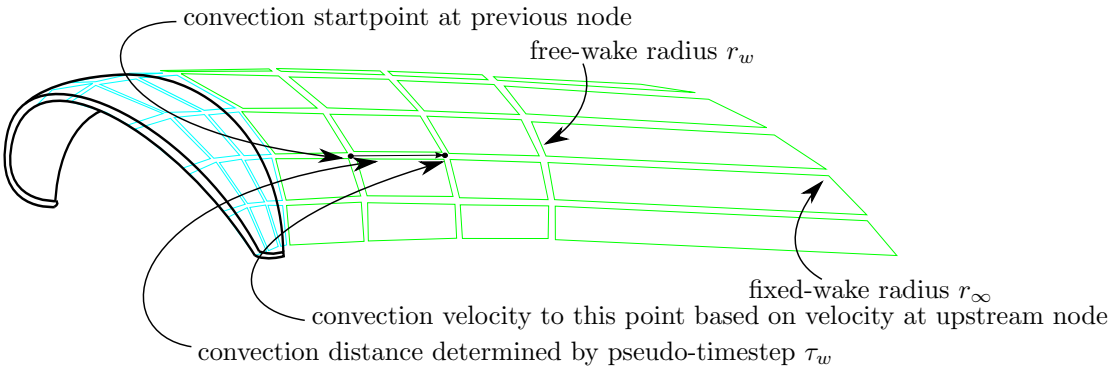

Figure 5.8: A concept sketch of the convection of a free-wake vortex lattice node

5.3.4 Wake Convection

A wake vortex lattice node is convected downstream from the wake node immediately upstream; the velocity with which it is convected is the total velocity at the upstream location node. Within the solver, this requires iteration until the induced velocity at the node locations convects the node to that particular location. As an initialization step, all of the vortex node locations experience no induced velocity, only the global apparent velocity.

The downstream distance between the wake nodes is dependent on a user-dependent pseudo-timestep τ_w. This pseudo-timestep designates the time that it would have taken the node to convect to its current position, if the simulation actually experienced time. As the simulation is steady, there is no need for a "true" timestep. This pseudo-timestep is set to allow N_W wake nodes - in the downstream direction - to be placed within the free-wake radius r_w of the chordwise last bound vortex - that is, within the region where the wake shape changes in response to the velocities induced by the vortex lattice.

Where there exists a meaningful free-wake area - that is, $N_W > 1$ such that the wake is not fixed everywhere - the pseudo-timestep can be found:

$$\tau_w = \begin{cases} 0 & n_w = 1 \\ \frac{r_w}{N_W - 1} \frac{1}{||\mathbf{U_A}||} & \text{if } 2 \leq n_w \leq N_W \\ \frac{r_\infty - r_w}{||\mathbf{U_A}||} & \text{if } n_w = N_W + 1 \end{cases}$$

That is, the first node is placed at the separation location - here, the trailing edge; the last node is placed "infinitely-far" downstream, and the intermediate nodes are placed regularly within the free-wake radius.

In comparison, when the wake is fixed everywhere, there is no particular wake discretization - the wake vortex ring begins at the trailing edge of the wing, and extends "infinitely-far" downstream according to the apparent velocity:

$$\tau_{w,\infty} = \frac{r_\infty}{||\mathbf{U}_A||}$$

The convection velocities are determined at the node immediately prior, following the example of Fiddes & Gaydon [66]:

$$\begin{aligned} \mathbf{x}_w(n_b, 1, :) &= \mathbf{x}(n_b, N_C - 1, :) \\ \mathbf{x}_w(n_b, 2 \leq n_w \leq N_W, :) &= \mathbf{x}(n_b, n_w - 1, :) + \tau_w(n_w) \left(\mathbf{U}_{i,w}(n_b, n_w - 1, :) + \mathbf{U}_A\right) \\ \mathbf{x}_w(n_b, N_W + 1, :) &= \mathbf{x}(n_b, N_W, :) + \tau_w(N_W + 1)\mathbf{U}_A \end{aligned}$$

At this "infinitely-far downstream" location, the last vortex ring is closed.

The difference between the convected behavior of a free- and fixed-region can be seen in Figure 5.9.

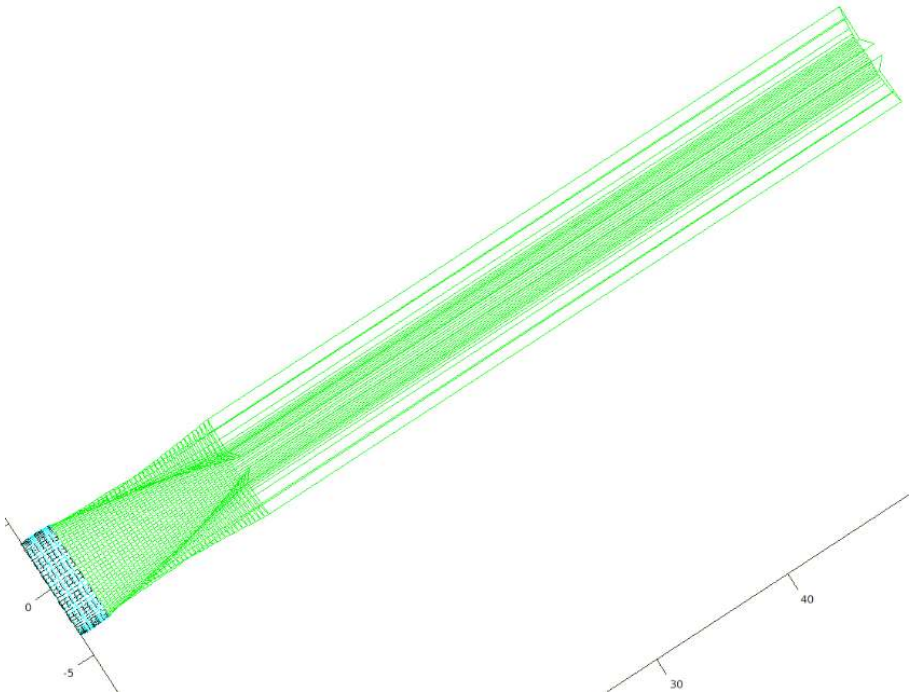

(a) Free- and fixed-wake convection

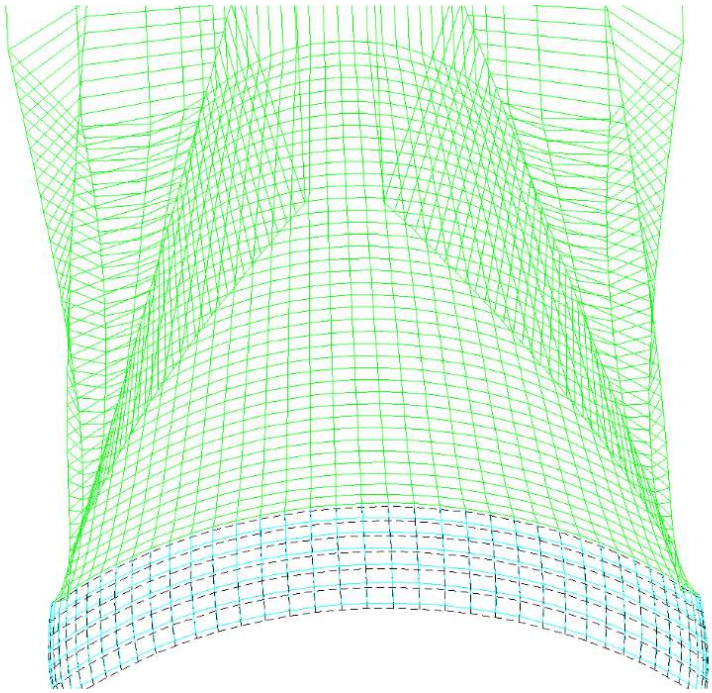

(b) Close-up of the wake roll-up allowed in the free-wake region.

Figure 5.9: The free- and fixed-wake regions in a simulation of the flow over a CYKG wing with quarter-chord vortex-lattice overlaying: $\alpha = 4^o$, $N_B = 40$, $N_C = 8$, $N_W = 40$.

5.3.5 Vortex Models and the Modified Biot-Savart

The standard Biot-Savart expression of the Kernel function induces infinite velocity near the vortex. To eliminate this unphysical result of the vortex representation, the Biot-Savart function can be modified to give finite velocities within some small core-radius r_c of the vortex.

There exist many modified forms of the standard Biot-Savart. Cut-off models simply disregard all induction within $r < r_c$ of the vortex; smoothing models prescribe a decay in the induction within the core radius intended to preserve a desired feature of the flow.

Where the surface distances are small, the choice of which modified Biot-Savart to use can have a large influence on the vortex method solution. Particularly when the scale of relevant distances approaches the core-radius, the decision to use a cut-off vortex model may end up hiding relevant behavior. [182]

Some of the standard choices for vortex smoothing model include:

- The *Rankine Vortex* is the simplest vortex core model, with a discontinuous tangential induced velocity. The tangential induced velocity within the core behaves as a solid rotation, with a linear radial characteristic. [115]

$$U_{i,\theta}^{2D}(r) = \begin{cases} \frac{\Gamma}{2\pi r_c}\frac{r}{r_c} & \text{if } -r_c \leq r \leq r_c \\ \frac{\Gamma}{2\pi r} & \text{otherwise} \end{cases}$$

- The *Lamb-Oseen Vortex* is a solution to the 1D laminar Navier-Stokes equation with the vorticity distributed radially as a Gaussian normal with the peak vortex at r_c. [115]

$$U_{i,\theta}^{2D}(r) = \frac{\Gamma}{2\pi r}\left(1 - \exp\left(-a\left(\frac{r}{r_c}\right)^2\right)\right)$$

- The *Scully Vortex*, also known as a Kaufmann vortex, is a simplification of the Lamb-Oseen vortex. [104]

$$U_{i,\theta}^{2D}(r) = \frac{\Gamma}{2\pi r_c}\frac{r}{(1+r^2)}$$

In order to easily assess the effect of changing the vortex core model, it was determined to use the *Vatistas Core Model*. The Vatistas Core Model (VCM) is the result of a dimensional analysis of the Navier-Stokes z-direction cylindrical coordinate momentum equation; see Vatistas [184] or Leishman [104] for a derivation. In a 3D vector format, modified to prevent divide-by-zero errors, from that used by Sebastian & Lackner [157], the VCM calculates the induced velocity as:

$$\mathbf{U}_i^{3D} = C_\nu \frac{\Gamma}{4\pi}\frac{(|\mathbf{r}_1| + |\mathbf{r}_2|)(\mathbf{r}_1 \times \mathbf{r}_2)}{|\mathbf{r}_1||\mathbf{r}_2|(\epsilon_{OT} + |\mathbf{r}_1||\mathbf{r}_2| + \mathbf{r}_1 \cdot \mathbf{r}_2)}$$

with a divide-by-zero prevention epsilon[10] ϵ_{OT} to avoid singularities when either $\mathbf{r}_1$ or $\mathbf{r}_2$ approaches $\mathbf{0}$, and an introduced effective viscous parameter C_ν that depends on a Vatistas parameter n_{VCM}. Notice that a small vortex core radius causes C_ν to approach 1.

$$C_\nu = \left(\frac{(|\mathbf{L}||\mathbf{r}_1|)^2 - (\mathbf{L}\cdot\mathbf{r}_1)^2}{|\mathbf{L}|^2 + \epsilon_{OT}}\right)\left(r_c^{2n_{VCM}} + \left(\frac{(|\mathbf{L}||\mathbf{r}_1|)^2 - (\mathbf{L}\cdot\mathbf{r}_1)^2}{|\mathbf{L}|^2 + \epsilon_{OT}}\right)^{n_{VCM}}\right)^{-1/n_{VCM}}$$

Here, for $n_{VCM} = 1$, the VCM gives a Scully vortex; for $n_{VCM} = 2$, a Lamb-Oseen vortex; for $n_{VCM} \to \infty$ a Rankine vortex. [201]

[10] Units are [m] or [m^2] as applicable; suggested values are less than the vortex core radius size but greater than 10^{-10} [m] or [m^2]. Values much smaller than 10^{-10} tend to cause asymmetric induction when this divide-by-zero epsilon comes into play. This is a danger during wake-convection near the tips, and when the bound chord-wise resolution becomes very high, as is the case when the modelling of flow separation requires the bunching(See Section 4.2.4) of geometric nodes.

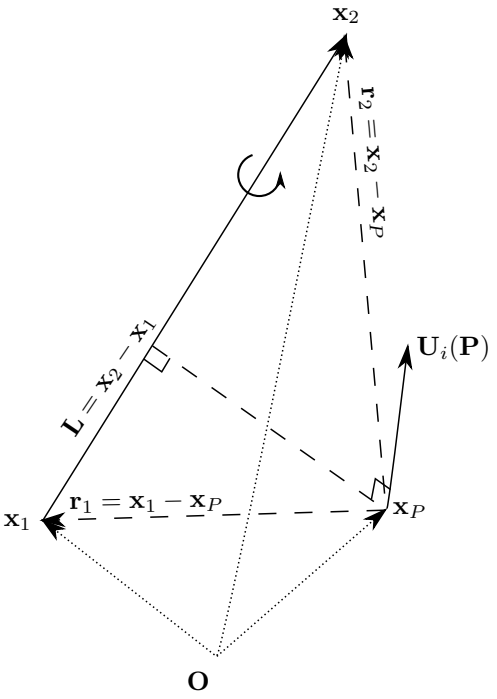

(a) A graphical definition of the vectors involved in the Vatistas Core Model induction calculation.

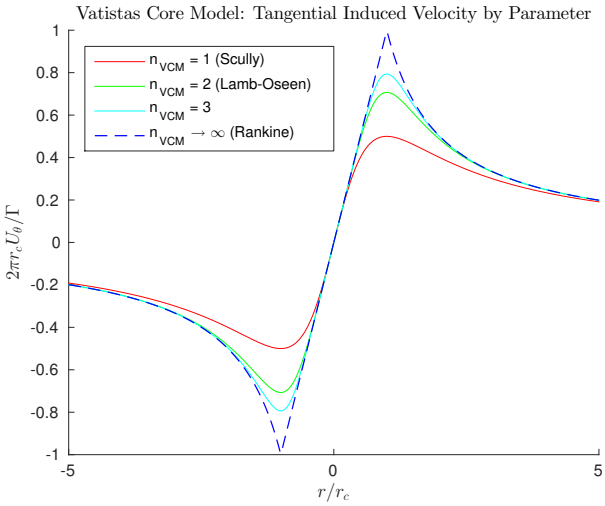

(b) The normalized tangential induced velocity vs. distance from the vortex as determined with the Vatistas Core Model for different parameter n_{VCM} values.

Figure 5.10: The Vatistas Core Model

It should be stated explicitly that the Vatistas core model is only valid for finite, real parameter values $n_{VCM} \geq 1$. For smaller parameter values, the solution experiences singularities. The use of a complex parameter value would distort the circulation within the core. [184] Instead, the VLM_{MW} considers all non-valid parameters (ie, 0) as requests for the implementation of a cut-off vortex model.

In the case that a cut-off vortex model is used, the altitude a_V of the evaluation point from a vortex filament is determined, and used as the condition deciding which induction formula to use:

$$
\begin{aligned}
s_V &= \frac{1}{2}\left(|\mathbf{r}_1| + |\mathbf{r}_2| + |\mathbf{L}|\right) \\
a_V &= 2\frac{\sqrt{s_V\left(s_V - |\mathbf{r}_1|\right)\left(s_V - |\mathbf{r}_2|\right)\left(s_V - |\mathbf{L}|\right)}}{\epsilon_{OT} + |\mathbf{L}|} \\
\mathbf{U}_i^{3D} &= \begin{cases} 0 & \text{if } a_V < r_c \\ \frac{1}{4\pi}\frac{(\mathbf{r}_1 \times \mathbf{r}_2)}{(|\mathbf{r}_1 \times \mathbf{r}_2| + \epsilon_{OT})}\left(\mathbf{L} \cdot \left(\frac{\mathbf{r}_1}{\epsilon_{OT} + |\mathbf{r}_1|} - \frac{\mathbf{r}_2}{\epsilon_{OT} + |\mathbf{r}_2|}\right)\right) & \text{if } a_V \geq r_c \end{cases}
\end{aligned}
$$

5.3.6 Vortex Core Radius

Too large[11] of a vortex radius will cause the circulation strengths to oscillate in sign (see Figure 5.11) as a result of the sharp magnitude and sign-change of the induced velocity within the modelled core.

To prevent this oscillation, the vortex core radius should be set as small as possible. There is a practical limit, however, given by unpredictable rounding errors occurring when $r_c^{2n_{VCM}}$ is small; it is strongly suggested that values of r_c less than 10^{-10} be avoided.

[11] Note that the vortex particle method convergence requirement that the vortex cores overlap is not in effect here, despite the fact that the vortex filaments are still convected according to their own induction and so may bunch and twist under the large strains they themselves create. [121] [23] The accepted alternative, as presented by Katz & Plotkin [98] for steady simulations is simply to limit the number of wake-convection updates in effect. This is discussed further in Section 5.4.1.

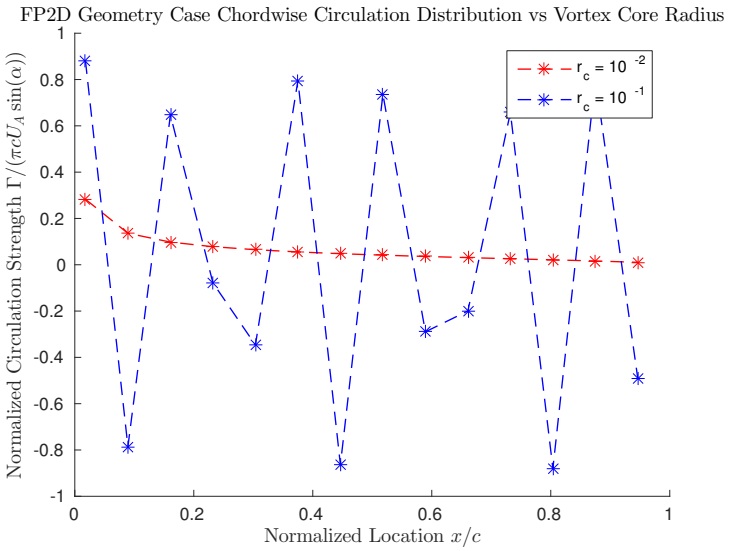

Figure 5.11: Influence of Vortex Core Radius on the Chordwise Circulation Distribution at the Root of an FP2D geometry. (Here, the dimensional form of r_c [m] and the non-dimensionalization with respect to the unity-length chord are equivalent.)

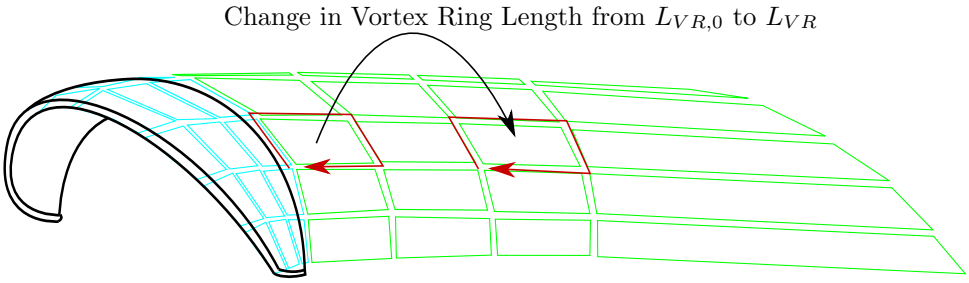

Figure 5.12: The change in vortex ring filament length downstream.

When the wake vortex nodes shift position, the length of each vortex ring changes. To prevent the accidental generation of circulation that might result from this change in vortex length, the core radius can be changed to compensate for the change in vortex length such that the effective vortex strength remains constant. The effective core radius $r_{eff,c}$ can be found by comparing the length of the vortex ring $L_{VR}(n_b, n_w)$ with the length of the last bound vortex ring which determined the circulation strength $L_{VR}(n_b, N_C - 1) = L_{VR,0}$. Using the vortex stretching model used by Sebastian & Lackner [157]:

$$r_{eff,c}(n_b, n_w) = r_c \left(\frac{L_{VR}(n_b, n_w)}{L_{VR,0}} \right)^{-1/2}$$

Consequently, if the vortex ring expands as it "travels" downstream, $r_{eff,c}$ is smaller than r_c, and the region where the majority (approximately 70 percent [184] for $n_{VCM} = 2$) of the vorticity occurs will be shrunk, inducing less tangential velocity on the total body. If the vortex ring contracts, $r_{eff,c}$ is larger than r_c, and the region with the majority of the vorticity will be expand.

To find the length of a vortex ring, the magnitudes of the vectors between the edge points are taken:

$$\begin{aligned} L_{VR}(n_b, n_w) &= |\mathbf{x}_{LEPE} - \mathbf{x}_{LENE}| + |\mathbf{x}_{TEPE} - \mathbf{x}_{LEPE}| + |\mathbf{x}_{TENE} - \mathbf{x}_{TEPE}| + |\mathbf{x}_{LENE} - \mathbf{x}_{TENE}| \\ &= |\mathbf{x}(n_b + 1, n_w) - \mathbf{x}(n_b, n_w)| + |\mathbf{x}(n_b + 1, n_w + 1) - \mathbf{x}(n_b + 1, n_w)| ... \\ &\quad + |\mathbf{x}(n_b, n_w + 1) - \mathbf{x}(n_b + 1, n_w + 1)| + |\mathbf{x}(n_b, n_w) - \mathbf{x}(n_b, n_w + 1)| \end{aligned}$$

Vector magnitudes are not directional, so the direction of the subtraction is irrelevant; however, the same clockwise direction as used to evaluate the induction by the directional vortex ring is used here for consistency.

5.4 The Vortex Lattice Method

The induced velocity at a point is the superposition of the induced velocities at that point from all of the vortices in the domain. That is, for the induced velocity at a point $\mathbf{x}_j$:

$$\begin{aligned}
\mathbf{U}_i(\mathbf{x}_j) &= \mathbf{U}_{ind,surf}(\mathbf{x}_j) + \mathbf{U}_{ind,wake}(\mathbf{x}_j) \\
&= \sum_{n_{\gamma s}}^{(N_B-1)(N_C-2)} \mathbf{U}_{i,n_{\gamma s}\mathbf{x}_j} + \sum_{n_{\gamma w}}^{(N_B-1)(N_W+1)} \mathbf{U}_{i,n_{\gamma w}\mathbf{x}_j} \\
&= \sum_{n_{\gamma s}}^{(N_B-1)(N_C-2)} \mathbf{a}_{i,n_{\gamma s}\mathbf{x}_j}\Gamma_{n_{\gamma s}} + \sum_{n_{\gamma w}}^{(N_B-1)(N_W+1)} \mathbf{a}_{i,n_{\gamma w}\mathbf{x}_j}\Gamma_{n_{\gamma w}} \\
\mathbf{U}_i(\mathbf{x}_j)\cdot\hat{\mathbf{n}}(\mathbf{x}_j) &= \sum_{n_{\gamma s}}^{(N_B-1)(N_C-2)} \left(\mathbf{a}_{i,n_{\gamma s}\mathbf{x}_j}\cdot\hat{\mathbf{n}}(\mathbf{x}_j)\right)\Gamma_{n_{\gamma s}} + \sum_{n_{\gamma w}}^{(N_B-1)(N_W+1)} \left(\mathbf{a}_{i,n_{\gamma w}\mathbf{x}_j}\cdot\hat{\mathbf{n}}(\mathbf{x}_j)\right)\Gamma_{n_{\gamma w}} \\
&= \sum_{n_{\gamma s}}^{(N_B-1)(N_C-2)} A_{n_{\gamma s}\mathbf{x}_j}\Gamma_{n_{\gamma s}} + \sum_{n_{\gamma w}}^{(N_B-1)(N_W+1)} A_{n_{\gamma w}\mathbf{x}_j}\Gamma_{n_{\gamma w}}
\end{aligned}$$

Because the wake circulation strength is the convected circulation strength of the last (TE) bound vortex ring, the normal induced velocity at the point $\mathbf{x}_j$ can be written as a summation of the products of influence coefficients and the unknown bound circulation strengths.

$$\mathbf{U}_i(\mathbf{x}_j)\cdot\hat{\mathbf{n}}_j = (\mathbf{A}_{sj} + \mathbf{A}_{wj})\,\tilde{\mathbf{\Gamma}} = \mathbf{A}_j\tilde{\mathbf{\Gamma}}$$

The equation to be solved requires that there be no normal velocity through the kite surface. The boundary conditions are therefore Neumann conditions over the bound vortex lattice.

As the kite surface is moving - at every point on the surface:

$$(\mathbf{U}_A + \mathbf{U}_i)\cdot\hat{\mathbf{n}} = \mathbf{U}_m\cdot\hat{\mathbf{n}}$$

As the collocation points are where the boundary conditions are enforced, it is there that the induced velocities must be calculated.

The Vortex Lattice Method consequently solves the following equation at the defined collocation points:

$$\begin{aligned}
\mathbf{U}_i\cdot\hat{\mathbf{n}} &= ((\mathbf{U}_m - \mathbf{U}_A)\cdot\hat{\mathbf{n}}) \\
\mathbf{A}\tilde{\mathbf{\Gamma}} &= ((\mathbf{U}_m - \mathbf{U}_A)\cdot\hat{\mathbf{n}}) \\
\tilde{\mathbf{\Gamma}} &= \mathbf{A}^{-1}\left((\mathbf{U}_m - \mathbf{U}_A)\cdot\hat{\mathbf{n}}\right)
\end{aligned}$$

The normalized net circulation distribution for the FP2D validation case - comparable to the inviscid 2D flat plate whose circulation can be determined from an infinitely long vortex at the quarter-chord of a thin-airfoil to be $\pi U_A c\sin(\alpha)$ - can be seen in Figure 5.13 Left. Note how the normalized net circulation strength at each of the root measurement locations sums to approximately one - approaching the total circulation for the flat plate. When the net-circulation found for a flat-plate lifting-line model with a high aspect ratio (LL2D), as seen in Figure 5.13 Right, the net circulation at the root of the wing is close to the invisid 2D flat plate net circulation.

The span-wise distribution can be seen not to extend fully to either wing-tip; this is because the represented circulations are at the span-wise center of their respective vortex rings.

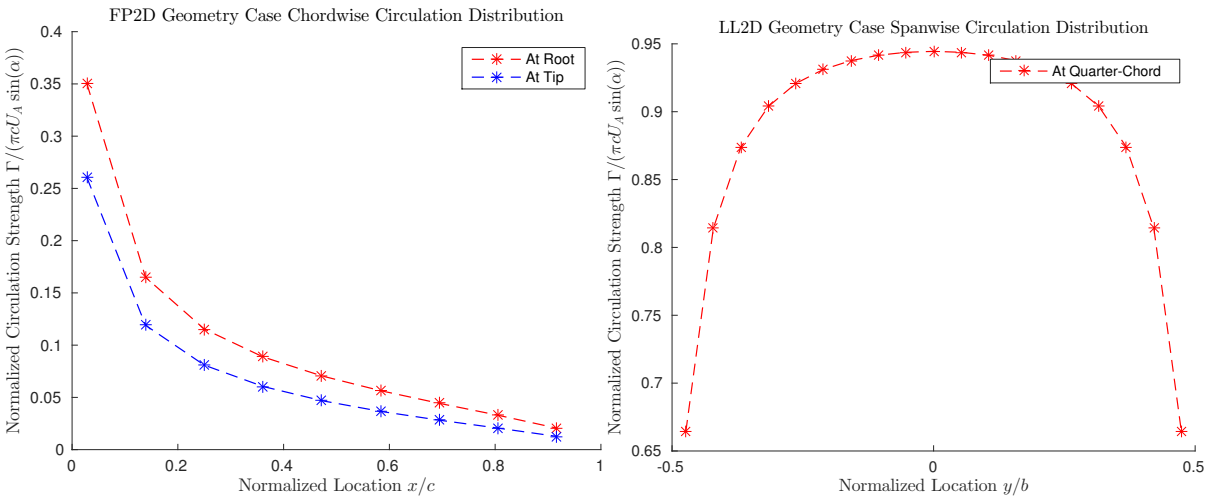

Figure 5.13: The chordwise net circulational distribution of a chordwise-and spanwise-discretized FP2D Geometry (left); and a spanwise net circulation distribution of an LL2D Geometry (right). (Results from a quarter-chord overlayed bound vortex lattice.)

5.4.1 Convergence Criteria

Because $\mathbf{A}_{wj}$ depends on the relative vectors between the wake - deforming within the free-wake radius due to the changing circulation strength - and the body fixed collocation points, $\mathbf{A}_{wj}$ must be recalculated for every consecutive guess at the circulation strength.

Ideally, this loop of determining the influence coefficient matrix, recalculating the vortex strength, re-determining the influence coefficient matrix, etc. would continue until the wake-node locations would no longer change. However, because the vortex rings are convected according to the velocities that they themselves induce, the system can tip from stable to dynamically unstable.

The wake vortex lattice location - determined through convection mainly by the circulation strengths of the trailing vortex rings - has its greatest effect on the inductions of those bound vortex rings near the trailing edge, and therefore influences itself in progressive iterations. Consequently, it can be that disturbances in the wake shape can create a positive feedback loop with the wake circulation, without necessarily having a large influence on the bound circulation distribution.

Further, this instability is exacerbated by insufficient resolution in the tip region. Especially near the center of the convected tip-vortices, the rapid jump from a strong upwards induced velocity to a strong downwards induced velocity can cause the wake-node locations to explode. Since it is not always practical to require a high model resolution - due to the fact that vortex methods without special speed-up algorithms typically require a computational time proportional to $\mathcal{O}(N^2)$, where N here is the total number of filaments - we must take extra care to limit the growth of this model instability.

Katz & Plotkin [98] suggest that the "safe" way to deal with this dynamic instability is to cut the wake-updating cycle after some fixed number iterations, where this fixed number is sufficient to capture the majority of the flow down-wash but the unstable effects are still small. They suggest that the industry standard number of iterations is $N_I = 3$.

5.4.2 Aerodynamic Coefficients for Pressure and Force

The general form of the Kutta-Joukowski relationship between aerodynamic force-per-unit-span[12] and circulation is:

$$\Delta\mathbf{F}' = \rho\mathbf{U} \times \underline{\mathbf{\Gamma}}_F$$

[12] designated by the "prime" accent in $\mathbf{F}'$.

The Kutta-Joukowski formula refers to the vortex filament across the leading edge of the vortex ring, with a circulation strength given by the net circulation Γ_F. The strength of this vortex filament is given as a vector ($\underline{\mathbf{\Gamma}}_F$) to include, not only its circulation strength, but also the direction of the filament.

$$\underline{\mathbf{\Gamma}}_F = \Gamma_F \frac{(\mathbf{x}_{LEPE} - \mathbf{x}_{LENE})}{||\mathbf{x}_{LEPE} - \mathbf{x}_{LENE}||}$$

Further, the general Kutta-Joukowski referes to the total flow velocity at the point in question.

$$\mathbf{U} = \mathbf{U}_i + \mathbf{U}_A$$

To find the aerodynamic force on a panel, then:

$$\Delta\mathbf{F}_\mu = \Delta\mathbf{F}'_\mu \Delta b = \rho \mathbf{U}_\mu \times \underline{\mathbf{\Gamma}}_F \Delta b$$

The subscript "$_\mu$" is included here to indicate that the velocity is evaluated at the center of the leading-edge vortex filament. The Δb here is the spanwise width of the panel. For further details, the reader is referred to equations 9.17 and 9.30 of Katz & Plotkin. [98]

The pressure difference between the pressure- and suction-surfaces of the panel must be the aerodynamic force normal to the surface acting over the area of the panel. The pressure coefficient then normalizes this pressure difference against the dynamic freestream pressure.

$$C_{P,\mu} = -\frac{\Delta\mathbf{F}_\mu \cdot \hat{\mathbf{n}}_j}{S_j} \frac{1}{q_\infty}$$

The normal force is the integration of the pressure over the body. Note that there's a sign change, to direct a positive normal force along the positive normal-vector. This also serves to indicate a positive normal force when the lift - the dominant force in this inviscid model - is positive:

$$C_N = \sum_\mu C_{N,\mu} = \frac{1}{q_\infty S} \sum_\mu (\Delta\mathbf{F}_\mu \cdot \hat{\mathbf{n}}_j)$$

The lift, drag, and steering force coefficients are, by an analogous method, the integrated normalized projections of the aerodynamic panel force. The lift, drag, and steering directions are determined geometrically. The drag acts in the direction of the apparent velocity, along the unit vector $\hat{\mathbf{D}}$; the steering force acts in the positive $\hat{y}$ direction, along the unit vector $\hat{\mathbf{S}}$; the lift force acts perpendicular to both, along $\hat{\mathbf{L}}$.

$$C_L = \sum_\mu C_{L,\mu} = \frac{1}{q_\infty S} \sum_\mu \left(\Delta\mathbf{F}_\mu \cdot \hat{\mathbf{L}}\right)$$
$$C_D = \sum_\mu C_{D,\mu} = \frac{1}{q_\infty S} \sum_\mu \left(\Delta\mathbf{F}_\mu \cdot \hat{\mathbf{D}}\right)$$
$$C_S = \sum_\mu C_{S,\mu} = \frac{1}{q_\infty S} \sum_\mu \left(\Delta\mathbf{F}_\mu \cdot \hat{\mathbf{S}}\right)$$

Again, the normalization area S is the projected area found by multiplying the maximum span by the mean aerodynamic chord. The dynamic pressure q_∞ is found with the free-stream velocity, such that:

$$q_\infty = \frac{1}{2}\rho_{air}||\mathbf{U}_A||^2$$

We can demonstrate the aerodynamic forces found with the VLM_{MW} by considering the forces predicted to be acting on a 90 degree extruded Clark Y arc-shaped wing (CYKW). A polar of the lift and drag coefficients found for the CYKW geometry - with various model choices - can be seen in Figure 5.14, as well as those results for the same geometry reported by Leloup [105] and Maneia [120].

Some characteristics of the forces predicted by the VLM_{MW} for fully attached flow can be seen:

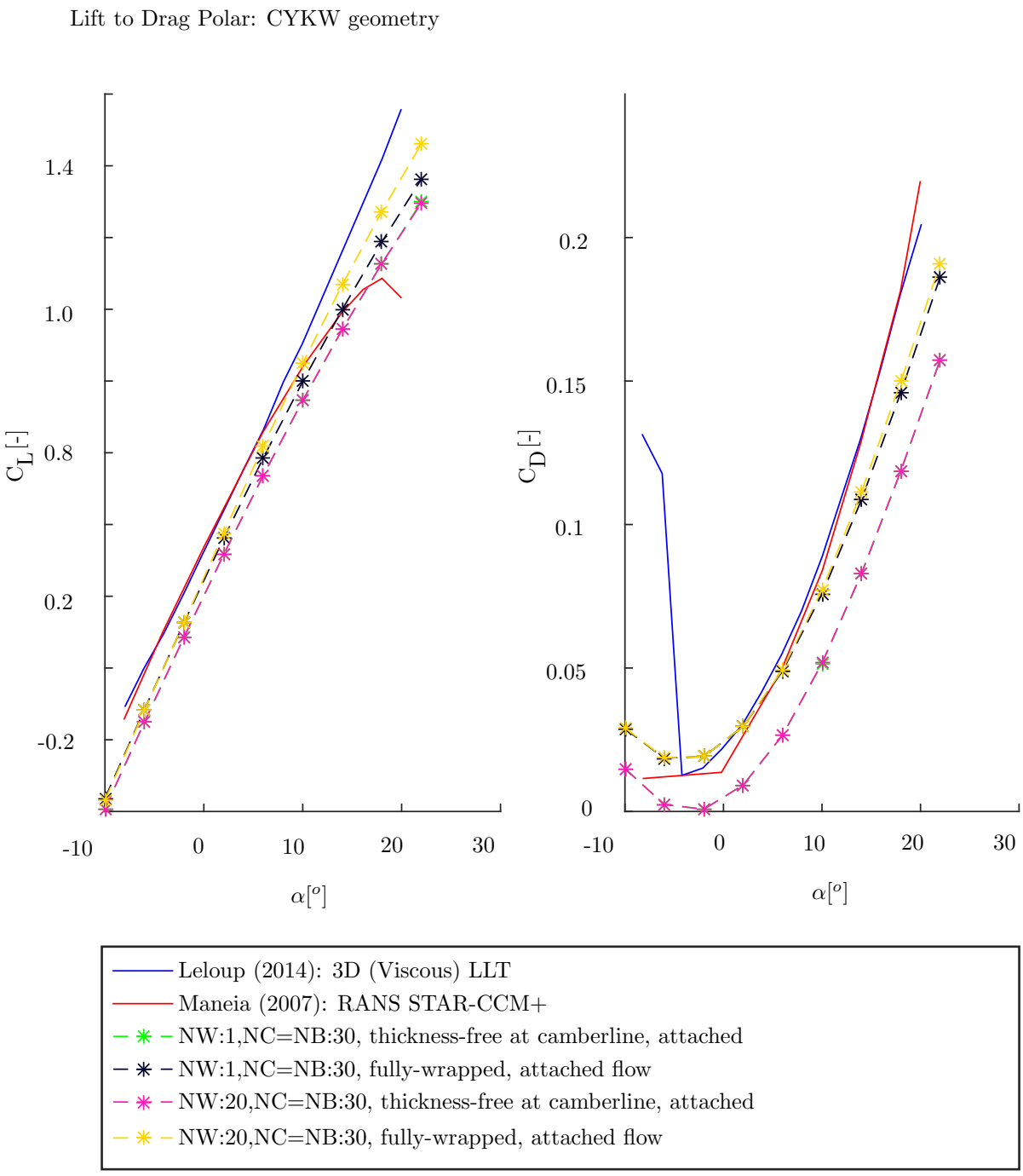

Figure 5.14: A comparison of the effect of a fixed- vs. combined free-and-fixed-wake and a thickness-free vs. finite-thickness geometry for the Clark Y arc-shaped wing on the aerodynamic coefficient polar. Note that the thickness-free results (magenta and green) are so close that the green result is very difficult to see.

- We see that the slope of the C_L vs. α curve is equivalent to that given by both a viscous angle-of-attack correction method (VACM) applied to a lifting-line theory (LLT) and a Reynolds-Averaged Navier-Stokes (RANS) solution, at angles of attack where the flow is expected to remain attached.
- We can further see that the VLM_{MW}, as it has been described up until this point, cannot predict the forces on the wing under the effects of flow separation. The size of the error between the RANS result and the combined free-and-fixed-wake, finite-thickness VLM_{MW} model (yellow) increase as the size of the separation region increases. This is particularly apparent in the drag polar at angles of attack greater than 10^o.
- That is, the fully-attached flow form of the VLM_{MW} predicts a linear C_L vs. α relationship, and a parabolic C_D vs. α relationship as we would expect, for an inviscid potential flow method.
- The difference in predicted results between a fixed-wake model (depicted by green and black in Figure 5.14, with $N_W = 1$) and a model with a combined free-and-fixed-wake (shown in Figure 5.14 as pink and yellow, where $N_W > 1$) are small when the magnitude of the lift on the body is small and the influence of downwash is small. Conversely, the ability to free the wake will represent downwash and pull the solution at high angles of attack closer to the viscous LLT solution.
- When a thickness-free discretization of the bound vortex lattice on the camberline (green and pink) is used to model a thick airfoil like the Clark Y, there is a tendency to underpredict the lift. This is logical, as a thicker airfoil effectively tightens the neck of the half-venturi tube through which the flow is forced, increasing its local velocity and decreasing its corresponding static pressure.
- The inclusion of a boundary layer model has the same effect as increasing the thickness of the airfoil, from the perspective of the potential flow exterior to the boundary layer. Consequently, a vortex method without a boundary-layer model - such as the VLM_{MW} - must be expected to under-predict the lift in comparison to models that include a boundary-layer - such as a LLT model with an applied VACM via a coupled boundary-layer-potential-flow solver, and a CFD model.
- The drag source for a vortex method with fully attached flow is induced drag, which is related to the square of the lift. When the vortex method lift coefficient is positive, then the effect of a lift under-prediction will manifest as a drag under-prediction. However, when the lift coefficient is negative, the effect of the lift under-prediction will cause a drag over-prediction, in comparison to a model that represents the boundary-layer. However, in comparison to a vortex model to which the iterative VACM is applied, the drag prediction is not subject to wild overshooting when the vortex model predicts negative lift values.

We can say that the fully-attached form of the VLM_{MW} behaves as we would expect from an attached flow vortex method.

5.4.3 Coefficient Distributions

The aerodynamic coefficients can be evaluated purely for a subset of the full body - such as over the panels in the middle of the span to give a chord-wise force distribution at the root, or for the combined influence of all of the panels at each span-wise location to give a span-wise force distribution - by replacing the area-normalization with the area of the subset panels and only summing the coefficients of that subset.

If we plot an example of such a span-wise force distribution for the CYKW finite-thickness arc-shaped wing, as in Figure 5.15, we can see that it behaves qualitatively as we would expect:

- We can see that lift force behaves almost like an elliptical wing, except for near the wing tips. This is reasonable, since the flattened kite has an elliptical shape.
- Further, we see that the induced drag increases towards the edges of the kite, before decreasing again where the local-chord-to-mean-aerodynamic-chord ratio becomes small at the tips. This is also an expected result, as the influence of the tip vortices will be strongest near the tips - due to the $1/r^2$ Biot-Savart induction relation.

- We can see that the lift- and drag- coefficients are even functions of the span, and the steering force is an odd function of the span. This is because the steering force is defined positive in the positive $\hat{y}$ direction. The aerodynamic force on positive camber airfoil at a positive angle of attack will tend to be in the positive-positive quadrant of the $\hat{x}', \hat{z}'$ plane, which changes $\hat{y}$ signs when rotated into the body-fixed coordinate system.
- Further, we can see that there is a fairly large change in the lift coefficient at the root between a fixed-wake model and a model which includes downwash. The influence of downwash converges as the wake resolution increases, showing little difference in the force distributions between a $N_W = 30$ and $N_W = 40$ model.

5.4.4 Resolution for Computational Speed and Accuracy when Modelling Fully-Attached Flow

Increasing the number of panels in the chordwise and spanwise direction on the fixed-wake, single-wake VLM over the FP2D geometry causes the circulation at the root to approach the 2D flat plate circulation $\Gamma_{FP} = \pi c U_A \sin(\alpha)$ quickly. The difference in circulation between the low resolution and high resolution normalized circulation at root is small, on the order of .01 percent for the chordwise resolution, and order of .1 percent for the spanwise resolution.

The chordwise resolution converges from the bottom as the impermeability of the wing is enforced across more points of the chord. The spanwise resolution converges from the top, as the tip vortices are better represented. Further, the spanwise resolution has a toothed pattern, due to the fact that the "circulation at root" is evaluated at the panel closest to root. That is, for an odd N_B, corresponding to an even spanwise panel number $N_B - 1$, the panel closest to root is determined to be the panel with its y-negative-edge at the root. Consequently, the influence of the tip vortices is effectively increased "at root" for odd N_B simulations in comparison to "at root" for even N_B simulations.

As the chordwise resolution increases, the FP2D pressure distribution at root converges quickly to the expected 2D flat plate pressure distribution.

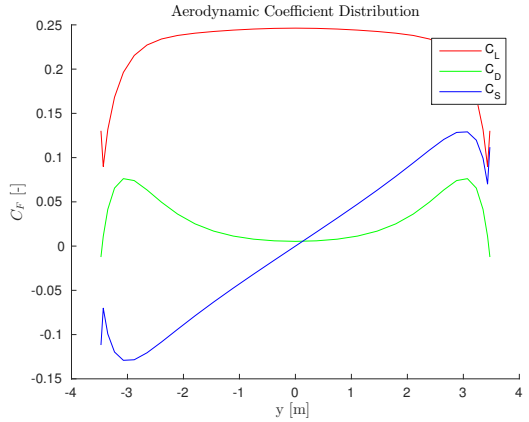

(a) $N_W = 1$, fixed wake

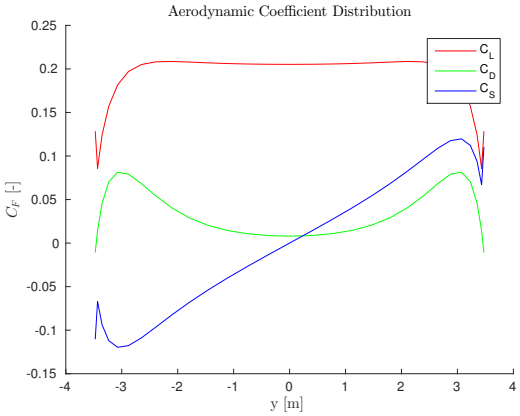

(b) $N_W = 10$

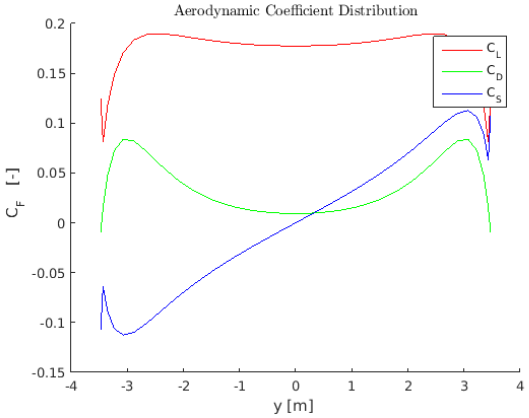

(c) $N_W = 20$

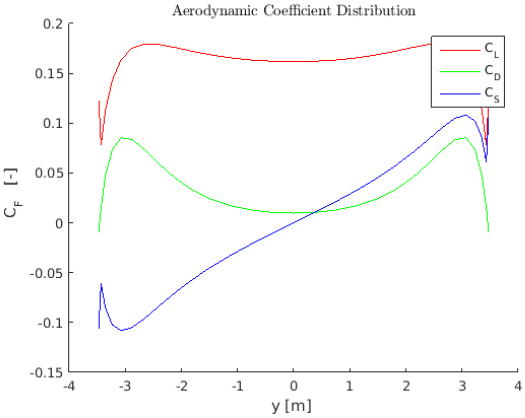

(d) $N_W = 30$

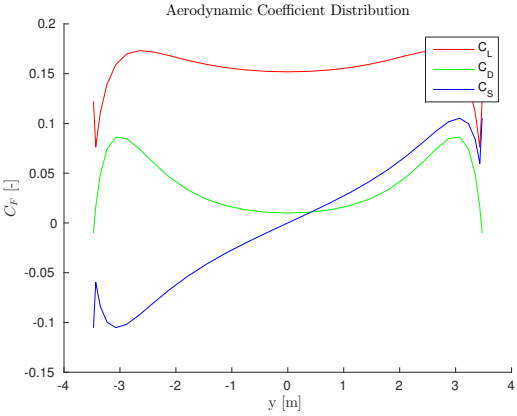

(e) $N_W = 40$

Figure 5.15: Span-wise distribution of the aerodynamic coefficients for a CYKW wing at $\alpha = 2^o$, with increasing resolution of the free-wake region. $N_B = 30$, $N_C = 41$, $n_{VCM} = 2$, $r_c = 10^{-4}$m, $\epsilon_{OT} = 10^{-8}$m.

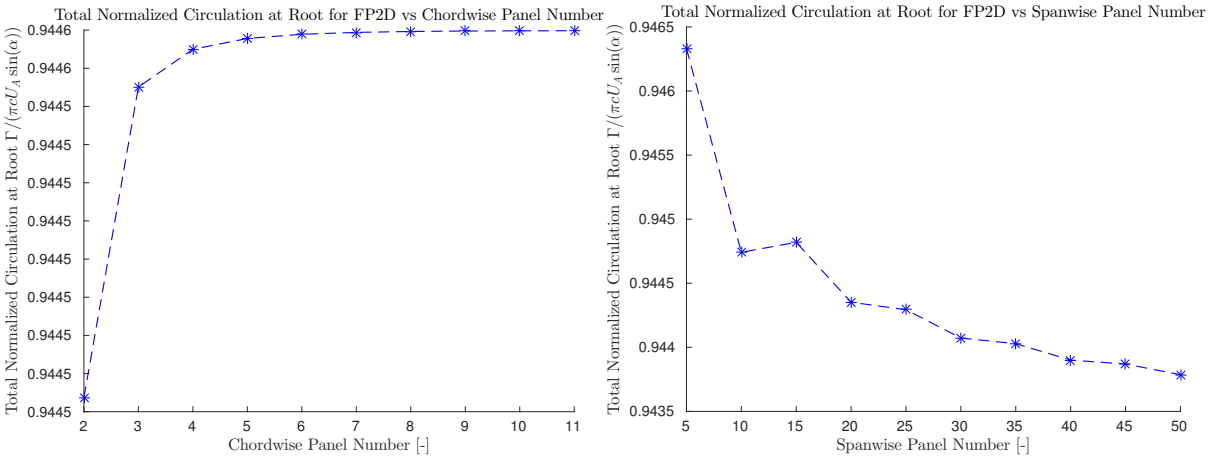

Figure 5.16: Convergence of the Total Normalized Circulation at the Root of the FP2D geometry towards the 2D Flat Plate Circulation, for Increasing Chordwise (Left, $N_B = 20$) and Spanwise (Right, $N_C = 6$) Resolution.

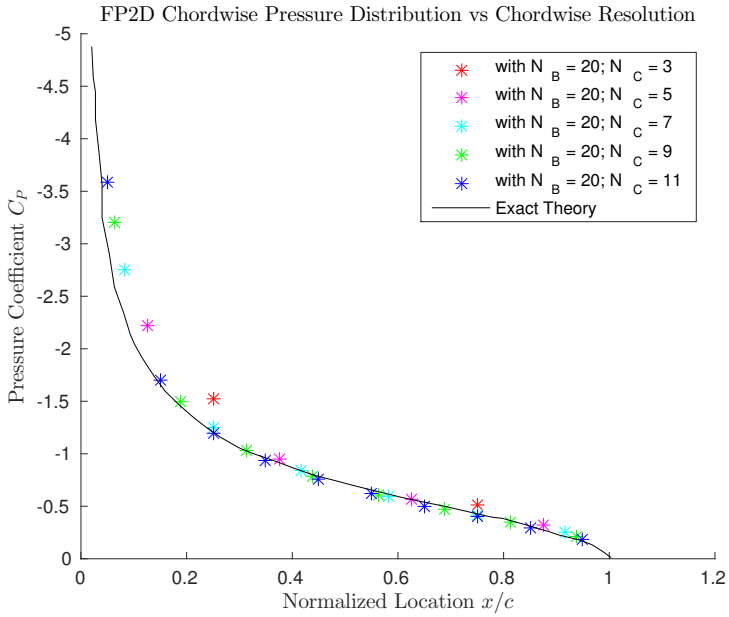

Figure 5.17: Increasing the chordwise resolution causes the pressure distribution (without VFP correction) at the root of the FP2D geometry to approach the analytical flat plate potential-flow solution for $\alpha = 10^o$, $U_A = 10\text{m/s}$, and $\rho_{air} = 1\text{kg/m}^3$, as found in Figure 3.17 (p. 87) of McCormick [127].

5.5 The Inclusion of Separation

Under the influence of an adverse pressure gradient, it can occur that a fluid element - decelerating as it travels from the leading-edge towards the trailing edge of a surface[13] - meets a fluid element that was accelerated from the trailing edge in the direction of the leading edge. Rather than collide at this intersection point, these incompressible fluid elements instead turn and begin to travel away[14] together.

A curious feature is that the surface which includes the following collection of points:

- the almost-collision-point where the two fluid elements left the surface (called the separation point),
- the separation line made up of those separation-points along the span of the surface, and
- continuing between the paths of the two separated fluid elements

is a stream surface. [199] In a steady[15] situation, this means that fluid elements from either side of the separation stream-surface will never pass through the separation stream-surface. The points immediately next to the surface have no velocity normal to the stream-surface as well as, due to fluid viscosity, the same velocity tangential to the stream-surface.

However, we know that fluid elements that are further away from the stream-surface do not share this common stream-surface-tangential velocity. The extreme demonstration of this fact can be found far upstream of the geometry in the flow. This implies that there is a tangential-velocity change the occurs centered on the separation stream-surface. If we assume that this tangential-velocity change occurs over a short distance, we could model the separation stream-surface by overlaying it with vortices, as we did for the surface itself.

Due to our "in-universe" assumptions of steady, inviscid flow with conservative forces, Helmholtz's Third Theorem says that the vortex rings which have been convected from the same separation line must have the same circulation strength, accounting for the stretching of the vortex rings as they are convected.

If we know how to determine the vortex strength of the separation-surface vortex rings, we can better predict the velocity in a separated flow.

5.5.1 The Additional Kutta Condition

Luckily, the Kutta condition applies just as much to a separation line on the geometry's surface, as it does to the separation line at the trailing edge. We can see that the flow still separates tangentially to the surface and does not rotate around the separation line. Again, this lack of rotation implies that the net circulation strength of the vortex filament which lays on the separation line must be zero. This is sketched in Figure 5.18.

Consequently, we can determine the strength of the separation-surface vortex rings with vector addition. That is:

$$\Gamma_F(n_c = N_{C,\ Sep.}) = 0$$

Alternatively formulated:

$$\Gamma_w(n_w = 1) = \Gamma(n_c = N_{C,\ Sep.} - 1) - \Gamma(n_c = N_{C,\ Sep.})$$

With the inclusion of the condition the Kutta condition be satisfied at the separation point, we add one equation to compensate for what would otherwise be an additional unknown: the circulation strength of one downstream-direction row of vortices in the separation stream-surface.

[13] Just above the surface where the no-slip condition would be in a viscous "universe."

[14] They can't turn in towards the wall, unless the wall is porous.

[15] Reiterating an assumption made at the beginning of this report because of the oddness to the idea of a "steady" assumption concerning separation at Reynolds numbers that are associated with turbulent flow, we have restricted the scope of this thesis to speaking about time-averaged terms. Unsteady behavior falls within the sub-scale that is not included in this model.

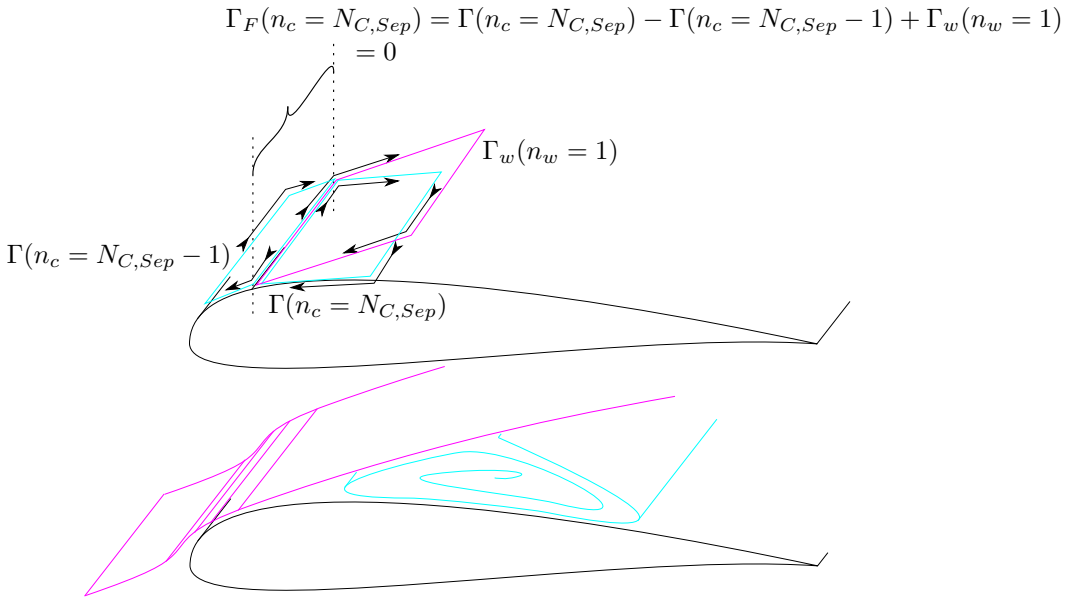

Figure 5.18: The Kutta condition and net circulation summation for smooth separation, as demonstrated on the suction surface.

Note that the enforcement of the Kutta condition in unsteady situations is more complicated that what is applied here, as the separated flow needs to convect away the vorticity as it is generated on the surface, and therefore requires a time-derivative. Further, this model assumes that the separation line is known, and does not include the additional solver loop which would iteratively refine a separation location.

5.5.2 Resolution Concentration for the Separated Wake

Because the VLM_{MW} is set up to first convect all of the wake vortex nodes according to purely the free-stream velocity, then iteratively determine the circulation strengths of the vortex rings and re-convect them according to the velocities they induce on themselves, there are some practical concerns in regards to the resolution of the wake.

First, however the vortex nodes are convected in their initial placement, they must be on the correct side of the various vortex lattices in play. That is, a nodes for a suction-surface separation stream-surface should not initially be placed below the geometry nodes, the trailing edge stream-surface nodes, or the pressure-surface separation stream-surface nodes. Similarly, nodes for a pressure-surface separation stream-surface should not be placed above the geometry nodes, the trailing edge stream-surface nodes or the suction-surface separation stream-surface nodes. Logically, the inductions at these locations would be such to drive the relevant nodes further away from their physical location.

Second, other than the summed induced velocities of the modelled vortex rings, there is nothing preventing convected wake nodes from travelling through the geometry or other vortex lattice stream-surfaces. Since, by physical definition, stream-surfaces should not cross, there is a practical requirement that the vortex lattices must have a resolution high enough that any given shed node would be repelled away from other vortex-lattice stream surfaces in the direction consistent with the convection of a continuous flow.

Because the danger that the stream-surfaces might cross due to insufficient resolution is much higher above the geometry and the portion of the trailing edge shed vortex lattice close to the geometry, the VLM_{MW} "concentrates" or "bunches" the wake nodes of the surface-separated vortex lattices within a shortened free-wake radius. That is:

$$r_{w,\ Sep.} = f_S r_w$$

where $f_S < 1$ is the separation concentration factor.

The separation concentration factor is a parameter available to the VLM_{MW} user, where values between one-half and one-fifth are suggested. The value $f_S = \frac{1}{2}$ corresponds to about 2.8 chord lengths, and the value $f_S = \frac{1}{5}$ corresponds to about 1.1 chord lengths. Given that the furthest-forwards a separation line can lay is at the leading edge, the selection of a concentration factors smaller than one-fifth may not cover the full chord-length of the geometry, and miss the region behind the trailing edge where downwash is concentrated. An example concentrated resolution of a separation vortex-lattice can be seen in Figure 5.19.

5.5.3 Demonstration of Separation for a 3D Flat Plate

We can demonstrate the aerodynamic forces found with the double wake VLM_{MW} by considering the normal force predicted to be acting on a unity-aspect ratio rectangular flat plate (FP3D) over a 90 degree range of angles of attack. These results can be compared (see Figure 5.20) to results for the same geometry, as reported by Winter [198] and Ortiz et al [143].

From these results, we can see the same general trends as were depicted in the demonstration lift- and drag-polars of the CYKW geometry. The flow at small angles of attack ($\alpha \leq 5^o$) is well approximated with a fully-attached (single wake) VLM_{MW} with a combined free-and-fixed wake. At larger angles of attack where the flow is still attached, the lack of a boundary layer method causes an under-prediction of the normal force, due to the missing thickness of the boundary layer from the perspective of the external flow.

Further, we can see the influence of the Kutta condition on the flow at 90^o angle of attack. Potential flow without the influence of the Kutta condition has no reason to redirect flow asymmetrically around a geometry, causing the drag of a bluff body to be zero. Since at 90^o, a flat plate will not generate any lift, the normal force at 90^o without the Kutta condition would be zero. However, we can see a non-zero form[16] drag. Consequently, we can state that the VLM_{MW} has the ability to predict form drag, however much it under-predicts this form drag.

The under-prediction of form drag for a multiple-wake vortex method is expected. Fage & Johanson [62] who used a double-wake vortex method to predict the normal force on a 2D flat plate and also performed wind tunnel testing of this same flat plate[17], also predict a normal force at 90^o angle of attack which is about a factor of two (2.45, reportedly) below their wind tunnel measurement. This missing drag is possible due, in part to the neglected skin friction of an inviscid vortex method, and also due to the fact that the area within the wake is not truly the irrotational "dead-water" whose velocity can be well predicted by summing the free-stream velocity and the induction by the modelled vortex lattices. Ultimately, skin friction and the flow-properties within a wake are pieces of information that a detailed boundary layer model might be able to provide.

The VLM_{MW} requires an assumed flow separation location. In order to generate a polar including the effect the separation line moving forwards after separation, we need to combine the "fully-attached" and "separation at leading edge" polars. When we have wind tunnel estimates for the angles of attack when the flow first separates and when the flow separation occurs at the leading edge, we can make a best guess polar. Such a combined "best-guess" polar can be found in Figure 5.21.

One effect of the additional Kutta condition can be seen very clearly on the resulting pressure distributions generated with the multiple-wake form of the VLM_{MW}. That is, the aerodynamic pressure, for a panel whose vortex ring's leading edge filament lies on the separation line, must be zero. This is a direct result of the Kutta-Joukowski formulation of Bernoulli's pressure relation:

$$\Delta \mathbf{F}' = \rho \mathbf{U} \times \underline{\mathbf{\Gamma}}_F$$

[16] this term also includes skin friction, but the magnitude of the skin friction on a flat plate normal to the flow should be significantly smaller than the form drag behind the same bluff obstruction.

[17] This would have been a fantastic validation data-set except that the author is suspicious of their reported normalization values. That is, Fage & Johanson [62] report the normal force coefficient in the Engineering style k_N [2], despite appearing in a British Royal Society journal, and normalizing by ρU_∞^2, making no mention of an area term. In any case, the ratios between coefficients reported within the same paper ought to be trustworthy.

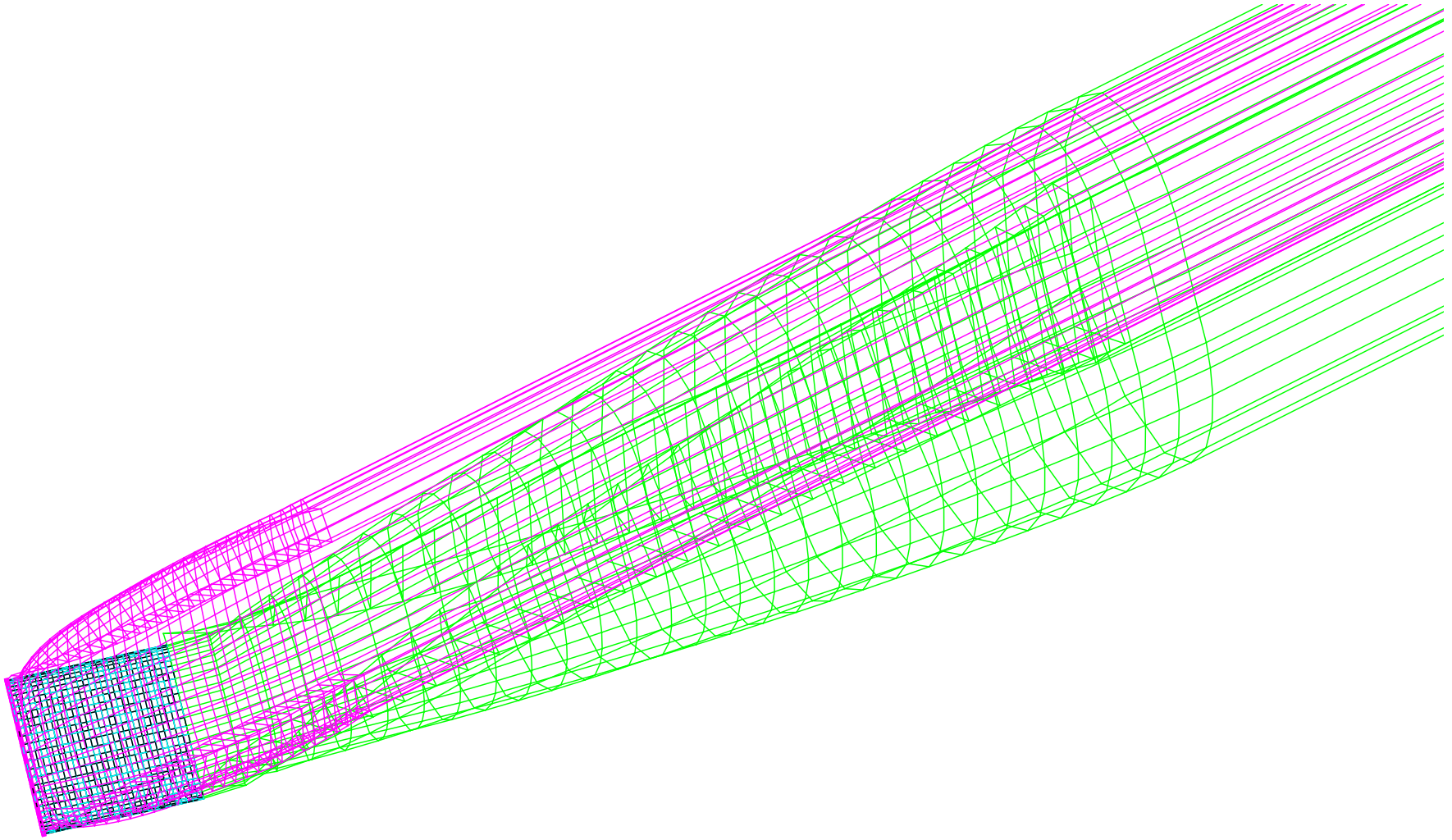

Figure 5.19: A demonstration of the concentration of resolution on a suction-surface separation vortex lattice (magenta), in comparison to the trailing-edge shed vortex lattice (green), at $\alpha = 45^o$, for $N_W = N_L = N_B = 30$ and $f_S = 1/3$.

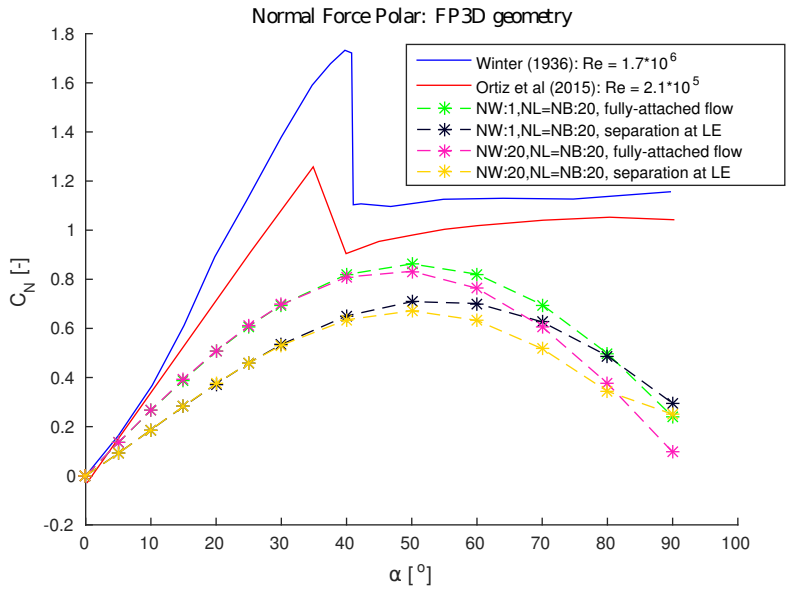

Figure 5.20: The normal force polar predicted for a unity-aspect ratio flat plate (FP3D) by the VLM_{MW} with either fully attached flow or separation at the leading edge and trailing edge, and a fully-fixed or combined free-and-fixed wake, in comparison to the experimental results of Winter [198] and Ortiz et al [143].

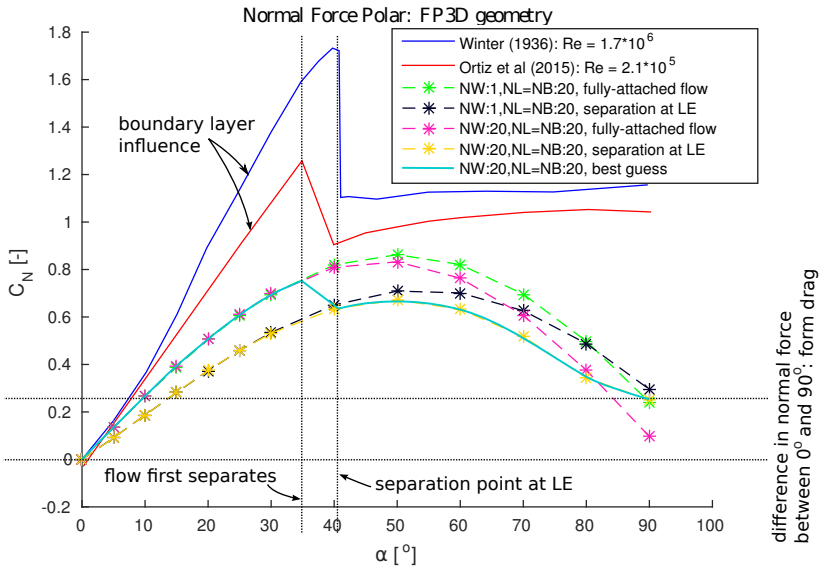

Figure 5.21: A guess at constructing a normal force polar for a unity-aspect ratio flat plate (FP3D) with the VLM_{MW} allowing the separation line to travel forwards, in comparison to the experimental results of Winter [198] and Ortiz et al [143].

Consequently, when analysing the pressure-distribution results of the VLM_{MW}, we have to keep in mind that the pressure distribution of the panels at $n_c = N_{C,\ Sep.}$ are unreliable. This could, in theory, be avoided by applying a very high chord-wise resolution to the $N_{C,\ Sep.}$ panel, but this is not practical in terms of computational expense.

We can see the unreliable pressure-distribution immediately following the separation location by comparing the pressure distributions on the FP3D geometry as given by Winter [198] and as generated by the double wake VLM_{MW} with flow-separation at the leading edge. This comparison is shown in Figure 5.22.

In the $\alpha = 8^o$ result, we can see the influence of the leading edge pressure spike, as well as the gradual increase in pressure towards the trailing edge. We don't see the smaller pressure spikes that Winter measures at the side edges and trailing edges of the plate. In the $\alpha = 30^o$ case, we do not predict the leading-edge pressure spike to be spread over a longer chord-wise area than in the $\alpha = 8^o$ case, as is measured by Winter. It is here, in the center of the plate, that the majority of the error visible in the force polars occurs.

It appears that the VLM_{MW} is able to predict the trends in the flow, when separation locations are known a priori, but the magnitudes of the force coefficients are not very reliable when the boundary layer significantly influences the flow. Further, with finite chord-wise resolution, the pressure distribution at those panels immediately following a separation line are likely to be suspect. In the end, the VLM_{MW} relies heavily on the assumption that boundary layers are thin, and that tangential velocity jumps within the length-scale of the vortex core radius.

5.5.4 Resolution for Computational Speed and Accuracy when Modelling Separated Flow

For increasing spacial resolution, the double wake VLM_{MW} approaches an asymptotic solution, though this asymptotic solution still has an offset from experimentally-determined values. The magnitude of this asymptotic error depends on the degree of influence of the boundary layer character on the potential flow solution, as discussed in the previous section.

It is important to remember that the resolution of the bound vortex lattice is directly responsible for the number of places where we can enforce the boundary condition. If the boundary condition is not sufficiently enforced, there will be mass flow through the geometry in the normal-direction. In that surface-normal mass-flow is associated with separation[18], this means that an insufficient resolution will behave as though the degree of separation is greater. Since separation has the effect of decreasing the experienced lift, and the VLM_{MW} already under-predicts the forces on the geometry, an insufficient resolution will cause an increased error.

Increasing our spacial resolution increases our run-time. If we assume that this relationship is proportional to $\mathcal{O}(N^2)$, we can approximate that:

$$\text{runtime} \propto \left(N_B(N_C + 2N_W)\right)^2$$

for a double-wake model. We can see then that increasing the span-wise resolution will have a larger effect on runtime than increasing the chord-wise resolution. Further, increasing the downstream resolution will also have a large effect on the runtime, though not quite as much as the span-wise resolution. These relationships are demonstrated the run-times found for certain combinations of N_B, N_C, and N_W in Figure 5.24.

At a certain point the additional runtime for a higher spacial resolution will not justify the increased model accuracy. This trade-off point is dependent on the geometry in the flow and the amount of separation in play.

For an aspect ratio 1 flat plate with leading edge separation, it is suggested - based on the combination of Figures 5.23 and 5.24 - that it is unlikely that that the trade-off point will be reached for a span-wise resolution $N_B < 20$ and a downstream resolution less than $N_W < 10$.

[18] In fact, one empirical method of including the effects of separation on vortex lattice methods is to relax the flow tangency requirement at the collocation points. [18]

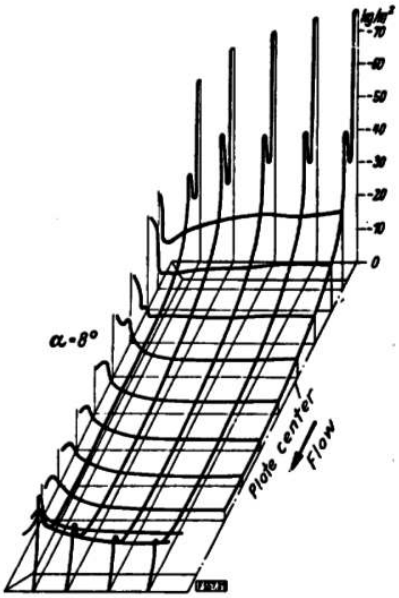

Figure 21.- Pressure distribution on the suction side of the square plate at 8° angle of attack.

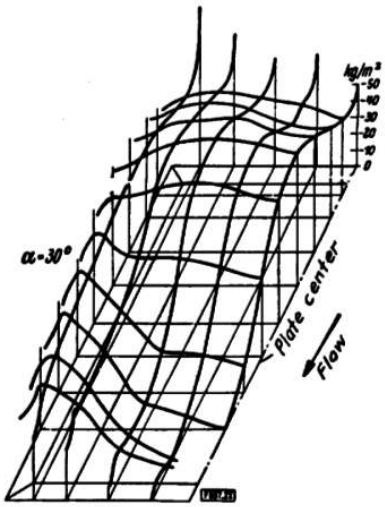

Figure 22.- Pressure distribution on the suction side of the square plate at 30° angle of attack.

(a) Experimentally measured FP3D pressure distributions, reproduced from Winter [198]. Note that only half of the square plate is shown and that the leading edge is positioned away from the viewer.

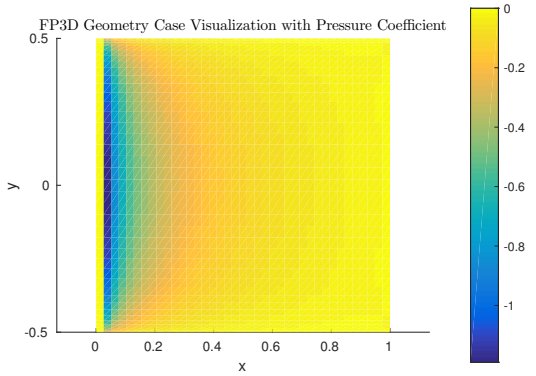

(b) VLM_{MW} FP3D pressure distribution at $\alpha = 8^o$. Leading edge to the left.

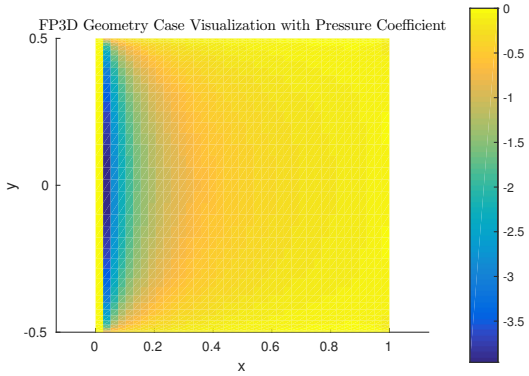

(c) VLM_{MW} FP3D pressure distribution at $\alpha = 30^o$. Leading edge to the left.

Figure 5.22: Comparison of experimental to predicted pressure distributions for a FP3D geometry with leading-edge separation.

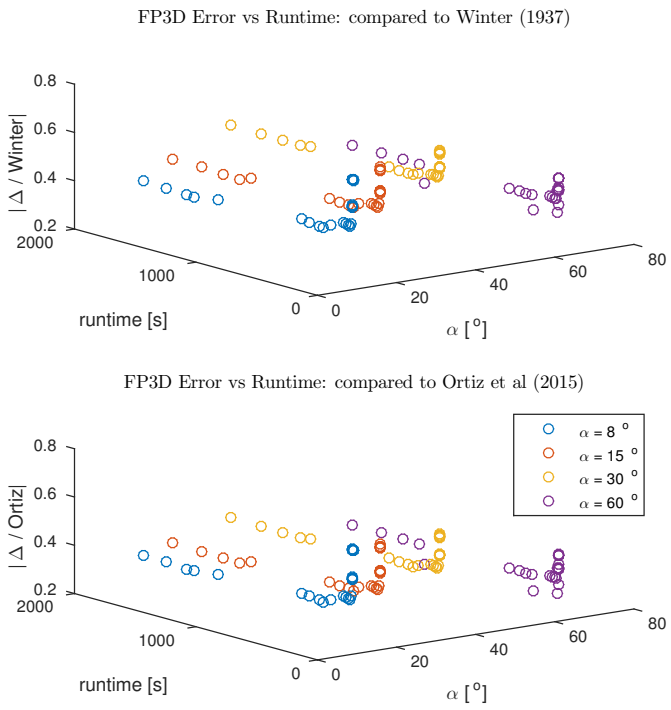

Figure 5.23: Error vs Resolution for the FP3D case with leading-edge separation, as judged against Winter [198] and Ortiz et al [143].

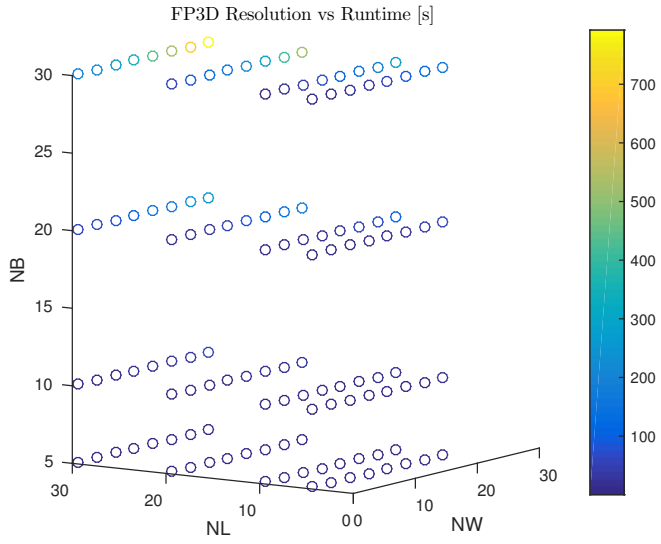

Figure 5.24: Runtime vs Resolution for the FP3D case with leading-edge separation.

Chapter 6

Results for a Leading-Edge Inflatable Kite

We can use the VLM_{MW} to predict the pressure-distribution over a sample LEI-kite, such as the TUDX geometry described in Chapter 4.

An aerodynamic coefficient polar can be seen in Figure 6.1. This polar demonstrates certain model behaviors:

- The VLM_{MW} generally overpredicts lift for the TUDX kite in comparison to the RANS result. This would seem unusual since the previous validation tests suggested that the missing boundary layer influence within the VLM_{MW} caused an underprediction of lift. However, we should consider that - in the 3D flat plate case - only the results for positive angles of attack were shown. For positive angles of attack in the FP3D case, the separation recirculation region lies above the wing; for the TUDX case, the primary separation recirculation region lies under the wing. Consequently, the direction of the pressure difference caused by the combined missing boundary-layer thickness and "dead-water" behavior will reverse.
- As we would expect, the degree to which the fully-attached flow VLM_{MW} model under-predicts drag increases as the angle of attack increases. This would appear to be consistent with the lack of boundary-layer modelling.
- Deaves [51] reports an uncertainty on the order of 10 percent due to the influence of profile smoothing on steady-state RANS results. At high angles of attack, the overprediction of lift by the VLM_{MW} falls into this uncertainty region. This is an important indication that such an VLM_{MW} may - for development phases past this feasibility study - be an effective method to estimate aerodynamic force at high angles of attack, and may be a useful tool within the AWE group's aerodynamic modelling code-base.
- If we attempt to model a suction-surface separation for a small incidence, such as at $\alpha = -5^o$, we significantly mispredict the aerodynamic coefficients. One possible response to this result is that suction-surface separation at such a small angle of attack is very unphysical. However, that interpretation raises the question of why this misprediction doesn't occur for the other tested angles of attack less than the 14^o cut-off found by Deaves [51]. One explanation may consider that the slope of the TUDX canopy after the maximum $\hat{z}$ point is fairly constant. Because we have assumed that separation occurs at the surface-freestream-tangent location, a negative angle-of-attack may initialize the suction-surface separation vortex lattice placement almost directly over the remaining canopy. This overlaying may require large negative circulation strengths in the effected bound vortex rings in order to satisfy the boundary conditions, without including the suction-surface separation circulation strength in the net-circulation strengths of those bound vortex filaments which have been overlaid.

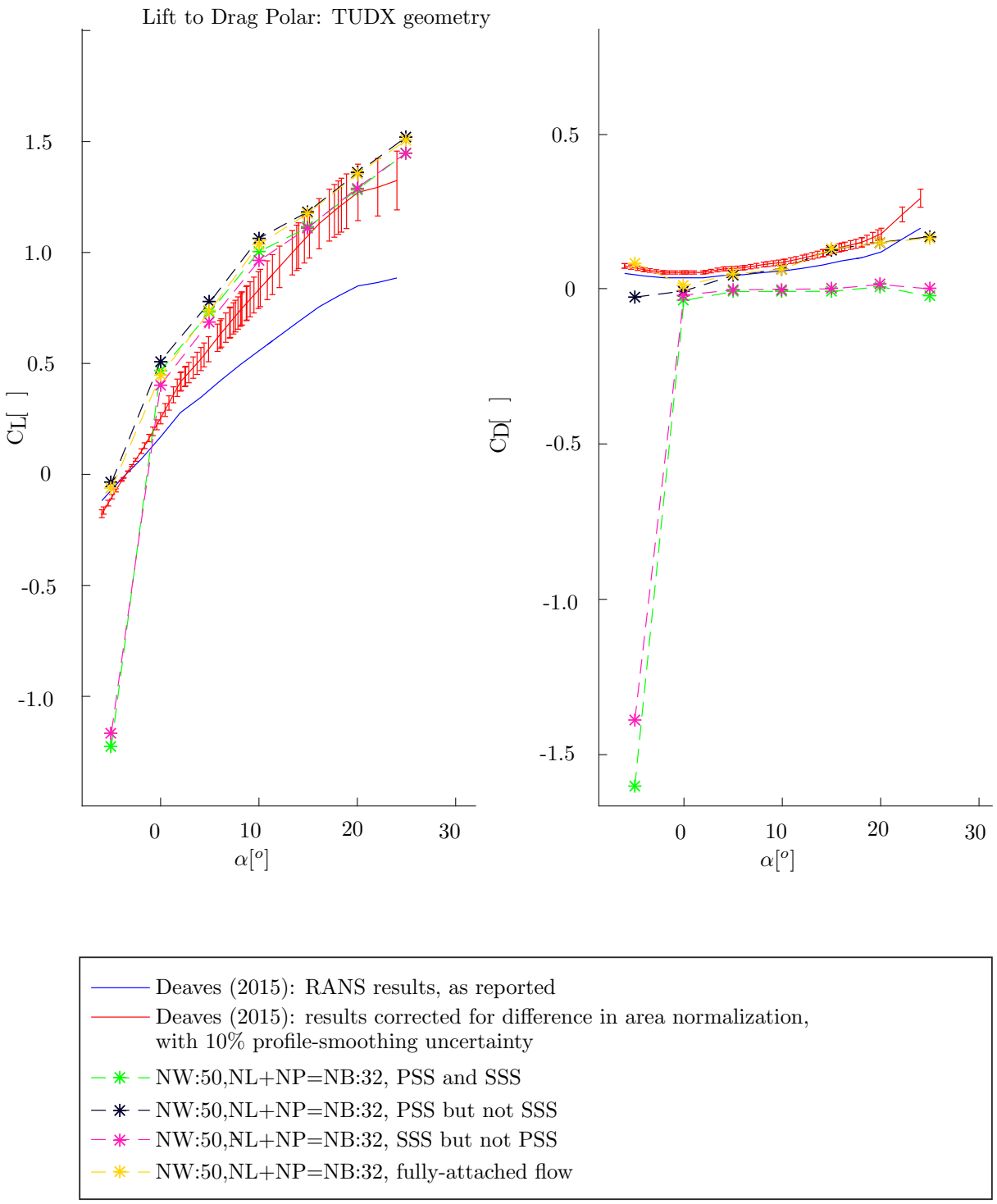

Figure 6.1: Lift and Drag polar for angles of attack between $-5^o \leq \alpha \leq 25^o$, where the key "PSS" includes a pressure-surface separation vortex lattice and the key "SSS" includes a suction-surface separation vortex lattice, in comparison to the coefficients reported by Deaves [51], and the Deaves coefficients accounting for the differing normalization areas and the uncertainty due to Deaves' profile smoothing. $f_S = 1/3$.

- Another interesting note is that the drag coefficients are predicted to be negative when there is either pressure-surface separation modelled at small angles-of-attack or there is suction-surface separation modelled in general. This behavior resembles strongly the result for a finite-thickness wing (such as the CYKW) when the suction-surface and pressure-surface trailing edge filaments do not coincide. It is supposed that these occurrences are related, as a moderate instance of the suction-surface separation expression for small angles of attack. That is, in these cases some percentage of the separation vortex lattice lies quite close to the body geometry, without being counted into the net circulation strength. Effectively, this behavior is an occurrence of the reattachment problem (see Section 6.1).
- Interestingly, the results predicted when separation is not modelled and the flow is assumed to be fully attached (yellow) do not appear to be significantly different from those predicted when pressure-surface separation is modelled without suction-surface separation (black) at moderate angles of attack. This is also assumed to occur as an expression of the reattachment problem. We know that the effect of a pressure-surface separation region will be a decrease in the normal force on the geometry[1]. If a separation vortex lattice is under the geometry for approximately half of the geometry's chord-length, and above the geometry for approximately half of the geometry's chord, it is logical that the total decrease in (upwards) normal force where the separation vortex lattice is above the body might compensate for the total increase in (upwards) normal force where the separation vortex lattice is below the body. If - at the same time - the panel whose leading-edge filament is the presumed separation line is small, then the effect on the Kutta-Joukowski force determination of forcing a non-zero net circulation to be zero will be small. Consequently, the fact that modelling pressure-surface separation does not significantly change the aerodynamic coefficient polar, is - quite possibly - an expression of the reattachment problem.

6.1 Resolution and the Reattachment Problem

Reattachment problems appear to be common for multiple wake vortex methods applied to membrane-problems with bluff leading edges of significant thickness. At least, Wilkinson [196] also mentions explicitly problems with the modelling of flow reattachment. The behavior of the relevant vortex lattices for an example of a pressure-surface separation reattachment-problem is shown in Figure 6.2.

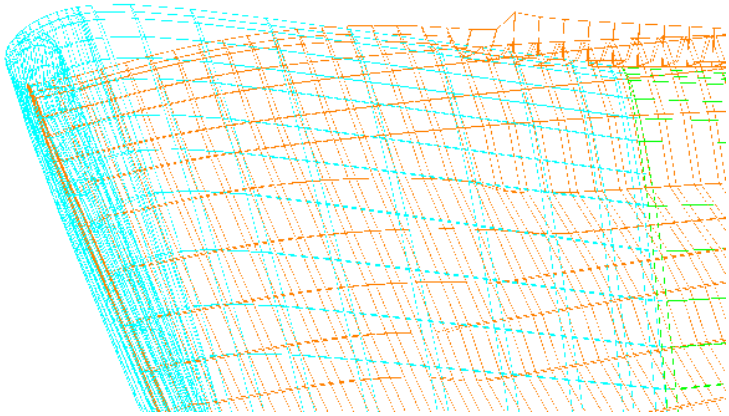

Figure 6.2: The reattachment problem as the pressure-surface separation vortex lattice passes through the bound vortex lattice at $\alpha = 0^o$.

[1] from the results on the FP3D case, but also intuitively because separation is equivalent to a relaxation of the boundary conditions

This comes down to the problem mentioned in Section 5.5.2 that the only method of preventing one vortex lattice from passing through another is the resolution of each vortex lattice. When the distance between the nodes is large enough, then the vortex lattice nodes near a potential reattachment location - who are convected based on the velocity at their upstream neighbor node - overshoot and pass through the next vortex lattice. When this happens over the body, the net circulation at the bound leading-edge vortex lattice filaments should be - but are not - compensated for the additional vortex filaments that are close by. The reattachment problem is an inherent difficulty in the method, because the vortex lattices represent either material surfaces - which are assumed to be impermeable - or stream-surfaces - which ought not cross-one another.

The LEI shape - or the sail-and-mast configuration of Wilkinson [196] - is particularly susceptible to the reattachment problem, because the separated flow from both of the surfaces takes the form of a separation bubble rather than an open-separation (refer back to Deaves' predicted separation regions, shown in Figure 2.11) for a large portion of the relevant flight angles-of-attack.

This reattachment problem demonstrates itself - not only by visually inspecting whether one vortex lattice passes through another - but also by unreasonable aerodynamic coefficients, including negative drag values. The wake vortex lattice which passes through the surface induces velocities with both a surface-normal and surface-tangential component. The bound vortex lattice must assume larger circulation strengths to cancel the surface-normal flow, but the compensating wake vortex circulation strengths are not explicitly considered in the net circulation strengths of the bound vortex rings to which they are near. Consequently, this reattachment induces a larger magnitude surface-tangential velocity. When the Kutta-Joukowski relation for aerodynamic force is applied to the velocity at the force-evaluation points - the sum of the surface-tangential components of all of the induced velocities and the apparent velocity - this increased velocity and circulation strength cause a spike in the pressure at the location where the wake vortex lattice passes through the bound vortex lattice.

This reattachment point is likely to be on the canopy. We can logically refine this estimation to say that, because flow reattachment occurs smoothly[2], and because recovery means that the separation bubble surface will curve in towards the surface rather than flatly following the free-stream, we expect the reattachment points to occur closer to the trailing edge than the freestream-canopy-tangent point. The further that the reattachment point is behind the freestream-canopy tangent point, the more the surface-normal vector will shift into the freestream direction. Remember that the Kutta-Joukowski aerodynamic force relation always determines forces which are perpendicular to the leading-edge filament, due to the cross product in the relation. Since drag is defined as being the component of the aerodynamic force that is parallel to the free-stream, we logically expect that the influence of the separation vortex lattice passing through the bound vortex lattice will have a larger effect on the drag than the lift.

Ultimately, it appears that when reattachment should happen, it is very difficult both, to adjust the boundary conditions to reflect the Kutta condition on a thickness-free membrane, and also to sufficiently resolve the geometry to properly enforce those boundary conditions. The fact that vorticity is discretized in vortex methods, rather than behaving continuously as is physical, allows vortex sheets to disregard flow tangency, while nominally satisfying the Neumann-boundary condition computational constraints at the collocation points. That is, the reattachment problem - the inability of the VLM_{MW} to model reattachment, instead allowing stream-surfaces to pass through one another - is a result of the discretization process of the flow vorticity, and is particularly relevant to thickness-free geometries with a reattachment line - on one surface - crossing a separation line - that should lay on the other surface.

[2] where reattachment, again, should satisfy the Kutta condition at the reattachment point, though it may not be possible to enforce this condition due to the thickness-free model for a membrane wing.

6.2 Possible Avenues to Solving the Reattachment Problem

It would be logical that one method of resolving this problem is to set the resolution sufficiently high that that the downstream-direction distance between the wake vortex lattice nodes is small. However, as previously mentioned, the runtime scales with the number of vortex filaments squared. Consequently, it occurs that the elimination of the reattachment problem may require an extraordinary computational expense. In the VLM_{MW}'s current form, this additional expense is such that the run-time can exceed the run-time required for a RANS - approximately 30 hours, from Deaves' [51] work - simulation, and risks that the VLM_{MW}, run on a desktop version of Matlab, may hang prior to completion.

If we cannot sufficiently increase the resolution with the current form of the VLM_{MW}, there are a few possible avenues to tackling the reattachment problem which would be suggested for further study. These possible avenues could be used separately or together.

6.2.1 Speed-Up

That which makes it infeasible from a practical perspective to sufficiently increase the resolution to probably eliminate the reattachment problem, is the run-time of the VLM_{MW} in its current form. Some adjustments which could be made to the method that may enable code speed-up, might include:

- *language selection* Matlab is not known for being an extraordinarily fast language. Were a future VLM_{MW} written - or compiled - into another language, such as C, C++, or Fortran, it is likely that code-speed up could be significant.
- *code vectorization* The current form of the VLM_{MW} was developed as a proof-of-concept, where the ability to easily read and develop the code functionality was judged to be more important than computational speed. This led to methods of matrix allocation which are not ideal from a computational speed perspective. For example, a coefficient matrix $\mathbf{A}$ is assembled from a summation (over every modelled vortex lattice) of for-loop summations of N_J single rows, each corresponding to a single boundary-condition. There are, in effect, many nested for-loops which run from $n_c = 1$ to $n_c = N_C + 1$ and from $n_b = 1$ to $n_b = N_B + 1$. It should be possible to gain a code speed-up by swapping these for-loop computations to a vector-algebra form.
- *parallelization* One of the advantages of potential-flow methods is their suitability for massive parallelization. Those for-loops which are not-well suited to vectorization might benefit from parallel loop computation[3], to be run on a multicore system.
- *information transfer* Repeatedly passing large matrices into and out-of multiple functions cannot be expected to be computationally fast. Unfortunately, from the perspective of speed, many of the functions within the VLM_{MW}, in its current form, are built for modular testing. The result, is that the geometric vortex-lattice matrices are passed into the functions in their entire form, rather than in a trimmed form containing purely the relevant matrix index values.
- *warm-starting* Those portions of the large influence coefficient matrices which do not change - or change very little - for small changes to model geometries or small wake deformations would benefit heavily from warm-starting.
- *geometric simplification for symmetry* If it were decided that the input kite geometry would always be symmetric about $\hat{y}$, it would be possible to remove half of the kite and geometrically determine the additional influence coefficients to add to the influence coefficient matrix based on a mirroring of positions. This would half the number of span-wise nodes required for a constant span-wise resolution. Since run-time scales with N_B^2, assuming a symmetric kite could potentially save up to three-quarters of the computation time. However, this possibility would prevent the application of a future-form VLM_{MW} to the asymmetric deformation-modes that are a natural product of non-zero side-slip angles.

[3] as with `parfor` in the Matlab parallel computing toolbox

- *alteration of wake structure* It might be useful to reconsider the discretization of vorticity in the wake, either by grouping nearby vortex nodes in a manner similar to a Fast Multipole Method (FMM), for whom runtime is known to be scale with $\mathcal{O}(N \log N)$, or to progressively increase the pseudo-timestep for vortex rings as they travel downstream, rather than splitting the wake into the free-wake and fixed-wake regions applied here. It is possible that altering this wake structure might decrease run-time for a given effective resolution. However, it does not appear that either of these methods would be able to decrease the cost of increasing resolution within the area relevant to the separation vortex-lattice behavior - at the risk of losing information rather than increasing computational speed - in comparison to the wake resolution-concentration which is already applied in the described VLM_{MW}.

6.2.2 Include Reattachment

It would be tempting to think that the reattachment problem could be solved by including those wake leading-edge vortex-ring filaments which are close to the body into the bound net-circulation calculations.

However, this step may not be as trivial as it might appear, due - as hinted at above - to the thickness-free modelling geometry for the canopy.

It is particularly difficult to model flow reattachment for membrane wings. On a membrane wing, there is no distinction between the suction- and pressure-surfaces in the modelling of the bound vortex lattices. This requires that the separation line on the suction surface and the reattachment line on the pressure surface may occupy the same space. Unfortunately, if the reattachment line - which should lay on the pressure surface - and the separation line - which should be on the suction surface - cross, then the lines cannot occupy constant chord-wise geometric node indices. That is, if the canopy is modelled as a thickness-free geometry, then it is not possible to include crossing pressure- and suction-surface separation- and reattachment-lines onto non-crossing constant-chord-wise-index geometric node lines. If this is the case, then the net circulation at the separation and/or reattachment lines cannot be adjusted to reflect the Kutta condition. Then, on this thickness-free surface[4], the flow requirements for reattachment may not be enforceable.

We know from Van Kappel [183] that attempting to model an LEI kite entirely as finite-thickness surface has convergence problems, due to the resolution requirement caused by the small thickness.

One hope, then, might be to restrict the multiple-wake method to flow conditions where the separation-line and reattachment-line do not cross, such that the Kutta condition is enforceable. The difficulty, then, would be in predicting which flow conditions are allowed under this restriction, and which flow conditions are disallowed.

Unhappily, for the LEI-kite case, we know from Deaves [51], that the reattachment line on the pressure-surface of the canopy frequently passes through those points where the separation bubble on the suction-surface can be found.

The alternative, then, may be to force the kite geometry to hold a finite-thickness representation where the separation-bubble would lay. This possible goal could be achieved by profile-smoothing along the wind-shadow curtain found in a two-iteration application of the VLM_{MW}.

6.2.3 Wind-Shadow Curtain Double-Step Method

The method for eliminating the reattachment problem which the author believes to be the most promising is to skip the problem entirely by running the VLM_{MW} twice per LEI-kite simulation.

[4]It is relevant to mention that the reattachment problem does not seem to be typical for finite-thickness wings, such that multiple wake vortex methods are frequently used for wind-turbine blades - a fact which partially inspired the initial proposal of this method as a potential solution-method for the LEI-kite aerodynamics problem.

In the first run, the geometry mesh could be built to resemble the physical deformation state, with known separation locations. The locations of the separated wake nodes until the predicted reattachment locations could be extracted from the results of this first run. With these node locations, a wind-shadow curtain[5] could be added to the LEI-kite geometry, effectively smoothing the profiles as done by Deaves.

This smoothed LEI-kite could be re-entered as an input into another aerodynamic model - reasonably speaking, the VLM_{MW} again - for a second run to better determine the pressure distributions.

This double-step method would of course increase the aerodynamic-model runtime, but it is rather likely that this runtime would still be noticeably less than the runtime for a CFD simulation while producing results which are "close-enough" to be useful for the rough iterations of FSI-based design work.

The primary difference between the uncertainty in such a double-step profile-smoothing method than in the assumed profile-smoothing used in many existing models - such as in Deaves [51] is that the smoothed profile generated by such a double-step would be a function of the inflow, rather than an assumed geometry. This may potentially decrease the uncertainty caused by introducing this profile-smoothing.

While VLM_{MW} does have the error - explicitly in comparison to RANS results - caused by the lack of a boundary-layer model that VACM methods, such as van Kappel's $\text{VLM}_{\text{N-VK}}$, do not have, the VLM_{MW} also is not susceptible to the unpredictable integration-step convergence-failure which makes VACM methods difficult to apply to significant-separation problems. Further, qualitatively-speaking, the general lift and drag coefficients found with the VLM_{MW}, in cases without a significant reattachment problem, appear to be reasonably in accord with the RANS results.

6.3 Resolution for Computational Speed and Accuracy on a Leading Edged Inflatable Kite

Of course, assessments of the engineering trade-off between computational expense and accuracy require quantitative analysis in addition to qualitative comparisons.

In Figures 6.3, 6.4, and 6.5 we can see the error in predicted lift and drag coefficients for various angles-of-attack, in comparison with the normalization-area corrected results from Deaves' [51] RANS study of the same geometry.

Notably, we can see that the influence of the reattachment problem can be very large, prompting maximum C_L errors on the order of 10^4 and maximum C_D errors on the order of 10^6. However, errors on the order of 1.0, 0.1 and 0.001 also appear to be possible for various resolution selections, largely dependent on the behavior of the separation-region at a given angle-of-attack.

Here, increasing the computational-time has a less obvious correlation with increasing model accuracy than can be seen in the results for the FP3D case (Figure 5.23) again, because including separation modelling under the influence of the reattachment problem can produce a result that is numerically similar to the VLM_{MW} result for fully-attached flow - but with, naturally, a runtime that is a factor of two or three larger, dependent on the number of separation surfaces modelled.

[5] As far as the author is aware, the credit for the term "wind-shadow curtain" in relation to LEI-profile smoothing belongs with Anderson [14].

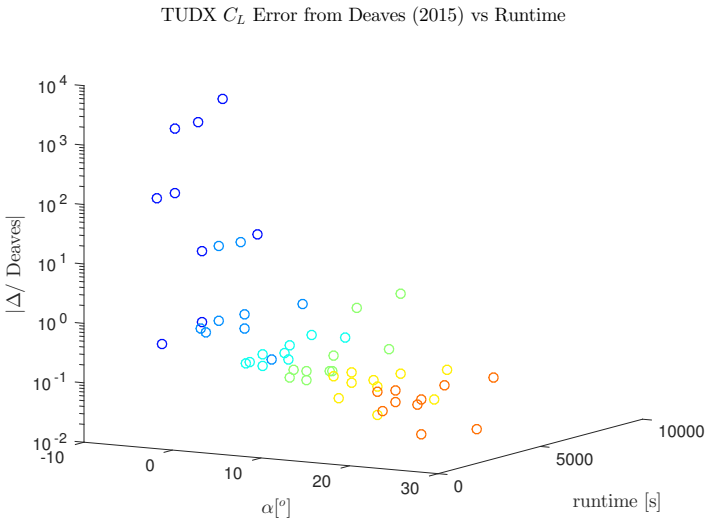

Figure 6.3: The difference between VLM_{MW} and RANS predicted C_L values, as function of angle of attack and runtime. Note that the bubble coloring corresponds to angle-of-attack.

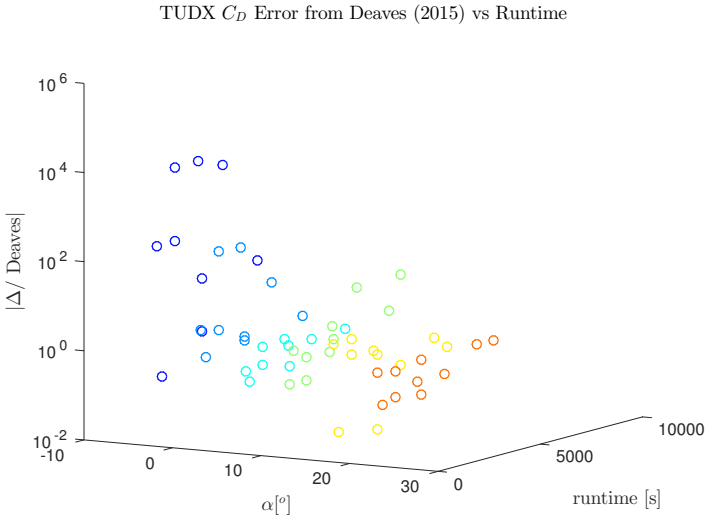

Figure 6.4: The difference between VLM_{MW} and RANS predicted C_D values, as function of angle of attack and runtime. Note that the bubble coloring corresponds to angle-of-attack.

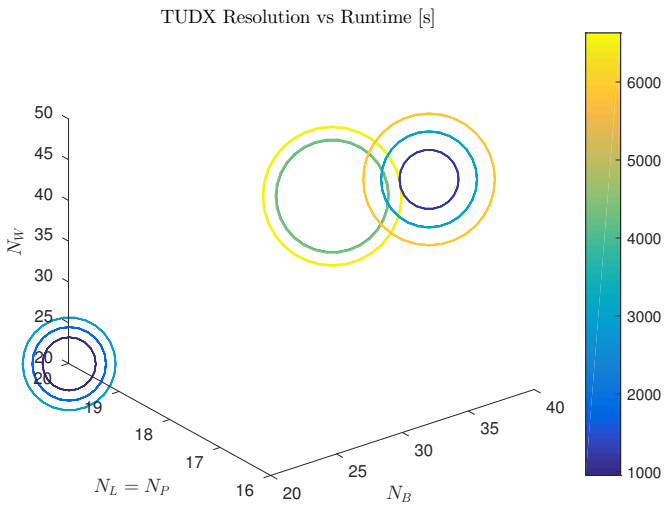

Figure 6.5: The model resolutions corresponding to the runtimes in Figures 6.3 and 6.4.

6.4 Demonstration of Pressure-Distribution Predictions

While net aerodynamic coefficients are useful for assessing the accuracy - in comparison to RANS - of the VLM_{MW}, they are not themselves the intended output of the aerodynamic model. Rather, if this method[6] were applied to the LEI-kite FSI problem, the pressure distributions themselves are needed.

An example of such a pressure distribution can be seen in Figure 6.6.

Notably, we can again see the $C_P = 0$ line where the Kutta condition is enforced, though in this case, the separation line is taken as the line of the surface-freestream-tangent. We can also see where the pressure coefficients are large on the thick LEI-tube; the pressure growth where the separation bubble is at it's thickest; and the pressure spike when the separation vortex lattice becomes close to the surface, prior to its pass though the bound vortex lattice (refer again to Figure 6.2).

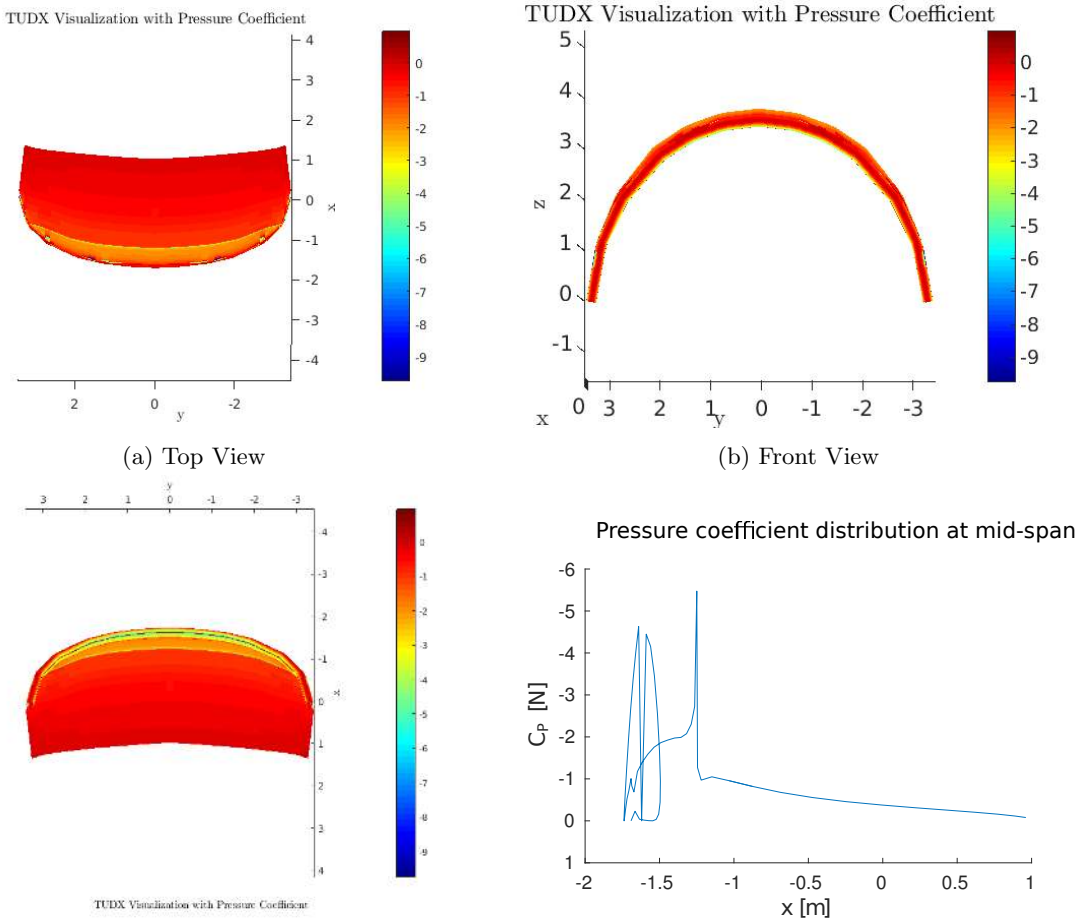

(a) Top View

(b) Front View

(c) Bottom View

(d) Distribution at Root

Figure 6.6: TUDX Pressure Distribution with $N_B = N_L + N_P = 60$, $N_W = 10$, and $f_S = 1/5$ at $\alpha = 0$, including pressure-surface separation, but not suction-surface separation.

[6] though in a accelerated form rather than this proof-of-concept form

Chapter 7

Conclusions

We can assess the hypothesis of this thesis, proposing that:

> The ability of a quasi-steady multiple-wake vortex lattice method to quickly and accurately model surf-kite aerodynamics is heavily limited by the method's inability to model reattachment, though the results for the double-wake method appear promising, depending on the respective understanding of "quickly" and "accurately".

Notwithstanding the reattachment problem and the neglected effects of the boundary-layer, it appears that a careful selection of resolution parameters for the LEI-kite geometry can bring errors for net lift and drag coefficient predictions with the VLM_{MW} to approximately ten percent of the RANS simulation results. That is, it appears possible for the VLM_{MW} to have the same order of uncertainty with respect to RANS results as is generated by profile-smoothing in Deaves' [51] RANS study.

However, the model is strongly limited by an inability to enforce the Kutta condition on a reattachment-line when this reattachment-line crosses a separation-line in the thickness-free representation. Further, the model appears to require - near a reattachment-location - a very high body- and wake-resolution to extend the proper enforcement of the flow-tangency constraint to the space between the collocation points and ensure that geometric surfaces are impermeable to the separation stream-surfaces.

Given that reattachment is expected on both the suction- and pressure-surfaces of the LEI kite in the majority of its flight regime, the reattachment problem constitutes a serious modelling restriction.

Based on the results found with this code it would appear promising to further develop this method, primarily with the hope of finding a path around the reattachment problem. The following questions may be part of such an exploration:

- What is the influence of the quasi-steady flow assumption on the pressure distributions predicted by the VLM_{MW}?
- How would we validate the predictions of quasi-steady aerodynamic models intended for LEI-kite geometries, such as the VLM_{MW}, against wind-tunnel test results?
- What is the influence of assuming that transition does not occur in the boundary layer on the pressure distributions predicted by the VLM_{MW}?
- How does the selection of different vortex core models (from the $n_{VCM} = 2$ used in the presented results) effect the VLM_{MW} predictions?
- How would the code speed-up methods described in Section 6.2.1 influence the tradeoff between compuational-cost and accuracy (again, with respect to a RANS solution)?

- Can the introduction of a double-step wind-shadow curtain solution step, as mentioned in Section 6.2.3 eliminate or minimize the effect of the reattachment problem when the VLM_{MW} is applied to an LEI-kite?
- Would a multiple-wake vortex method constructed such that separation surfaces are always assumed to be bubble-shaped, but occasionally pop "infinitely-far" downstream - rather than the current method where separation surfaces are assumed to be open-separation representations, of which combinations occasionally end up bubble-shaped - be less suceptible to the reattachment problem?
- How would the addition of an MVP separation-location solution-loop, based on the pressure-coefficients found in a primary run, influence the tradeoff between computational-cost and accuracy (again, with respect to a RANS solution)?

The author believes that with further development the LEI-kite aerodynamic modelling method concept tested in this proof-of-concept thesis could be a useful module within the AWE's FSI-modelling codebase. However, in its current form, good engineering judgement is necessary to restrict the use of the VLM_{MW} to situations where flow-reattachment is either avoided or does not coincide with a separation-location, and where boundary-layer effects are small.

Based on the quantitative result evaluating the proof-of-concept form of the VLM_{MW} for computational speed and model accuracy, in comparison to windtunnel measurements for a unity-aspect ratio flat plate (FP3D), and CFD results for the extruded Clark Y arc-shaped wing (CYKW) and an LEI-kite geometry based on the TU Delft AWE group's TUD-25mV2 25m^2 kite (TUDX), that this thesis work has satisfied its stated success criteria.

Appendix A

Leading-Edge Inflatable Kite Geometric-Mesh Generation from TUD-25mV2 Datafiles

The LEI-geometries TUD7 and TUDX are based on the seven-profiles-at-thirteen-spanwise-locations-fit determined and used by Deaves [51] to the TUD-25mV2 $25m^2$ kite. These geometric points are given as seven coordinate tables in the $\hat{x}'$, $\hat{z}'$ cross-sectional reference frame plane, and a table giving the locations of the profile leading- and trailing-edge in the body-fixed reference frame, as well as an orientation vector for the $\hat{z}'$ vector.

It should be mentioned that Deaves uses a rotated set of body-fixed axes. To convert from his body-fixed coordinates $\hat{x}_{MD}$, $\hat{y}_{MD}$, $\hat{z}_{MD}$ to the body-fixed coordinates used here $\hat{x}$, $\hat{y}$, $\hat{z}$:

$$\begin{aligned} \hat{x} &= -\hat{z}_{MD} \\ \hat{y} &= -\hat{x}_{MD} \\ \hat{z} &= \hat{y}_{MD} \end{aligned}$$

When we have the locations of the leading-edge point $\mathbf{x}_{LE}$, $\mathbf{x}_{TE}$ and $\mathbf{z}$ in the body-fixed reference frame used here, we can geometrically find the cross-sectional axes:

$$\begin{aligned} \mathbf{c} &= \mathbf{x}_{TE} - \mathbf{x}_{LE} \\ &\quad \hookrightarrow \hat{x}' = \frac{\mathbf{x}_{TE} - \mathbf{x}_{LE}}{||\mathbf{x}_{TE} - \mathbf{x}_{LE}||} \\ &\quad \hookrightarrow c = ||\mathbf{x}_{TE} - \mathbf{x}_{LE}|| \\ &\quad \hookrightarrow \hat{c} = \frac{\mathbf{c}}{c} \\ \hat{z}' &= \frac{\mathbf{z}}{||\mathbf{z}||} \end{aligned}$$

Then, we can convert a point $\mathbf{x}_g = x'_g\hat{x}' + y'_g\hat{y}' + z'_g\hat{z}'$ in the cross-sectional reference frame to the body-fixed reference frame $\mathbf{x}_g = x_g\hat{x} + y_g\hat{y} + z_g\hat{z}$:

$$\mathbf{x}_g = \left(x'_g c\mathbf{x}' + z'_g c\hat{z}'\right) + \mathbf{x}_{LE}$$

If we write a system of 2 equations for the x' and z' terms, we can find the conversion in the opposite

direction:

$$\begin{aligned} x_g &= \left(x'_g c\mathbf{x}'_x + z'_g c\hat{z}'_x\right) + x_{LE} \\ z_g &= \left(x'_g c\mathbf{x}'_z + z'_g c\hat{z}'_z\right) + z_{LE} \\ &\updownarrow \\ x'_g &= \left(\frac{z_g - z_{LE}}{c}\hat{z}'_x - \frac{x_g - x_{LE}}{c}\hat{z}'_z\right)\left(\hat{z}'_x\mathbf{x}'_z - \mathbf{x}'_x\hat{z}'_z\right)^{-1} \\ z'_g &= \left(\frac{x_g - x_{LE}}{c}\mathbf{x}'_z - \frac{z_g - z_{LE}}{c}\mathbf{x}'_x\right)\left(\hat{z}'_x\mathbf{x}'_z - \mathbf{x}'_x\hat{z}'_z\right)^{-1} \end{aligned}$$

The next concern is to find the assumed separation point on the profile. With uncertainty about the separation locations, we make the assumption that the flow separation location occurs where the freestream is tangent to the surface.

This tangent location can be found in a fairly straightforward manner by minimizing the norm of the cross-product of the estimated the unit-surface-parallel vector and the unit-freestream-velocity vector.

For the pressure-surface separation point - which will always be on the LEI tube, with this assumption of a surface-freestream-tangent separation-point:

$$x_{sep,PS} = x \;\Big|\; \min_x \left((\sin(\theta)\hat{c} - \cos(\theta)\hat{z}) \times \hat{U}_A\right)$$

If the suction-surface separation point is on the LEI tube, it will be at the opposite radial position ($\theta_{sep,SS} = \theta_{sep,PS} + \pi$) from the pressure-surface separation point. If the suction-surface separation point is on the canopy:

$$x_{sep,SS} = x \;\Big|\; \min_x \left(\left(\mathbf{c} + \frac{dy}{dx}\mathbf{z}\right) \times \hat{U}_A\right)$$

Then, we distribute the geometric nodes evenly between the intersection point, the pressure-surface separation point, the intersection point, the suction-surface separation point, and the trailing edge. Note that if the suction-surface separation point is on the LEI tube, then the second intersection-point node will occur after the suction-surface separation point, in the prior list.

There are, then $N_C = N_P + N_L + 1$ nodes in a profile.

In order to build a kite from these 13 profiles, we apply some interpolation scheme to the $\hat{y}$ points, evenly distributed according to the kite-arc angle.

$$y_{interp} = \frac{1}{2}\left(1 - \cos(\beta_{XZ} b(n_c)) + \min(y(n_c))\right)$$

It is strongly suggested that a simple interpolation scheme for x_{interp} and z_{interp} be used. In the input files generated here, linear interpolation is used.

It is further, strongly recommended that spline interpolation **not** be used, as there is a risk of generating unexpected geometries near the leading edge - particularly in cases where the suction-surface separation point shifts between the leading-edge tube and the canopy.

Appendix B

Artificial Geometric-Mesh Generation

It can occasionally be handy to have a method that will create an "arbitrary" geometry with the notable topological features of an LEI kite but without the complexities of an LEI kite interpolated from multiple datafiles with assumed separation lines. This is especially true when debugging.

In order to test the VLM without a true matrix of surface-point locations, a geometric mesh can be generated for an idealized kite. This artificial kite is built by placing LEI-profile kite sections along a LEI centerline, so that the center of the LE tube of the profile sits on the LEI centerline, and the profile is rotated in the body-fixed reference frame according to the angle of the LEI centerline in the spanwise direction and the desired pitch of the section profile.

B.1 The Artificial LEI Centerline

The centerline is assumed to contain the origins of the cross-sectional reference frame coordinate system, where b is the kite wingspan - for the TU Delft V2 kite $b = 6.662$m - and h_K is the kite arc-height - for the TU Delft V2 $h_K = 3.577$m..

The y_{cntl} points of the centerline can be distributed either linearly in the $\hat{y}$ direction, or with a sine distribution ($y_{cntl} = \frac{b}{2}\sin(\theta_X)$ so that the geometry is described with higher resolution near the tips of the kite.

The x_{cntl} points of the centerline are defined to allow for sweep in the downwards direction. This can be:

- *elliptical* such that:
$$x_{cntl} = x_{cntl}(\text{tip}) - \frac{x_{cntl}(\text{tip})}{b/2}\sqrt{\frac{b^2}{4} - y_{cntl}^2}$$
- *linear* with a given sweep angle γ_s, expressed in radians:
$$x_{cntl} = |y_{cntl}|\tan\gamma_s$$
- *no-sweep* where by default, the centerline x_{cntl} is linear with a sweep angle of $\gamma_s = 0$ rad.

The z_{cntl} points of the centerline are defined to allow an elliptical centerline that covers some given

arc-angle of an ellipse θ_{XZ}. Then:

$$\begin{aligned}
\beta_{XZ} &= \arcsin\left(\frac{b/2}{R_I \tan\left(\frac{1}{2}\theta_{XZ}\right)}\right) \\
R_O &= \frac{b/2}{\cos(\beta_{XZ})} \\
z_{cntl,0} &= \frac{b/2}{\tan\left(\frac{1}{2}\theta_{XZ}\right)} \\
z_{cntl} &= R_I \sin\left(\arccos\left(\frac{y_{cntl}}{R_O}\right)\right) - z_{cntl,0}
\end{aligned}$$

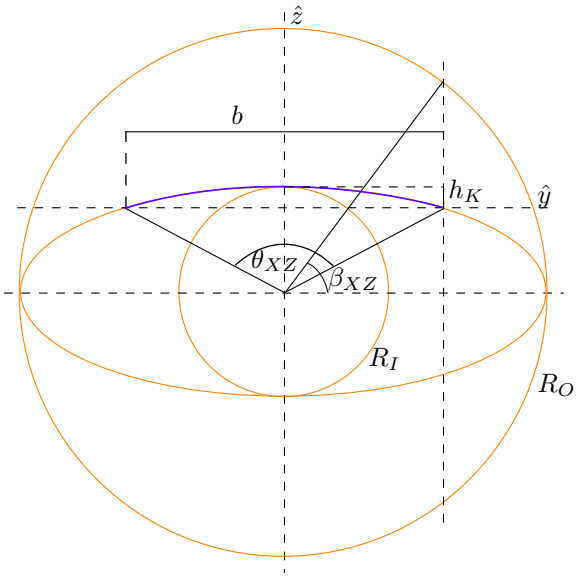

Figure B.1: The y-z relationship of the elliptical centerline.

B.2 The LEI-Profile Family

The points **M**, **N**, **O**, **P**, and **S** are defined according the 2D section geometry coordinates $\hat{x}', \hat{z}'$:

$$\begin{aligned}
\mathbf{x}'(O) &= \langle 0,\ 0\rangle \\
\mathbf{x}'(M) &= \langle -r_{LEI},\ 0\rangle \\
\mathbf{x}'(N) &= \langle x'_{cLEI},\ -z'_{cLEI}\rangle \\
\mathbf{x}'(P) &= \langle c - r_{LEI},\ 0\rangle \\
\mathbf{x}'(S) &= \frac{r_{LEI}}{r_{Canopy} - r_{LEI}}\langle -x'_{cLEI},\ z'_{cLEI}\rangle
\end{aligned}$$

Applying Pythagoras, with the definition that $a = c - r_{LEI} - x'_{cLEI}$:

$$\begin{aligned}
(r_{Canopy} - r_{LEI})^2 &= z'^2_{cLEI} + x'^2_{cLEI} \\
r^2_{Canopy} &= z'^2_{cLEI} + a^2
\end{aligned}$$

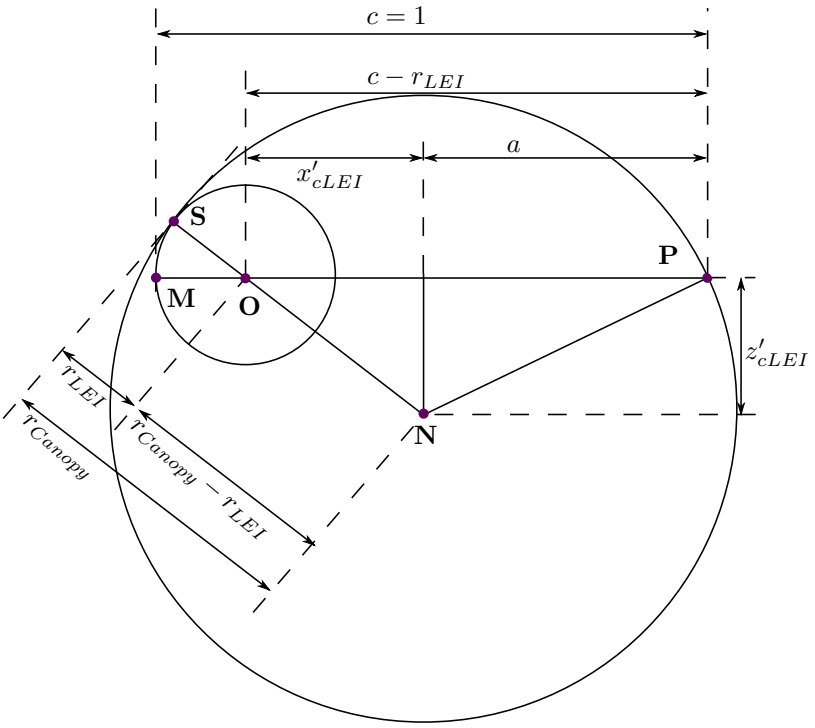

Figure B.2: 2D LEI Kite Section Geometry

Solving these two expressions for x'_{cLEI} and z'_{cLEI} gives:

$$x'_{cLEI} = -\frac{(-c^2 + 2cr_{LEI} - 2r_{LEI}^2 + 2r_{Canopy}r_{LEI})}{(2(c - r_{LEI}))}$$
$$z'_{cLEI} = \frac{(-c(c - 2r_{Canopy})\sqrt{(c - 2r_{LEI})(c + 2r_{Canopy} - 2r_{LEI})})}{(2(c - r_{LEI}))}$$

Then, the 2D canopy follows the large-circle arc between points **S** and **P** as $(x'_g - x'_{cLEI})^2 + (z'_g + z'_{cLEI})^2 = r_{Canopy}^2$, and the 2D LEI tube follows the small-circle as $x_g'^2 + z_g'^2 = r_{LEI}^2$.

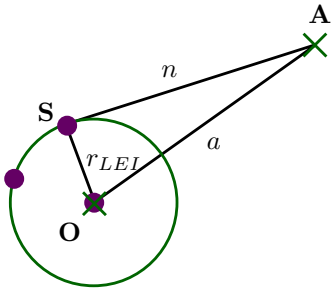

Figure B.3: Close up at connection between 2D LEI tube vortex lattice and canopy vortex lattice

From two known points $\mathbf{x}'(A)$ and $\mathbf{x}'(O)$. and a circle about **O** of radius r_{LEI}, a Pythagorean identity and the equation of the circle can be solved simultaneously to give the location of the tangential intersection

point **S** can be found:

$$\begin{aligned} a &= \sqrt{((x'_A - x'_O)^2 + (z'_A - z'_O)^2)} \\ n &= \sqrt{((x'_S - x'_A)^2 + (z'_S - z'_A)^2)} \\ a^2 &= n^2 + r_{LEI}^2 \\ (x'_S - x'_O)^2 + (z'_S - z'_O)^2 &= r_{LEI}^2 \end{aligned}$$

This determines the coordinates of $\mathbf{x}'(S) = \langle x'_S,\ z'_S \rangle$:

$$\begin{aligned} \mathbf{x}'(S) = & \left(\frac{1}{(x'^2_A - 2x'_A x'_O + x'^2_O + z'^2_A - 2z'_A z'_O + z'^2_O)} \right) \\ & \langle r^2_{LEI} x'_A - r^2_{LEI} x'_O - 2x'_A x'^2_O + x'^2_A x'_O + x'_O z'^2_A + x'_O z'^2_O \\ & + x'^3_O - r_{LEI} z'_A \sqrt{(-r^2_{LEI} + x'^2_A - 2x'_A x'_O + x'^2_O + z'^2_A - 2z'_A z'_O + z'^2_O)} \\ & + r_{LEI} z'_O \sqrt{(-r^2_{LEI} + x'^2_A - 2x'_A x'_O + x'^2_O + z'^2_A - 2z'_A z'_O + z'^2_O)} - 2x'_O z'_A z'_O, \\ & r^2_{LEI} z'_A - r^2_{LEI} z'_O + x'^2_A z'_O + x'^2_O z'_O - 2z'_A z'^2_O + z'^2_A z'_O \\ & + z'^3_O + r_{LEI} x'_A \sqrt{(-r^2_{LEI} + x'^2_A - 2x'_A x'_O + x'^2_O + z'^2_A - 2z'_A z'_O + z'^2_O)} \\ & - r_{LEI} x'_O \sqrt{(-r^2_{LEI} + x'^2_A - 2x'_A x'_O + x'^2_O + z'^2_A - 2z'_A z'_O + z'^2_O)} - 2x'_A x'_O z'_O \rangle \end{aligned}$$

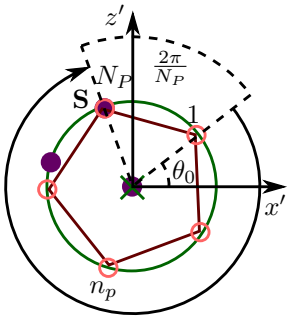

Figure B.4: 2D Vortex Lattice Nodes Distribution over the LEI Tube

The LEI tube can be represented geometrically as a regular polygon, drawn clockwise to end with its last cross-sectional meshpoint at the intersection point **S**:

$$\mathbf{x}'_g(1 \le n_j \le N_P) = \mathbf{x}'_g(O) + r_{LEI} \langle \cos(\theta_\Sigma),\ -\sin(\theta_\Sigma) \rangle$$

where

$$\begin{aligned} \theta_\Sigma &= \theta_P - \theta_0 - \theta_{shift} \\ \theta_P &= \frac{2\pi}{N_P}(n_p - 1) \\ \theta_0 &= \frac{\pi}{2} - \arctan\left(\frac{-S_x}{S_z} - \frac{2\pi}{N_P} \right) \\ \theta_{shift} &= \frac{\pi}{N_P} \end{aligned}$$

In order to ensure that the LEI tube is a closed body, the first cross-sectional meshpoint ($n_p = 1$), should then be moved onto the canopy. Depending on the relative dimensions of the geometry, the distance moved is likely to be small wrt. the LEI tube radius. Consequently, it is proposed to keep the $\hat{x}'$ coordinate of the polygonal location, and calculate the $\hat{z}'$ coordinate according to the canopy circle formula.

B.3 Assembly of the LEI-Profiles along the LEI Centerline

The chord of this idealized kite is assumed to vary between its root and tip values, c_{root} and c_{tip} respectively. This variation can be:

- *elliptical* for an elliptical planform:

$$c(y_{cntl}) = c_{tip} + (c_{root} - c_{tip})\sqrt{1 - \left(\frac{y_{cntl}}{b/2}\right)^2}$$

- *linear* for a linear chord distribution:

$$c(y_{cntl}) = c_{root} - \frac{(c_{root} - c_{tip})}{b/2}|y_{cntl}|$$

- *cosine* as the cosine of the span-wise location:

$$c(y_{cntl}) = c_{tip} + (c_{root} - c_{tip})\cos\left(\frac{\pi}{b}|y_{cntl}|\right)$$

To rotate a vector between the sectional reference frame and the body-fixed reference frame, two rotational angles are needed. The pitch angle θ_R is given to vary linearly between the root and the tip of the kite. The roll angle ψ_R is determined from the arc-tangent of the derivative of the centerline $\psi_R = \arctan\left(\frac{\partial z_{cntl}}{\partial y_{cntl}}\right)$. Note that no yaw angle is given, because body yaw asymetries are assumed to be included into the inflow conditions.

A rotation matrix $\mathbf{M}_R$ can be determined:

$$\mathbf{M}_R = \begin{pmatrix} \cos(\theta_R) & \sin(\theta_R)\sin(\psi_R) & \sin(\theta_R)\cos(\psi_R) \\ 0 & \cos(\psi_R) & -\sin(\psi_R) \\ -\sin(\theta_R) & \cos(\theta_R)\sin(\psi_R) & \cos(\theta_R)\cos(\psi_R) \end{pmatrix}$$

To place a point $\mathbf{P}'$ from the cross-sectional reference frame into the body-fixed reference frame:

$$\mathbf{P} = \langle x_{cntl},\ y_{cntl},\ z_{cntl} \rangle + \mathbf{M}_R\mathbf{P}'$$

B.4 Generation of an Idealized Kite Geometry

An idealized kite 2D cross-section is generated to test the above descriptions, with the following dimensions:

Reference	Symbol	Value
Chord	c	1
LEI Radius	r_{LEI}	$c/10$
Canopy Radius	r_{Canopy}	$5c$

Note how the airfoil chord - despite being shifted forwards by the choice of coordinate origin - is still one, as the LE sits at the leftmost point of the LEI tube, and the TE sits at the rightmost canopy collocation point.

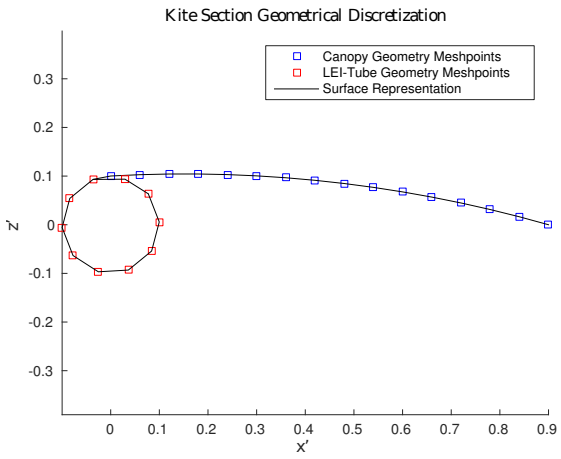

Figure B.5: An Arbitrary Kite Profile Generated and Discretized According to the Described Rules

B.4.1 Matlab Geometrical Kite Generation and Discretization

Again, to test and demonstrate the above descriptions, a 3D kite is generated as an elliptical connection of idealized LEI-profile sections. This idealized 3D kite is generated following the dimensions of the kite TUD-V2.

Reference	Symbol	Value
Kite Arc-Span	b	6.662m
Kite Arc-Height	H_K	3.577m
Sweep Angle	γ_s	0rad
Chord at Root	c_{root}	2.724m
Chord at Tip	c_{tip}	1m
LEI Radius	r_{LEI}	0.1m
Canopy Radius	r_{Canopy}	$5c_{root}$
Span-Wise Discretization Nodes	N_B	20
Polygonal LEI-Tube Discretization Nodes	N_P	5
Canopy Discretization Collocation Points	N_L	5

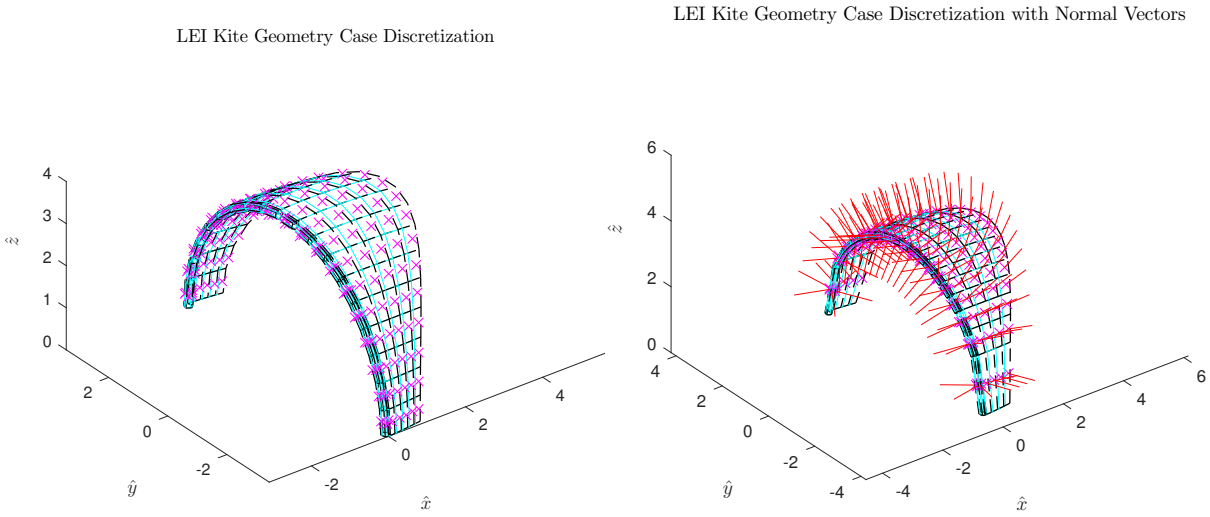

Figure B.6: An Arbitrary 3D Kite Generated and Discretized According to the Described Rules, with and without Panel Normal Vectors Displayed

B.4.2 Alternate Geometry Generation

For testing purposes, it can be useful to allow alterations to the standard geometry.

To flatten the ellipse in the $\hat{y}, \hat{z}$ plane, the arc height can be set to zero. Some of these coordinate transformations must be rewritten to prevent singularities:

$$\begin{aligned} \frac{\partial f}{\partial z} &= 0 \\ \hat{y}' &= \langle 0,\ 0,\ 1 \rangle \\ \hat{z}' &= \langle 0,\ -1,\ 0 \rangle \end{aligned}$$

To flatten the canopy in the cross-sectional plane, the canopy radius can be set to be very large in comparison to the chord. For practical purposes, three orders of magnitude $r_{Canopy} = 1000c$ is obviously very large in comparison to chords between one and ten meters.

To remove the LEI tube, N_P and r_{LEI} can be set to zero.

A linear chord distribution can be generated by applying:

$$c(y) = c_{root} - (c_{root} - c_{tip}) \frac{|y|}{\frac{1}{2}b}$$

An elliptical chord distribution can be generated, with c_{tip} is set as some small non-zero number (ie, 10^{-5}) in order not to cause singularities in the tip vortex-filament influences:

$$c(y) = c_{tip} + (c_{root} - c_{tip}) \sqrt{1 - \frac{(y - y_0)^2}{\left(\frac{1}{2}b\right)^2}}$$

FP2D: 2D Flat Plate Geometry

Altering the following dimensions from their default (kite) values and applying a linear chord distribution:

Reference	Symbol	Value
Chord at Root	c_{root}	1m
Chord at Tip	c_{tip}	c_{root}
Aspect Ratio	AR	20
Kite Arc-Span	b	$AR \cdot c_{root}$
Kite Arc-Height	H_K	0m
Canopy Radius	r_{Canopy}	$10^{10} c_{root}$
Polygonal LEI-Tube Discretization Nodes	N_P	0

W12F: Warren 12 Planform with Flat Plate Profile Geometry

Altering the following dimensions from their default (kite) values and applying a linear chord distribution to an odd number of chord-wise geometric meshpoints, we can generate a flat plate in a Warren 12 [4] configuration.

Reference	Symbol	Value
Kite Arc-Span	b	$2\sqrt{2}$m
Kite Arc-Height	H_K	0m
Sweep Angle	γ_s	0.9344rad
Chord at Root	c_{root}	1.5m
Chord at Tip	c_{tip}	1m
Canopy Radius	r_{Canopy}	$10^{10}c_{root}$
Polygonal LEI-Tube Discretization Nodes	N_P	0

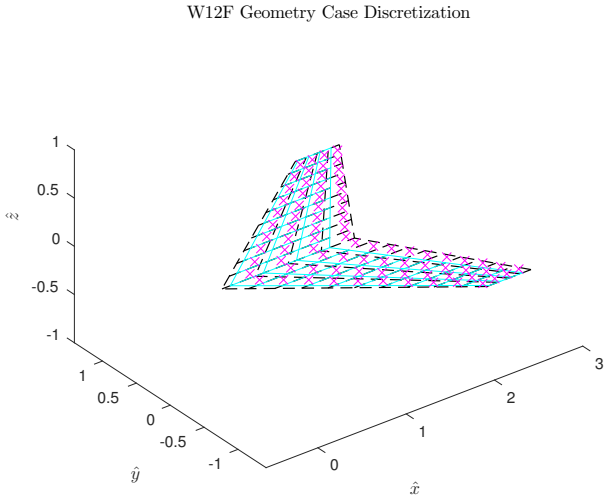

Figure B.7: A Warren 12 Planform with Flat Plate Profile Geometry (W12F) Generated According to the Described Rules

ELFW: Elliptical Planform with Flat Plate Profile Geometry

In order to test the effects of the free-wake, the lift coefficient can compared to the lift coefficient formula given by McCormick [127] for an elliptical wing with wake deflection due to downwash.

Applying the same alterations as an FP2D geometry, including an elliptical chord distribution - and an aspect ratio $AR = 18$ for comparison with the results of Sebastian & Lackner [157] - will give an ELFW geometry.

Bibliography

[1] Bainbridge Ripstop Specification Sheet. Technical report, Bainbridge, http://www.kitebuilder.com/techsheets/BainbridgeRipstopSpec.pdf, accessed 26 Nov. 2014.

[2] Conversion of Coefficients. *Popular Aviation*, 15(2):103, 1934.

[3] International Standard Atmosphere. Technical report, International Organization for Standards. ISO 2533-1975 (E), 1975.

[4] Surfaces User Manual: Vortex-Lattice Module. Technical report, Flight Level Engineering, http://flightlevelengineering.com/downloads/vlm.pdf, accessed 17 April. 2015, 2009.

[5] Y. J. Abudaram, P. G. Ifju, J. P. Hubner, and L. Ukeiley. Controlling pre-tension of silicon membranes on micro air vehicle flexible wings. In *50th AIAA Aerospace Sciences Meeting including the New Horizons Forum and Aerospace Exposition*, Nashville, Tennessee, USA, 2012.

[6] A. R. Ahmadi and S. E. Widnall. Unsteady lifting-line theory as a singular perturbation problem. *Journal of Fluid Mechanics*, 153(-1):59, Apr. 2006.

[7] U. Ahrens, M. Diehl, and R. Schmehl, editors. *Airborne Wind Energy*. Springer, Heidelberg, Germany, 2014.

[8] S. Alben. Simulating the dynamics of flexible bodies and vortex sheets. *Journal of Computational Physics*, 228(7):2587–2603, Apr. 2009.

[9] S. Alben. Regularizing a vortex sheet near a separation point. *Journal of Computational Physics*, 229(13):5280–5298, July 2010.

[10] S. Alben and M. Shelley. Flapping States of a Flag in an Inviscid Fluid: Bistability and the Transition to Chaos. *Physical Review Letters*, 100(7):074301, Feb. 2008.

[11] S. Alben, M. Shelley, and J. Zhang. How flexibility induces streamlining in a two-dimensional flow. *Physics of Fluids*, 16(5):1694, Apr. 2004.

[12] R. Albertani, B. Stanford, J. P. Hubner, and P. G. Ifju. Aerodynamic Coefficients and Deformation Measurements on Flexible Micro Air Vehicle Wings. *Experimental Mechanics*, 47(5):625–635, Feb. 2007.

[13] J. J. Allen, A. H. Techet, R. M. Kelso, and A. J. Smits. Energy Harvesting Eel. In *14th Australasian Fluid Mechanics Conference*, Adelaide, Australia, 2001.

[14] W. Anderson, L. Rieti, and R. Schmehl. Aerodynamic Load Modeling on Inflated Leading Edge Wing Airfoils. *submitted to AIAA Journal of Aircraft*, 2015.

[15] S. Arbós-Torrent, B. Ganapathisubramani, and R. Palacios. Leading- and trailing-edge effects on the aeromechanics of membrane aerofoils. *Journal of Fluids and Structures*, 38:107–126, Apr. 2013.

[16] C. L. Archer and K. Caldeira. Global Assessment of High-Altitude Wind Power. *Energies*, 2(2):307–319, May 2009.

[17] M. Argentina and L. Mahadevan. Fluid-flow-induced flutter of a flag. *Proceedings of the National academy of Sciences of the United States of America*, 102.6:1829–1834, 2005.

[18] I. Asher, M. Drela, and J. Peraire. A Low Order Model for Vertical Axis Wind Turbines. In *28th AIAA Applied Aerodynamics Conference*, Chicago, IL, USA, 2010. AIAA 2010-4401.

[19] P. A. Aswatha Narayana. Influence of turbulence on the derivation of the drag from wake measurements. Technical report, Technische Universiteit Delft. Report LR-748., Delft, Netherlands, 1995.

[20] B. Augier, P. Bot, F. Hauville, and M. Durand. Dynamic behaviour of a flexible yacht sail plan. *Ocean Engineering*, 66:32–43, July 2013.

[21] K. I. Bailey, P. S. Jackson, and R. G. J. Flay. Modelling viscous flow around 2D yacht mast and sail configurations. In *13th Australasian Fluid Mech. Conf.*, pages 519–522, Melbourne, Australia, 1998.

[22] S. Banerjee and M. Patil. Aeroelastic analysis of membrane wings. *Proc. 49th AIAA/ASME/ASCE/AHS/ASC Structures, Structural Dynamics, and Materials Conference*, 2008.

[23] L. A. Barba, A. Leonard, and C. B. Allen. Advances in viscous vortex methods meshless spatial adaption based on radial basis function interpolation. *International Journal for Numerical Methods in Fluids*, 46:1–32, 2004.

[24] B. Béguin, C. Breitsamter, and A. Nikolaus. Aerodynamic Investigations of a Morphing Membrane Wing. *AIAA Journal*, 50(11):2588–2599, 2012.

[25] J. Berens. *Dynamic Nonlinear Aeroelastic Behaviour of Flexible Wings in an Airflow*. Msc, Technische Universiteit Delft, 2015.

[26] M. Blair. A compilation of the mathematics leading to the doublet lattice method. Technical report, US Air Force Wright Laboratory. WL-TR-92-3028, 1992.

[27] A. Bosch. Personal Communivation to Roland Schmehl, 24 Aug. 2014.

[28] H. A. Bosch. *Finite element analysis of a kite for power generation*. Msc, Technische Universiteit Delft, 2012.

[29] J. Breukels. *An Engineering Methodology for Kite Design*. Phd thesis, TU Delft, 2011.

[30] J. Breukels and W. J. Ockels. A Multi-Body System Approach to the Simulation of Flexible Membrane Airfoils. *Aerotecnica Missili \& Spazio*, 89(3):119–134, 2010.

[31] A. Bruining. Aerodynamic characteristics of a curved plate airfoil section at Reynolds numbers 60.000 and 100.000 and angles of attack from -10 to +90 degrees., 1979.

[32] B. T. Buerge. The Influence of Surface Roughness on the Drag of Very Large Airships. In *AIAA Aerodynamic Decelerator Systems Technology Conference 2013 (and AIAA Balloon Systems Technology Conference and AIAA Lighter-Than-Air Systems Technology Conference)*, pages 1760–1765, Daytona Beach, Florida, USA, 2013. AIAA.

[33] U. Bunge, T. Rung, and F. Thiele. Turbulent Two-Dimensional Flow Around a Flexible Membrane Airfoil. In S. Wagner, U. Rist, H.-J. Heinemann, and R. Hilbig, editors, *New Results in Numerical and Experimental Fluid Mechanics III*, volume 77, chapter 10, pages 273–280. Springer Berlin Heidelberg, Berlin, Heidelberg, 2002.

[34] P. F. P. Carqueija. *Aerodynamic Investigations of a High-altitude Wind Energy Extraction System Kite Energy System*. Msc thesis, Technical University of Lisbon, 2010.

[35] T. Cebeci, G. J. Mosinskis, and A. M. O. Smith. Calculation of Separation Points in Incompressible Turbulent Flows. *Journal of Aircraft*, 9(9):618–624, Sept. 1972.

[36] L. G. Chambers. A variational formulation of the Thwaites Sail Equation. *The Quarterly Journal of Mechanics and Applied Mathematics*, 19(2):221–231, Jan. 1966.

[37] T. Charvet, F. Hauville, and S. Huberson. Numerical simulation of the flow over sails in real sailing conditions. *Journal of Wind Engineering and Industrial Aerodynamics*, 63(1-3):111–129, Oct. 1996.

[38] P. Cicala. Present state of development in nonsteady motion of a lifting surface. Technical report, National Advisory Council for Aeronautics. NACA TM 1277., Washington DC, USA, 1951.

[39] R. Clements and D. Maull. The representation of sheets of vorticity by discrete vortices. *Progress in Aerospace Sciences*, 16(2):129–146, Jan. 1975.

[40] J. G. Coder and M. D. Maughmer. Numerical Validation of the Squire-Young Formula for Profile Drag Prediction. In *51st AIAA Aerospace Sciences Meeting including the New Horizons Forum and Aerospace Exposition*, Grapevine, Texas, USA, 2013.

[41] E. G. M. Coenen, A. E. P. Veldman, and G. Patrianakos. Viscous-inviscid interaction method for wing calculation. In *European Congress on Computational Methods in Applied Sciences and Engineering*, Barcelona, Spain, 2000.

[42] G.-H. Cottet and P. D. Koumoutsakos. *Vortex Methods: Theory and Practice*. Cambridge University Press, Cambridge, UK, 2000.

[43] S. Cyr and B. Newman. Flow past two-dimensional membrane aerofoils with rear separation. *Journal of Wind Engineering and Industrial Aerodynamics*, 63(1-3):1–16, Oct. 1996.

[44] S. de Groot. *Modelling the Dynamics of an Arc-shaped Kite for Control Law Design*. Msc, Technische Universiteit Delft, 2010.

[45] E. de Langre. Effects of Wind on Plants. *Annual Review of Fluid Mechanics*, 40(1):141–168, Jan. 2008.

[46] A. M. de Luca, M. F. Reeder, M. V. Ol, J. Freeman, I. Bautista, and M. Simonich. Experimental investigation into the aerodynamic properties of a flexible and rigid wing micro air vehicle. In *24th AIAA Aerodynamic Measurement Technology and Ground Testing Conference*, Portland, Oregon, USA, 2004.

[47] G. de Matteis and L. de Socio. Nonlinear aerodynamics of a two-dimensional membrane airfoil with separation. *Journal of Aircraft*, 23(11):831–836, Nov. 1986.

[48] G. de Nayer and M. Breuer. Numerical FSI investigation based on LES: Flow past a cylinder with a flexible splitter plate involving large deformations (FSI-PfS-2a). *International Journal of Heat and Fluid Flow*, Sept. 2014.

[49] G. de Nayer, A. Kalmbach, M. Breuer, S. Sicklinger, and R. Wüchner. Flow past a cylinder with a flexible splitter plate: A complementary experimentalnumerical investigation and a new FSI test case (FSI-PfS-1a). *Computers & Fluids*, 99:18–43, July 2014.

[50] G. de Oliveira. A Reflection on the Biot-Savart Law. Technical report, Technical University of Delft., Delft, Netherlands, 2014.

[51] M. Deaves. *Reynolds-Average-Navier-Stokes Methods Applied to the Non-Linear 3D Flow Effects Relevant for Leading Edge Inflatable Kites*. Msc, Technische Universiteit Delft, 2015.

[52] R. den Boer. Low speed aerodynamic characteristics of a two-dimensional sail wing with adjustable slack of the sail. Technical report, Technische Hogeschool Delft, Delft, Netherlands, 1980.

[53] R. G. den Boer. Numerical and experimental investigation of the aerodynamics of double membrane sailwing airfoil sections. Technical report, Technische Hogeschool Delft, Delft, Netherlands, 1982.

[54] M. Drela. XFOIL: An Analysis and Design System for Low Reynolds Number Airfoils. In T. J. Mueller, editor, *Low Reynolds Number Aerodynamics*, volume 54 of *Lecture Notes in Engineering*, pages 1–12. Springer Berlin Heidelberg, Berlin, Heidelberg, 1989.

[55] M. Drela. Lecture 2 Notes, 16.Uni Unified Engineering - Fluids. Massachusetts Institute of Technology, 2008.

[56] M. Drela. Lecture 6 Notes, 16.Uni Unified Engineering - Fluids. Massachusetts Institute of Technology, 2008.

[57] M. Drela. Design Commentary. 16.821 Flight Vehicle Engineering. Massachusetts Institute of Technology, 2010.

[58] J. P. Dugan. A free-streamline model of the two-dimensional sail - download.php. *Journal of Fluid Mechanics*, 42(3):433–446, 1970.

[59] J. A. Ekaterinaris and M. F. Platzer. Computational prediction of airfoil dynamic stall. *Progress in Aerospace Sciences*, 33(11-12):759–846, Apr. 1998.

[60] J. D. Eldredge. Numerical simulation of the fluid dynamics of 2D rigid body motion with the vortex particle method. *Journal of Computational Physics*, 221(2):626–648, Feb. 2007.

[61] J. D. Eldredge. Dynamically coupled fluidbody interactions in vorticity-based numerical simulations. *Journal of Computational Physics*, 227(21):9170–9194, Nov. 2008.

[62] A. Fage and F. C. Johansen. On the Flow of Air behind an Inclined Flat Plate of Infinite Span. *Proceedings of the Royal Society A: Mathematical, Physical and Engineering Sciences*, 116(773):170–197, Sept. 1927.

[63] C. Farhat. Hierarchy of Mathematical Models. AA 214B Numerical Methods for Compressible Flows., 2014.

[64] U. Fechner, R. V. D. Vlugt, E. Schreuder, and R. Schmehl. Dynamic Model of a Pumping Kite Power System. *Renewable Energy*, 83:705–716, 2015.

[65] L. Feldman. XERXES: a sail bladed wind turbine. In *Proceedings of the 24th Intersociety Energy Conversion Engineering Conference*, pages 2087–2095. IEEE, 1989.

[66] S. P. Fiddes and J. H. Gaydon. A new vortex lattice method for calculating the flow past yacht sails. *Journal of Wind Engineering and Industrial Aerodynamics*, 63(1-3):35–59, Oct. 1996.

[67] M. P. Fink. Full-scale investigation of the aerodynamic characteristics of a model employing a sailwing concept. Technical Report July, National Aeronautics and Space Administration. NASA TN D-4062, Washington DC, USA, 1967.

[68] M. P. Fink. Full-scale investigation of the aerodynamic characteristics of a sailwing of aspect ratio 5.9. Technical Report February, National Aeronautics and Space Administration. NASA TN D-5047, Washington DC, USA, 1969.

[69] R. G. J. Flay and P. S. Jackson. Flow simulations for wind-tunnel studies of sail aerodynamics. *Journal of Wind Engineering and Industrial Aerodynamics*, 44(1-3):2703–2714, Oct. 1992.

[70] F. Fossati and S. Muggiasca. Experimental investigation of sail aerodynamic behavior in dynamic conditions. *Journal of Sailboat Technolgy*, 3:2011–02, 2011.

[71] F. Fossati and S. Muggiasca. Motions of a sailing yacht in large waves: an opening simple instationary modelling approach. In *22th International Symposium on Yacht Design and Yacht Construction*, Amsterdam, Netherlands, 2012.

[72] B. Franca. Kite Data Sheet V2 V3. Technical report, Technical University of Delft, Delft, Netherlands, 2012.

[73] F. Friedl. *Fault-Tolerant Design of a Pumping Kite Power Flight Control System,*. Msc, Graz University, 2015.

[74] C. Galliot. Biaxial Test Report: Ripstop Nylon (Spinnaker). Technical report, EMPA Center for Synergetic Structures, Dübendorf, Switzerland, 2011.

[75] R. Galvao, E. Israeli, A. Song, X. Tian, K. Bishop, S. Swartz, and K. Breuer. The Aerodynamics of Compliant Membrane Wings Modeled on Mammalian Flight Mechanics. In *36th AIAA Fluid Dynamics Conference and Exhibit*, San Francisco, California, USA, 2006.

[76] M. Gaunaa, P. F. P. Carqueija, P.-E. E. Réthoré, and N. N. Sø rensen. A computationally efficient method for determining the aerodynamic performance of kites for wind energy applications. In *EWEA 2011*, Brussels, 2011. EWEA.

[77] F. C. Gerhardt, R. G. J. Flay, and P. Richards. Unsteady aerodynamics of two interacting yacht sails in two-dimensional potential flow. *Journal of Fluid Mechanics*, 668:551–581, Dec. 2011.

[78] A. Ginevsky and A. I. Zhelannikov. *Vortex wakes of Aircrafts*. Springer Science & Business Media, 2009.

[79] R. E. Gordnier. High fidelity computational simulation of a membrane wing airfoil. *Journal of Fluids and Structures*, 25(5):897–917, July 2009.

[80] K. Graf, A. Hoeve, and S. Watin. Comparison of full 3D-RANS simulations with 2D-RANS/lifting line method calculations for the flow analysis of rigid wings for high performance multihulls. In *3rd International Conference on Innovation in High Performance Sailing Yachts*, pages 71–84, Lorient, France, July 2013.

[81] S. Greenhalgh. A three dimensional inextensible lifting membrane wing-experimental results. Technical report, Naval Air Development Center. NADC-83130-60., Warminster, Pennsylvania, USA, 1983.

[82] S. Greenhalgh, H. C. J. Curtiss, and B. Smith. Aerodynamic properties of a two-dimensional inextensible flexible airfoil. In *AIAA Applied Aerodynamics Conference*, volume 22, pages 865–870, Danvers, Massachusetts, USA, May 1983.

[83] A. He. *Conformal mapping and variational methods for interfacial dynamics in fluids*. Phd, Pennsylvania State University, 2011.

[84] S. Heathcote, D. Martin, and I. Gursul. Flexible Flapping Airfoil Propulsion at Zero Freestream Velocity. *AIAA Journal*, 42(11), 2004.

[85] H. E. Heffner and R. S. Heffner. Hearing Ranges of Laboratory Animals. *Journal of the American Association for Laboratory Animal Science*, 46(1):20–22, 2007.

[86] V. S. Holla, K. P. Rao, C. B. Asthana, and A. Arokkiaswamy. Aerodynamic characteristics of pretensioned elastic membrane rectangular sailwings. *Computer Methods in Applied Mechanics and Engineering*, 44(1):1–16, June 1984.

[87] B. J. C. Horsten and L. L. M. Veldhuis. A New Hybrid Method to Correct for Wind Tunnel Wall- and Support Interference On-line. *World Academy of Science, Engineering and Technology*, 58:507–514, 2009.

[88] J. P. How. Lecture 4, 16.333 Aircraft Stability and Control, 2004.

[89] M. Howe. *Acoustics and Aerodynamic Sound*, volume 30. Cambridge University Press, 2014.

[90] H. Hu, A. G. Kumar, G. Abate, and R. Albertani. An experimental investigation on the aerodynamic performances of flexible membrane wings in flapping flight. *Aerospace Science and Technology*, 14(8):575–586, Dec. 2010.

[91] J. Hubner and T. Hicks. Trailing-edge scalloping effect on flat-plate membrane wing performance. *Aerospace Science and Technology*, 15(8):670–680, Dec. 2011.

[92] G. Iaccarino, A. Ooi, P. A. Durbin, and M. Behnia. Reynolds averaged simulation of unsteady separated flow. *International Journal of Heat and Fluid Flow*, 24:147–156, 2003.

[93] H. M. Irvine. A note on luffing in sails. *Proceedings of the Royal Society of London. Series A, Mathematical and Physical Sciences*, 365(1722):345–347, 1979.

[94] P. S. Jackson. A Simple Model for Elastic Two-Dimensional Sails. *AIAA Journal*, 21(1):153–155, Jan. 1983.

[95] P. S. Jackson and S. P. Fiddes. Two dimensional viscous flow past flexible sail section close to ideal incidence. *Aeronautical Journal*, 99(986), 1995.

[96] M. A. Jones. The separated flow of an inviscid fluid around a moving flat plate. *Journal of Fluid Mechanics*, 496:405–441, 2003.

[97] D. D. Joseph. Viscous potential flow. *Journal of Fluid Mechanics*, 479:191–197, Mar. 2003.

[98] J. Katz and A. Plotkin. *Low-speed aerodynamics*. Cambridge University Press, Cambridge, UK, 2 edition, 2010.

[99] S. Kawabata and M. Niwa. Objective measurement of fabric mechanical property and quality: Its application to textile and clothing manufacturing. *International Journal of Clothing Science and Technology*, 3(1):7–18, 1991.

[100] M. Kiya and M. Arie. A contribution to an inviscid vortex-shedding model for an inclined flat plate in uniform flow. *Journal of Fluid Mechanics*, 82(02):223–240, Apr. 1977.

[101] J. J. Knight, A. D. Lucey, and C. T. Shaw. Fluidstructure interaction of a two-dimensional membrane in a flow with a pressure gradient with application to convertible car roofs. *Journal of Wind Engineering and Industrial Aerodynamics*, 98(2):65–72, Feb. 2010.

[102] I. M. Kroo. Aerodynamics, Aeroelasticity and Stability of Hang Gliders - Experimental Results. Technical Report April, National Aeronautics and Space Administration. Technical Memorandum 81269, Moffett Fields, California, USA, 1981.

[103] J. Lee and S. Lee. Fluidstructure interaction analysis on a flexible plate normal to a free stream at low Reynolds numbers. *Journal of Fluids and Structures*, 29:18–34, Feb. 2012.

[104] J. G. Leishman. *Principles of Helicopter Aerodynamics*. Cambridge University Press, New York, New York, USA, 2 edition, 2006.

[105] R. Leloup. *Modelling approach and numerical tool developments for kite performance assessment and mechanical design; application to vessels auxiliary propulsion*. Phd, Universite de Bretagne Occidentale, 2014.

[106] A. Leonard. Vortex methods for flow simulation. *Journal of Computational Physics*, 37(3):289–335, Oct. 1980.

[107] T. Levi-Civita. *Scie e leggi di resistenza , volume t.II*. Publ. a cura dell Acad. naz. dei Lincei, Bologna, Italy, 1956.

[108] Y. Lian and W. Shyy. Numerical Simulations of Membrane Wing Aerodynamics for Micro Air Vehicle Applications. *Journal of Aircraft*, 42(4):865–873, 2005.

[109] Y. Lian, W. Shyy, D. Viieru, and B. Zhang. Membrane wing aerodynamics for micro air vehicles. *Progress in Aerospace Sciences*, 39(6-7):425–465, Aug. 2003.

[110] J. H. Lienhard. Synopsis of lift, drag, and vortex frequency data for rigid circular cylinders. Technical report, Washington State University. Bulletin 300., Pullman, Washington, USA, 1966.

[111] A. C. Limache. Hodograph method for airfoil design: the general case. *Journal of Aircraft*, 33(4), 1996.

[112] P. F. Linden and J. S. Turner. The formation of 'optimal' vortex rings, and the efficiency of propulsion devices. *Journal of Fluid Mechanics*, 427:61–72, 2001.

[113] J. Liouville. Extension au cas des trois dimensions de la question du tracé géographique. In J. Liouville, editor, *Applications de l'analyse à la géométrie. G. Monge.*, chapter Note VI, pages 609–616. Bachelier, Paris, 5 edition, 1850.

[114] J. Liouville. Théorème sur l'équation dx^2+dy^2+dz^2=\lambda(d\alpha^2+d\beta^2+d\gamma^2). *Journal de mathématiques pures et appliquées 1re série*, 15:103, 1850.

[115] C. Liu. *Wake Vortex Encounter Analysis with Different Wake Vortex Models Using Vortex-Lattice Method*. Msc, Delft University of Technology, 2007.

[116] S. G. Llewellyn Smith. How do singularities move in potential flow? *Physica D: Nonlinear Phenomena*, 240(20):1644–1651, Oct. 2011.

[117] O. Lorillu, R. Weber, and J. Hureau. Numerical and experimental analysis of two-dimensional separated flows over a flexible sail. *Journal of Fluid Mechanics*, 466:319–341, Sept. 2002.

[118] J. Madsen, K. Lenz, P. Dynampally, and S. P. Investigation of grid resolution requirements for detached eddy simulation of flow around thick airfoil sections. In *EWEC 2009.*, 2009.

[119] H. R. Malonek and R. de Almeida. A note on a generalized Joukowski transformation. *Applied Mathematics Letters*, 23(10):1174–1178, Oct. 2010.

[120] G. M. Maneia. *Aerodynamic study of airfoils and wings for power kites applications.* Msc thesis, Politecnico di Torino, 2007.

[121] L. Manickathan. *Hybrid Eulerian-Lagrangian Vortex Particle Method.* Msc, Technical University of Delft, 2014.

[122] D. Mateescu and M. Abdo. Nonlinear theoretical solutions for airfoil aerodynamics. In *21st Applied Aerodynamics Conference AIAA 2003-4296*, Orlando, Florida, 2003.

[123] D. Mateescu and B. G. Newman. Analysis of flexible-membrane and jet-flapped airfoils using velocity singularities. *Journal of Aircraft*, 28(11):789–795, Nov. 1991.

[124] D. Mateescu, J. F. Seytre, and A. M. Berhe. Theoretical Solutions for Finite-Span Wings of Arbitrary Shapes Using Velocity Singularities. *Journal of Aircraft*, 40(3):450–460, 2003.

[125] M. D. Maughmer. Optimization and characteristics of a sailwing windmill rotor. *Princeton Univ. Report*, Mar. 1976.

[126] L. May. OpenFOAM CFD on kites. Technical report, Technical University of Delft, Delft, Netherlands, 2014.

[127] B. W. McCormick. *Aerodynamics, aeronautics, and flight mechanics.* Wiley, Danvers, Massachusetts, USA, 1979.

[128] U. B. Mehta and Z. Lavan. Starting vortex, separation bubbles and stall: a numerical study of laminar unsteady flow around an airfoil. *Journal of Fluid Mechanics*, 67(02):227–256, Mar. 1975.

[129] M. R. Mendenhall, J. N. Nielsen, and S. B. Spangler. Review of methods for predicting the aerodynamic characteristics of parawings. *Journal of Aircraft*, 5(6):597–605, Nov. 1968.

[130] M. R. Mendenhall, S. B. Spangler, and J. N. Nielsen. Investigation of methods for predicting the aerodynamic characteristics of two-lobed parawings. Technical report, National Aeronautics and Space Administration. NASA CR-1166, Palo Alto, California, USA, 1968.

[131] S. Michelin and S. G. Llewellyn Smith. An unsteady point vortex method for coupled fluidsolid problems. *Theoretical and Computational Fluid Dynamics*, 23(2):127–153, May 2009.

[132] S. Michelin and S. G. Llewellyn Smith. Resonance and propulsion performance of a heaving flexible wing. *Physics of Fluids*, 21(7):071902, July 2009.

[133] S. Michelin, S. G. Llewellyn Smith, and B. J. Glover. Vortex shedding model of a flapping flag. *Journal of Fluid Mechanics*, 617:1, Nov. 2008.

[134] S. Müller. *Modellierung, Stabilität und Dynamik von Gleitschirmsystemen.* Phd thesis, TU Munich, 2002.

[135] E. Muntz. Rarefied Gas Dynamics. *Rev. Fluid. Mech.*, 21:387–417, 1989.

[136] H. Murai and S. Maruyama. Possibility of various airfoil shape modes and their steady-state stability of single membrane sailwing. *Bulletin of the JSME-Japan Society of Mechanical Engineergs*, 27(225):450–457, 1984.

[137] J. Murua, R. Palacios, and J. M. R. Graham. Applications of the unsteady vortex-lattice method in aircraft aeroelasticity and flight dynamics. *Progress in Aerospace Sciences*, 55:46–72, Nov. 2012.

[138] B. G. Newman. Aerodynamic theory for membranes and sails. *Progress in Aerospace Sciences*, 24(1):1–27, Jan. 1987.

[139] B. G. Newman and H. T. Low. Two-dimensional impervious sails: experimental results compared with theory. *Journal of Fluid Mechanics*, 144:445–462, Apr. 1984.

[140] B. G. Newman and M. P. Païdoussis. The stability of two-dimensional membranes in streaming flow. *Journal of Fluids and Structures*, 5(4):443–454, July 1991.

[141] J. N. Nielsen. Theory of Flexible Aerodynamic Surfaces. *Journal of Applied Mechanics*, 30(3):435, Sept. 1963.

[142] R. A. Ormiston. Theoretical and experimental aerodynamics of the sailwing. *Journal of Aircraft*, 8(2):77–84, May 1971.

[143] X. Ortiz, D. Rival, and D. Wood. Forces and Moments on Flat Plates of Small Aspect Ratio with Application to PV Wind Loads and Small Wind Turbine Blades. *Energies*, 8:2438–2453, 2015.

[144] K. Padian and J. M. V. Rayner. The wings of pterosaurs. *American Journal of Science*, 293(A):91–166, 1993.

[145] C. S. Peskin. The immersed boundary method. *Acta Numerica*, 11:479–517, July 2003.

[146] A. Raj. Investigation on modelling fluid-structure interaction of a LEI kite. Technical report, Danish Technical University. Special Course - Kite Power., 2013.

[147] M. Ranneberg. Direct Wing Design and Inverse Airfoil Identification with the Nonlinear Weissinger Method. *Cornell Physics.Flu-Dyn*, Jan. 2015.

[148] F. M. Rogallo, J. G. Lowry, D. R. Croom, and R. T. Taylor. Preliminary investigation of a paraglider. Technical report, National Aeronautics and Space Agency. Technical Note D-443, Langley Field, Virginia, USA, 1960.

[149] P. Rojratsirikul. *Aerodynamics of flexible membranes*. Phd, University of Bath, 2010.

[150] P. Rojratsirikul, M. S. Genc, Z. Wang, and I. Gursul. Flow-induced vibrations of low aspect ratio rectangular membrane wings. *Journal of Fluids and Structures*, 27(8):1296–1309, Nov. 2011.

[151] P. Rojratsirikul, Z. Wang, and I. Gursul. Unsteady fluidstructure interactions of membrane airfoils at low Reynolds numbers. *Experiments in Fluids*, 46(5):859–872, Feb. 2009.

[152] P. Rojratsirikul, Z. Wang, and I. Gursul. Effect of pre-strain and excess length on unsteady fluidstructure interactions of membrane airfoils. *Journal of Fluids and Structures*, 26(3):359–376, Apr. 2010.

[153] M. B. Ruppert. *Development and validation of a real time pumping kite model*. Msc, Technische Universiteit Delft, 2012.

[154] T. Sarpkaya. Computational Methods With Vortices - The 1988 Freeman Scholar Lecture. *Journal of Fluids Engineering*, 111(1):5, Mar. 1989.

[155] R. Schmehl. Personal Communication to Rachel Leuthold, 4 Sept. 2014.

[156] R. Schmehl. *Tropfendeformation und Nachzerfall bei der technischen Gemischaufbereitung*. Phd, Universitaet Karlsruhe, 2003.

[157] T. Sebastian and M. Lackner. Development of a free vortex wake method code for offshore floating wind turbines. *Renewable Energy*, 46:269–275, Oct. 2012.

[158] P. Seide. Large deflections of rectangular membranes under uniform pressure. *International Journal of Non-Linear Mechanics*, 12(6):397–406, Jan. 1977.

[159] C. Sequeira, D. Willis, and J. Peraire. Comparing Aerodynamic Models for Numerical Simulation of Dynamics and Control of Aircraft. In *44th AIAA Aerospace Sciences Meeting and Exhibit. January*, Reno, Nevada, USA, 2006.

[160] R. K. Shukla and J. D. Eldredge. An inviscid model for vortex shedding from a deforming body. *Theoretical and Computational Fluid Dynamics*, 21(5):343–368, July 2007.

[161] S. Shukla, R. Govardhan, and J. Arakeri. Flow over a cylinder with a hinged-splitter plate. *Journal of Fluids and Structures*, 25(4):713–720, May 2009.

[162] C. W. Smith and I. C. Bhateley. Application of the Vortex-Lattice Technique to the Analysis of Thin Wings with Vortex Separation and Thick Multi-Element Wings. *Vortex-Lattice Utilization. NASA SP-405*, 1976.

[163] R. Smith and W. Shyy. Computation of unsteady laminar flow over a flexible twodimensional membrane wing. *Physics of Fluids*, 7(9):2175–2184, Sept. 1995.

[164] R. Smith and W. Shyy. Computational model of flexible membrane wings in steady laminar flow. *AIAA Journal*, 33(10):1769–1777, Oct. 1995.

[165] R. Smith and W. Shyy. Computation of aerodynamic coefficients for a flexible membrane airfoil in turbulent flow: A comparison with classical theory. *Physics of Fluids*, 8(12):3346, Dec. 1996.

[166] R. W. Smith. *A viscous flow based membrane wing model*. Phd, University of Florida, 1994.

[167] A. D. Sneyd. Aerodynamic coefficients and longitudinal stability of sail aerofoils. *Journal of Fluid Mechanics*, 149:127–146, Apr. 1984.

[168] A. Song, X. Tian, E. Israeli, R. Galvao, K. Bishop, S. Swartz, and K. Breuer. Aeromechanics of Membrane Wings with Implications for Animal Flight. *AIAA Journal*, 46(8):2096–2106, May 2008.

[169] A. J. Song and K. S. Breuer. Dynamics of a Compliant Membrane as Related to Mammalian Flight. In *45th AIAA Aerospace Sciences Meeting and Exhibit*, Reno, Nevada, USA, 2007.

[170] B. Stanford, R. Albertani, and P. Ifju. Static Finite Element Validation of a Flexible Micro Air Vehicle. *Experimental Mechanics*, 47(2):283–294, Jan. 2007.

[171] B. Stanford, P. Ifju, R. Albertani, and W. Shyy. Fixed membrane wings for micro air vehicles: Experimental characterization, numerical modeling, and tailoring. *Progress in Aerospace Sciences*, 44(4):258–294, May 2008.

[172] J. Steinhoff and K. Suryanarayanan. The treatment of vortex sheets in compressible potential flow. Technical report, AIAA. 83-1881, Tullahoma, Tennessee, USA, 1983.

[173] T. Sugimoto. A theory for inextensible and high aspect-ratio sails. *Journal of Wind Engineering and Industrial Aerodynamics*, 63(1-3):61–75, Oct. 1996.

[174] M. Tamai, J. T. Murphy, and Hu. An Experimental Study of Flexible Membrane Airfoils at Low Reynolds Numbers. In *46th AIAA Aerospace Sciences Meeting and Exhibit*, Reno, Nevada, USA, 2008.

[175] C. Thill, J. Etches, I. Bond, K. Potter, and P. Weaver. Morphing Skins. *The Aeronautical Journal*, 112(1129):117–139, 2008.

[176] B. Thwaites. The Aerodynamic Theory of Sails. I. Two-Dimensional Sails. *Proceedings of the Royal Society A: Mathematical, Physical and Engineering Sciences*, 261(1306):402–422, May 1961.

[177] A. Timpe, Z. Zhang, J. Hubner, and L. Ukeiley. Passive flow control by membrane wings for aerodynamic benefit. *Experiments in Fluids*, 54(3):1471, Feb. 2013.

[178] R. Tojeiro. Liouville's theorem revisited. *Lenseignement mathématique 2e Série*, 53:67–86, 2007.

[179] A. Uranga. *Investigation of transition to turbulence at low Reynolds numbers using Implicit Large Eddy Simulations with a Discontinuous Galerkin method*. Phd, Massachusetts Institute of Technology, 2011.

[180] P. C. M. van den Borne. Ontwerp en experimentele verificatie van een profiel voor een zeildoekvleugel. Technical report, Technische Hogeschool Delft, Delft, Netherlands, 1984.

[181] M. van Dyke. *An Album of Fluid Motion*. Parabolic Press, Stanford, CA, USA, 1982.

[182] W. van Hoydonck. *Computation of Rotorcraft Wake Geometry using NURBS*. Phd, Technische Universtiteit Delft, 2013.

[183] R. H. M. van Kappel. *Aerodynamic analysis tool for dynamic leading edge inflated kite models: a nonlinear vortex lattice method*. Msc, Technische Universiteit Delft, 2012.

[184] G. H. Vatistas, V. Kozel, and W. C. Mih. A simpler model for concentrated vortices. *Experiments in Fluids*, 11(1):73–76, Apr. 1991.

[185] S. L. Veldman. *Design and Analysis Methodologies for Inflated Beams*. Phd, Technische Universiteit Delft, 2005.

[186] G. R. Vemaganti, E. A. Thornton, and A. R. Wieting. Structured and unstructured remeshing method for high-speed flows. *Journal of Spacecraft and Rockets*, 28(2):158–164, 1991.

[187] M. Visbal and R. Gordnier. Numerical simulation of the interaction of a transitional boundary layer with a 2-D flexible panel in the subsonic regime. *Journal of Fluids and Structures*, 19(7):881–903, Aug. 2004.

[188] H. T. Vivian and L. V. Andrews. Application of the Subsonic Kernel Function to Nonplanar Lifting Surfaces. Unsteady Aerodynamics for Advanced Configurations. Technical report, U.S. Air Force Flight Dynamics Laboratory. FDL-TDR-64-152 Part I., 1965.

[189] K. Voelz. Profil und Auftrieb eines Segels. *Z. Angew. Math. Mech.*, 30:301–317, 1950.

[190] R. M. Waldman and K. S. Breuer. Shape, lift, and vibrations of highly compliant membrane wings. In *43rd Fluid Dynamics Conference*, San Diego, California, USA, 2013.

[191] R. M. Waldman, A. J. Song, D. K. Riskin, S. M. Swartz, and K. S. Breuer. Aerodynamic Behavior of Compliant Membranes as Related to Bat Flight. In *AIAA 38th Fluid Dynamics Conference and Exhibit*, Seattle, Washington, USA, 2008.

[192] M. R. Waszak, L. N. Jenkins, and P. G. Ifju. Stability and control properties of an aeroelastic fixed wing micro aerial vehicle. In *AIAA Atmospheric Flight Mechanics Conference and Exhibit*, Montréal, Canada, 2001.

[193] Y. Watanabe, S. Suzuki, M. Sugihara, and Y. Sueka. An experimental study of paper flutter. *Journal of Fluids and Structures*, 16(4):529–542, May 2002.

[194] C. E. Watkins, J. L. Runyan, and H. J. Cunningham. A systematic kernel function procedure for determining aerodynamic forces on oscillating or steady finite wings at subsonic speeds. Technical report, NASA R-48, 1959.

[195] M. T. Wilkinson. Sailing the skies: the improbable aeronautical success of the pterosaurs. *The Journal of experimental biology*, 210(Pt 10):1663–71, May 2007.

[196] S. Wilkinson. Simple Multilayer Panel Method for Partially Separated Flows Around Two-Dimensional Masts and Sails. *AIAA Journal*, 26(4):394–395, Apr. 1988.

[197] D. J. Willis. *An unsteady, accelerated, high order panel method with vortex particle wakes*. Phd, Massachusetts Institue of Technology, 2006.

[198] H. Winter. Flow phenomena on plates and airfoils of short span. Technical report, National Advisory Committee for Aeronautics. NACA-TM-798., Washington DC, USA, June 1936.

[199] J.-Z. Wu, H.-y. Ma, and M.-D. Zhou. *Vorticity and Vortex Dynamics*. Springer Science & Business Media, 2007.

[200] S. C. Yen and Y. F. Fei. Winglet Dihedral Effect on Flow Behavior and Aerodynamic Performance of NACA0012 Wings. *Journal of Fluids Engineering*, 133(7):071302, 2011.

[201] L. A. Young. Vortex Core Size in the Rotor Near-Wake. Technical report, National Aeronautics and Space Administration. NASA/TM-2003-21227., Moffett Field, California, USA, 2003.

[202] Z. Zhang, L. Hopper, A. Wrist, J. P. Hubner, and L. Ukeiley. Nondimensional frequency scaling of aerodynamically-tensioned membranes. *Journal of Fluids and Structures*, 48:14–26, July 2014.

[203] Z. Zhang, N. Martin, A. Wrist, J. P. Hubner, Y. J. Abudaram, L. Ukeiley, and P. Ifju. Force and Deformation Measurement on Low Aspect Ratio Membrane Airfoils (AIAA). In *51st AIAA Aerospace Sciences Meeting including the New Horizons Forum and Aerospace Exposition*, Grapevine, Texas, USA, 2013.